

**Distributed sensing in flexible robotic fins: propulsive force prediction and
underwater contact sensing**

A Thesis

Submitted to the Faculty

of

Drexel University

by

Jeffrey C Kahn, Jr.

in partial fulfillment of the

requirements for the degree

of

Doctor of Philosophy

November 2016



© Copyright 2017

Jeffrey C Kahn, Jr. All Rights Reserved

Dedication

This work is dedicated to Lizzie.

Acknowledgments

Thank you to the many researchers who have deeply inspired me through your deep engagement in scientific inquiry. We may have met only briefly, but your ideas have influenced this work and my thinking in meaningful ways. Thanks to Ben Mitchinson, Jonathan Platkiewicz, Vincent Hayward, Nathan Lepora, Mitra Hartmann, Melina Hale, and George Lauder.

Thank you to the team of people that have looked at my work and seen more within me than I was able to see in myself. Without you I do not believe that I would have found nearly as much meaning, fulfillment, and excitement in my work. Having you work with me has helped me develop an overwhelming amount of all three for myself. Thank you M. Ani Hsieh and Yon Visell.

And to Professor Tangorra, thank you for demonstrating a model of what truly good work looks like, and for showing me how to find this for myself. Thank you for your support, encouragement, and mentorship in research and science. Thank you for creating a lab in which our team can work together and learn together. It is truly my privilege to have served in the Laboratory of Biological Systems Analysis and to have worked with you.

To the members of the Laboratory of Biological Systems Analysis, thank you for all of your encouragement and support that helped me develop personally and professionally. I've learned so much from working with all of you and had a lot of fun doing so. Thank

you for your extensive paper edits, commentary on my work, encouragement to move forward, and for your many instructional sessions in the machine shop. Thanks to Deeksha Seth, Anthony Mignano, Gabe Carryon, David McDevitt, Sam Shepherd, and Liam Hernandez.

Thanks to the further members of my committee, Antonios Kontsos and Harry Kwatny, both of whom have helped me better communicate my work and clarify my thinking in the thesis. Thanks for your guidance and for your contributions to our many meetings along the way.

Thank you, Bill Mather, for helping me find a path forward through the many possible options for a thesis and for always encouraging me to go forward. Sharing many a lunch chat has been a bright spot in my time at Swarthmore and Drexel.

Thanks to David Peretz, for being a great friend and a fantastic collaborator. Whenever we get together, great things happen. I look forward to many more great things.

Thank you, Lizzie, for being a true partner. I can think of no one more wonderful to share this journey with, and I am so happy to have you by my side. You have always encouraged me to be my best self, and your love and support has made this process even richer and better. I look forward to many more years of adventures with you.

Table of Contents

List of Tables	x
List of Figures	xi
Abstract	xx
Chapter 1. Introduction	1
1.1 Objective	1
1.2 Thesis Organization	8
1.3 Contribution and Novelty	11
Chapter 2. Background	13
2.1 Chapter summary	13
2.2 Pectoral Fins of the Bluegill Sunfish	14
2.2.1 Swimming in the Bluegill Sunfish	14
2.2.2 Touch in the Bluegill Sunfish	15
2.2.3 Sensors in the Bluegill Sunfish	16
2.2.4 Control in the Bluegill Sunfish	17
2.3 Flexible, high-DOF, robotic fins	18
2.3.1 Propulsion in flexible, robotic fins	19
2.3.2 Touch in flexible, robotic fins	20
2.3.3 Sensors in flexible, robotic fins	21
2.3.4 Control in flexible, robotic fins	22
2.4 Sensing and control framework for the thesis	23

2.4.1	Prediction of propulsive forces	24
2.4.2	Discrimination of contact loading from fluidic loading	26
Chapter 3.	Fin-intrinsic sensation for understanding underwater touch.....	29
3.1	Chapter summary	29
3.2	Paper 1: The effects of fluidic loading on underwater contact sensing with robotic fins and beams.....	31
3.2.1	Abstract	31
3.2.2	Introduction.....	31
3.2.3	Methods.....	35
3.2.4	Results.....	44
3.2.5	Discussion	60
3.2.6	Conclusion	65
3.3	Paper 2: An evaluation of contact classification techniques during underwater contact with compliant beams and fins	67
3.3.1	Abstract	67
3.3.2	Introduction.....	67
3.3.3	Methods.....	70
3.3.4	Results.....	75
3.3.5	Discussion and conclusion.....	85
Chapter 4.	System identification methods for force prediction.....	88
4.1	Chapter summary	88
4.2	Input-output models	88

4.3	MISO regression and estimation.....	91
4.4	Nonlinear estimation: Volterra series	94
4.5	Dimensionality reduction of the input matrix by SVD.....	98
4.6	Application of MISO model to force prediction.....	99
4.7	Metrics of estimation performance	100
4.7.1	Sum of squared error (SSE) and mean squared error (MSE).....	100
4.7.2	Variance accounted for (VAF).....	101
4.7.3	Akaike information criterion (AIC)	104
4.7.4	Minimum description length (MDL)	105
Chapter 5.	Estimation of propulsive forces from intrinsic sensory data	107
5.1	Chapter summary	107
5.2	Paper 3: Predicting propulsive forces using distributed sensors in a compliant, high DOF, robotic fin.....	109
5.2.1	Abstract	109
5.2.2	Methods.....	115
5.2.3	Results.....	126
5.2.4	Discussion	145
5.2.5	Conclusion	149
5.3	Paper 4: Distributed sensing and nonlinear MISO models for predicting the propulsive forces of flexible, multi-DOF robotic fins	152
5.3.1	Abstract	152
5.3.2	Introduction.....	152
5.3.3	Methods.....	155

5.3.4	Results.....	162
5.3.5	Discussion and Conclusion.....	173
Chapter 6.	Biologically-inspired control framework for fin-intrinsic sensing	176
6.1	Chapter summary	176
6.2	Paper 5: Hover kinematics and distributed pressure sensing for force control of biorobotic fins	178
6.2.1	Abstract.....	178
6.2.2	Introduction.....	178
6.2.3	Methods.....	181
6.2.4	Results.....	183
6.2.5	Conclusion	195
6.3	Paper 6: Application of a micro-genetic algorithm for gait development on a bio- inspired robotic pectoral fin.....	198
6.3.1	Abstract.....	198
6.3.2	Introduction.....	198
6.3.3	Methods.....	202
6.3.4	Results and Discussion	207
6.3.5	Conclusions.....	212
6.4	Biologically-inspired control framework for closed-loop control of propulsive force using fin-intrinsic sensing.....	215
6.4.1	Sensory feedback and control architecture	215
Chapter 7.	Conclusions.....	224

Chapter 8. Future work	229
Bibliography	235
Appendix A Supplemental Written Materials.....	251
8.1 Scope of the Thesis	251
8.1.1 For sensory mediated control of high speed propulsion.	252
8.1.2 For characterization of the fluid environment.	253
8.1.3 For sensory mediated control of low speed maneuvers and hovering.	255
8.1.4 For touch sensing and interaction with obstacles.	256
8.2 Tracking of fins.....	258
8.2.1 Implementation of kinematics on biorobotic fin.....	259
8.2.2 Kinematic Analysis of fish fins with POD/PCA.....	261
Appendix B Equipment datasheets	264
8.3 Major Equipment	264
8.4 Actuators	264
B1. Touch fin motor gearhead	264
B2. Touch fin motor	266
B3. Touch fin motor general specifications and encoder settings.....	267
B4. Servomotor for pectoral fin.....	269
8.5 Sensors	271
8.5.1 Strain gages for instrumented pectoral fin	271
8.5.2 Pressure sensors for instrumented pectoral fin	274
8.5.3 Pressure sensor amplifier	284

Vita.....	294
-----------	-----

List of Tables

Table 1. Experimental parameters for robotic platform, environment, and obstacles.....	40
Table 2. Summary of contact classification techniques.....	72
Table 3. Confusion matrix of contact classification accuracy	75
Table 4. Error in classification of the instant of contact for beams and fins of moderate stiffness.	84
Table 5. Experimental conditions tested using the biorobotic pectoral fin.....	119
Table 6. Prediction performance for different sensory systems on the robotic fin. ^a	135
Table 7. Hypothesis testing to evaluate model prediction performance across fin gait and fin stroke timing.	145
Table 8. Parameter space of fin ray kinematics	206

List of Figures

Figure 1. Block diagram illustrating the relationship between fin ray stiffness k , driven kinematics g , and the outputs of sensors S and propulsive forces F . The i -th subscript represents the i -th degree of freedom of the robot, i.e. a fin ray in this example. Kinematics are strictly a function of time though stiffness can be either only a function of space or a function of time and space. The propulsive force is created through the fluid structure interaction (FSI) which involves both the force created by the fluid acting on the fin and vice-versa. Actual mechanical phenomena (subscript a), e.g. strain, are measured by the j fin intrinsic sensors (subscript m).	5
Figure 2. A bluegill sunfish hovering in a static water tank. The sunfish primarily uses its pectoral fins at low swimming speeds (e.g. hovering, maneuvering through obstacles, low speed steady swimming). Courtesy of George V. Lauder and Brooke Flammang.....	14
Figure 3. Sunfish contact obstacles using their pectoral fins in cluttered environments. No stereotypical contact patterns have been identified. The mechanics and sensory phenomena of fin contact with obstacles are not well understood. Figures adapted from [3]. Courtesy of Brooke Flammang and George V. Lauder.	16
Figure 4. Afferent nerve fibers in the bluegill sunfish pectoral fins. Fibers terminate in free nerve endings which respond to bending stimuli. Adapted from [20]. Courtesy of Melina Hale.....	17
Figure 5. Simplified control framework for sensory-based control of propulsive forces and of touch interactions.....	24
Figure 6. Close up of block diagram for prediction of propulsive forces.....	25
Figure 7. Close up of block diagram of underwater contact discrimination using fin-intrinsic sensors.....	27
Figure 8. Cross-sectional second moment of inertia as a function of length for the three beams used in this study. The y axis is scaled logarithmically.....	36
Figure 9. Robotic fins and beams used in contact experiments in air and underwater. Flexible, moderate, and stiff beams instrumented with strain gages at proximal and distal locations (a); instrumented beams in silicone webbing create a fin (b); the robotic platform used to drive the beams and fins into obstacles.	37
Figure 10. Obstacles that the fins and beams contact in the study. An acrylic plate obstacle mounted on an aluminum rod (a). A modular obstacle box containing three drawers that can be repositioned to different depths and interchangeable faceplates for presentation of obstacles with different materials (b). Close-up of depth adjustment rail and wingnut to fix drawer depth (c).....	38
Figure 11. Conceptual drawing of the experimental configurations of the obstacle. The beam tips (a) either approached a configuration with a single surface offset by a distance d (b), or a configuration with a stair step pattern of equal relative depths (c). The arrow indicates the direction of motion for the beams (a).	40

- Figure 12. Phases of contact for an fin driven into contact with a rigid obstacle underwater. Phases are shown relative to measured strains (top) and beam position (bottom) in an overhead view. The *initiation* phase lasts from the initiation of movement to the first peak in the distal strain data [A,B], then the *movement* phase begins and continues until the distal strains increase at obstacle approach [B,C] at the start of the *approach* phase. The *approach* phase [C,D] lasts until *contact* starts, and *contact* continues until a peak in the distal strain data [D,E]. *Relaxation* follows until both proximal and distal beams reach a steady state [F]..... 42
- Figure 13. Photographs and strain data of typical contacts for moderate beams in air (a), moderate beams in water (b), and a fin in air (c). Relative contact times and angular offsets are indicated with beams in air as a zero-reference. Data were low pass filtered at 10 Hz for clarity. 45
- Figure 14. The effect of changing beam stiffness on the proximal and distal strains underwater during contact. Representative data are shown for stiff, moderate, and flexible fins and data were low pass filtered at 10 Hz for clarity. 47
- Figure 15. Photographs and strain data of typical contacts for a fin in air (a) and a fin in water (b). Relative contact times and angular offsets are indicated with the fin in air as a zero-reference. Data were low pass filtered at 10 Hz for clarity. 48
- Figure 16. The effect of changing speed of the fins on the strain data of proximal (top) and distal (bottom) sensors underwater during contact. Representative data are shown for trial conditions of 0.1, 0.2, and 0.3 rotations per second. Data were low pass filtered at 10 Hz for clarity. 49
- Figure 17. A representative *approach* phase of obstacle contact for a fin driven underwater. Small increases in strain on fin beams and reaction force on the obstacle were observed during this period. Data were low pass filtered at 5Hz for clarity..... 50
- Figure 18. Comparison of average strains during movement phase for groups of sensors: dorsal proximal and dorsal distal (a), dorsal proximal and medial proximal (b). Second-order polynomial regression fits were applied to the data. Standard error bars correspond to one standard deviation in each direction..... 52
- Figure 19. Comparison of average strains during the *relaxation* phase of contact on the dorsal proximal and dorsal distal sensors. Linear fits were applied to the data. Standard error bars correspond to one standard deviation in each direction. 53
- Figure 20. Peak strains reached during *movement* and *contact* phases for beams and fins underwater measured at dorsal proximal and dorsal distal sensors. Peak strains for proximal sensors on fins (a), peak strains for distal sensors on fins (b), peak strains for proximal sensors on beams (c), and peak strains for distal sensors on beams (d). Representative data are shown from randomly selected trials of listed conditions. 55
- Figure 21. The effects of adding webbing to beams in air (a) and underwater (b) on distributed strain measures during a typical high speed contact (0.3 rot/s). Data were low pass filtered at 10 Hz for clarity..... 57

Figure 22. Comparison of distributed strain measures during typical contacts with an offset obstacle: (a) in air with beams, (b) underwater with beams, (c) in air with beams in webbing, and (d) underwater with beams in webbing. First and second contacts are indicated with dashed red lines and their angular distance is shown. Contact differences between air and water are shown based on initial air contact angles compared to initial water contact angles for beams (b) and beams in webbing (d). Representative data were smoothed with a 3 point averaging filter for clarity and are from a trial at 0.2 rot/s speed with an obstacle offset of $d = 10\text{mm}$. Strains are shown at 0.67 mm/m per division and time is shown at 0.5s per division. 58

Figure 23. Distal strain signals for a typical contact between a fin and a stair-step obstacle underwater. Signals shown are representative of a contact with a [0 10 20]mm rigid obstacle. Contacts are indicated with dashed vertical lines corresponding to each beam within the fin. Data were low pass filtered at 10 Hz for clarity and are from a trial at 0.2 rot/s speed. 59

Figure 24. The effects of webbing on strain sensing with complex obstacle geometries. Photo of a typical contact for a fin underwater with legend overlaid for sensor locations (a); distributed strain signals for beams (b) and fins coming into contact with a stair step obstacle in water. Signals shown are representative of a contact with a [0 10 20]mm rigid obstacle. Data were low pass filtered at 10 Hz for clarity. Strains are shown at 0.67 mm/m per division and time is shown at 0.5s per division. 63

Figure 25. Instrumented beams and fin used in contact experiments. Beams of three stiffnesses instrumented with proximal and distal strain gage sensors (a). A fin, with three embedded beams instrumented with sensors along each beam (b), comes into contact with a complex, stair-step obstacle. 71

Figure 26. Test environments for beams and fins: beams driven in air (a), fin in air (b), beams in water (c), and fin in water (d). 71

Figure 27. Illustration of three contact classification techniques tested: (a) strain threshold, (b) strain rate threshold, and (c) strain difference threshold. For (c), distal strains are subtracted from proximal strains and the difference is used to compute contact. Colored classification bars are shown beneath each time series example. 73

Figure 28. Performance of strain threshold technique. Time series graphs (top; a-d) are representative of typical strains for each structure and environment, and were driven at 0.1 rot/s in pictured examples. Classification rates are shown for each condition. 77

Figure 29. Breakdown of performance in strain threshold technique when the strain due to fluidic loading exceeds the strain due to contact loading. Time series data from stiff beam driven at 1 rot/s and sampled from the proximal sensor. 77

Figure 30. Performance of the strain rate threshold technique. Representative time series data and classification performance are shown for beams in air and underwater (a,b) and fins in air and underwater (c,d). Platform was driven at 0.2 rot/s. 79

Figure 31. Performance of strain differencing technique for beams in air and underwater (a,b) and fins in air and underwater (c,d). Time series data shown are representative of

general trends for beams and fins at moderate speed (0.2 rot/s for fins, 0.5 rot/s for beams). Confusion matrices are shown for each condition's data.....	81
Figure 32. The effect of beam stiffness on strain differencing classification performance during underwater contact. Representative time series data are shown at 0.5 rot/s are shown for beams underwater to illustrate the effects of significant fluidic loading on flexible (a), moderate (b), and stiff (c) beams.	82
Figure 33. The effect of sensor placement (proximal/distal) on performance of the strain threshold classifier for fins in air and fins underwater.	83
Figure 34. The system identification loop. Redrawn from [99].	89
Figure 35. The process of developing a multi-input-single-output (MISO) Sensory-Force prediction model. The user assembles training and testing data from the Data Library by selecting experimental parameters of interest. The force component to be predicted is also selected (e.g. thrust force). Properties of the MISO model are chosen based on the desired complexity of the underlying model. A Trained Kernel is computed from the Training Data, and this kernel is used to predict forces from the Testing Data. Predicted forces are compared to measured forces to determine the error of the model.....	100
Figure 36. Sensory instrumentation and experiments with robotic pectoral fin. Catheter style pressure sensors (a) measured local pressures on both sides of fin webbing and half-bridge strain gages (b) measured local strains (bending). Propulsive forces were measured in the thrust and lateral directions while the fin executed complex kinematic trajectories in experiments (c).	116
Figure 37. Picture summary of all gaits and stroke phases executed by the biorobotic pectoral fin in experiments. Gaits of steady swimming (SS; a), ventral steady swimming (VSS; b), and maneuver (M; c) were divided into outstroke (OUT, abduction) and instroke (IN, adduction) phases. Subsequent pictures were captured at time intervals of $T/8$, where T was the sum of the outstroke and instroke execution times.	120
Figure 38. Force estimation performance of the MISO convolution model. Full stroke (FULL), outstroke (OUT), and instroke (IN) forces estimated for ventral steady swimming (VSS), maneuver (M), and steady swimming (SS) gaits (a). Performance metrics of variance accounted for (b) and mean squared error (c) were computed across conditions. "X" markers on the bar graph indicate that variance accounted for was negative in that case. Representative force magnitudes are shown with $f=1.0\text{Hz}$ at 600x stiffness. Force data were low pass filtered at 7 Hz for clarity and displayed with 0.2N/division in force and 0.2s/division in time.....	128
Figure 39. Force prediction across fin parameter changes. Experimental 2D propulsive force magnitudes can be predicted across changing conditions to flapping frequency (0.65Hz, 1.00Hz, 1.30Hz; left to right) and mechanical properties (400x, 600x, 800x flexural rigidity; top to bottom) without changing sensory model weights. Forces and predictions are shown for steady swimming outstrokes (SS OUT) and are representative of trends in the fin system when gait and stroke phase are held constant. Sensory model weights were trained with delays from $[-200,0]\text{ms}$. Data were low pass filtered at 7 Hz for clarity.....	129

Figure 40. Effects of MISO model time window parameters on force prediction performance. Representative experimental 2D propulsive force and the predicted force from combined (pressure and bending-based models), pressure-based, and bending-based models are shown as the number and value of delay elements are varied in the MISO convolution model (a-c, top) and MSE is computed for these cases (a-c, bottom). Time series predictions are shown for steady swimming outstrokes at 0.65Hz. Mean squared error is shown as the delay (ms) of a single time lag is increased (d). Time series data were low pass filtered at 7 Hz for clarity. 131

Figure 41. Force prediction across changes to stroke phase. Full stroke (FULL), outstroke (OUT), and instroke (IN) forces predicted for ventral steady swimming (VSS), maneuver (M), and steady swimming (SS) gaits (a). Performance metrics of variance accounted for (b) and mean squared error (c) were computed across conditions. “X” markers on the bar graph indicate that variance accounted for was negative in that case. Representative force magnitudes are shown with $f=1.0\text{Hz}$ at 600x stiffness. Data were low pass filtered at 7 Hz for clarity and displayed with 0.2N/division in force and 0.2s/division in time. 134

Figure 42. Force prediction across changes to fin gait. Ventral steady swimming (VSS), steady swimming (SS), and maneuver (M) gait forces are predicted for fin full strokes, outstrokes, and instrokes individually (a). Performance metrics of variance accounted for (b) and mean squared error were computed across conditions (c). “X” markers on the bar graph indicate that variance accounted for was negative in that case. Representative peaks are shown with $f=1.0\text{Hz}$ at 600x stiffness. Data were low pass filtered at 7 Hz for clarity and displayed with 0.2N/division in force and 0.2s/division in time. 137

Figure 43. Optimal sensor combinations for a fixed number of sensors as fin gait and stroke phase are varied. Shaded cells indicate the sensors used in the force magnitude predictions (see Figure 1 for sensor locations). Variance accounted for was computed as a performance metric for each subset of sensors tested on data from fins at 400, 600, and 800x stiffness and 0.65, 1, and 1.3Hz flapping frequency. VAF was averaged for each subset across ten or more trials. Representative fits are shown across changes to flapping frequency (force magnitude peaks at 0.65, 1.00, 1.30 Hz shown; right column). Model time windows of 0 to 20ms (inclusive) were used in fits. Force data were low pass filtered at 5 Hz for clarity. 141

Figure 44. Optimization of model time windows for a fixed gait/stroke combination (a). 1D plots show the optimal time window of sensory weights when variance accounted for (left) and Akaike information criterion are used as optimization criteria. Model performance is compared when VAF and AIC are used as metrics against a baseline of a full 200ms window (b). Force magnitude predictions are compared using these three approaches (c). 144

Figure 45. A biorobotic pectoral fin was submerged underwater (a) and instrumented with distributed strain sensors (b; A, B, C) and pressure sensors (c; outer sensors Ao, Bo, Co shown, inner sensors omitted). Intrinsic sensory measurements were used to predict the measured propulsive forces of the fin during multiple swimming gaits. 156

Figure 46. Comparison of model performance with linear (K1) and nonlinear (K1&K2) kernels for prediction of full stroke forces across multiple swimming gaits.

Representative time series force data and model predictions are shown for thrust forces, lateral forces, and force magnitudes. Percent of variance accounted for (%VAF) is shown with statistics for each case. Error bars show one standard deviation from the sample mean ($N=5$ trials) and asterisks indicate significant differences in %VAF ($P<0.005$)... 164

Figure 47. Prediction of propulsive forces across outstroke and instroke. Performance is shown for time-series data, percent of variance accounted for (%VAF), and MDL cost. Data shown are representative of general trends. Data were filtered at 10Hz..... 166

Figure 48. Prediction of propulsive forces across multiple swimming gaits with linear (K1) and nonlinear (K1&K2, K2) models. The performance of a model trained on multiple gaits, tested on unseen trial data from similar swimming gaits. Performance is shown for time-series data (top), percent of variance accounted for (%VAF, bottom left), and MDL cost (bottom right). Data shown are representative of general trends. Data were filtered at 10Hz for clarity..... 166

Figure 49. Comparison of prediction performance between models formed with pressure versus bending sensory data. Best performance (%VAF, MDL) was observed with a K1&K2 model using bending sensors, regardless of forces and fin conditions. Performance was compared between models formed from outer pressure data, inner pressure data, bending data, and all pressure data. Performance metrics were computed for all three model structures (K1,K1&K2,K2). Thrust force prediction and lateral force prediction are shown. Trial datasets were randomly selected for training and prediction. 168

Figure 50. Force prediction performance compared with data from individual sensors. Performance was compared between models formed from each of the individual sensors (Ao,...,C). Performance metrics were computed for all three model structures (K1,K1&K2,K2). Lateral force prediction is shown as representative of general trends. 170

Figure 51. Optimal subsets of sensors as the number of sensors (N_s) is varied. For example, if thrust forces are predicted, only 2 sensors are used, and a K1&K2 kernel is used, then the optimal sensor choice is (B,C), resulting in 51.39%VAF and an MDL cost of 31.71. Optimal subsets were chosen based on %VAF and were computed for all three model types (K1, K1&K2, K2). Thrust force and lateral force prediction results are shown for predictions across both gait and stroke phase..... 171

Figure 52. Some of the diverse fin motions associated with hover, classified as outstroke (TOP), transitional (MIDDLE), and instroke (BOTTOM) features. Each column represents an observed fin motion from top to bottom. E.g. Column one shows a “flat plate” outstroke with little temporal lag between fin segments, a “upward push” as the transition feature, and a “lift and drop” instroke where the fin rotates downward to meet the body..... 184

Figure 53. Sunfish (TOP) and biorobotic fin (BOTTOM) executing the dominant hover motion of “Ventral led cupping” outstroke to “Flat Plate Lift and Drop” instroke. Robotic fin trajectories were derived by point and velocity tracking of the fin segments through 3D high speed video and mapping of trajectories to the degrees of freedom on the robot.

Robotic trajectories were consistent with sunfish fins through time varying curvature and velocities of fin regions..... 186

Figure 54. Characteristic forces of hover in the thrust-lateral directions. 2D magnitude of force (A.TOP), thrust force (A.MIDDLE), and lateral force (A.BOTTOM) are graphed as fin beat period is varied from 1-4 s in duration. Forces representative of hover in the biology would typically be executed over 1 s (highlighted) and slower. Forces shown in the thrust-lateral plane (B) through varied stiffness show the characteristic representative forces through one fin beat (outstroke to instroke) and allow envisioning of body movement in the thrust-lateral plane. Through the outstroke a strong force is mostly directed laterally, whereas the instroke motion creates strong forces in the thrust and lateral directions. Data are representative of a six-cycle average of the forces and were low-pass filtered at 5Hz for clarity. 188

Figure 55. Hover mean 2d forces (thrust-lateral plane) over one fin beat. Mean force magnitudes increase monotonically as fin beat periods are decreased. Increasing stiffness increases mean magnitudes monotonically. For varied frequencies, data are shown from an 800x fin; for varied stiffness, 0.65Hz flapping frequency data were used. These data are representative of general trends through varied frequencies and stiffness. 190

Figure 56. Distributed pressure measurements on the biorobotic fin during hover motion are good estimates of the magnitude and direction of forces during swimming. Trends are representative across testing conditions. Data are grouped in proximal (black) and distal (grey) measures along the dorsal and ventral leading edges on both inner (black circle, grey outline) and outer (white circle, black outline) fin faces. Data shown at fin beat period of $T = 1.54$ s with an 800x fin. 192

Figure 57. Distributed pressure means through hover with varied fin beat periods and stiffness are useful predictors of two-dimensional force magnitudes. Time varying pressure magnitudes from indicated points were added over the course of one fin beat of hover and then averaged (e.g. (A) shows the mean pressures that result from the sum of all dorsal leading edge pressure signals on the inner and outer faces). Distributed pressures on the ventral leading edge (B) increased monotonically as fin beat period decreased. Pressures on the outer and inner faces of the fin (C), (D) generally increased and pressures on the inner face (D) showed monotonic decrease as fin stiffness increased. 194

Figure 58. In this study, a biologically-inspired pectoral fin platform was used to test the effectiveness of a micro-genetic algorithm for developing gaits in large kinematic spaces. The biorobotic fin (A) matches the kinematics, mechanical properties, and hydrodynamics of the steady swimming gait of a bluegill sunfish (C). The fin is composed of 5 fin rays (B) connected by a flexible webbing (D) that is driven by a servo tendon system to produce forces underwater. The kinematics of the first DOF ("cupping") were labeled FR1, FR4, FR7, FR10, and FR14; these indices refer to their biological counterparts. The kinematics of the second DOF ("sweeping") were labeled FR1b, FR10b, and FR14b. The fin was functionally divided into segments. The long, flexible *dorsal leading edge* is formed by the fin rays and webbing of FR1 and FR4; the *ventral leading edge* formed by the shorter length FR10,FR14 and webbing; the *medial area*

formed by FR7 and webbing. Sunfish image (C) used with permission of George V. Lauder. 201

Figure 59. A block diagram shows the steps of the live testing μ GA - a genetic algorithm that tests small populations and allows for reinitialization of the evolving population. The fitness of candidate gaits was determined through testing when the random population was first generated, and at the generation of each new population (shaded blocks). The main program iterated (dotted line) and tested generations of initial populations until the convergence criterion was reached. Convergence was determined by number of generations per iteration. Diagram modified from [166]. 203

Figure 60. The μ GA evolved a new non-biological swimming gait for thrust production. Evolution of the “bimodal” candidate gait over fifty generations in a local optima region shows the improvement of thrust production (A). The evolution of kinematics (B) show an increase of amplitude on the dorsal leading edge fin rays, causing increase in thrust production through the outstroke ($t=[0,0.25]$ s) and instroke ($t=[0.75,1.25]$ s). “Bimodal” gaits evolved to employ a delayed movement of the ventral kinematics to produce slight thrust in the late instroke ($t=[1.0,1.5]$ s). Data were low pass filtered at 7Hz for clarity. 209

Figure 61. Elite gaits (local optima) of the μ GA approximated the kinematics and force production of known bio-inspired gaits of steady swimming and hovering (not shown). A comparison of an elite (i.e. locally optimal) candidate gait of the μ GA (TOP) to a sunfish steady swimming gait (BOTTOM). Small phase differences in the μ GA solution led to near-optimal performance of the gait. Steady swimming in both the evolved gait and the biology produces a strong thrust force using the dorsal leading edge segment of the fin with little phase lag between fin segments. μ GA solutions typically produced between 80 and 90% of the average thrust of a biologically-inspired steady swimming gait. Steady swimming images modified from [5]. 210

Figure 62. The μ GA revealed fine tuning strategies for fin ray degrees of freedom (DOF) in the biorobotic platform. The kinematic parameters of “Amplitude” and “Frequency” are varied along each of the DOF. “Phase” variations had unclear impacts on fitness and are excluded from these figures. Landscapes were constructed by meshing of 300 candidate solution fitnesses over the broad range explored in one trial of the μ GA. 212

Figure 63. Block diagram showing the mapping from desired robot body dynamics to optimized stroke kinematics. Stroke kinematics are selected from a reference library or evolved using a search algorithm in order to optimize forces to a reference criterion. ... 219

Figure 64. Block diagram of feedback control on fin ray kinematics. Measured kinematics are compared to reference kinematics and the error is fed into a controller which modulates the kinematics of the biorobotic fin. The fin produces forces which are compared to desired forces in order to determine the error in forces. The stroke selection/evolution block is detailed in Figure 63. 220

Figure 65. Block diagram of switching control of propulsive forces. The inner loop executes feedback control on fin ray kinematics (c.f. Figure 64) while the outer loop uses fin-intrinsic sensors to estimate forces from the top and bottom sections of the fin and

compares force estimates to force reference signals. Inspired by the bluegill sunfish, the stroke kinematics can switch multiple times per fin beat in order to modulate forces... 221

Figure 66. Block diagram of control updates within a swimming stroke. Errors in local force and kinematics are used to update the stiffness and kinematic control of the biorobotic fin using an inverse kinematic model that maps from force errors and current kinematics to modified kinematics mid-stroke. 222

Figure 67. Block diagram of a hybrid control approach for controlling propulsive forces, including force control within a stroke, switching control of kinematics, and triggered sensory events based on fin-intrinsic sensory data. 223

Figure 68. Interface of DLTdv5 tracking program during tracking of points on sunfish pectoral fin. Points along the pectoral fins were assigned by subdividing major fin rays into ten equal components. Tracking was performed by hand based on visual features in the fins..... 259

Figure 69. Tracking points along fictive rays A through G and the local coordinate frame on body of the bluegill sunfish..... 260

Abstract

Distributed sensing in flexible robotic fins: propulsive force prediction and underwater contact sensing

Jeff C Kahn, Jr.

James L. Tangorra, Ph.D.

There is recent biological evidence that the pectoral fins of bluegill sunfish are innervated with nerves that respond to bending, and these fish contact obstacles with their fins. However, it is not known how fin-intrinsic sensing could be used to mediate propulsion and touch in engineered fins. The objective of this thesis is to understand the use of distributed sensing in robotic fins, inspired by bony fish fins, for the prediction of propulsive forces and for the discrimination between fluidic loading and contact loading during underwater touch. The research integrates engineering and biology and builds an understanding of fin-intrinsic sensing through study of swimming fish and robotic models of fish fins and sensors. Multiple studies identify which sensor types, sensor placement locations, and model conditions are best for predicting fin propulsive forces and for predicting the state of contact. Comparisons are made between linear and nonlinear Volterra-series convolution models to represent the mapping from sensory data to forces. Best practices for instrumentation and model selection are extracted for a broad range of swimming conditions on a complex, multi-DOF, flexible fin. This knowledge will guide the development of multi-functional systems to navigate and propel through complex, occluded, underwater environments and for sensing and responding to environmental perturbations and obstacles.

Ineluctable modality of the visible: at least that if no more, thought through my eyes. Signatures of all things I am here to read, seaspawn and seawrack, the nearing tide, that rusty boot. Snotgreen, bluesilver, rust: colored signs. Limits of the diaphane. But he adds: in bodies. Then he was aware of them bodies before of them colored. How? By knocking his scone against them, sure.... Diaphane, adiaphane. If you can put your five fingers through it it is a gate, if not a door. Shut your eyes and see.

- James Joyce, *Ulysses*

What you think is the point is not the point at all but only the beginning of the sharpness.

- Flann O'Brien, *The Third Policeman*

Chapter 1. Introduction

1.1 Objective

The objective of this work is to understand the use of distributed sensing in a flexible, robotic fish fin for the prediction of propulsive forces and the discrimination of fluidic loading from contact loading during underwater contact with a rigid object. The core research question is: *How should fin-intrinsic sensing, inspired by bony-finned fish, be adapted for use in flexible, robotic fins to predict propulsive forces and discriminate contact loading?*

As our climates change, the oceans around us will become increasingly a part of our daily lives. Into the more distant future, we may need to live in environments that are threatened by flooding, water damage, waves, and significant water pressure. High sea levels will affect coastal environments and existing cities may need to engineer infrastructure in and around bodies of water. Travel in cities may involve personal and public transport that is both terrestrial and aquatic. Transport of physical goods and services may involve aquatic vehicles and robotic devices that must interact with water and underwater structures. The search for energy may turn to oceanic vents in dangerous, dark, and deep areas, and exploration will be carried out by specialized humans and machines working in partial or complete autonomy.

Terrestrial robots have been inspired by our own sensibilities as highly successful terrestrial animals, but we have yet to apply our knowledge of successful underwater animals to develop aquatic robots. Robotics arms and hands have been developed for handling, assembly, and manufacturing tasks based heavily on the human anatomy of the arm, wrist, and fingers. In recent years, the role and utility of sensory feedback in robotic

hands has been investigated, notably first with capacitive touch sensors, and then with biologically-inspired sensors in the skin surfaces and digits of robotic hands. The Syntouch BioTac, for example, uses multimodal sensing in a fingertip to capture a distribution of contact pressure, vibration, and force signals within a single robotic fingertip sensor. These advances in sensing, coupled with actuation, have enabled robots to execute highly dexterous manipulation of objects and tools. Underwater robots, however, have been inspired by the body morphology of animals, but the mechanisms of propulsion and sensing have yet to see significant development in commercial (non-research) underwater robots. Bony-finned fish (*teleostei*), which include such diverse species as knifefish, catfish, cod, and sunfish, are fish with rich sensory systems in their bodies and fins. Their fins are capable of manipulating fluid and obstacles for propulsion and navigation.

Human fine motor control is enabled by a rich variety of distributed, heterogeneous sensors including the mechanoreceptors of the hands and arms, the visual system, the auditory system, and proprioception that provide the relative position of the body and its limbs as it manipulates. Sensory cell bodies are *distributed* in that they are spread through the skin and underlying tissue, muscles, and ligaments. For example, when a human runs, she initiates motor commands from the frontal cortex, which activates circuits in the cerebellum and then pathways in the spine where firing patterns enable locomotion in the muscles [1]. Even if she were running in the dark, proprioceptors in her legs and joints would give her a sense of the relative position of upper legs, lower legs, and ankles. With each stride, she can feel the muscles stiffen and relax from the information gathered by populations of muscle spindles, and can adjust the

degree of stiffness through co-contraction of opposing muscles depending on the force and stiffness required. With each ground contact, she can feel the spread of deformation through her footpads [2] as well as the vibrations of bone and tissue due to impact. All of these sensory systems participate in modification of her running gait through feedback control to change the kinematics and stiffness of her joints and muscles. Both the *distribution* and the *modality* of the sensory cells are important in achieving good functionality for motor control.

Fish achieve fine movement and positioning of their bodies using their fins. These species use complex 3d kinematics, flexible fins and bodies, and distributed sensors systems (both interoceptive and exteroceptive) to swim, but these key features have yet to see application in most underwater vehicles. Currently, most unmanned underwater vehicles (UUVs) use distributed propeller systems for control of propulsion and centralized inertial measurement units (IMUs) and GPS to track movement of the body and joints of the robot. Vehicles with fins may have some flexibility, but will typically swim with stereotyped 2d kinematics as opposed to the rich 3d kinematics seen in fishes.

The bluegill sunfish (*Lepomis macrochirus*) relies heavily on its pectoral fins for many aspects of swimming and navigation, at a broad range of swimming speeds. When the fish is hovering in place, or station-keeping, the pectoral fins execute complex 3d kinematics to maintain its body position. At low swimming speeds, its pectoral fins are used to navigate by touch through occluded environments [3]. During steady forward swimming at moderate speeds, the pectoral fins execute a patterned gait to produce thrust through abduction and adduction phases [4]. At higher speeds during steady swimming, perturbations that would cause the fish body to roll are mitigated by torques created by

the pectoral and caudal fins. Fast yaw turn maneuvers to avoid incoming obstacles are enabled by turns initiated in the pectoral fins [5]. At low swimming speeds, or when station-keeping, the sunfish relies on a variety of hovering motions of its pectoral fins to create forces to remain stably positioned under perturbations.

Fish are capable of a wide variety of complex maneuvers underwater enabled by their fins, which too have distributed, heterogeneous sensory systems within them, though we do not know how the sensory information is used. Work in neurobiology aims to answer this question, where sensory afferents are instrumented to measure cellular firing patterns as fins swim or are held in place and perturbed. These studies show that cells respond to a range of sinusoidal stimuli, step stimuli, and ramp-and-hold stimuli. The population of cells includes both fast- and slow-adapting afferents of multiple types [6]. Additionally, knocking out fin sensation changes the amplitude and frequency of patterned gaits such as hovering [7]. These advances in knowledge are significant, but they do not fully map out the feedback path of the sensory signals to show how this information is used directly. It is unknown, for instance, if intrinsic sensors are used in the feedback control of stroke-to-stroke kinematics, or in feedback control of propulsive forces. Overall, the current knowledge suggests that fin-intrinsic sensation is used in the control of fin outputs, which could include both contact with objects and propulsive forces.

Flexible fins engage in a complex interaction with surrounding fluid to create propulsive forces. These fins engage in a fluid-structure interaction (FSI) where fluidic loading causes deformation of the fin surface and the deformation in turn affects the fluid displacement. The FSI can be affected by the geometry of the fin, which can change

through time depending on the driven kinematics of the fin (c.f. Figure 1). Small changes to kinematics, such as phase delays between fin sections, can cause large changes to the forces produced by fins. Changes to the velocities of kinematic patterns can also have significant effects on the fluidic loading experienced by fins, and in turn the forces that those fins produce. Fins are flexible structures, and therefore changes to their stiffness can also impact the FSI: for example, changing the uniform stiffness of a fin that is flapping can change the magnitude and direction of the propulsive force vector.

One of the key mechanisms of force production in finned propulsion is the bending of fins as they are actuated through the water [8]. Bending, as a function of time, can be modulated through changes to the kinematics of the fins as well as changes to the stiffness of fins (Figure 1). Animals make significant changes to their kinematics through changes of gait, and fine adjustments to their kinematics while executing that gait. For finned fish, gait changes can result in large changes to kinematics, the FSI, the bending of fins, and the propulsive forces produced. Therefore a key link between the fin kinematics and the propulsive force is the mechanical deformation of the fins, or more simply, the bending of fins.

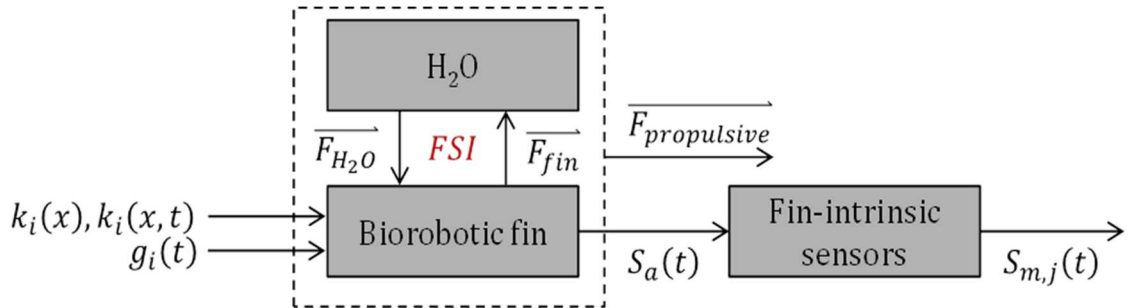


Figure 1. Block diagram illustrating the relationship between fin ray stiffness k , driven kinematics g , and the outputs of sensors S and propulsive forces F . The i -th subscript represents the i -th degree of freedom of the robot, i.e. a fin ray in this example. Kinematics are strictly a function of time though stiffness can be either only a function of space or a function of time and space. The propulsive force is created through the fluid structure interaction (FSI) which involves both the force created by the fluid acting on the fin and vice-versa. Actual mechanical phenomena (subscript a), e.g. strain, are measured by the j fin intrinsic sensors (subscript m).

Bending afferents are distributed throughout the sunfish pectoral fins, and these cells respond to bending at multiple fin locations. It has been verified that distributed bending sensation plays a role in fish swimming, but it is not known from a practical standpoint how this information could be used for underwater behaviors in robotic applications. The sunfish, for example, engages in multiple complex behaviors, including (but not limited to): steady forward swimming, nest guarding, hovering in place, maneuvering and turning, contacting obstacles, and building nests. Each of these behaviors may involve the use of several gaits depending on desired swimming speed, desired body configuration, and body constraints and obstacles. Bending sensation and feedback from fin afferents could mediate several of these behaviors but its utility and practical considerations are unknown.

From study of these animal behaviors, two tasks of high value are apparent: the control of propulsive forces and the prediction of contact states. The control of propulsive force first involves the prediction or estimation of propulsive force, which could be attempted using distributed bending sensors. The *contact state* is simply the classification of whether or not a fin is in contact with an extrinsic obstacle. Prediction of the contact state could involve interpretation of the signals from distributed bending sensors. Thus these two tasks can both be approached through the use of robotic models of fins with distributed bending sensors. The robotic models have distinct advantages from the biology in that they can be instrumented more easily and precisely, and can be controlled to execute larger numbers of repeated experiments for statistical power.

A major challenge of controlling underwater robots to swim like fish is to understand the control of the fin's propulsive forces, which, to achieve fish-like performance, hinges on understanding the use of fin-intrinsic sensors. Generally, fish-like swimming involves the deployment of 3d kinematics in gaits, the modulation of stiffness between strokes, the fine tuning of kinematics of individual gaits mid-stroke, and the use of fins to contact and interact with obstacles. This rich behavior may be achieved through the gathering and processing of intrinsic sensory data. To execute 3d kinematics in the presence of fluid disturbances or a modified plant (e.g. a damaged fin) requires some knowledge of the state of the fin's 3d kinematics. Being able to fine tune kinematic patterns may be driven by proprioceptive cues from sensory inputs. Contact with objects may be incidental, but the reflexive responses require the knowledge of being in contact with an object, whether inferred from sensing of the body dynamics or discrimination of contact locally from sensory cells. The many sensory inputs in the fin that respond to step stimuli may mediate fin control when contacting obstacles.

Knowledge of how to use sensors in robotic systems is of great importance for developing robots that are capable of adapting to real-world environments and responding appropriately to perturbations. Biological systems can serve as exemplars of how sensing can be useful to mediate locomotion and drive interaction with the outside world. Neurobiologists have successfully identified sensory cell bodies and afferent nerves in diverse animal systems and determined how they respond to different mechanical stimuli. Sensing in animal systems can often be *distributed* (spread throughout tissue and organs), *heterogeneous* (cells and nerves that transduce different

mechanical phenomena), and *intrinsic* (contained wholly within the organ which it senses).

Engineers have only started to understand the implications of sensing that is inspired by biological systems, and how to use these types of sensing for the design of better robotic platforms. Most engineering approaches to adopting biological sensing strategies use low numbers of homogeneous sensors or one sensor per type, and these sensors are centrally located, which is entirely unlike the distributed, heterogeneous, and intrinsic sensors seen in animals. It is understandable that most engineering systems have not adopted biologically-inspired approaches to sensing, as the costs and benefits of distributed and heterogeneous sensing have not been deeply explored or characterized for robotic systems. It is not known during which tasks distributed, heterogeneous, intrinsic sensing would be useful, how many sensors are needed, and what sensor modalities are appropriate given the robot's goals and environment. Intrinsic sensors and nerves are a part of the body they innervate and it is not always known how the kinematics and mechanical properties of these bodies affect sensory measures. These are core questions that must be addressed in order to develop robots with rich sensory capabilities akin to animals.

1.2 Thesis Organization

Chapter 2 addresses the Background and the biological inspiration for the work, and specifically how bony-finned fish use their fins to create propulsive forces using kinematics, mechanics, and sensors. It also presents the state of the art in flexible, high degree-of-freedom (DOF), robotic fins for propulsion and sensing applications. Lastly, a

sensing and control framework is posed that forms the main motivation for the thesis in addressing challenges in closed-loop control of propulsive forces using sensing in fins.

Chapter 3 presents main results on the use of fin-intrinsic bending sensors for the discrimination of fluidic loading from contact loading. For both the prediction of propulsive forces and of contact state from bending sensors, it is first necessary to understand some of the effects of fluidic loading on bending sensation. These effects are made more complex by the presence of obstacles, which act on the fluid and the fin as the fin approaches a target obstacle. These effects are explored through the results of experiments with a robotic fin and underwater obstacles. Understanding these effects builds the foundation for experiments that involve the prediction of propulsive force and of contact state. The chapter concludes with a signals-based analysis that demonstrates the discrimination of contact loading from fluidic loading during underwater touch.

Chapter 4 describes the framework selected and developed to estimate sensory data from propulsive forces. This includes a description of linear and nonlinear multiple-input-single-output (MISO) models from the field of System Identification. A primer on linear and nonlinear regression is given, along with detailed development of the Volterra series models used to analyze experimental data in later chapters. Techniques are introduced to reduce the dimensionality of the estimation problem for nonlinear models. Lastly, metrics of estimation performance are introduced and compared to form the basis for later analysis.

Chapter 5 presents the core results of the thesis, where the prediction of propulsive forces from sensory data is investigated. To address the practicality of using distributed bending and pressure sensors to predict the propulsive forces of fins, a large

series of experiments was executed that varied the fin gait, speed within the gait, and stiffness of the fin rays while forces and sensory data were measured. An analysis was constructed to identify best practices for hardware implementation (placement location, number of sensors, type of sensors) and algorithm implementation (time window of sensory data, linearity of model, degree of model order reduction) to predict the propulsive forces from sensory data. From this work, practical principles emerge for implementing sensors and software for force prediction from distributed sensors. These principles can be used for design of flexible underwater propulsors with integrated sensing systems, as well as for the design of experiments and sensory systems for predicting important locomotive outputs.

Chapter 6 addresses the extension of the work from prediction of propulsive forces to the control of propulsion using biologically-inspired and algorithmic techniques. Prediction of propulsive forces is useful for monitoring the force production of individual fins, but the natural extension of such work is to use prediction of forces to control propulsive forces. However, the parameter space for kinematics of flexible, multi-DOF fins is massive, so general principles and algorithmic techniques are needed to determine how to generate desired forces. Work is presented that examines sunfish hovering, where multiple kinematic patterns are used to create a variety of forces and control of body position is achieved through switching between gaits and fine tuning kinematics. An algorithmic approach is presented for exploring the massive parameter space of a biorobotic pectoral fin using genetic algorithms. These two studies form the foundation for a control framework that is biologically-inspired and sufficiently complex to handle the behavioral requirements of underwater vehicles with flexible propulsors.

Chapter 7 presents the conclusions of the thesis and provides a higher level discussion of their implications for the design and instrumentation of flexible, high-DOF, robotic devices for sensing and propulsion tasks.

Chapter 8 presents directions for future work in order to achieve control of propulsion using distributed, fin-intrinsic sensors.

1.3 Contribution and Novelty

The main contribution of this work is that a method for force prediction on a flexible, high-DOF, robotic fin is demonstrated and guiding principles are developed for sensor and model choices. The secondary contribution of this work is the development of methods for discrimination between fluidic loading and contact loading for touch sensing in the underwater environment.

The novelty of this work is that it successfully demonstrates an approach for the estimation of propulsive forces on a high-DOF, flexible robotic fin without an explicit physics-based model. Other approaches have modeled the relationship between kinematics and forces for low-DOF robotic fins and flapping foils, but these models typically do not allow for 3d kinematics or 3d deformation of the flexible fins. The use of a general multi-input-single-output (MISO) model also allows for a refinement of understanding of the important parameters that relate sensory phenomena to force production. Forces have been estimated using inertial measurement units and extrinsic load cells, but estimation of forces using sensors within a fin allows for monitoring of the fin's performance locally, and for extension of the algorithms into predicting local forces. Ultimately the prediction of local forces (i.e. forces from different regions of fins) can be

extended to execute control of local forces. This work also presents some of the first research that characterizes the sensory phenomena of underwater contact with objects.

Chapter 2. Background

2.1 Chapter summary

This research involves deriving knowledge from a biological system and applying that knowledge for the design of engineering systems with similar capabilities. The biological model of this work is the bluegill sunfish (*Lepomis macrochirus*), which uses its pectoral fins to navigate at low speeds and to contact obstacles in cluttered environments. In past work, a biorobotic pectoral fin was designed to match the mechanical, kinematic, and force production properties of the sunfish pectoral fin and this fin was used as the primary robotic device for work in this thesis.

The objective of this chapter is to present the state of the art in both biological and engineering research on sensing and control of flexible fins and to provide the foundation for the work of the thesis that follows. This section first gives an overview of the pectoral fins of the bluegill sunfish and summarizes what is known about pectoral fin swimming, pectoral fin touch, sensors in the pectoral fins, and control of pectoral fins. The same four areas are reviewed from the perspective of engineered robotic fins and their performance during swimming, touch, sensing, and control. Lastly, a biologically-inspired control framework is presented and motivated in order to contextualize the main results of the thesis.

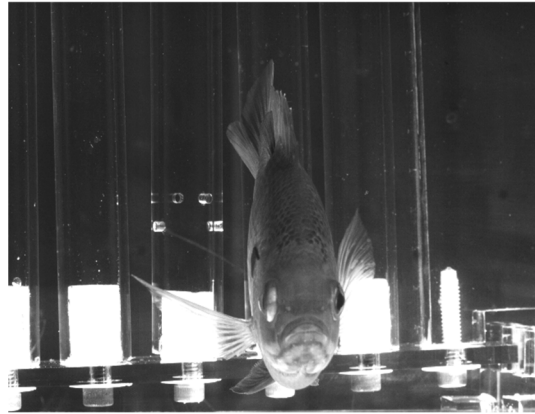


Figure 2. A bluegill sunfish hovering in a static water tank. The sunfish primarily uses its pectoral fins at low swimming speeds (e.g. hovering, maneuvering through obstacles, low speed steady swimming). Courtesy of George V. Lauder and Brooke Flammang.

2.2 Pectoral Fins of the Bluegill Sunfish

2.2.1 *Swimming in the Bluegill Sunfish*

Fish have been researched as a model for maneuverable, underwater systems, and fish fins have been studied as a model for creating propulsors with the capability to produce complex, three-dimensional forces [4, 9-11]. The bluegill sunfish (*Lepomis macrochirus*) was selected as the biological inspiration for this research because it uses its pectoral fins to execute highly agile swimming behaviors and navigates in occluded environments using its fins. Further, the bluegill sunfish is a model organism for bony-finned fish and the propulsive performance of its fins has been extensively studied during multiple swimming gaits and behaviors. Bony-finned fish use their fins to maintain their body position while hovering and searching for prey [12], to rapidly change direction during yaw turns [5], and to execute steady forward swimming in flow [4, 13].

Fish control their propulsive forces by controlling their fin's mechanical properties and their 3D kinematics during swimming [9]. They can change the forces on

their bodies from stroke to stroke with kinematic changes to their fins [9, 11]. Changes to kinematics can change based on the driven base motion of the fins, the stiffness of the fin rays (which fish can modulate), and the speed of muscle actuation. Significant amounts of bending, twisting, cupping, and feathering can be seen in the pectoral fin kinematics of swimming bony finned fish [11, 14, 15] and these are coupled to the magnitude and direction fin's propulsive force through time. Fish can also change the stiffness of their fins in order to alter the magnitude and direction of the propulsive force through time. Some bony-finned fish can change the stiffness of their fins by orders of magnitude [16], significantly altering the magnitude and direction of the propulsive force through time [17, 18].

To understand the control of pectoral fins it is important to examine fish behaviors where the kinematics of pectoral fins are most diverse and highly responsive to perturbations. Large changes to pectoral fin kinematics are seen during hovering behavior and low speed maneuvers, and the control of pectoral fins may be more complex during these behaviors. During these swimming modes, sunfish use their pectoral fins to drive motion and orient the body [9, 10], though it is not known how the pectoral fins are used to control body position during hovering.

2.2.2 Touch in the Bluegill Sunfish

Sunfish use their fins to contact obstacles when placed in cluttered environments. It is not known how much of the contact is incidental, but when the fish is deprived of vision and its lateral line receptors it will make many more obstacle contacts than with intact sensory systems [3]. This suggests that fish may use their fins as touch sensors in cluttered environments. Unlike what is seen in patterned swimming gaits, we have not

identified a stereotypical set of kinematics that the sunfish uses to contact obstacles. While the sunfish will touch obstacles using its pectoral fins (Figure 3), it will also do so using its caudal fins, anal fins, and multiple sections of its body (Unpublished video data, Flammang and Lauder 2013). However, the role of fin-intrinsic sensory information during obstacle contact has not been investigated.



Figure 3. Sunfish contact obstacles using their pectoral fins in cluttered environments. No stereotypical contact patterns have been identified. The mechanics and sensory phenomena of fin contact with obstacles are not well understood. Figures adapted from [3]. Courtesy of Brooke Flammang and George V. Lauder.

Sunfish use their fins and bodies in a variety of circumstances that would likely benefit from a sense of touch underwater. Sunfish build nests using their fins by gathering plant material and moving sediment. They navigate through cluttered and dark lake environments, where contact with plants, rocks, and sediment is a necessity. They interact with directed flows from river sources as well as turbulent flows and eddies shed off of obstacles and other bluff bodies. Being able to sense and respond to the conditions of obstacles as well as the fluidic environment would be valuable for survival.

2.2.3 *Sensors in the Bluegill Sunfish*

The pectoral fins of sunfish are innervated with nerve fibers which spread through the bony segments of fin rays, and terminate in free nerve endings throughout the fins [19,

20] (Figure 4). Recent work has shown that these afferents respond to the amount and rate of bending in the fins [6, 21]. Studies with the fish have not yet isolated the exact mechanical stimulus that produces a response and so either bending of fin rays or stretch of membrane between fin rays could be reasonable sensory measures. The nerve fibers also play a role in modulating the amplitude and the phase relationships between fin rays during hovering [7]. When the afferent nerves to the pectoral fins are cut, the pectoral fin kinematics change: phase lags increase between leading edges of the fin, and fin ray amplitudes change [22]. However, the role of afferent nerves during swimming is not well understood and it is not known which locations or types of bending sensors aid in control of propulsion.

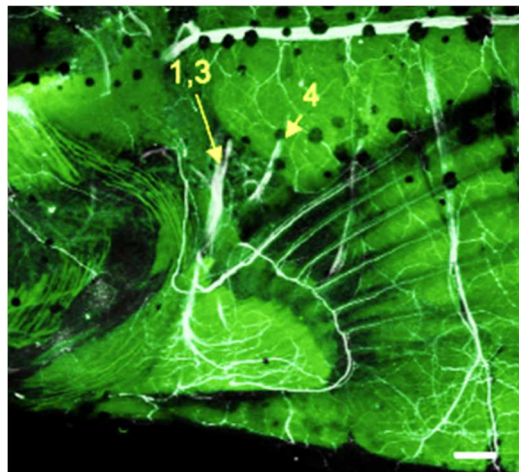


Figure 4. Afferent nerve fibers in the bluegill sunfish pectoral fins. Fibers terminate in free nerve endings which respond to bending stimuli. Adapted from [20]. Courtesy of Melina Hale.

2.2.4 Control in the Bluegill Sunfish

There are different behavioral responses in the fins of sunfish depending on the speed that the sunfish is swimming, which suggests that control strategies change depending on

speed. For instance, during steady swimming at low speeds (<1 body length per second) where the pectoral fins execute a patterned gait, experiments with a vortex perturber have shown that the pectoral fin can be crushed against the body without any update to the kinematics within the stroke. During this swimming mode, the only observed type of perturbation that elicits a significant pectoral fin response is one that induces a roll in the fish body. This evidence suggests that the pectoral fin kinematics are not tightly controlled during patterned steady swimming. At lower speeds of steady swimming, the introduction of an obstacle can induce a yaw turn maneuver [5], and some vortex perturbations to one fin beat can elicit a change in kinematics in the next fin beat. It is not until lower swimming speeds that the kinematics of swimming sunfish seem to change during a fin beat.

When the sunfish is hovering in place using most of its fins (pectoral, anal, dorsal), the pectoral fin kinematics vary significantly from stroke to stroke [23]. In addition, during hovering, the sunfish pectoral fins will change kinematic patterns within a fin beat, meaning that the pectoral fin will begin to execute a patterned gait and then will quickly change the kinematics mid-stroke. Sunfish are statically unstable [9], such that their center of mass is located above their center of buoyancy, and therefore active fin control is required even during hovering. While the exact role of afferent nerves is not known in this behavior, the diverse kinematic patterns and rapid changes to kinematics suggest that the pectoral fins are under more direct sensory-modulated control during hovering than in other swimming behaviors.

2.3 Flexible, high-DOF, robotic fins

2.3.1 Propulsion in flexible, robotic fins

Many engineering studies have used flexible foils as low order physical models to study the effects of kinematics and mechanical properties on fin propulsive forces [24], but much fewer have used fins with 3D kinematics and degrees of freedom that approximate those of swimming fish. Flapping foil experimental studies have investigated the effects of stiffness [25], flapping frequency [26, 27], heaving amplitude, propulsor shape [28], drag coefficients [29], and ground effect [30] on hydrodynamics and propulsive force outputs. A recent study demonstrates that flexible foils may serve as sufficient models of force production for caudal fin swimming as seen in two types of bony finned fish [26]. However, understanding force production in fish fins often requires complex 3D kinematics and specific mechanical properties [4, 9]. A few studies have used robotic models of bony-fish fins to study the effects of kinematics and mechanical properties on the propulsive forces. Robotic models of the knifefish have been used to investigate the kinematics, mechanical properties, and hydrodynamics of the dorsal ribbon fin during propulsion [31].

Our lab's robotic models of the bluegill sunfish (a bony-finned fish) have been used to understand the mechanisms of force production in fins during multiple swimming gaits [5, 23, 32, 33], as well as the relationship between mechanical property changes and force production [17]. In general, these studies validate that complex 3d kinematics and fin bending play a large role in determining the propulsive forces produced by fins. They also suggest that the creation of 3d propulsive force is a function of kinematics from multiple regions of the pectoral fin, and that there are complex nonlinear relationships between kinematics and fin forces.

2.3.2 *Touch in flexible, robotic fins*

A sense of touch gives biological and robotic systems the ability to perceive physical properties of the environment and to execute agile maneuvers while responding to perturbations. Touch may be a very important sense underwater, where there are significant interactions between manipulators and their targets through the fluidic medium. Robotic touch and contact sensing has been extensively studied in the terrestrial domain, but has received much less attention underwater. Few researchers have utilized active touch sensing to explore underwater environments. Much prior work in robotic exploration has focused on vision and sonar-based sensing for simultaneous localization and mapping (SLAM) [34-39]. SLAM is effective for visualizing object shapes but does poorly in occluded environments and provides little information about flows or mechanical properties of objects. To characterize flows, researchers have constructed artificial lateral line arrays. These efforts have demonstrated that flow characterization is sensitive to sensor orientation, spatial distributions, and spectral sensitivities [40, 41]. The use of actuators to reorient a sensory system relative to flow has been shown to improve the estimates of the flow field [42, 43].

Whisker-based sensors have been shown useful in flow characterization and object exploration underwater, but fins have not received the same level of attention. In seals and walruses, facial whiskers provide distributed sensory information used to identify object shapes [44, 45], follow wake profiles from objects and prey [46, 47], and distinguish prey while foraging [48]. Engineering research with tapered cantilever whisker sensors has shown that the geometry and structural properties of target objects

can be reconstructed from bending measurements [49, 50], but there has been little work that utilizes beam-like sensors for active sensing and flow characterization in the underwater environment [51, 52], and almost no studies of the role of membranes coupled to these systems [53]. The limited work on underwater tactile sensing has closely followed gripper design for terrestrial robots [54-56].

The sensory phenomena associated with touch sensing underwater with fins is not well understood, including the phenomena that arise due to the fluidic environment, and the phenomena that arise due to the presence of compliant webbing between bony segments of fins. Understanding these phenomena associated with underwater touch would help create a fuller picture of the role and performance of fins as they aid in navigation and touch in the underwater environment, enabling underwater robotic technologies that exploit touch to perceive obstacles and flows.

2.3.3 Sensors in flexible, robotic fins

Engineers have successfully adapted many principles of force production from study of fish fins (see above). However, there have been few studies that investigate the use of sensing within fins. Several studies using ionic polymer metal composites (IPMCs) have suggested the use of embedded strain sensing within polymer fins to provide bending information for force control of fins [57, 58]. These sensors have been used to estimate the curvature of fins during flapping and heaving motions. Robotic models of a bluegill sunfish pectoral fin have been instrumented with bending and pressure sensors within the fin [23, 32, 33], and general trends have been identified that relate sensory measures to propulsive forces. Being able to predict the fin's propulsive forces during swimming could contribute to closed-loop control of forces with robotic fins and foils. Further,

understanding which sensors are best for the task of force prediction can help in the design of more effective propulsors. It is not well understood which sensors are useful for force prediction or contact prediction underwater.

2.3.4 Control in flexible, robotic fins

New methods are required to control the propulsive forces of flexible robotic fins. One of the primary challenges of force control with flexible robotic fins is the large parameter space formed by the kinematics and stiffness of the fin's actuated degrees of freedom. While the webbing between fin rays will dynamically constrain the space of possible trajectories, it is still too large a space for random exploration or even hill-climbing optimization algorithms. Search techniques have been applied to optimize kinematics for force production in robotic fins (by the author in [59], and others in [60]), but the algorithms employed are infeasible for finding an optimal kinematic pattern in real time.

While the kinematics and mechanisms of force production are well understood, few studies have been done to execute force control using flexible fins with 3d kinematics. When the parameter space of kinematics is very large, computation of the inverse kinematics for an unseen force trajectory may not be feasible in real time. Several approaches use mathematical oscillators to control the kinematics of robots with large numbers of degrees of freedom (see [61] for extensive review). Nonlinear oscillator models have been used to control flexible foils close to their resonant frequency by using bending sensation as a feedback signal [62]. Hopf oscillators have been coupled together for control of fin kinematics in a 3d robotic manta ray system [63], and to generate stable trajectories for a robotic bat wing [64].

2.4 Sensing and control framework for the thesis

Based on the state of the art in both the animal and robotic systems, a broader framework for sensory-based control of fins is proposed, and the thesis addresses key gaps in the state-of-the-art. The control framework is described herein and is simplified where possible (Figure 5). A more detailed treatment of the control is given in Chapter 6.

Broadly, based on a physics model of the robot, a desired force, \vec{F}_d , is computed. The desired force is used to select the proper *stroke* that will result in the desired force, based on a library or an algorithmic approach. Each stroke has associated reference signals of the forces of that stroke (\vec{F}_r), the kinematics of that stroke (\vec{x}_r), and the sensory signals associated with that stroke (\vec{S}_r). These reference signals are critical in two major inner loops of the control diagram: control of propulsive forces, and control when contact occurs.

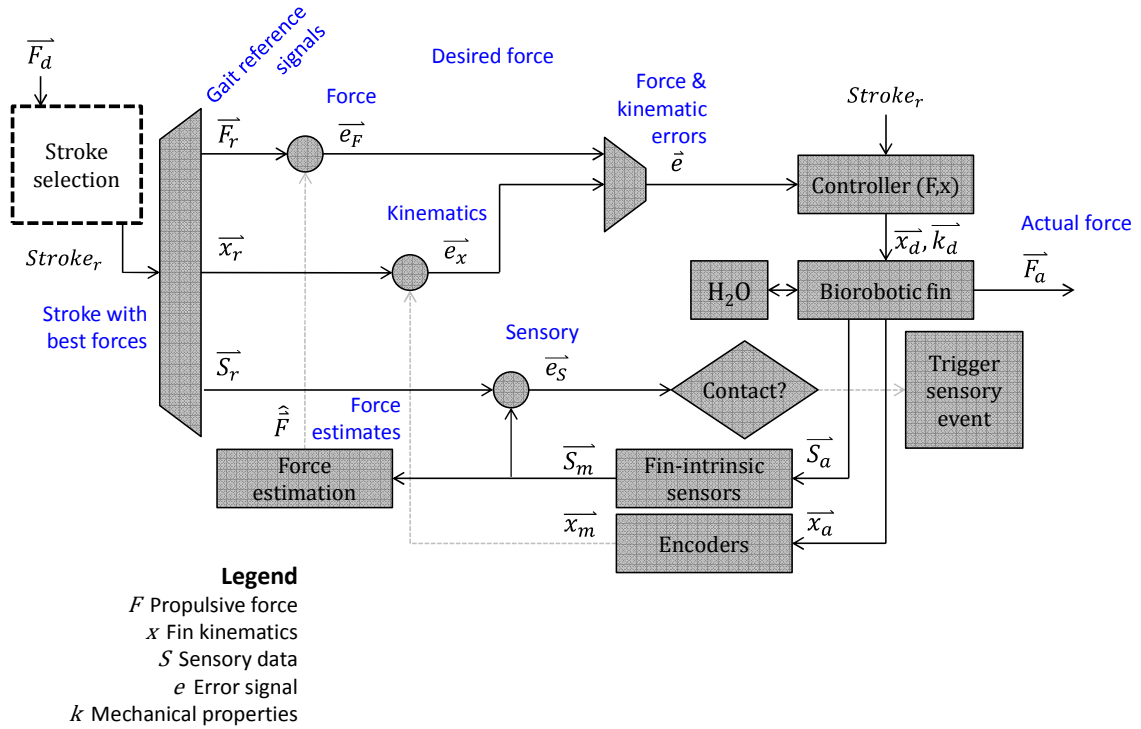


Figure 5. Simplified control framework for sensory-based control of propulsive forces and of touch interactions.

2.4.1 Prediction of propulsive forces

Control of propulsive forces is crucially based on the prediction of propulsive forces using data from fin-intrinsic sensors (c.f. Figure 6). When the robotic fin is executing a given stroke, it generates the actual propulsive force \vec{F}_a through the interaction of the fin and the water (H_2O). This interaction produces mechanical phenomena which are represented as a vector of sensory signals, \vec{S}_a , which is measured by actual sensors to yield the measured sensory signals \vec{S}_m . These sensory signals are then used to predict the propulsive forces of the fin. The reference force of the stroke, \vec{F}_r , is compared to the prediction of force, $\hat{\vec{F}}$, to compute an error.

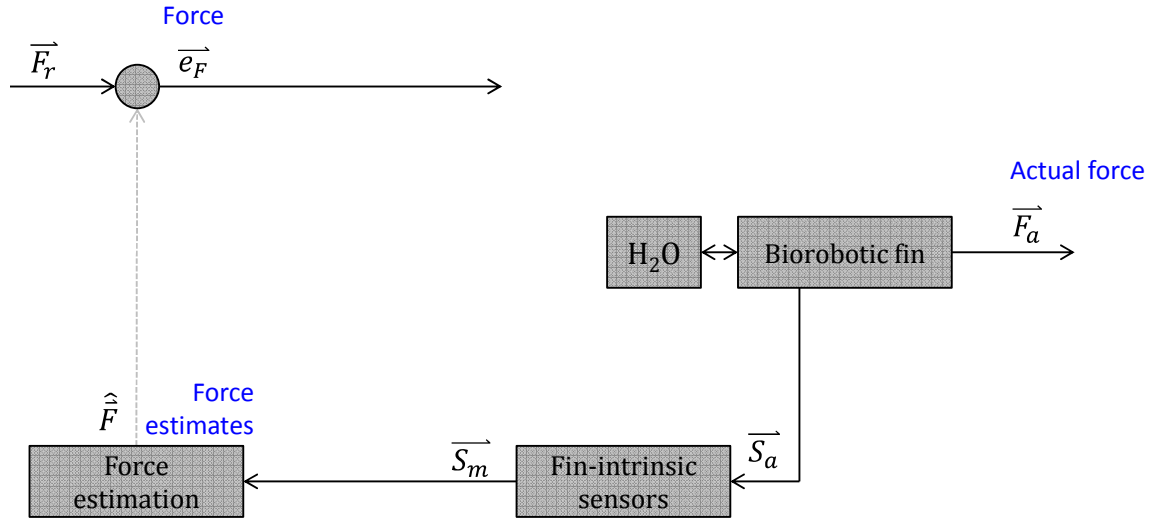


Figure 6. Close up of block diagram for prediction of propulsive forces.

There are other reasonable approaches to obtaining the error between reference force and actual force, but most suffer limitations for application with flexible, multi-DOF fins. The first obvious solution to obtaining an estimate of force is to measure or infer propulsive force directly. With mechanical design, it may be possible to instrument the fin with a multi-axis force sensor at its base connection to the robot body and obtain an estimate of force. This is a significant design challenge with tendon driven systems, but may be achieved with calibration techniques. If force cannot easily be measured, force may also be inferred from the dynamics of the robot body. This could be achieved with a well calibrated inertial measurement unit to capture the position, velocity, and acceleration of the robot and to estimate the forces from these measurements. The estimate could be improved with multiple IMUs and fusion of GPS information, or similar. However, these techniques fail to associate forces with kinematics on the fins.

While the force may be known perfectly in time and direction with a force sensor, there is no clear knowledge of where the force is arising from in the fin. More specifically, since the forces are created through the fluid structure interaction of the fin, and the fin is controlled along multiple degrees of freedom, the measurement/inference of forces is not necessarily sufficient to allow for control of multiple degrees of freedom in a fin. For example, if the upper part of the fin is creating more thrust than is desired by the reference signal, this information is unknown even to a perfect force sensor. Local estimates of force are required to know from where the forces arise, in order to control them properly.

2.4.2 *Discrimination of contact loading from fluidic loading*

Another critical perception task is the determination of if/when contact has occurred with an underwater obstacle. In open water applications, this case is normally ignored for the closed-loop control of underwater vehicles, but in cluttered environments such as lakes, streams, and near shore regions, the determination of contact with obstacles can be a mission-critical task.

In the proposed control framework (Figure 7), as before, the biorobotic fin is driven with a desired kinematic pattern (\bar{x}_d) and at a desired stiffness (\bar{k}_d) and produces actual sensory measures which are measured by a suite of distributed fin-intrinsic sensors. The sensory measures can be compared to the reference sensory data (\bar{S}_r) for the *stroke*, and this can be used to determine if damage or a contact is occurred.

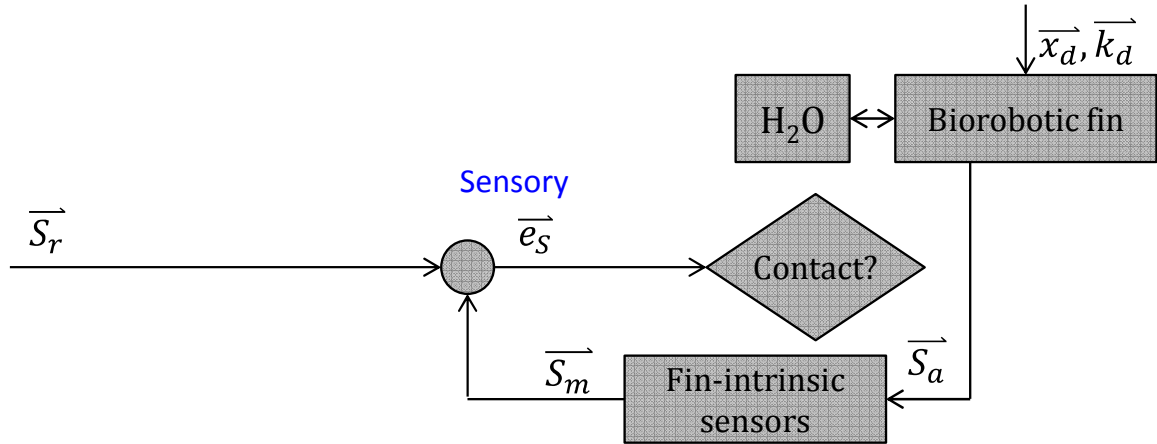


Figure 7. Close up of block diagram of underwater contact discrimination using fin-intrinsic sensors.

The discrimination of contact can then be used to trigger a specific strategy to deal with contact, depending on the dynamics of the vehicle and the location of the underwater obstacle. For instance, upon detection of contact, the fin could be stiffened to push off of the object or relaxed to allow a controlled collision with it. Reflexive motions of the fins or body could be used to resolve a contact or to minimize damage due to a high speed collision.

Even without a reference sensory signal, how to use distributed, intrinsic sensors to determine the location, onset, and duration of contact are critical to being able to control the fins and body to mediate contact with underwater obstacles. It is important to localize contact on a fin so that actuation of the fin ray(s) in contact can be controlled. The location of contact on a fin cannot be easily determined using a single force sensor, as the mapping between contact location and force/torque is likely many-to-one for a multiple DOF fin. Distributed strain sensors can likely be used to localize contact on individual fin rays, as well as the location of contact along a single fin ray. Determining the onset of contact, or the instant when contact occurs, is important for localizing

obstacles in space as well as understanding if contact has occurred at all. Lastly, knowing how long contact has occurred, or when contact has ceased, is important information for the perception of the environment.

Chapter 3. Fin-intrinsic sensation for understanding underwater touch

3.1 Chapter summary

Underwater robots operating in cluttered marine environments such as lakes, streams, and near shore environments will interact with fluid and will come into contact with compliant, dynamic objects. These environments can be riddled with obstacles, plant life, and sediment and can have complex flow patterns that will affect both the propulsive and sensory performance of underwater propulsors such as fins.

The role of touch and bending sensing underwater has not been explored in detail in the literature, especially as probes interact with fluid and contact obstacles. This chapter presents some of the first detailed experiments and analysis using compliant fins and beams that are instrumented with strain sensors for the exploration of underwater contact with fluid and rigid obstacles.

Due to the complex interaction between the fin, the fluid, and the target object, the sensation of contact is affected by the fluid during multiple stages of contact. This interaction, termed the *structure-fluid-structure-interaction (SFSI)*, can make it challenging to classify the difference between *contact* and *non-contact* states for the probe.

The objective of this chapter is to present an understanding of the use of distributed sensors in a flexible robotic fin to discriminate between fluidic loading and contact loading during contact with an underwater obstacle. First, the effects of fluidic loading and the effects of changing fin and obstacle properties on the sensing of fluid and contact loading are explored. Additionally, signals-based techniques are developed for the discrimination of *contact* from *non-contact* conditions. The efficacy of several

thresholding and differencing techniques are evaluated across changing fin conditions of speed, structure, and stiffness, both in air and underwater.

This chapter is comprised of one published journal paper reprint and a journal paper in review: (1) a journal paper published in the *IEEE Transactions on Haptics Journal*, Volume 9, Issue 2, April, 2016 and (2) a journal paper in preparation for submission to the *IEEE Robotics and Automation Letters (RA-L)*. Both studies were used to explore the role of fin-intrinsic sensing during movement through fluid and contact with obstacles underwater.

3.2 Paper 1: The effects of fluidic loading on underwater contact sensing with robotic fins and beams

3.2.1 Abstract

As robots and teleoperated systems become more involved in underwater operations, understanding underwater contact sensing with compliant systems is fundamental to engineering useful haptic interfaces and underwater vehicles. Despite knowledge of contact sensation in air, little is known about contact sensing underwater and the impact of fluid on both the robot probe and the target object. The objective of this work is to understand the effects of fluidic loading, fin webbing, and target object geometry on strain sensation with compliant robotic fins and beams during obstacle contact. General descriptions of underwater obstacle contact are sought for strain measurements in fins and beams. Multiple phases of contact are characterized where the robot, fluid, and object interact to affect sensory signals. Unlike in most air applications, the underwater structure-fluid-structure interaction (SFSI) caused changes to strain in each phase of contact. The addition of webbing to beams created a mechanical coupling between adjacent beams, which changed the strains of contact. Complex obstacle geometries tended to make contact strains less apparent and caused stretch in fins. This work demonstrates several of the effects of fluidic loading on strain sensing with compliant robotic beams and fins as they contact obstacles in air and underwater.

3.2.2 Introduction

As robots and teleoperated systems become more in-volved in underwater operations, understanding underwater contact sensing with compliant systems is fundamental to

engineering useful haptic interfaces and perceptive underwater vehicles. Knowledge of underwater contact sensing has the potential to change the way that robots and humans operate in the underwater environment by conveying relevant fluidic and contact information to a human operator. Underwater robots in operations such as coastal surveying, military demining, specimen collection, and pipeline repair are likely to come into contact with underwater obstacles as well as objects of interest, and these systems should be designed with proper mechanical properties and sensory instrumentation for these jobs. However, the effects of fluid loading on the phenomena of contact with obstacles are not well documented for robotic touch systems.

Recent evidence has shown that fish fins may serve a dual role as both propulsors and sensors, and this new understanding has inspired research questions regarding the sensation of contact underwater using compliant robotic systems. Studies of the bluegill sunfish (*Lepomis macrochirus*) have identified afferent nerves in their pectoral fins that innervate multiple regions and respond to bending with rapidly adapting and slowly adapting afferent populations [1, 2]. The function of bending sensors in fish fins has not been fully explored, but it may have roles in controlling propulsion and mediating touch, as the sunfish have been observed to use their pectoral fins to touch obstacles more frequently under sensory deprivation conditions [3]. In air, the whiskers of rodents have inspired studies of contact sensing [4-7], as these animals use their whiskers for active perception of new environments. One major difference between sensing in fins and sensing in whiskers is that the fin afferent nerves are distributed throughout the fin webbing and bony fin rays, but whisker sensory cells are located in the sinus complex of rats and mice [8]. This suggests that the spatial distribution of sensors in fish fins may be

relevant to its functional role. Compliant robotic fins and beams are a natural starting point to investigate sensation during underwater contact.

Despite knowledge of contact sensation in air, little is known about contact sensing underwater and the impact of fluid on both the robot probe and the target object. In work with whisker sensors in air, it has been shown that torque measurements from a cantilever beam that was pressed against an object can be used to estimate the shape of that object [49, 65, 66]. Unlike whisker sensing in air, where contact loading exceeds the loading from the air, whisker sensing in water would likely be complicated by the loading from the fluid, which is dependent on the velocity, profile, and stiffness of the whisker. Adding webbing to whiskers to create fin-like surfaces is likely to further complicate the fluidic loading experienced by sensors within fins.

A compliant fin and a target object may also interact with each other through the fluid medium, depending on the geometry of both systems and their motions. Models of the fluid-structure-interaction (FSI) have been developed to understand the effects of fluidic loading on compliant beams and flexible plates underwater. FSI models typically focus on characterizing deformations during flapping motions and the effect of deformation on propulsive forces [67-70]. Some studies examine the *ground effect* or *wall effect*, where a propulsor's proximity to substrate or objects changes the hydrodynamics of swimming and flying [30, 71, 72]. However, most studies have not taken a sensory perspective, where the FSI between robot, water, and objects may have strong effects on proprioception and touch. Perhaps it may be more appropriate to call the interaction between a flexible fin, the water, and a target object a *structure-fluid-structure*

interaction (SFSI) because each system will physically interact with the other through the fluid coupling.

Recent work has started to address some of the challenges associated with underwater contact sensing and to identify some of the haptic attributes of underwater environments as compared to air environments. A few recent studies with robotic whisker sensors have identified that fluidic loading can increase bending and potentially change the perception of object contact from air to underwater [52, 73]. Fluidic loading has been observed on pairs of oscillating beams as a function of movement speed, cross sectional area, and spacing between beams [74]. Vortex shedding, which causes *vortex induced vibrations* (VIV) has long been studied for cylinders and beams design study with underactuated robotic hands showed that creating suction forces at fingertips greatly improved the hand's ability to stably grasp objects underwater, suggesting the prevalence of SFSI effects [75]. Early work with the underwater AMADEUS robotic hand indicated that in order to operate effectively at depth, contact sensing mechanisms had to be independent of ambient pressures [76]. Animals provide behavioral examples of how the properties of the fluid environment can be exploited for survival. It has been show that zebrafish evade predators reflexively by sensing the bow waves of approaching predators [77]. Multiple species of fish execute rheotaxis, or orientation of their bodies relative fluid flows, through use of directionally-tuned flow sensing in their lateral lines [78].

The objective of the work presented herein is to understand the effects of fluidic loading, fin webbing, and target object geometry on strain sensation with robotic fins and beams as robotic fins and beams come into contact with obstacles underwater. Since few studies look at underwater contact sensing using robots, general descriptions of

underwater obstacle contact are sought for strain measurements in fins and beams. This is addressed through the development of an instrumented robotic fin platform and the execution of experiments where the fin contacts obstacles in air and underwater at different speeds. The stiffness and structure of the robot are varied in experiments to understand how strain is affected by these changes. Strain data are analyzed to determine signal features and physical phenomena that may be relevant during contact.

This paper is structured as follows. The methods are presented in section 2, with emphasis on the robotic platform and its sensors, the experiments executed using the robot, and the analysis techniques used on experimental data. The results are presented in section 3, and are grouped by experimental type. First, typical results for fluidic loading are described for multiple phases of the contact experiment: *acceleration*, *constant velocity*, *approach*, *contact*, and *relaxation* phases. Second, the effects of fluidic loading are analyzed as a function of robot speed and beam stiffness. Third, the effects of fluidic loading are analyzed in the presence and absence of webbing between beams in air and underwater. Finally, the effects of fluidic loading are analyzed as a function of varied obstacle geometry. A discussion of the results is provided in section 4, highlighting implications of the results on active touch sensing in underwater environments with compliant beams and fins. The conclusion is given in section 5.

3.2.3 *Methods*

3.2.3.1 *Equipment*

A robotic platform was designed to evaluate the effects of fluidic loading on the strain experienced by beams and fins and the effects of webbing in air and underwater on the

strains experienced by fins. Beams were manufactured with fused deposition modeling of extruded ABS plastic (Dimension Elite, Stratasys, Eden Prairie, MN, USA). Three beam geometries were selected to examine fluidic effects on stiff, moderate, and highly compliant sensors. Beams were designed with a linear taper of cross section, and were designed to test a range of flexural rigidities across three orders of magnitude (Figure 8).

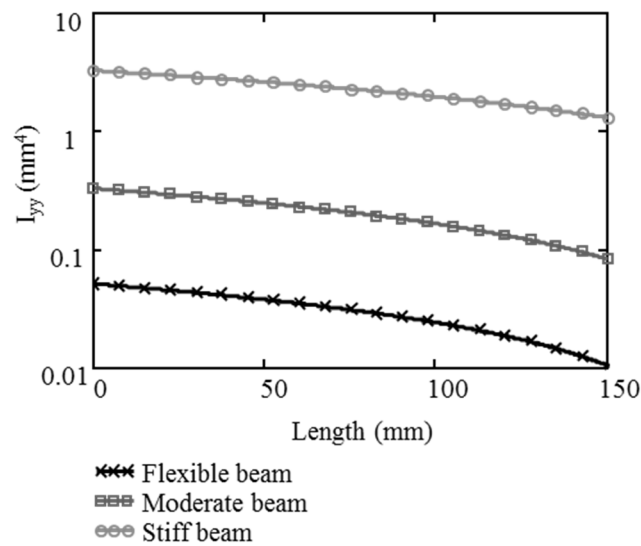


Figure 8. Cross-sectional second moment of inertia as a function of length for the three beams used in this study. The y axis is scaled logarithmically.

Each compliant beam was instrumented with two strain sensors in half bridge configurations at 10mm (proximal) and 100mm (distal) along the beam's length. (Figure 9a). These locations were chosen such that the proximal sensors would capture the net loading of the beam and the distal sensors would capture primarily the tip loading. Since beam cross sections were tapered from base to tip, tip sensors had very little mass to support and it was expected that drag effects (c.f. Vogel [79]) would be negligible on distal sensors.

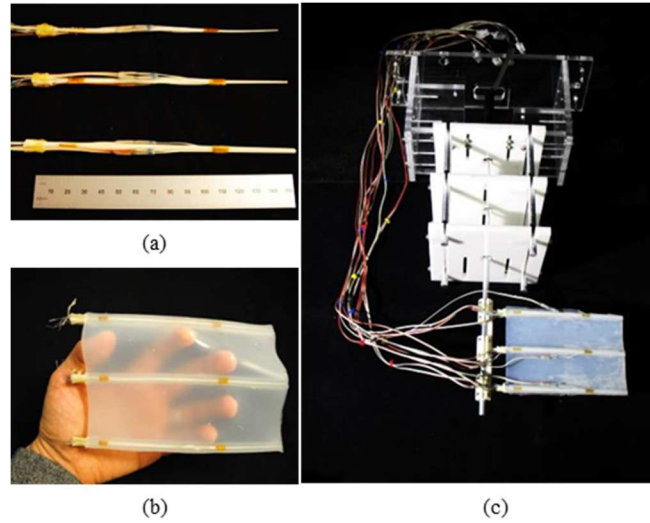


Figure 9. Robotic fins and beams used in contact experiments in air and underwater. Flexible, moderate, and stiff beams instrumented with strain gages at proximal and distal locations (a); instrumented beams in silicone webbing create a fin (b); the robotic platform used to drive the beams and fins into obstacles.

Beams with webbing (i.e. fins) were manufactured using a sacrificial mold box (based on techniques in [80]) used to create a 0.5mm sheath around each beam element and a 1mm thick webbing between beams using two-part silicone (Ecoflex 0030, Smooth-On, Easton, PA). The fin was 150 mm in length and approximately 100 mm in height, similar to the aspect ratios of caudal fins in sunfish. Beams were spaced 50 mm apart in the webbing; this spacing was chosen to allow for some stretch in the webbing during fluidic loading, and to allow for independent contacts of each of the beams with objects of different geometries.

Experiments were executed to investigate the effects of fluidic loading on beams and fins, and the effects of this loading on the strain distribution measured in the beams and fins. Beams of multiple stiffnesses (Figure 8, Figure 9a) and the fin were driven into contact with the flat plate obstacle in air and underwater (Figure 10a). Experiments were

executed to understand how adding webbing to beams affected the beam's strain distribution during contact with obstacles in air and underwater. Experiments were executed to investigate how obstacle geometry affects strain. A rectangular planform was chosen to simplify the fluidic loading due to symmetry about the rotational axis. All three beams used in the fin had identical geometry to isolate the effects of adding webbing. A single fin was prototyped using beams of moderate stiffness, equivalent to that of the bare sensory beams of *moderate* stiffness (Figure 8, Figure 9b). Beams and fins were driven by a velocity controlled servomotor (416134, Maxon Motor, Fall River, MA) on a robotic platform using a real time controller and custom DAQ and control software (Figure 9c). The shaft position at the base of the beams was measured using a motor encoder on the motor shaft, which was connected via a 1:1 gear belt drive. These are described in detail in [32, 62].

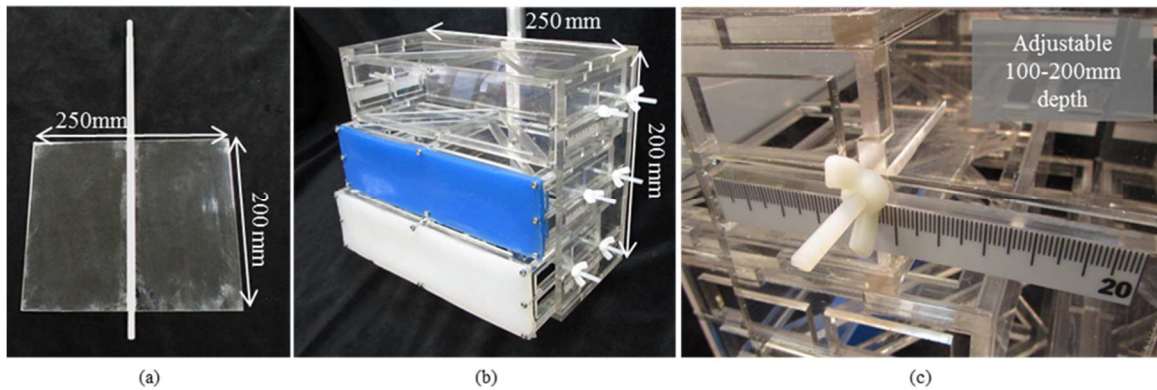


Figure 10. Obstacles that the fins and beams contact in the study. An acrylic plate obstacle mounted on an aluminum rod (a). A modular obstacle box containing three drawers that can be repositioned to different depths and interchangeable faceplates for presentation of obstacles with different materials (b). Close-up of depth adjustment rail and wingnut to fix drawer depth (c).

Two obstacles were designed for experiments to determine the effects of obstacle geometry on strain sensation during contact in air and underwater. The first obstacle was a flat plate which was selected to present a simple contact geometry to the robotic platform. The flat obstacle was an acrylic plate (200 x 250mm x 6.35 mm) mounted on a machined aluminum rod (9mm diameter; Figure 10a). The plate was made slightly larger than the footprint of the fin in order to capture the added mass of fluid on the fin as it approached the obstacle, and so that the interaction forces between the robot and obstacle could be measured prior to contact.

The second obstacle consisted of three flat, parallel surfaces, each with adjustable depth (Figure 10b,c). The position of each surface can be adjusted and can be bolted into place depths of up to 100 mm towards the fin (Figure 10c). This was designed for experimentation with obstacle geometry, allowing for the experimenter to change the timing of contact of beams and fins along their height, such that the upper, middle, and lower beams contact the obstacle at different times. Setting large differences in surface positions can also allow for investigation of the effects of stretch between beams in webbing.

3.2.3.2 *Experiments*

Experiments were executed to investigate the effects of fluidic loading on beams and fins, and the effects of this loading on the strain distribution measured in the beams and fins. Beams of multiple stiffnesses (Figure 8, Figure 9a) and the fin were driven into contact with the flat plate obstacle in air and underwater (Figure 10a). Experiments were executed to understand how adding webbing to beams affected the beam's strain distribution during contact with obstacles in air and underwater. Experiments were

executed to investigate how obstacle geometry affects strain in beams and fins during obstacle contact in air and underwater. The profile of the second obstacle was adjusted by positioning the three contact surfaces of the second obstacle at different distances from the fin. Thus, the position of contact was varied along the height of the fin and the timing of contacts varied between beams. Contact geometry was varied in two ways, either a single surface was offset by a fixed distance from the other two, or the drawers were arranged in a stair step pattern at equal relative distances (Figure 11). Six trials were executed per set of experimental conditions to evaluate repeatability of results (see Table 1), resulting in over 8000 individual trials.

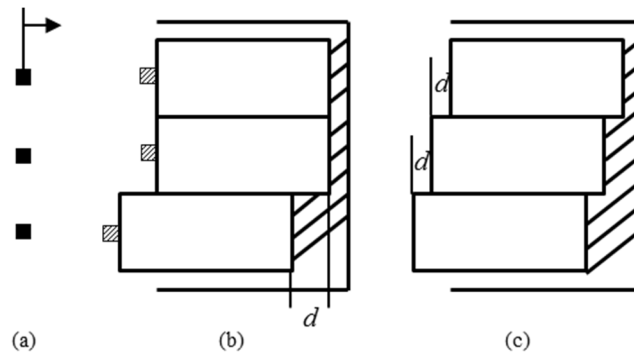


Figure 11. Conceptual drawing of the experimental configurations of the obstacle. The beam tips (a) either approached a configuration with a single surface offset by a distance d (b), or a configuration with a stair step pattern of equal relative depths (c). The arrow indicates the direction of motion for the beams (a).

Table 1. Experimental parameters for robotic platform, environment, and obstacles.

Experimental parameter	Settings
Robot structure	{moderate fin, stiff beam, moderate beam, flexible beam}
Robot speed (rot/s)	[0.05,1.5] in increments of 0.05, [0.05,0.4] for fins
Environment	{air, water}
Obstacle type	{n/a, simple, complex}
Obstacle spacing (top,middle,bottom) (mm)	{(0,0,0), (0,0,5), (0,0,10), (0,5,10), (0,0,15), (0,0,20), (0,10,20)}

During all experiments, the beams were accelerated from rest and driven with constant velocity into the obstacle while sensory data were measured from strain sensors within the fins and beams (Figure 12). Object distance was held constant across trials at 140mm away from the fin base so that only the tip of the 150mm beams came into contact with the obstacle surface. The robot's initial angular position was at least 270 degrees away from the obstacle in order to enable adequate time for the bending of the fin to reach a steady state. This angular position offset was determined experimentally. For experiments with beams, the robot's shaft was driven at speeds of $[0.1, 1.5]$ rot/s in increments of 0.05 rot/s. For experiments with fins, the shaft was driven at speeds of $[0.05, 0.4]$ rot/s in increments of 0.05 rot/s. The maximum fin speed tested was significantly lower than the maximum beam speed tested because the fluidic loading on the fins was significantly greater than that of the beams, and speeds higher than 0.4 rot/s resulted in damage to the fin and its strain sensors.

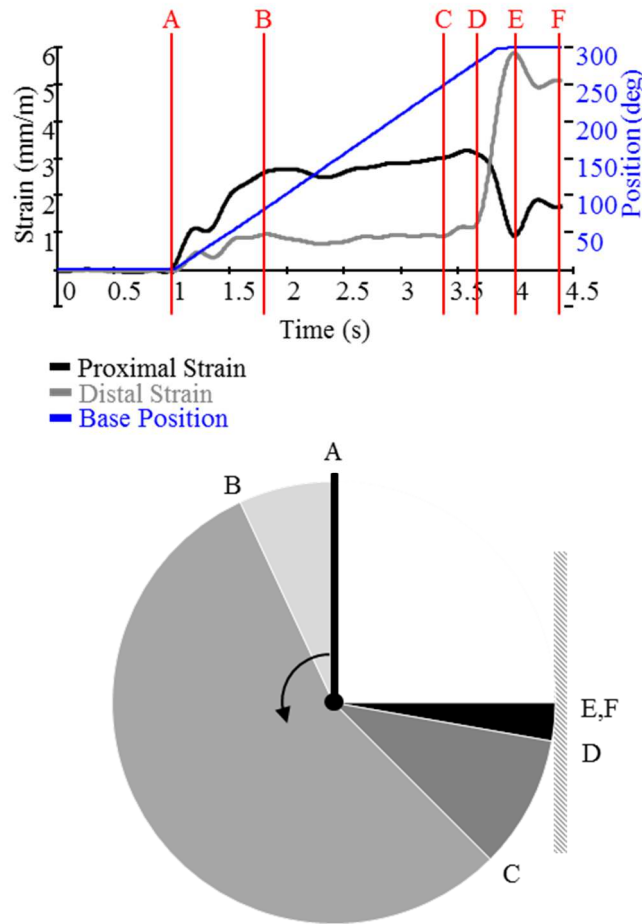


Figure 12. Phases of contact for an fin driven into contact with a rigid obstacle underwater. Phases are shown relative to measured strains (top) and beam position (bottom) in an overhead view. The *initiation* phase lasts from the initiation of movement to the first peak in the distal strain data [A,B], then the *movement* phase begins and continues until the distal strains increase at obstacle approach [B,C] at the start of the *approach* phase. The *approach* phase [C,D] lasts until *contact* starts, and *contact* continues until a peak in the distal strain data [D,E]. *Relaxation* follows until both proximal and distal beams reach a steady state [F].

3.2.3.3 Analysis

3.2.3.3.1 Beams and fins in air and underwater

The time courses of the strain data were analyzed to determine and compare features of strains that were typical of contacts of beams in air, beams underwater, fins in air, and fins underwater. Qualitative differences in the strain data were noted for the time course

of each strain signal. Basic statistical features of the strain data were studied, including the average strains, peak strains, and standard deviations of strain during each phase of contact. These features were compared between testing conditions to understand the basic effects of the fluid environment on fluidic loading and strain sensing of contact. Welch's two sided t-test was used to determine significant differences between trial conditions, with significance set at $P=0.0005$. For clear presentation of some strain data, a low pass filter with a Kaiser window at 10Hz was used [81], though all statistical calculations on data were made prior to filtering.

Analysis was conducted during five phases of contact, defined here. These include *acceleration*, *constant velocity*, *approach*, *contact*, and *relaxation* (Figure 12). The *acceleration* phase began when movement is initiated and lasts until transient strains die down (Figure 12: [A,B]). The *constant velocity* phase began after the strain transients died down and continued until the beam tips neared the object [B,C], ending the *constant velocity* phase and starting the *approach* phase [C,D]. In trials where force data were measured, the *approach* phase began as soon as the forces on the obstacle increased along with bending on the beams. The *approach* phase lasted until the first beam *contact* occurs, as marked by inspection from high speed video of the trial. The *contact* phase [D,E] continued until a peak strain was reached, and then the *relaxation* phase [E,F] began and continued until a steady state was reached on both proximal and distal beam strains. All peak strains were identified by inspection of the distal strain data, which typically had clearer maxima than proximal strain data.

3.2.3.3.2 The effect of speed on beams and fins

The effects of the speed of the beams and fins on fluidic loading were analyzed for both fins and bare beams underwater. Fluidic loading was quantified using the strain measured across the fins, as measured by strains taken at proximal and distal locations of the bare beams and beams in webbing (fins). Strain data were first compared qualitatively as speed was increased on both the beams and the fins. As noted above, statistical features of the strain data were used to draw comparisons between strains measured at proximal and distal locations at varied speeds.

3.2.3.3.3 The effect of adding webbing to beams

The effect of adding webbing to beams on fluidic loading was analyzed by comparing the strain signals measured in bare beams to those measured in fins. Strains from *dorsal* (upper), *medial* (middle), and *ventral* (lower) beams on the fin were compared to strains from bare beams. Time series data were compared for beams and fins in air, noting qualitative differences in the signals as well as magnitude and variance differences at multiple phases of contact.

3.2.3.3.4 The effect of changing obstacle geometry

The effect of changing obstacle geometry was analyzed by comparing the strains experienced during contact with the flat plate obstacle and those experienced during contact with the configurable obstacle in different geometric configurations. Time series data were compared for beams and fins using similar techniques to previous analysis subsections.

3.2.4 Results

3.2.4.1 Beams in air and underwater

The strains experienced by beams in air were very similar to the strains measured in experiments using cantilevered beams and whisker sensors in air. Beams in air (Figure 13a) had small oscillations during the *acceleration* phase of the contact experiment, which quickly settled out to a steady state during the *constant velocity* phase. For most of the *constant velocity* phase, distal and proximal strains were approximately equal to one another and nearly zero. Strains remained near zero during the *approach* phase and there was no measured change in forces on the object to suggest structure-fluid-structure interaction (SFSI) prior to *contact*. *Contact* was apparent in the strain measures of both distal and proximal sensors, and during *relaxation* both strains quickly reached steady state values, often with distal strains slightly exceeding proximal strains.

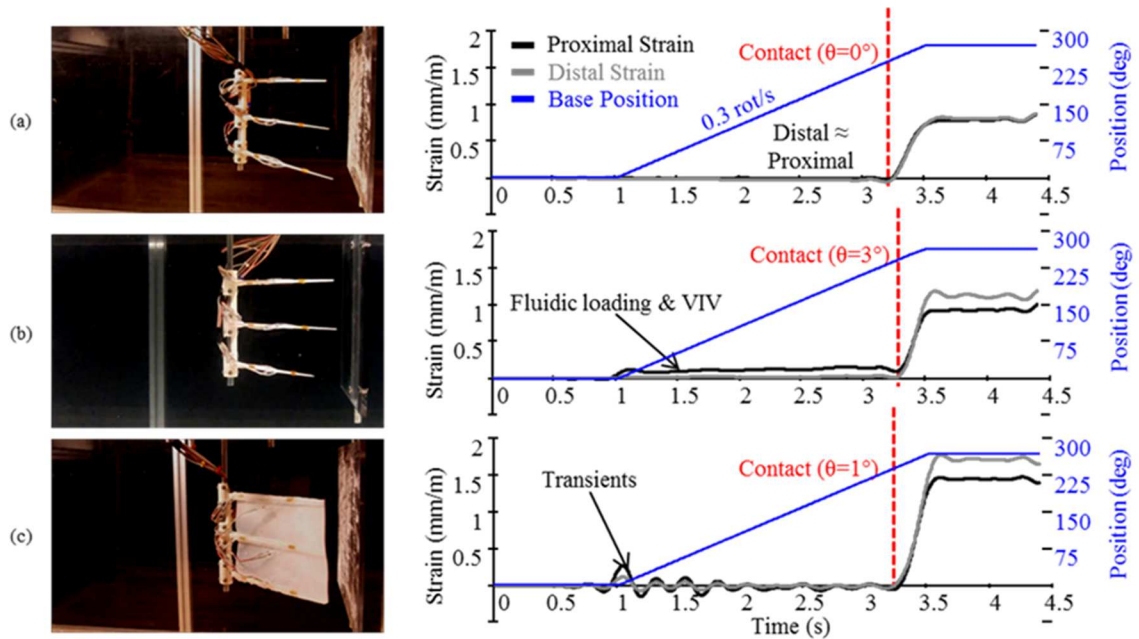


Figure 13. Photographs and strain data of typical contacts for moderate beams in air (a), moderate beams in water (b), and a fin in air (c). Relative contact times and angular offsets are indicated with beams in air as a zero-reference. Data were low pass filtered at 10 Hz for clarity.

Beams in water experienced greater strains than beams in air and the time of contact was delayed due to fluidic loading. Beams in water experienced an increase in strain during *acceleration* (Figure 13a), and at low speeds the strains reached a steady state value during the *constant velocity* phase. The magnitude of strain during *constant velocity* was significantly greater for beams in water than for beams in air and this effect was amplified by increasing stiffness and increasing speed. Proximal strains (at the base of the beam) were always greater than distal strains (at beam ends). At higher beam speeds (>0.2 rot/s), distal and proximal strains did not reach a steady state value prior to *contact*. A steady state value was never reached when very flexible beams were used, and this effect was consistent at a large range of speeds (>0.1 rot/s). Vortex induced vibrations were observed during the *constant velocity* phase when the beams were driven at high speeds (>0.3 rot/s). Strains during the *approach* phase were not significantly greater than strains during the *constant velocity* phase. At low speeds, *contact* was apparent on both proximal and distal sensors. *Contact* occurred later for beams in water than for beams in air, as a function of beam speed. Small oscillations were observed during *relaxation*, which typically lasted longer for beams in water than beams in air.

The strains on beams in water were more sensitive to changes in beam stiffness when the beams were underwater than when the beams were in air. The effect of beam stiffness on strain underwater was notable in multiple phases of the contact experiment. Decreasing the stiffness of beams underwater increased the magnitude of strain during the *constant velocity* phase and resulted in increased differences between the proximal and distal strains (Figure 14). For the flexible beams tested, the magnitude of strain

during the constant velocity phase could easily exceed the peak strains during contact and the steady state strains during the relaxation phase (Figure 20c). This effect was amplified at higher speeds (above 0.25 rot/s) and especially on the strains of the proximal sensor. As stiffness decreased, so did the magnitude of strain oscillations after contact, during the relaxation phase (Figure 14).

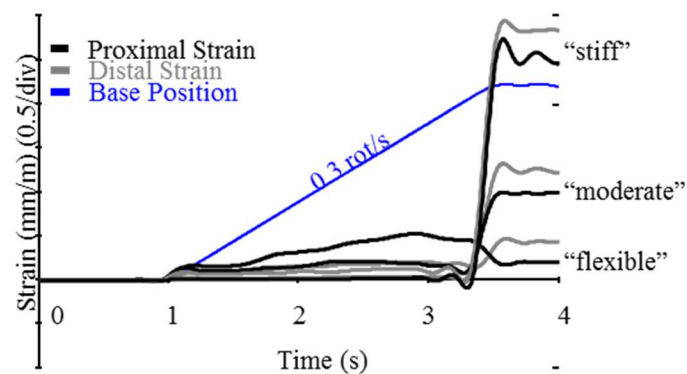


Figure 14. The effect of changing beam stiffness on the proximal and distal strains underwater during contact. Representative data are shown for stiff, moderate, and flexible fins and data were low pass filtered at 10 Hz for clarity.

3.2.4.2 Fins and beams in air

Fins in air experienced similar strains to beams in air, with slight differences between proximal and distal strains during *acceleration* and *relaxation* phases. Fins in air also exhibited small transient strains during *acceleration*, and proximal strains were noticeably greater than distal strains for *acceleration* and during the *constant velocity phase*. Both proximal and distal strains on fins took longer to reach a steady state than bare beams (e.g. Figure 15b). *Contact* was apparent for fins and beams in air at all stiffnesses, and often occurred slightly later for fins in air than for beams in air (Figure 13c). During the *relaxation* phase for fins in air, distal strains exceeded proximal strains,

whereas the difference was much smaller for beams in air (Figure 13a,c). Small transient oscillations were observed in the strains during *relaxation* for fins in air which were comparable to those of beams in air.

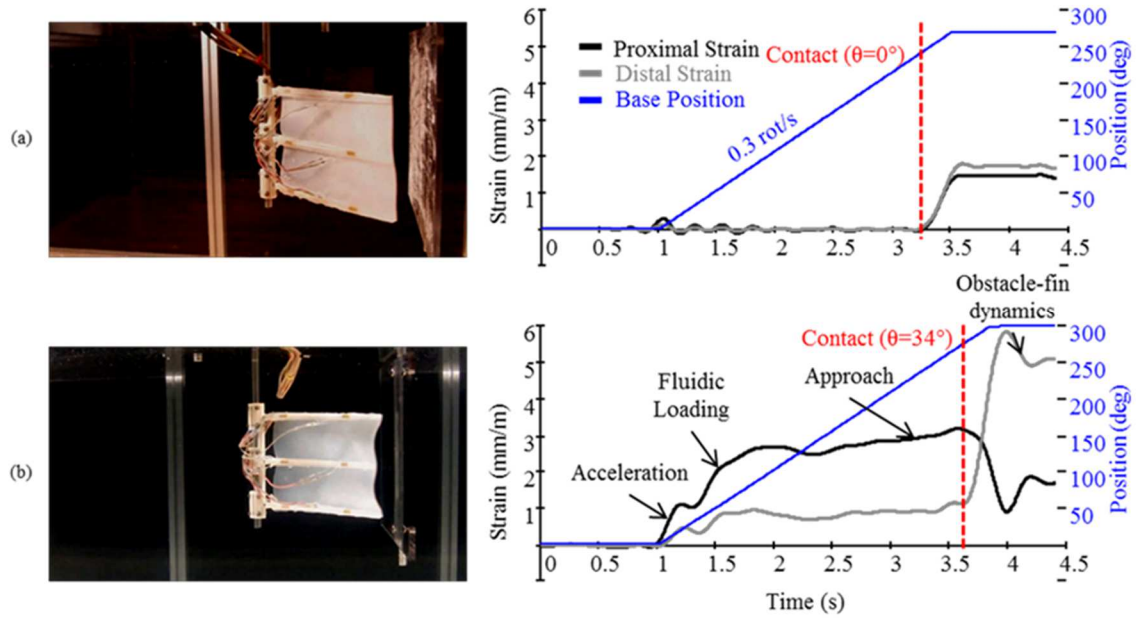


Figure 15. Photographs and strain data of typical contacts for a fin in air (a) and a fin in water (b). Relative contact times and angular offsets are indicated with the fin in air as a zero-reference. Data were low pass filtered at 10 Hz for clarity.

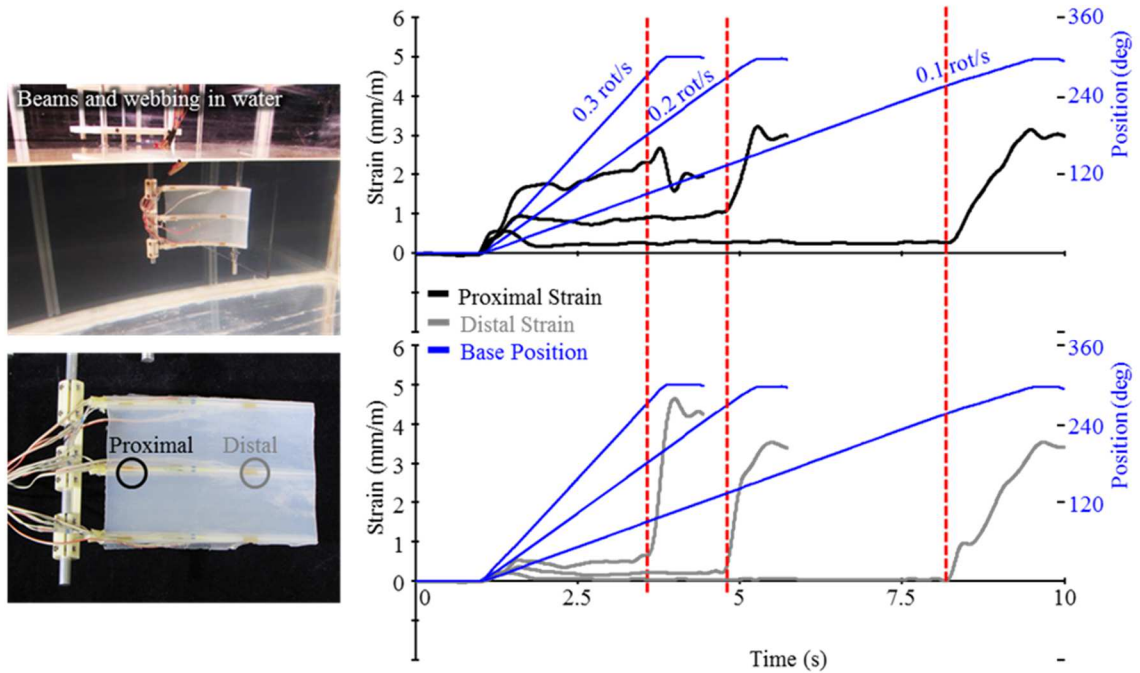


Figure 16. The effect of changing speed of the fins on the strain data of proximal (top) and distal (bottom) sensors underwater during contact. Representative data are shown for trial conditions of 0.1, 0.2, and 0.3 rotations per second. Data were low pass filtered at 10 Hz for clarity.

3.2.4.3 Fins in air and underwater

In contrast to fins in air (3.2), when in water, fins in water had large transient oscillations in the strain during *acceleration*, and proximal strains were significantly greater than distal strains in all phases prior to *contact*. At low speeds (<0.1 rot/s) steady state strains were reached, but at higher speeds settling times could not be established during *constant velocity*, especially for proximal strain data (c.f. Figure 15b). At high speeds (>0.1 rot/s), a clear *approach* phase was observed, where proximal and distal strains increased along with forces measured at the obstacle prior to contact (Figure 15, Figure 17). *Contact* was not always easily distinguished, as the strain on the fins during the *constant velocity* phase was often greater than the strain at the end of the *relaxation* phase (Figure 20a),

which occurred at high speeds due to the high fluidic loading on the fins. During *contact* the proximal strain frequently decreased, while the distal strain always increased, which was consistent with beams in water. As *relaxation* began the distal strains reached a larger steady state value than the proximal strains, and settling times for fins in water were typically very long (e.g. 0.5s) relative to other experimental conditions tested.

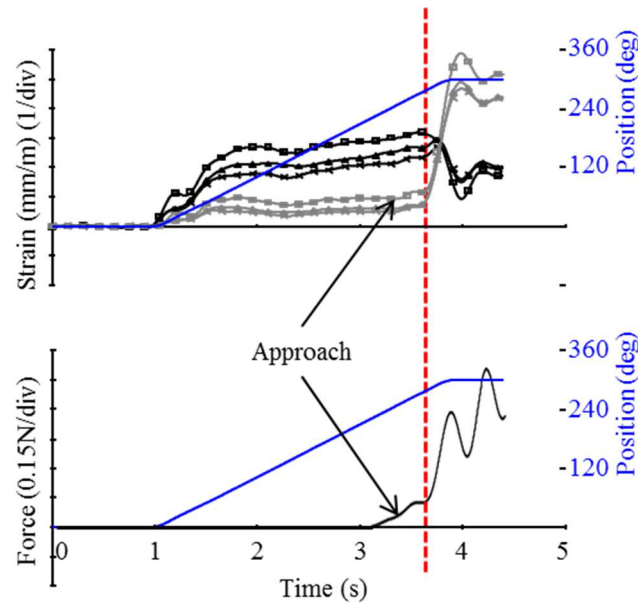


Figure 17. A representative *approach* phase of obstacle contact for a fin driven underwater. Small increases in strain on fin beams and reaction force on the obstacle were observed during this period. Data were low pass filtered at 5Hz for clarity.

3.2.4.4 The effect of speed on beams and fins

Increasing the speed of beams and fins caused strain to increase during *acceleration* and *constant velocity* phases, and this increase had significant impacts on strain during successive phases (*approach*, *contact*, and *relaxation*) of the contact experiment. At low speeds (less than 0.3 rot/s), beams had similar bending responses in air and underwater. At high speeds, beams underwater had much greater strain during *constant velocity* than

beams in air, and this effect was increased as beams were made more flexible. During the *constant velocity* phase underwater, average strains increased with increasing rotation speeds and these speed effects differed between proximal and distal sensors. As speed was increased, strain increases were well modeled by a quadratic fit on the proximal and distal sensors (e.g. $R^2=0.994$ and 0.991 for regressions, Figure 18a). Proximal strains measured on the fin were greater than distal strains during the *constant velocity* phase at all speeds tested, and proximal strains increased at a higher rate than distal strains as speed was increased (Figure 18a).

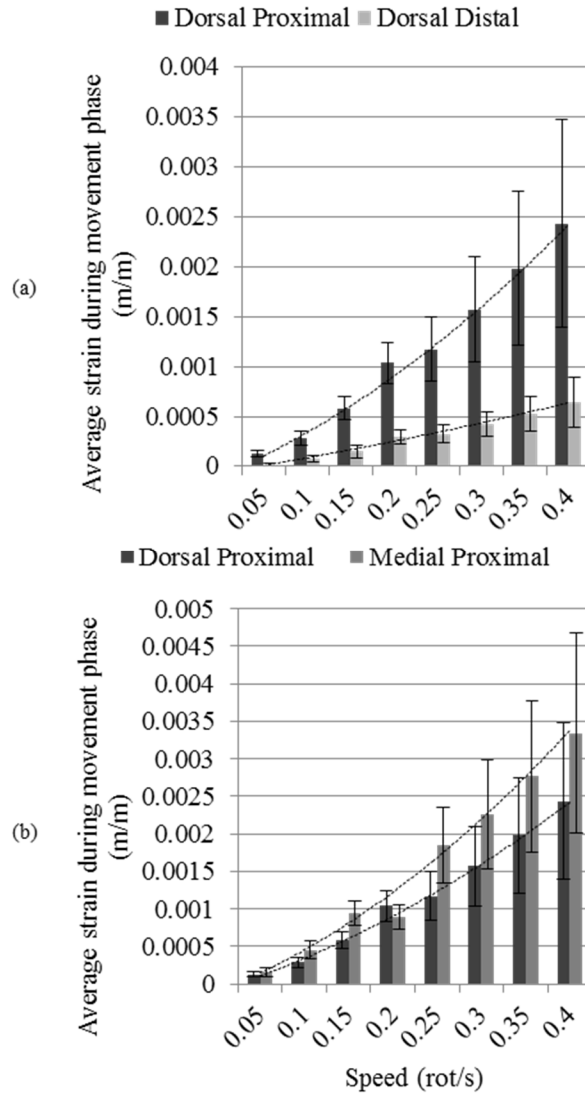


Figure 18. Comparison of average strains during movement phase for groups of sensors: dorsal proximal and dorsal distal (a), dorsal proximal and medial proximal (b). Second-order polynomial regression fits were applied to the data. Standard error bars correspond to one standard deviation in each direction.

At high speeds, small vibrations were commonly measured for beams in water during the *constant velocity* phase due to vortex induced vibrations, which were not observed in air. Analysis of high speed video revealed vibrations of the beams in the plane of rotation as well as perpendicular to the plane of rotation, which was consistent with vortex induced vibrations observed in experiments where circular or prismatic

beams are towed through fluid [82]. The strains induced by these vibrations (measured in the constant velocity plane) were small relative to the strains induced by *contact* (e.g. 0.05 mm/m versus 1 mm/m) but could be observed at high speeds (>0.25 rot/s; Figure 13b).

Increasing the speeds of beams and fins tended to create large differences in the *relaxation* strains of proximal and distal sensors underwater, but not in air. As speed was increased for fins underwater, distal strains in the *relaxation* phase were significantly greater than proximal strains (Figure 19). Increasing speed typically increased the average distal strains during *relaxation* and decreased the average proximal strains during *relaxation*. These relationships were somewhat linear for proximal and distal sensors ($R^2 = 0.834$ and 0.792 ; Figure 19).

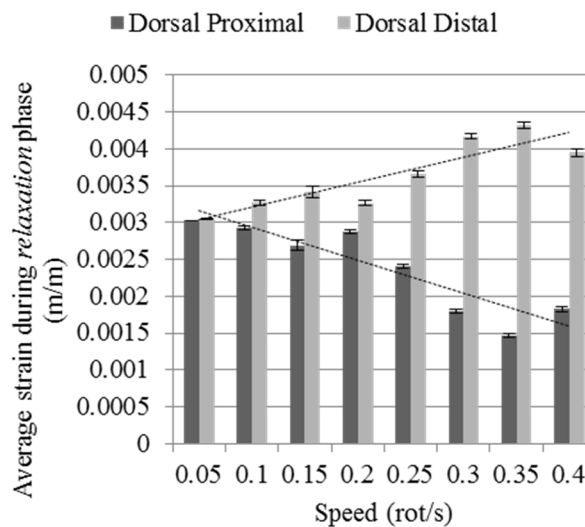


Figure 19. Comparison of average strains during the *relaxation* phase of contact on the dorsal proximal and dorsal distal sensors. Linear fits were applied to the data. Standard error bars correspond to one standard deviation in each direction.

3.2.4.5 *The effect of adding webbing to beams*

Adding webbing to beams caused significant increases in strain during *acceleration* and *constant velocity* phases underwater, which were much more significant than the differences in strain between beams in air and beams underwater. The subsequent phases of *approach*, *contact*, and *relaxation* were affected in that strain differed significantly between proximal and distal sensors as compared to beams underwater. During *acceleration* and *constant velocity* phases, oscillations in the strain were observed on both proximal and distal sensors (Figure 15b). These oscillations typically settled to a steady state prior to the *contact* phase, but were greater in magnitude than the oscillations observed in beams underwater.

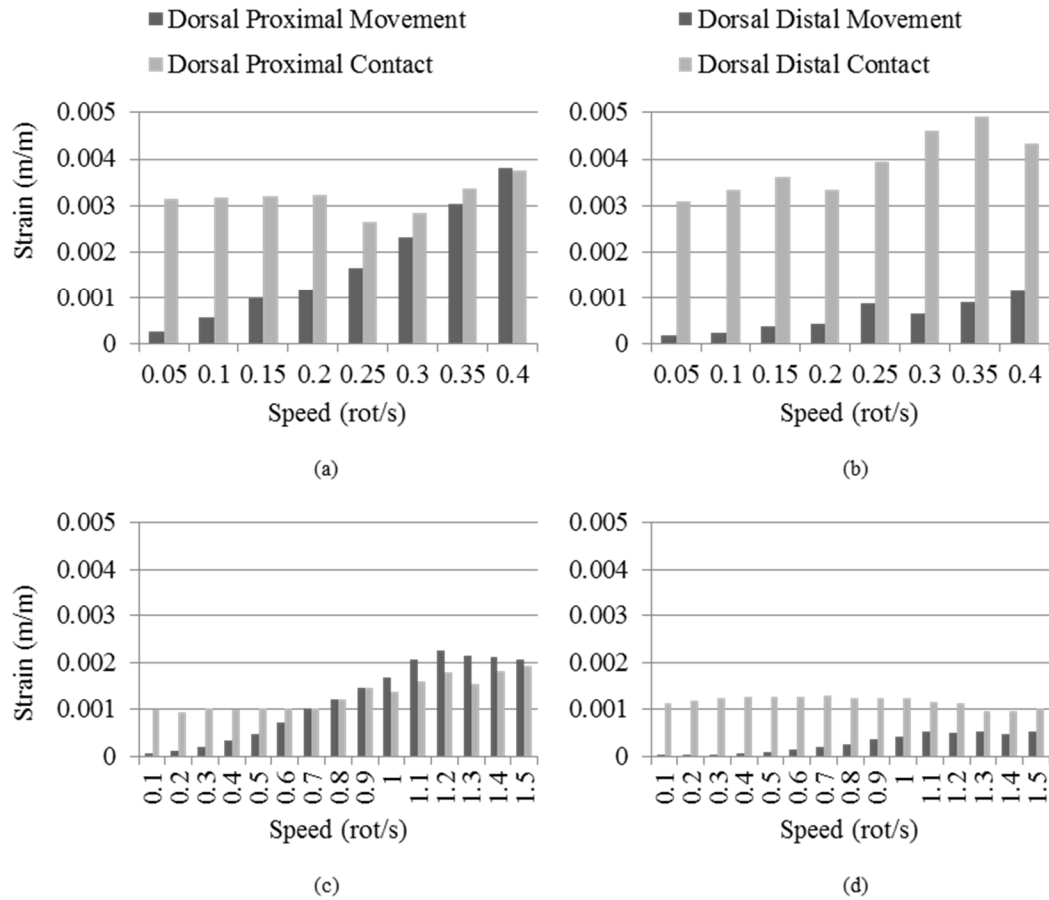


Figure 20. Peak strains reached during *movement* and *contact* phases for beams and fins underwater measured at dorsal proximal and dorsal distal sensors. Peak strains for proximal sensors on fins (a), peak strains for distal sensors on fins (b), peak strains for proximal sensors on beams (c), and peak strains for distal sensors on beams (d). Representative data are shown from randomly selected trials of listed conditions.

When driven underwater at high speeds, fins experienced strains during the *constant velocity* phase that were nearly as large in magnitude as the strains experienced during the *contact*. On proximal sensors, peak strains were achieved during *constant velocity* that exceeded the peak strains of *contact* (Figure 20). This effect was most pronounced on proximal sensors, whereas distal sensors typically had significantly smaller peak strains during *constant velocity* than during *contact*. Adding webbing to the

beams changed the strain distribution during the *relaxation* phase, where distal strains would settle to a higher steady state value than proximal strains after contact (Figure 18).

Adding webbing to beams significantly changed the strain distribution. Typically, strains along the edge beams were comparable to each other during all phases of *constant velocity* and *contact*, strains along the middle beam were greater than strains along edge beams in all phases prior to *contact* (Figure 21, Figure 18b). The difference between strains along edge beams and strains along the middle beam increased as speed was increased. For example, at moderate speeds (0.1,0.15,0.25 rot/s) there was a significant difference between proximal edge strains and proximal middle strains during the *constant velocity* phase, but no significant difference between the two at low (<0.1 rot/s) and high (>0.25 rot/s) speeds.

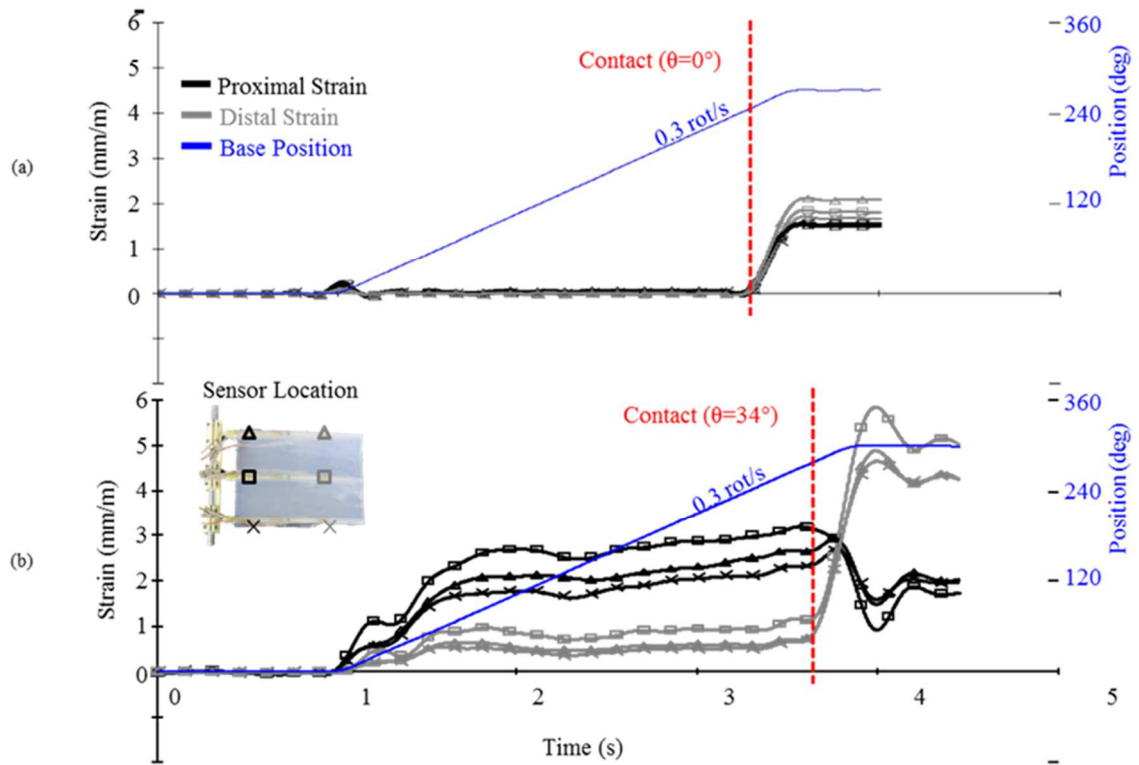


Figure 21. The effects of adding webbing to beams in air (a) and underwater (b) on distributed strain measures during a typical high speed contact (0.3 rot/s). Data were low pass filtered at 10 Hz for clarity.

Adding webbing to beams caused an increase in strain during the *approach* phase of the contact experiment, such that as the fin approached the obstacle, forces on the obstacle and strains on the fin increased due to the SFSI prior to contact. This effect was not observed for the bare beams. At high speeds (>0.2 rot/s), a small increase in strain on the fin and force on the obstacle was observed. Thus, as the fin approached the obstacle, the fin deformed away from the obstacle and loading on the obstacle increased prior to contact (e.g. forces of 0.1N were typical, c.f. Figure 17).

3.2.4.6 The effect of changing obstacle geometry

Compared to contact with a flat plate obstacle, the offset obstacle (Figure 11b) caused stretch in the webbing between beams in fins, which changed strain distributions during

approach, *contact*, and *relaxation* phases. Stretch was a result of offset surfaces in the complex obstacle. Changes to the obstacle geometry had no notable effects on strains during the *acceleration* and *constant velocity* phases of the contact experiment. In a typical example, after the first beam contact, the first beam was constrained against the obstacle (Figure 22c). As the latter two beams approached the obstacle, the webbing stretched and caused strain to increase prior to contact during the approach phase. For the first beam to approach the offset obstacle (c.f. Figure 23), strains were very similar during approach and contact phases compared to beam contact with a flat plate obstacle. During the approach phase, small increases in the first beam's strain were observed as the fin approached the first surface of the obstacle. However, the strain on the latter beams did not increase significantly during the *approach* phase.

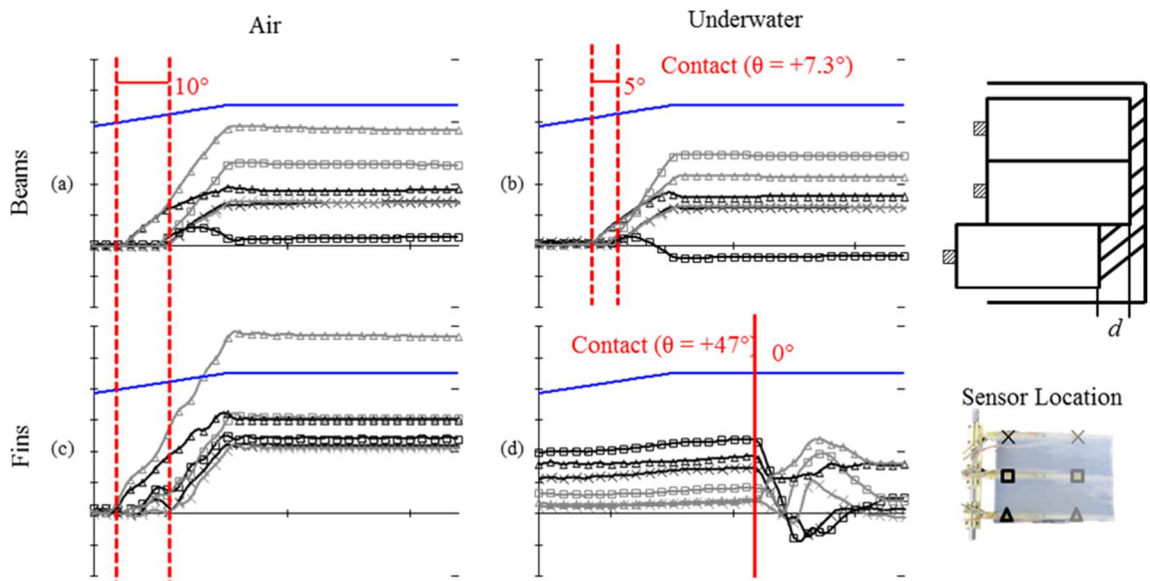


Figure 22. Comparison of distributed strain measures during typical contacts with an offset obstacle: (a) in air with beams, (b) underwater with beams, (c) in air with beams in webbing, and (d) underwater with beams in webbing. First and second contacts are indicated with dashed red lines and their angular distance is shown. Contact differences between air and water are shown based on initial air contact angles compared to initial water contact angles for beams (b) and beams in webbing (d). Representative data were smoothed with a 3 point averaging filter for clarity and are from a trial at 0.2 rot/s speed with an obstacle offset of $d = 10\text{mm}$. Strains are shown at 0.67 mm/m per division and time is shown at 0.5s per division.

When the fin system was brought underwater and driven into contact with an offset obstacle, fluidic loading increased strain during the *constant velocity* phase, caused strain to increase during *approach*, changed the time of *contact*, and changed the final strains of the beams during *relaxation* (Figure 22b,d). Just as fluidic loading delayed the time of contact for fins with flat plate obstacles (Figure 21b), time of contact was significantly delayed for fins with offset obstacles (Figure 22d). In air, offsetting the obstacle by a small distance was sufficient to create large timing differences in contact (e.g. Figure 22a). Underwater, despite the offset contact surfaces, successive beam contacts had smaller timing differences than in air (Figure 22b,d). At high speeds (≥ 0.2 rot/s) there was no difference in the time of contact between beams underwater (Figure 22d).

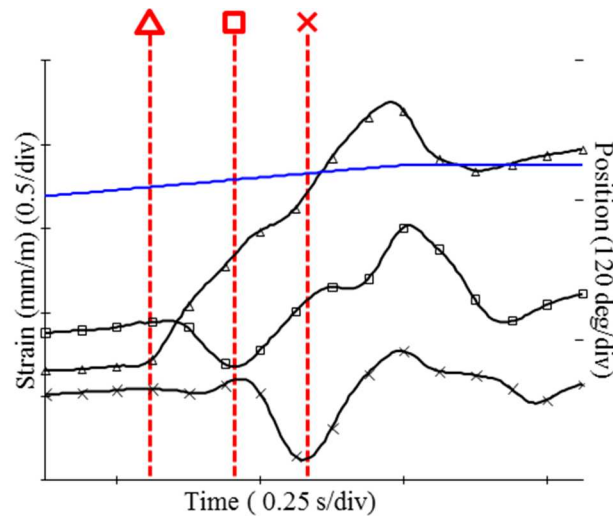


Figure 23. Distal strain signals for a typical contact between a fin and a stair-step obstacle underwater. Signals shown are representative of a contact with a [0 10 20]mm rigid obstacle. Contacts are indicated with dashed vertical lines corresponding to each beam within the fin. Data were low pass filtered at 10 Hz for clarity and are from a trial at 0.2 rot/s speed.

Fluidic loading delayed contact and changed the relative timing between contacts when stair step obstacles were used. These effects were observed most strongly in the *contact* and *relaxation* phases. Due to the large fluidic loading experienced during *constant velocity* with fins, the steady state values of fin strains during *relaxation* settled into much lower values than in air (Figure 22d). In air, the beams that contacted the obstacle first reached a higher magnitude of strain than those tested underwater in all cases.

3.2.5 Discussion

Beams and fins experienced similar strains during contact experiments in the air, but there were significant differences in strains during contact when these systems were tested underwater. The large increases and oscillations in strain during *acceleration* suggest that initiating movement underwater from rest can cause significant loading and measurable strain on sensing platforms. When moving at high speeds during *constant velocity*, vortex induced vibrations (VIV) may occur depending on the speed and geometry of the beams, whereas VIV are comparably negligible in air. Increasing speeds during *constant velocity* increased fluidic loading during this phase. With the large amount of fluidic loading on a flexible fin, fin strains during *constant velocity* could easily exceed the strains during *contact*. Though the impact of fluidic loading can affect underwater contact sensing, in some circumstances fluidic loading may affect sensing in air. Research by Quist et al. also distinguishes between the dynamics of rat whisking behaviors during movement without contact and when the whiskers come into contact with objects [83], finding that at high speeds, the dynamics of whisker movement can generate mechanical effects as large as the effects of contact. If robots are to be used for

underwater sensing and manipulation, the effects of fluidic loading must be further modeled in detail.

Unlike in most air applications, the underwater structure-fluid-structure interaction (SFSI) caused changes to strain in each phase of the contact experiment. Fluidic loading affects strains during multiple phases of contact underwater, and dynamics from early phases can affect subsequent phases. The increased strains on beams and fins during the *constant velocity* phase can have implications for later phases of the contact experiment, as the beams and fins can reach the obstacle in different deformed configurations. For instance, when the fins were moved at high speeds (>0.3 rot/s), strains were very high during *constant velocity* and increased even more due to the SFSI during the *approach* phase. These high strains meant that the fin was highly deformed when it reached the obstacle, such that when it stopped after *contact*, it settled into a configuration of very high strain on the distal ends, with much less strain proximally. This differed from fins or beams in air, which had very similar proximal and distal strains during *relaxation*. This suggests that the time history of fluidic loading may be important in contact perception underwater, because the dynamics of early movement can impact later phases of contact.

The addition of webbing to beams created a mechanical coupling between adjacent beams, which changed the strains that arose in complex contacts. When working with underwater robots with control surfaces, the sensors on a compliant control surface are coupled to one another. More specifically, the robotic degrees of freedom share sensory information and mechanical loading. On the downside, this may make modeling and signal analysis more complex, involving vibration effects and nonlinear coupling

between beams. If the bending of one beam causes strong bending of another beam through stretch, false contacts could be perceived without sophisticated models. On the upside, engineering design of the coupling may be useful to distinguish the sequence of contacts, which could be used for feedback control of a manipulation task, for example. Redundant sensory information could be exploited for more precise shape recognition, using principles of hyperacuity, for example [84, 85].

Complex obstacle geometries tended to make *contact* strains less apparent and caused stretch between the beams of fins. For obstacles with a single offset (Figure 11b), strain from the first beam to contact the obstacle could be used to detect subsequent beam contacts from small peaks in the strain measures (Figure 22c and Figure 24c). Though changes to strain magnitudes were typically small during subsequent contacts, changes in strain rate were more notable and could serve as a metric for detecting subsequent contacts. The propagation of mechanical stimuli through tissue has been observed in other haptics studies, where vibrations from textural exploration in fingertips are above sensory thresholds for human wrist receptors, and may be used for perception of object properties [86, 87]. However, strains during contact experiments with varied obstacle geometries may be difficult to interpret, as SFSI effects were observed during *constant velocity*, *approach*, and *contact* phases. At low speeds with fins, it may be possible to discern between stretch and contact, but at high speeds the significant fluidic loading during *constant velocity* will tend to increase fluidic loading during *approach* and make distinguishing contact more difficult.

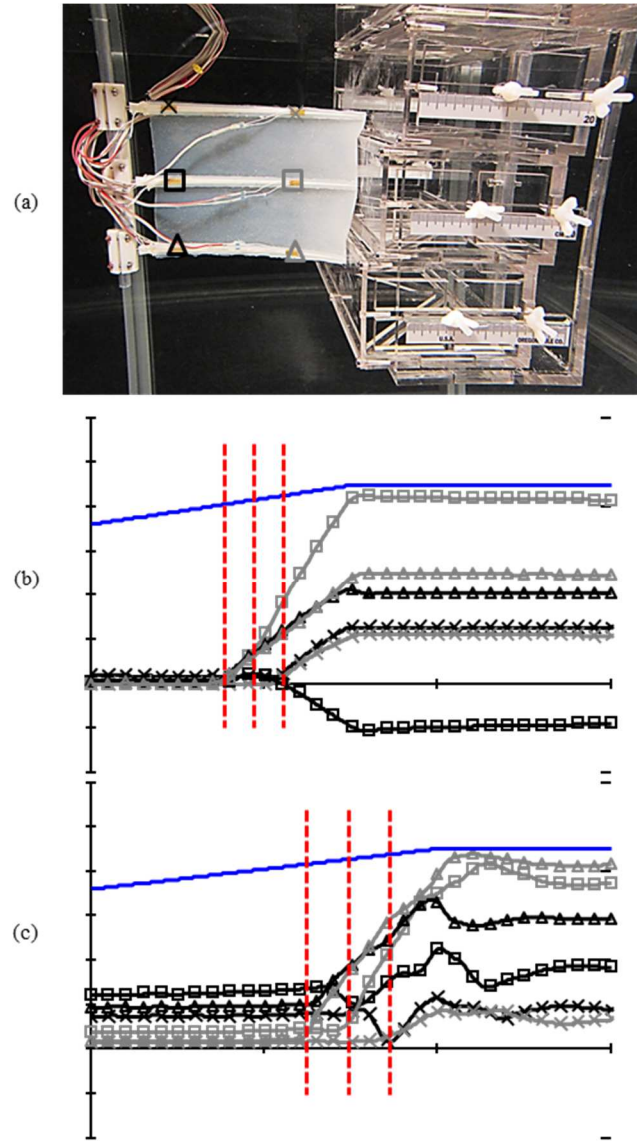


Figure 24. The effects of webbing on strain sensing with complex obstacle geometries. Photo of a typical contact for a fin underwater with legend overlaid for sensor locations (a); distributed strain signals for beams (b) and fins coming into contact with a stair step obstacle in water. Signals shown are representative of a contact with a [0 10 20]mm rigid obstacle. Data were low pass filtered at 10 Hz for clarity. Strains are shown at 0.67 mm/m per division and time is shown at 0.5s per division.

Active sensing and perception of underwater contact will present new challenges that have not been observed in air environments. Perceptual models of object contact should account for fluidic loading in order to understand the phenomenology of contact. Using fins to sense object contact may mean that flat objects appear curved, and the

degree of apparent curvature will be dependent on the stiffness distributions and velocity of the fins. Beams with webbing will amplify the velocity effects of fluidic loading, which can delay time of contact. To design an underwater active touch sensing platform, engineers must evaluate these tradeoffs between compliance and movement speed in order to effectively sense movement through fluid and contact with obstacles. This will often mean that in many cases, unless the robot is very stiff or contacts an object immediately upon excursion, beams with webbing will be in a deformed state when they come into contact with obstacles. Without accounting for this effect of fluidic loading, false percepts could easily arise. For example, the middle beams of fins experience more strain than the edges during the *constant velocity* phase, and therefore the edges of fins will tend to contact obstacles prior to the middle sections. In this case, flat objects could be falsely judged as sloped based on strain increases during *contact*.

The SFSI for fins and objects is complex, and multiple sensors may be required for understanding fluidic effects during multiple phases of contact. Unlike most whisker sensors in the literature which have multi-DOF sensors at the beam base, multiple regions of a fin may contact an object at the same time and so data from a distribution of sensors along a single beam could help resolve the shape of an object, whereas data from a single sensor may be insufficient. In addition, results indicated large differences between proximal and distal strains during the phases of contact, and careful spatial sampling might be exploited to improve contact perception. Work by the authors has shown that during propulsion the relationship between sensory measures and forces of a fin is nonlinear, and in order to estimate the propulsive forces of complex fins, distributed and heterogeneous sensors are needed [88]. In order to create underwater robotic limbs that

can drive locomotion and mediate contact with obstacles amidst fluidic loading, distributed and heterogeneous intrinsic sensors may be needed. Flexible webbings on sensory beams are already in use for underwater propulsion [23, 62, 88], and adapting them for use in active touch sensing may significantly expand their functionality.

3.2.6 Conclusion

This study demonstrated several of the effects of fluidic loading on strain sensing with compliant robotic beams and fins as they contacted obstacles in air and underwater. Multiple phases of contact were identified and described in order to better understand the phenomena introduced by the structure-fluid-structure interactions (SFSI) during *acceleration*, *constant velocity*, *approach*, *contact*, and *relaxation* phases. Large differences in measured strains were observed during the *constant velocity* phase depending on the robot's structure, stiffness, and speed. Large changes in sensory signals were observed through the introduction of small changes to obstacle geometry, and these effects were amplified through the addition of webbing to bare sensory beams.

Flexible membranes, webbings, and surfaces are important for compliant propulsion and manipulation, and these systems are affected by fluidic loading differently underwater than in air. Loading distributions on fins were different than those of bare beams, as strain signals varied from base to tip and from edge to middle. Changes to the geometry of obstacles also have the potential to perturb the loading distribution locally as beams and fins *approach* obstacles, affecting contact timing and deformation prior to contact.

As compliant robots are increasingly used in underwater applications, fluidic loading will play a significant role in the sensing of movement and contact.

Heterogeneous sensors may also be necessary in order to distinguish between fluidic loading, contact loading, and stretch, which arise from different physical phenomena. Future work will investigate the use of stretch sensors (c.f. [89]) in webbing to measure strain related to the deformation of the fin webbing and potentially to other aspects of fluidic loading. In the underwater environment, fish and robots are likely to come into contact with compliant obstacles (e.g. eel grass) and thus it is relevant to understand the effects of increased compliance on sensation with fins and beams underwater. In future work, the effect of obstacle compliance on strain in fins will be evaluated with different surfaces in the configurable obstacle.

3.3 Paper 2: An evaluation of contact classification techniques during underwater contact with compliant beams and fins

3.3.1 Abstract

In water, it is challenging to classify object contact using sensory data due to the interaction of the fluid with the sensing robot and the target object. Many techniques exist for contact classification in air, but these have not been evaluated on underwater contacts and may fail due to the changes introduced by the fluid interaction. Inspired by fish fins, beams and fins were instrumented with strain sensors and driven into contact with obstacles in air and in water. Three contact classification techniques were explored for the classification of contact underwater using beams and a fin instrumented with distributed strain sensors. Results suggest that fluidic loading can cause common thresholding techniques to fail, especially at high speeds and with stiff beams. Careful design of the flexural rigidity, the platform speed, and the sensor placement can lead to better performance at contact classification underwater.

3.3.2 Introduction

Underwater, the characterization of object contact using sensory data presents significant challenges due to the interaction of the fluid with the sensing robot with the target object. Early work with beams and compliant fins has shown that the interaction of the fluid with both the robot manipulator and the object is complex [73, 90], and that discrimination of contact from intrinsic sensory signals is still an open problem. The interaction, termed the structure-fluid-structure-interaction (SFSI) [90], causes loading and deformation to beams and fins during multiple stages of the contact: (a) when motion is initiated,

transient accelerations deform beams, (b) during movement through fluid, the beam deformation is affected by the beam flexural rigidity and driving velocity, (c) as the beams approach the object, they can be repelled from or attracted to the object depending on the SFSI, and (d) the beams will often contact the object in a deformed state, leading to a relaxation period after contact where the beams settle into a final configuration. Due to the compliance of sensory beams and fins, it is necessary to distinguish between the deformation caused by fluidic loading and that caused by contact loading. For these reasons, detecting the instant of contact and classifying contact loading versus fluidic loading are major challenges.

There are many effective approaches used to discriminate contact in air using end-effectors with sensors. Early researchers in contact sensing, inspired by whiskers and insect antennae, have shown that contact is easily detected using either strain or torque information within sensory beams [65, 66, 91-94]. Rapid changes in strain [90], contact pressure, reaction forces, or moments [50] can be used to precisely identify a contact event, by estimating both the time instant of contact and the duration of contact. Information from the contact event can be used to accurately characterize the geometry of objects using active sensing techniques and repeated contacts across 3d surfaces [49]. Sensory beams can be arranged in array formations [95], inspired by the facial vibrissae of rats and mice, in order to rapidly gather geometric information over a surface rather than a single contact point.

Distributed sensors within fins and beams may provide a way in which underwater contact can be more accurately discerned than with individual sensors. Recent studies of the sensory systems of bony fish have shown that the pectoral fins of the

bluegill sunfish aid in low speed navigation [3] and are richly innervated with multiple types of afferent nerve endings that respond to bending deformation [6, 21], distributed through their bony rays and membrane webbing [19, 20]. These biological studies have inspired the use of distributed sensors in robotic fins for both the estimation of propulsive forces and the characterization of contact with obstacles. Distributed pressure and bending sensors were necessary to predict the propulsive forces created by a multi-DOF, flexible fin [88], especially to predict complex propulsive forces where the direction and magnitudes of force were changing. It follows that since movement through fluid and contact with obstacles will create complex interaction forces [90], distributed sensors may aid in discerning aspects of the fluidic loading and contact loading.

The objective of the work presented herein is to evaluate the use of three contact classification techniques for the discrimination of contact underwater using beams and a fin with strain sensors distributed along the beams. Based on the extensive experiments of a prior study of underwater obstacle contact [90], data were analyzed using multiple contact classification techniques and the performance of these techniques was analyzed across changing experimental conditions to beams and beams in webbing (fins). For each contact discrimination technique, the best performing sensors and subsets of sensors were determined. Additionally, performance across changing trial parameters was analyzed to determine best practices for robot speed, beam stiffness, and sensor placement to discriminate contact loading from fluidic loading.

The paper is structured as follows. The Methods are presented in section 2, including a description of the robotic platform and experiments and the analysis techniques used to characterize contact from experimental data. The Results are presented

in section 3 and are grouped by specific contact discrimination technique. The Discussion and Conclusion are presented in section 4, highlighting the use of the results for the classification of contact in underwater environments using sensory data from compliant devices.

3.3.3 *Methods*

3.3.3.1 *Robotic platform and prior experiments*

Experiments were conducted to understand the effect of fluidic loading on underwater contact with beams and a fin [90] (Figure 25), and data from these experiments was selected and processed for analyzing multiple contact classification techniques herein. The robotic platform was designed to drive flexible beams and fins through fluid and into contact with obstacles in air and underwater (Figure 26). Beams of three flexural rigidity distributions were used – denoted *flexible*, *moderate*, and *stiff* – and were designed with a linear taper from base to tip, as in [17]. Beams were instrumented with strain gages in half-bridge configurations (KFG-5-120, Omega, Stamford, CT) at proximal ($x=10\text{mm}$ from base) and distal ($x=100\text{mm}$) locations. The fin consisted of three *moderate* beams cast into a 1mm thick silicone webbing, and it was instrumented with proximal and distal sensors along each beam (Figure 25). One fin was tested due to the complexity of manufacture and instrumentation. The robotic platform drove the beams and fins at a range of speeds ($[0.05,0.4]$ rotations/s (rot/s) for fins; $[0.05,1.5]$ rot/s for beams) into contact with a flat acrylic plate obstacle (200 x 250 x 6.25 mm). The beams and fin were programmed to accelerate from rest to a constant velocity trajectory and then to come into contact with the obstacle, and to decelerate to rest shortly after contact.

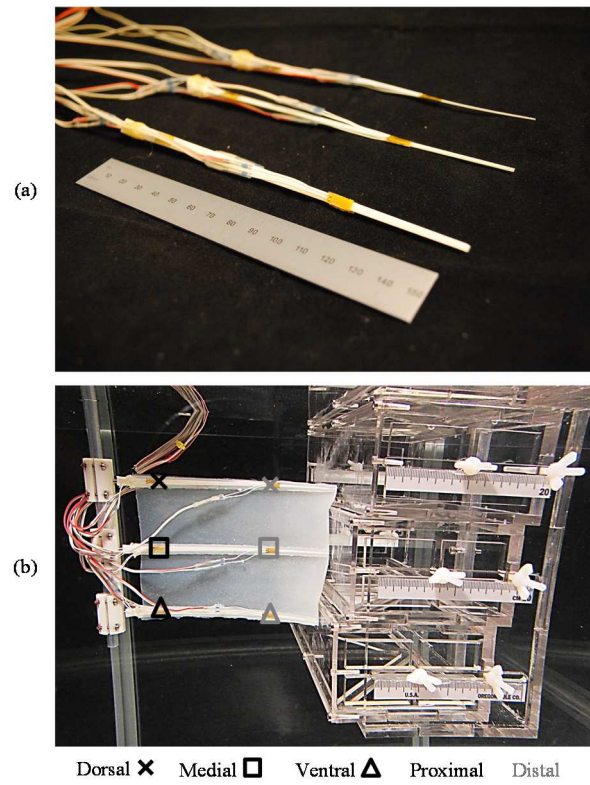


Figure 25. Instrumented beams and fin used in contact experiments. Beams of three stiffnesses instrumented with proximal and distal strain gage sensors (a). A fin, with three embedded beams instrumented with sensors along each beam (b), comes into contact with a complex, stair-step obstacle.

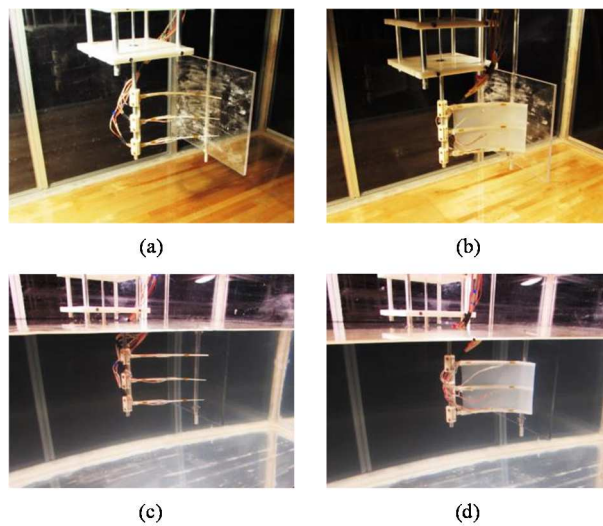


Figure 26. Test environments for beams and fins: beams driven in air (a), fin in air (b), beams in water (c), and fin in water (d).

3.3.3.2 Classification techniques

Multiple contact classification techniques were designed and their performance was compared across experimental conditions (Table 2). Simple contact classification techniques were chosen that have been successful in air, in order to explore the complexity introduced by the structure-fluid-structure-interaction between beams and objects during underwater contact. *Contact* and *No Contact* conditions are abbreviated as C and NC, respectively.

Table 2. Summary of contact classification techniques

Contact Classification Technique	Contact Conditions
A. Strain threshold	$\varepsilon_i(t) > \varepsilon_{i,t}, i = \{1, \dots, 6\}$
B. Strain rate threshold	$\frac{\varepsilon_i(t) - \varepsilon_i(t - \Delta t)}{t - \Delta t} > \delta \varepsilon_{i,t}$
C. Strain difference threshold	$\varepsilon_i(t) - \varepsilon_j(t) > 0, C : \varepsilon_{ij} > 0$ $\varepsilon_i(t) - \varepsilon_j(t) < 0, C : \varepsilon_{ij} < 0$

Strain threshold. The maximum strain prior to the time of contact was stored as the strain threshold, ε_t . C was classified by this technique when the measured strain ε_m exceeded the strain threshold, otherwise NC was classified (Figure 27a). Setting a threshold for sensory data (e.g. motor torque) is commonly used to detect the incidence of contact. This technique was based on work by Solomon and Hartmann [50], who set a

measured torque threshold to determine when a robotic whisker came in contact with a rigid object.

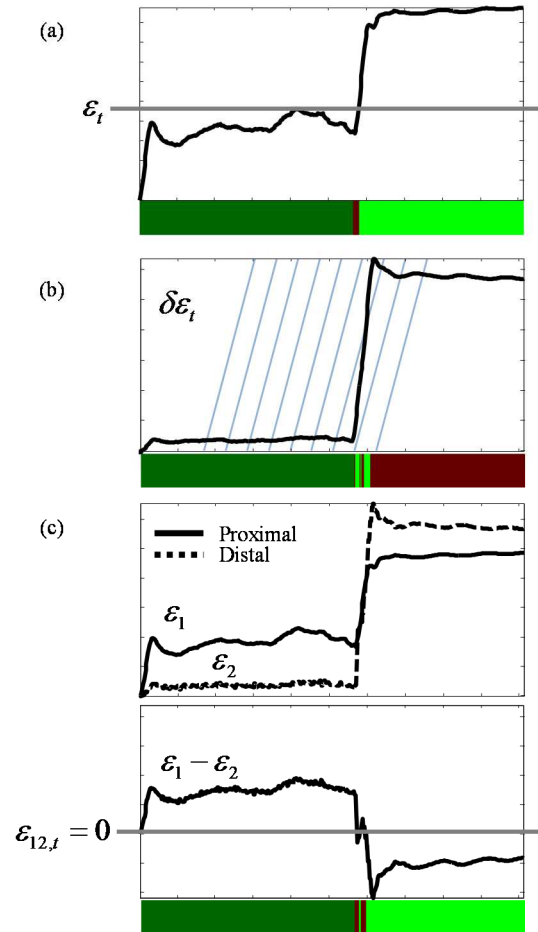


Figure 27. Illustration of three contact classification techniques tested: (a) strain threshold, (b) strain rate threshold, and (c) strain difference threshold. For (c), distal strains are subtracted from proximal strains and the difference is used to compute contact. Colored classification bars are shown beneath each time series example.

Strain rate threshold. The slope of the strain at the time of contact was stored as a rate threshold, $\delta\epsilon_t$. C was classified by this technique when the measured strain rate $\delta\epsilon_m$ exceeded the strain rate threshold, otherwise NC was classified. Since the strain rate was typically close to zero after contact, after 5 successive C classifications the robot was classified in C (Figure 27b). Rate thresholds have also been used to detect contact using

robotic whiskers in air, where a large rate of change of curvature of the whisker was used to determine the incidence of contact [96].

Strain difference threshold. For each ordered pair of sensors (ϵ_i, ϵ_j) along a single beam, the difference of those sensors' data was computed, forming ϵ_{ij} . ϵ_{ij} was computed after the instant of contact and the sign of the result was used to determine the conditions for contact. If ϵ_{ij} was negative after contact for the given pair, then a positive difference was classified as C and a negative difference was classified as NC (Figure 27c). This technique was selected based on the observation that the difference between proximal and distal strains often changed sign after contact [90], especially underwater.

3.3.3.3 *Performance metrics*

Contact discrimination was quantified in order to measure and compare the performance of each technique. Contact discrimination was defined as: (1) estimating the instant of contact, and (2) correctly classifying whether the robot is in contact or not in contact.

The estimated instant of contact (1) was evaluated using the error in time between the first predicted instant of contact and the actual instant of contact. Since most techniques had false positives, a standardized method was selected to calculate the estimated instant of contact. The instant of contact t_c was estimated by the first classified instance of C with at least 10 following C classifications. The choice of 10 classifications was selected based on preliminary analysis that suggested that 8-12 classifications resulted in best performance from all techniques.

Classification accuracy (2) was evaluated using a modified confusion matrix (from [97]) that classified the state of the system at each sampling time. For each entry of

the confusion matrix, the accuracy was evaluated at each time step and the average accuracy was reported (c.f. Table 3).

Table 3. Confusion matrix of contact classification accuracy

		Predicted	
		NC	C
Actual	NC	$\frac{\sum k_{(NC NC)}}{\sum k_{NC}}$	$\frac{\sum k_{C NC}}{\sum k_{NC}}$
	C	$\frac{\sum k_{(NC NC)}}{\sum k_{NC}}$	$\frac{\sum k_{C C}}{\sum k_C}$

The performance of each technique was analyzed using data from distributed strain sensors (2 for beams, 6 for fins; c.f. Figure 25). The best sensors and subsets of sensors were selected for each of the classification techniques. Since it was expected that each contact discrimination technique would have differing results depending on the speed, stiffness, and robot structure (i.e. beams, fin), each technique was analyzed individually for each subset of robot parameters. In order to assess the effects of fluid on contact classification, performance data were compared between contact made in air and contact made underwater. Technique-specific thresholds were calculated on data from one set of trials and techniques were tested on data from randomly selected trials with the same conditions. Beams in air using the strain threshold technique (Table 2A) are generally used as the gold standard for comparisons between techniques.

3.3.4 Results

3.3.4.1 Strain threshold

Using strain rate thresholding was generally effective at classifying beam contact in air, but the technique performance degraded for beams and fins underwater. In air with beams (Figure 28(a)), a strain threshold could be used to distinguish between “contact” (C) and “no contact” (NC) conditions with high true positive (C/C: 99%) and true negative rates (NC/NC: 98%). Couplings between beams in fins tended to cause significant oscillations in the strain data (Figure 28(b)), which delayed the estimation of the instant of contact (Table 4). The classifier performed very well at classifying underwater contact with fins (C/C>90%), except at high speeds (>0.2 rot/s), where classification failed. The strain threshold classifier had universally high true positive classification rates (C/C typically >95%).

At very high speeds (≥ 1.0 rot/s), contact was never detected, because the strains due to fluidic loading were often significantly greater than the strains due to contact loading and so the contact strain never exceeded the initial strain threshold (Figure 29). This occurred at even lower speeds (>0.5 rot/s) when *stiff* beams were used. When fins were driven underwater, the strain threshold technique typically failed at speeds greater than 0.2 rot/s.

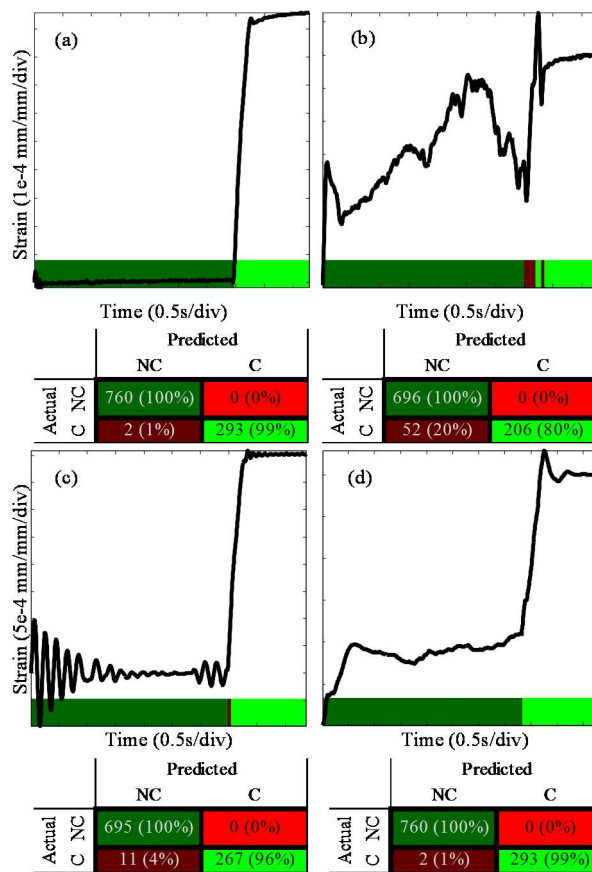


Figure 28. Performance of strain threshold technique. Time series graphs (top; a-d) are representative of typical strains for each structure and environment, and were driven at 0.1 rot/s in pictured examples. Classification rates are shown for each condition.

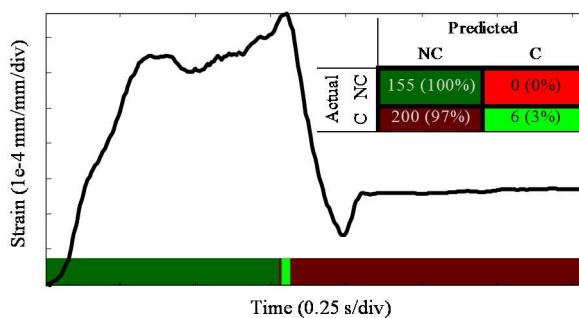


Figure 29. Breakdown of performance in strain threshold technique when the strain due to fluidic loading exceeds the strain due to contact loading. Time series data from stiff beam driven at 1 rot/s and sampled from the proximal sensor.

Despite performance degradation of the strain threshold technique at high speeds for the *proximal* sensory data, when the *distal* sensory data was used the technique performed very well across testing conditions (Table 4). The instant of contact was accurately estimated and the performance of the classifier was typically above 95%.

3.3.4.2 *Strain rate threshold*

The strain rate threshold technique performed well at classifying NC and C for beams in air and underwater, but performed poorly at both for fins (Figure 30). For example, with beams driven at 0.2 rot/s, the technique had high classification rates in air (NC/NC = 100%, C/C = 98%). With fins in air at 0.2 rot/s, true positives were well classified (C/C = 99%), and true negatives slightly less well classified (NC/NC = 91%). Fins underwater had acceptable true negative classification rates (NC/NC = 74%), but poor true positive classification rates (C/C = 38%).

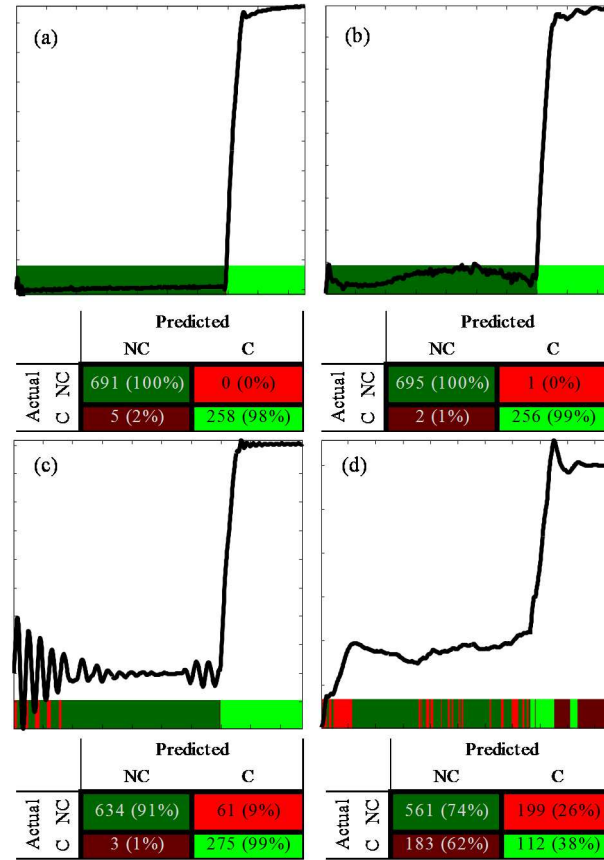


Figure 30. Performance of the strain rate threshold technique. Representative time series data and classification performance are shown for beams in air and underwater (a,b) and fins in air and underwater (c,d). Platform was driven at 0.2 rot/s.

As the platform speed increased underwater, the strain rate threshold technique performance worsened. At high speeds, vortex induced vibrations caused oscillations in beams at all stiffnesses that triggered classification of false positives (i.e. C/NC). As fin speed increased in air, the strain threshold technique performance worsened in a like manner, such that oscillations in the strain resulted in false positive classifications.

3.3.4.3 Strain difference threshold

The strain difference threshold technique was generally very effective at classifying underwater contact. During fluidic loading, NC was generally accurately classified

across conditions (NC/NC > 75%). During contact, C was generally very accurately classified (C/C > 80%).

Strain differencing had significantly different performance in classifying contact in air than contact underwater. When the beams were not in contact, the technique performed poorly in air but well underwater. Since fluidic loading was relatively insignificant in air in tested conditions, differences between proximal and distal sensors were generally small, and so many false contacts were detected (Figure 31(a,c); 18-25% error). However, underwater, fluidic loading generally caused greater proximal strain than distal strain (c.f. [90]), and so NC was classified with very low error (Figure 31(b,d); ~ 0% error).

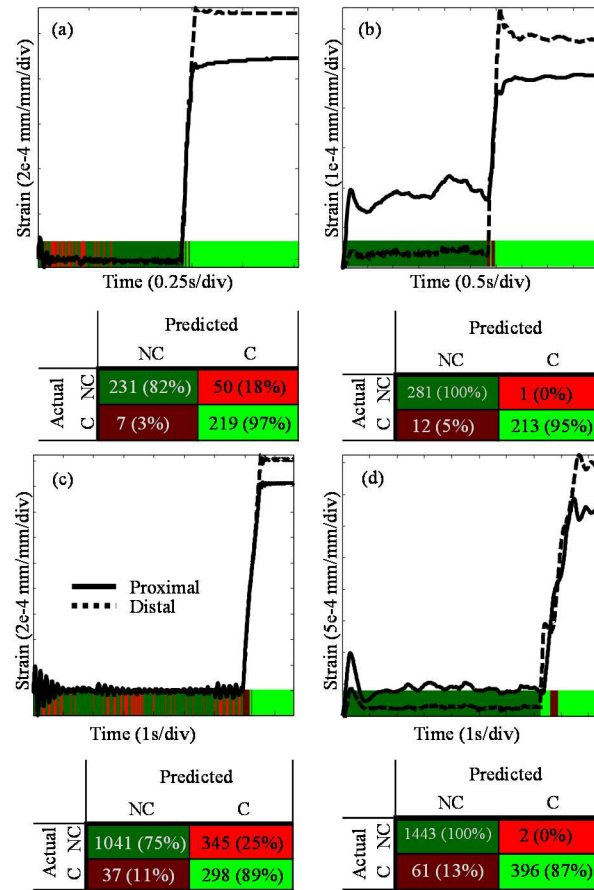


Figure 31. Performance of strain differencing technique for beams in air and underwater (a,b) and fins in air and underwater (c,d). Time series data shown are representative of general trends for beams and fins at moderate speed (0.2 rot/s for fins, 0.5 rot/s for beams). Confusion matrices are shown for each condition's data.

3.3.4.4 Speed and stiffness effects

Changing the speed of the robot affected the performance of the strain difference classifier. At low speeds (0.1 rot/s) underwater, NC was accurately classified (90.8%) and C was perfectly classified (100%). At moderate speeds (0.5 rot/s), NC was very accurately classified (99.6%) and C was accurately classified (94.7%). At high speeds (>1.0 rot/s), NC was still very accurately classified during movement through fluid (>90%), but C was generally poorly classified (<1%). Since high speeds tended to significantly deform the beams underwater, the beams reached the obstacle in a highly

deformed state, and after settling into contact, were strained such that there were very small differences between proximal and distal strains.

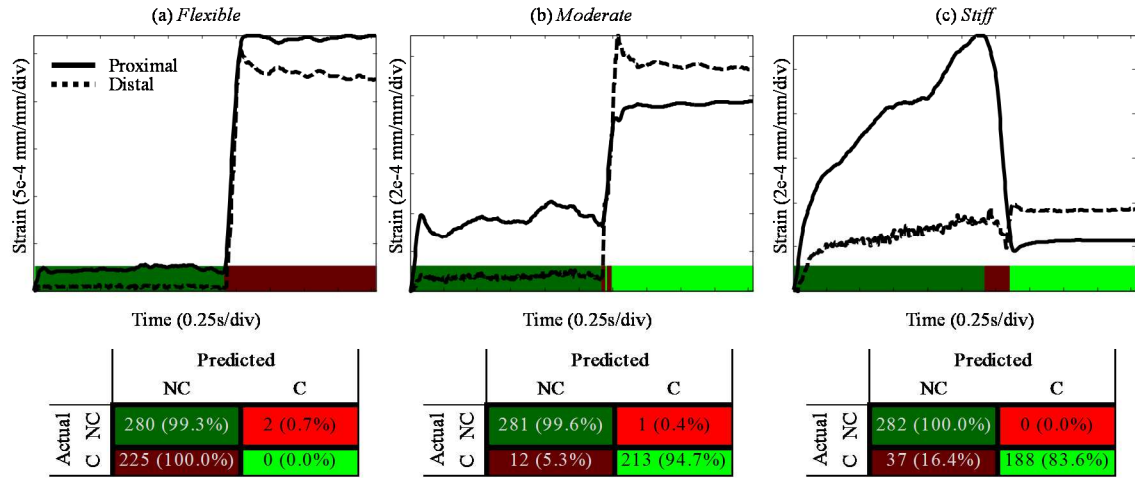


Figure 32. The effect of beam stiffness on strain differencing classification performance during underwater contact. Representative time series data are shown at 0.5 rot/s are shown for beams underwater to illustrate the effects of significant fluidic loading on flexible (a), moderate (b), and stiff (c) beams.

Using beams of *moderate* stiffness resulted in the best performance of the classifiers in air and underwater, and use of the *flexible* beams resulted in very poor classification performance. The use of *stiff* beams resulted in good classification performance that was slightly less than the performance achieved with beams of *moderate* stiffness.

3.3.4.5 Sensor location effects

The use of distal tip sensory data generally resulted in better performance than proximal sensors regardless of the technique used to discriminate contact (Figure 33). In air, the use of distal sensor data resulted in better classification performance for beams and fins. Underwater, the use of distal sensor data resulted in substantially better classification

performance than proximal sensors (c.f. Table 4). These differences were even greater at high speeds (>0.1 rot/s for fins, >0.4 for beams).

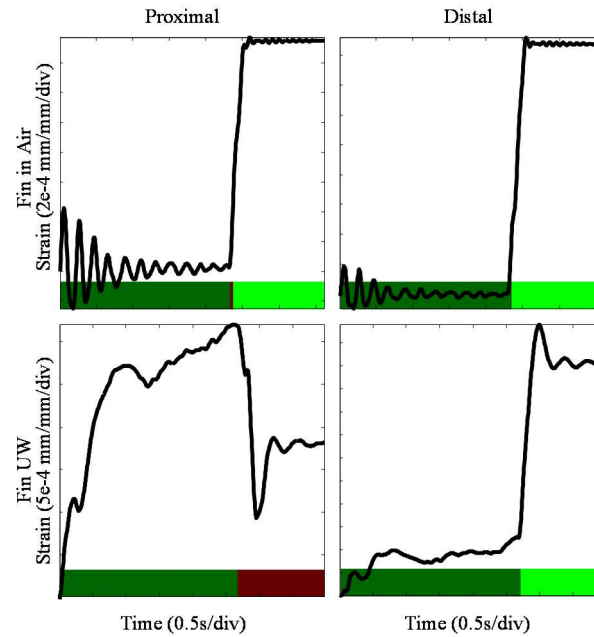


Figure 33. The effect of sensor placement (proximal/distal) on performance of the strain threshold classifier for fins in air and fins underwater.

When classifying contact underwater with fins, the use of medial sensor data resulted in better performance than the use of sensory data from the leading edges. There was little difference in performance between classification executed using data from the upper leading edge versus classification executed using data from the lower leading edge.

Table 4. Error in classification of the instant of contact for beams and fins of moderate stiffness.

(i) Beam in Air

Sensor Location	Proximal		Distal		Both
Technique	(A)	(B)	(A)	(B)	(C)
0.1 rot/s	-1	-1	-1	-98	1361
0.2 rot/s	-2	-1	-1	-2	679
0.3 rot/s	-2	-4	-1	-2	-19
0.5 rot/s	-2	-1	-1	-1	200
1.0 rot/s	-4	-1	-1	-2	102
1.5 rot/s	-3	-3	-1	-1	71

(ii) Beam Underwater

Sensor Location	Proximal		Distal		Both
Technique	(A)	(B)	(A)	(B)	(C)
0.1 rot/s	-7	-1	-1	-1	1271
0.2 rot/s	-4	-1	-1	-1	-3
0.3 rot/s	-5	465	-1	-1	-1
0.5 rot/s	8	282	-1	-1	-15
1.0 rot/s	X	159	2	155	4
1.5 rot/s	X	134	-1	-1	-5

(iii) Fin in Air

Sensor Location	Proximal		Distal		Both
Technique	(A)	(B)	(A)	(B)	(C)
0.1 rot/s	-12	1385	-8	1384	1361
0.2 rot/s	-11	694	-5	656	670
0.3 rot/s	-11	462	-3	-18	440

(iv) Fin Underwater

Sensor Location	Proximal		Distal		Both
Technique	(A)	(B)	(A)	(B)	(C)
0.1 rot/s	-57	1445	-5	-1	-3
0.2 rot/s	-34	766	-1	-1	-9
0.3 rot/s	X	539	-1	1433	-13

* Values represent the error (number of samples) for each technique (A,B,C; Table 2), where negative numbers correspond to a prediction of contact after the actual contact has occurred and positive numbers correspond to a prediction of contact before the instant of contact. "X" corresponds to cases where contact was not classified.

3.3.4.6 Instant of contact

For beams in air, both the strain threshold (Figure 27a) and strain rate threshold (Figure 27b) techniques accurately predicted the instant of contact (Table 4(i)). Using these techniques, contact was always predicted slightly after the true instant of contact, with errors of 1-100 samples (0.025-0.25 s). There were negligible differences between the performance when proximal versus distal sensory data were used.

For beams underwater (Table 4(ii)), there were large differences in classification performance of the instant of contact when proximal versus distal sensors were used. As speed increased, the performance of the strain thresholding and strain rate thresholding techniques degraded for proximal sensory data. However, the performance of the distal sensor was very good regardless of speed.

The instant of contact was generally poorly classified for fins in air for every technique but the strain threshold technique (Table 4(iii)). Large oscillations in strain caused many false positives (C|NC) for both the strain rate threshold and the strain difference threshold techniques, which meant that contact was often estimated prior to the true contact (e.g. $x < 0$).

For fins underwater, the best performing techniques for classifying the instant of contact were strain thresholding using distal sensors, or strain difference thresholding (which involved both sensors). Both techniques estimated contact after the true instant of contact ($x < 0$) due to the fluidic loading on beams, but were generally quite accurate across the speeds tested ($x = [-15, -1]$; (Table 4(iv))). Strain thresholding typically failed when proximal sensor data was used because the strain due to fluidic loading could exceed the strain due to contact loading. Strain rate thresholding performed poorly with proximal sensor data due to the large fluctuations in strain rate experienced as the fin was accelerated from rest into fluid, such that contact was estimated long before the true instant of contact ($x > 500$ samples).

3.3.5 Discussion and conclusion

Simple strain thresholding was very effective in limited conditions, where platform speed and stiffness were moderate. This technique was typically robust in air and in water, but

failed as soon as fluidic loading exceeded contact loading, which occurred at high speeds and high beam stiffnesses. This technique resulted in large errors in the estimated instant of contact when used for contact detection in water.

Strain rate thresholding yielded many misclassifications of C and NC at all speeds and in both environments. Since fluidic loading rates could easily exceed contact loading rates at any speed or stiffness, this technique may perform poorly underwater, despite being utilized often in air. Oscillations introduced by structural vibrations or fluidic effects could create false positives in complex robotic systems, such as compliant manipulators or soft robots.

Strain differencing between proximal and distal sensors was generally an effective way to detect contact in the underwater environment. This technique was not always effective at classifying contacts in air, but generally performed better than the other two methods at classifying underwater contact across broad conditions. It performed best when the fins and beams were moving, because at rest, proximal and distal strains were approximately equal. This technique does require an additional sensor compared to the other two techniques, but may allow for more robust detection of contact. Strain differencing performed poorly in some cases where beams were very flexible, so it may require careful design of beams to match contact conditions.

The stiffness of the beams significantly affected the classifier performance, and so the distribution of flexural rigidity should be co-designed based on platform speed and sensor placements to ensure robust detection of contact.

The choice of sensor location also impacted the performance of the classifiers; in order to classify complex contacts, careful design of the sensor distribution is necessary.

While using data from the distal tips of beams was effective for classifying tip contact, if contact occurs closer to the base of the beam the distal strain will not change significantly. As contact can occur at any point along the length of the beam, this suggests that it may be important to have distributed sensing along the beams' length. Future work will explore the use of distributed sensors to classify contact along the length of the beam.

Based on this initial evaluation, underwater contact classification can be made more robust by: (i) use of distal sensors when tip contacts occur, (ii) use of strain differencing to determine the duration of contact, (iii) and design of stiffness and speed based on contact conditions. Contact detection techniques will be used in future work to develop an active sensing paradigm for underwater touch with compliant manipulators.

Chapter 4. System identification methods for force prediction

4.1 Chapter summary

Models of flexible fins being driven for propulsion are not easily derived from first principles because the nonlinear fluid structure interaction between fin and fluid is still poorly understood [69]. When physical systems elude physics-based descriptions it is valuable to learn more about these systems through model development based on inputs and outputs of the system [98-100]. For instance, the relationship between propulsive forces and intrinsic sensory measures is not known, but studying input-output models between the two can be used to determine the sensory systems and model parameters required to build a good model to predict propulsive forces.

The objective of the work in this chapter is to develop the mathematical framework necessary for models used to map sensory data to propulsive forces. Some mathematics of linear and nonlinear system identification are developed in order to illustrate the progression from basic input-output models to more complex nonlinear models of propulsive forces. Several metrics for cost and performance are motivated and developed in detail.

4.2 Input-output models

System identification techniques allow for the development and refinement of mathematical models of physical systems through careful design and analysis of experiments. There are numerous representations of this process but a popular one is given by Ljung in his seminal text (redrawn in Figure 34; [99]), wherein prior knowledge of the system is used to select appropriate components of the process, including: experimental design, model type, and fit criterion. Planned experiments are executed,

data is gathered, and then a model for the system is calculated. The model is then validated on unseen data (i.e. data that was not used to develop the model). If the model meets the given criterion, it can be used. If the model does not meet the fit criterion, revisions can be made by designing new experiments, selecting a different model type, or modifying the fit criterion.

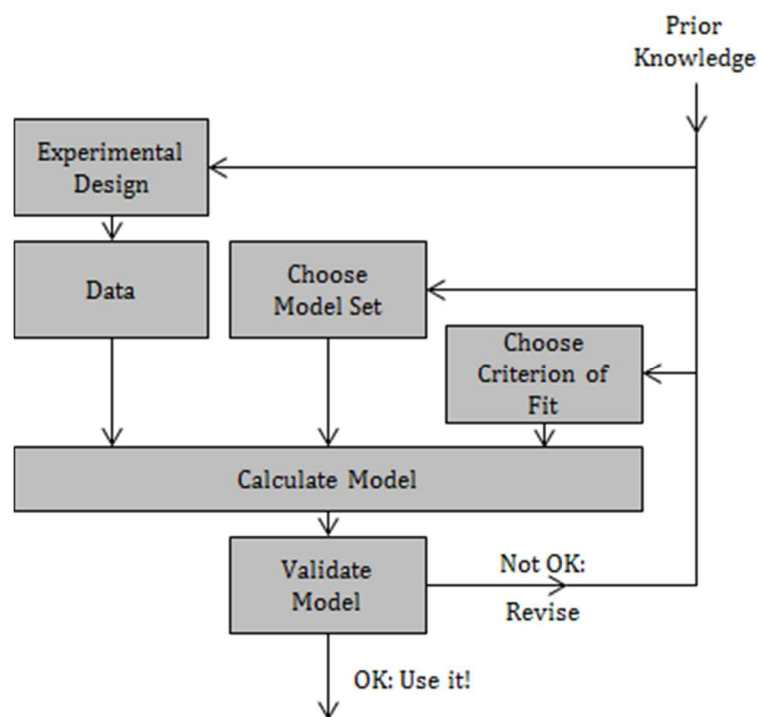


Figure 34. The system identification loop. Redrawn from [99].

In the first stages of identification, a common initial model choice is a linear parametric input-output model. Depending on the number and type of inputs and outputs, the summation structure of parametric models can vary slightly. At its most basic level, an input-output model is single-input-single-output (SISO), where the model acts entirely on a single signal input to produce the signal output. This framework can be scaled in

order to create models that are multiple-input-single-output (MISO), where the model acts on multiple input signals to produce an output signal; or even multiple-input-multiple-output (MIMO), where multiple signals are acted upon to produce multiple outputs. For example, many biological systems are MIMO systems, such that multiple sensory inputs can influence the outputs of multiple physical processes, and as such it can be very challenging to capture the complexity of the model for a biological system. Typically research efforts are done to isolate SISO pathways of the biological system where only a single sensory input is stimulated and a single motor or neuronal output is measured. These simpler models can be built upon and refined using techniques in system identification by utilizing prior knowledge from SISO models to inform the development of MISO, and eventually MIMO, models.

Model complexity should only be increased if aspects of the target output are not well captured by the current model. Quantitative metrics of success relate to both the cost of implementing the model as well as the model's performance. Common performance metrics typically include basic error statistics such as mean squared error (MSE) and sum of squared error (SSE). A higher order statistic that is common is the percent of variance accounted for ($\%VAF$) metric. Choice of error metrics depends on the design criteria of the model. Cost functionals can have further design choices associated with them, as specific parameters can be used to reward or penalize the functional based on performance and cost, respectively. Commonly used metrics include the Akaike information criterion (AIC) and many of its variants, as well as the minimum description length (MDL). Low performance, as measured by high error means or low variance

accounted for, as well as high implementation cost should call into question the choice of model as well as the model parameters chosen.

Parametric models can be tuned by adjusting the range of parameters, number of inputs, and type of the models. Typical range adjustments are made to the “memory” length of the system, which for a convolution model is simply the number of time delays of the input used in the convolution’s input matrix. For superlinear models, the number of basis series terms can be increased or decreased depending on model performance (though this can be a very expensive parameter to increase, see Section 4.4). Increasing the number of model inputs can be done computationally, or by physically adding sensors to the instrumentation. Computationally, this involves including additional sensors’ data in the input matrix, for example. Lastly, the type of underlying models can be changed by adding series terms to the representation, or adding linear and nonlinear block functions to the model structure. For instance, a linear convolution component can be chained to a static nonlinearity to model certain types of nonlinear systems.

4.3 MISO regression and estimation

One of the most basic input-output models is given by the *weighting sequence description*

$$y(k) = \sum_{i=0}^k Y_i \cdot u(k-i) \quad (1)$$

in which the parameters Y_i are used to map the input u to the output y at discrete time k [100]. This model assumes that the output is a weighted sum of prior input to the system.

Along this line of models is also the *linear difference equation*:

$$y(t) + a_1 y(t-1) + \dots + a_n y(t-n) = b_1 u(t-1) + \dots + b_n u(t-n) \quad (2)$$

When previous outputs are not known, this simplifies to the finite impulse response (FIR) model where:

$$y(t) = b_1 u(t-1) + \dots + b_m u(t-m) \quad (3)$$

and we define model parameters θ and inputs φ such that

$$\theta = [b_1 \quad b_2 \quad \dots \quad b_m]^T \in \mathbb{R}^m \quad (4)$$

$$\varphi(t) = [u(t-1) \quad u(t-2) \quad \dots \quad u(t-m)]^T \in \mathbb{R}^m \quad (5)$$

Thus the problem of estimation is simply obtaining an estimate such that $\hat{y}(t) = \varphi(t)^T \theta$.

The estimation problem can have different optimization objectives, but a common one is the minimization of mean squared error V :

$$V_N(\theta) = \frac{1}{N} \sum_{t=1}^N [y(t) - \varphi(t)^T \theta]^2 \quad (6)$$

which is expressed as the optimization objective

$$\hat{\theta} = \arg \min_{\theta} V_N(\theta) \quad (7)$$

and is solved by the following:

$$\begin{aligned} \frac{dV_N}{d\theta} &= 0 \\ \frac{2}{N} \sum_{t=1}^N [y(t) - \varphi(t)^T \theta] [-\varphi(t)] &= 0 \\ \sum_{t=1}^N [y(t) \varphi(t)] &= \sum_{t=1}^N [\varphi(t)^T \varphi(t) \theta] \\ \hat{\theta}_N &= \left\{ \sum_{t=1}^N [\varphi(t)^T \varphi(t)] \right\}^{-1} \sum_{t=1}^N [y(t) \varphi(t)] \end{aligned} \quad (8)$$

where $\hat{\theta}_N$ are the model parameters that minimize the output mean squared error. This type of parameter estimation can be referred to as least squares estimation or linear regression when the parameterization is linear as above.

It can be convenient for computation to form the least squares estimation problem using matrices (see Appendix II of [99]), defining:

$$Y_N \triangleq \begin{bmatrix} y(1) \\ \vdots \\ y(N) \end{bmatrix} \quad (9)$$

where Y_N is an $N \times 1$ column vector and

$$\Phi_N \triangleq \begin{bmatrix} \varphi^T(1) \\ \vdots \\ \varphi^T(N) \end{bmatrix} \quad (10)$$

where Φ is an $N \times d$ matrix and rewriting the minimization objective:

$$V_N(\theta) = \frac{1}{N} \|Y_N - \Phi_N \theta\|^2 \quad (11)$$

and the resulting optimal estimate becomes:

$$\hat{\theta}_N = (\Phi_N^T \Phi_N)^{-1} \Phi_N^T Y_N \quad (12)$$

This matrix formulation relies on the Moore-Penrose pseudoinverse to compute the optimal parameter estimates, which can be convenient when time series data from multiple sensors are augmented to form the input matrix (Φ_N).

For robotic systems, it can be especially important to use input data to estimate multiple outputs (e.g. distributed sensors to estimate multiple orthogonal components of the propulsive force). In this case, the variable $y(t)$ becomes a higher-dimensional column

vector and the parameters are a matrix with the i -th column containing the coefficients associated with the i -th component of y .

$$y(t) = \Theta^T \varphi(t) \quad (13)$$

$$V_N(\Theta) = \frac{1}{N} \sum_{t=1}^N |y(t) - \Theta^T \varphi(t)|^2 \quad (14)$$

yielding the parameter estimate

$$\hat{\Theta}_N = \left[\sum_{t=1}^N \varphi(t)^T \varphi(t) \right]^{-1} \sum_{t=1}^N [y(t) \varphi(t)] \quad (15)$$

The LU decomposition technique is a common way to compute the inverse of a matrix by decomposing the target matrix into a L(ower triangular) and an U(pper triangular) component such that (as in [101]):

$$L \cdot U = \Phi_N^T \Phi_N \quad (16)$$

and the linear set can be represented by

$$\Phi_N \cdot \Theta = L \cdot U \cdot \Theta = L \cdot (U \cdot \Theta) = y \quad (17)$$

and the following two equations can be solved to identify the parameters Θ :

$$L \cdot z = y \quad (18)$$

$$U \cdot \Theta = z \quad (19)$$

4.4 Nonlinear estimation: Volterra series

Linear estimation techniques may fail to capture the complexities of the dynamics between sensory signals and propulsive forces on flexible fins, so nonlinear modeling may be necessary. It is known that the mechanisms of force production in flexible fins are quite complex, involving the shedding of leading edge vortices and the directing of

turbulent jets into the fin's wake. Even for rigid bodies moving through flow, the drag based propulsive force (F_D) is approximated nonlinearly in the velocity term (V), such that (as in [102]):

$$F_D = C_D \frac{1}{2} \rho_w V^2 A_p \quad (20)$$

where C_D is the coefficient of drag based on the flow Reynolds number, ρ_w is the density of the fluid, A_p is the projected area of the cross section of the rigid body moving in flow. The addition of flexibility and multiple interacting panels is highly likely to also have a nonlinear relationship between the kinematics of the fins and the forces produced. Therefore, fin-intrinsic sensory measurements (such as bending of the fin rays or pressure along the fin surface) may not linearly relate to the propulsive forces. Nonlinear techniques are employed by this research to further understand the relationships between intrinsic sensors and the propulsive force.

Nonlinear estimates are more complex to obtain because the model representation changes form and it can be harder to guarantee optimality of the parameter estimates. Some representations and relevant techniques are summarized below. The general problem is to obtain a set of parameter estimates $\hat{\theta}_N$ that minimize an objective function $V_N(\theta)$ based on input ($\varphi(t)$) and output data ($y(t)$):

$$y(t) = g(\varphi(t), \theta) \quad (21)$$

$$V_N(\theta) = \frac{1}{N} \sum_{t=1}^N \alpha_t [y(t) - g(\varphi(t), \theta)]^2 \quad (22)$$

$$\hat{\theta} = \arg \min_{\theta} V_N(\theta) \quad (23)$$

The general form of a nonlinear estimator is useful for description, but for implementation, a proper functional of the input data and parameters must be chosen to represent the system output. A common way to describe a polynomial nonlinear system with memory is through use of the Volterra series expansion. The output $y(n)$ depends on coefficients of zeroth-order, linear, and higher order input terms, and is typically represented by (from [103]):

$$\begin{aligned}
 y(t) = & h_0 + \sum_{k_1=0}^{\infty} h_1(k_1) x(t-k_1) \\
 & + \sum_{k_1=0}^{\infty} \sum_{k_2=0}^{\infty} h_2(k_1, k_2) x(t-k_1) x(t-k_2) \\
 & + \sum_{k_1=0}^{\infty} \cdots \sum_{k_p=0}^{\infty} h_p(k_1, \dots, k_p) x(t-k_1) \cdots x(t-k_p) + \cdots
 \end{aligned} \tag{24}$$

where h_0 is a constant term and h_j is the j -th order Volterra coefficient.

In the nonlinear systems framework, the order of the representation can be changed to suit different modeling needs. Thus, from (24), the zeroth order Volterra model is given by

$$y(t) = h_0 \tag{25}$$

The first order Volterra model is given by

$$y(t) = h_0 + \sum_{k_1=0}^{\infty} h_1(k_1) x(t-k_1) \tag{26}$$

And the second order Volterra model is given by

$$\begin{aligned}
 y(t) = & h_0 + \sum_{k_1=0}^{\infty} h_1(k_1) x(t-k_1) \\
 & + \sum_{k_1=0}^{\infty} \sum_{k_2=0}^{\infty} h_2(k_1, k_2) x(t-k_1) x(t-k_2)
 \end{aligned} \tag{27}$$

and further until higher order terms are introduced. For implementation with real time-series data, the Volterra series is represented with M samples of “memory”:

$$y(t) = h_0 + \sum_{k_1=0}^{M-1} h_1(k_1)x(t-k_1) + \sum_{k_1=0}^{M-1} \sum_{k_2=0}^{M-1} h_2(k_1, k_2)x(t-k_1)x(t-k_2) \quad (28)$$

This flexibility of model order and memory length makes it possible to represent the global behavior of many types of nonlinear systems using a Volterra model.

Volterra models are not orthogonal, which can introduce difficulty in identifying unique coefficients for the series. Fortunately, multiple methods for obtaining the Volterra *kernels* (i.e. coefficients of the series) exist and are summarized in the literature [104-106]. By use of these orthogonalization schemes and traditional least-squares estimation approaches, approximations of the true kernel can be obtained for nonlinear input-output data.

The Laguerre expansion technique (LET) orthogonalizes the kernel while preserving the intuitive structure of Volterra models. The LET uses the orthonormal basis of Laguerre functions to expand the system kernels, and then estimates the basis coefficients through regression.

$$\begin{aligned} h_1(k_1) &= \sum_{j=0}^L c_1(j)b_j(k_1) \\ h_2(k_1, k_2) &= \sum_{j_1=0}^L \sum_{j_2=0}^L c_2(j_1, j_2)b_{j_1}(k_1)b_{j_2}(k_2) \\ &\dots \end{aligned} \quad (29)$$

where $\{b_j(k)\}$ are the Laguerre basis functions, the c values are coefficients to be determined through regression, and L is the number of basis functions used to

approximate the kernel. This modification to the kernel results in the following representation of the Volterra series from (28):

$$\begin{aligned}
y(t) &= h_0 + \sum_{k_1=0}^{M-1} \sum_{j=0}^L c_1(j) b_j(k_1) x(t-k_1) \\
&\quad + \sum_{k_2=0}^{M-1} \sum_{k_1=0}^{M-1} \sum_{j_2=0}^L \sum_{j_1=0}^L c_2(j_1, j_2) b_{j_1}(k_1) b_{j_2}(k_2) x(t-k_1) x(t-k_2) \\
v_j(t, k) &= \sum_{k=0}^{M-1} b_j(k) x(t-k) \\
\Rightarrow \\
y(t) &= h_0 + \sum_{j=0}^L c_1(j) v_j(t, k_1) + \sum_{j_2=0}^L \sum_{j_1=0}^L c_2(j_1, j_2) v_{j_1}(t, k_1) v_{j_2}(t, k_2)
\end{aligned} \tag{30}$$

4.5 Dimensionality reduction of the input matrix by SVD

As model complexity increases due to nonlinearity, high numbers of sensors, and large windows of sensory data, the input block-structured matrix can become too large and ill-conditioned to invert easily.

Singular value decomposition (*SVD*) is a common technique for computing the basis vectors of a matrix and reducing its dimensionality to the projection of only the largest singular values. The technique is applied as follows. The block structured data matrix X is factored into the product of three structured matrices:

$$X = USV^T \tag{31}$$

where $U^T U = I$, $V^T V = I$, and $S = \text{diag}(\sigma_1, \dots, \sigma_N)$, where $\sigma_1 \geq \sigma_2 \geq \dots \geq \sigma_N \geq 0$. The reduction of the dimensionality of the input matrix X can be achieved by setting $\sigma_i = 0$ for a range of i 's where i is set as a cutoff.

4.6 Application of MISO model to force prediction

The MISO model was used to map multiple inputs of sensory data to a single output of force data (Figure 35). Inputs to the MISO model were varied to determine best practices for model implementation. The kernel type was varied to study the differences in performance between linear and nonlinear models. A first order Volterra series was used for linear models, as in (26). Nonlinear models could either be a combination of first and second order Volterra series (28), or only the second-order terms of the series. The *memory* of the system was also varied as an input to the MISO model. Memory consisted of the M-samples of the data that were used to form the input data set. Memory could either consist of a window of data of fixed time length, or of multiple samples at different times. Best practices for memory length were determined. The lag relationships between sensory data and forces were also explored with this framework.

Experimental conditions were varied in both the training and the testing data in order to characterize the model performance and to determine best modeling practices for different swimming conditions. Experimental data were selected from the data library based on the gait, stiffness, stroke phase, and flapping frequency desired for both training and testing the MISO models. Additionally, the component of force (i.e. thrust, lateral, magnitude) was selected as the output of the MISO model for comparison. In this way, a model could be trained on data from one set of conditions and tested on data from either the same set of conditions, or a different set entirely. In all cases it was desirable not to train and test MISO models on data from the same trials.

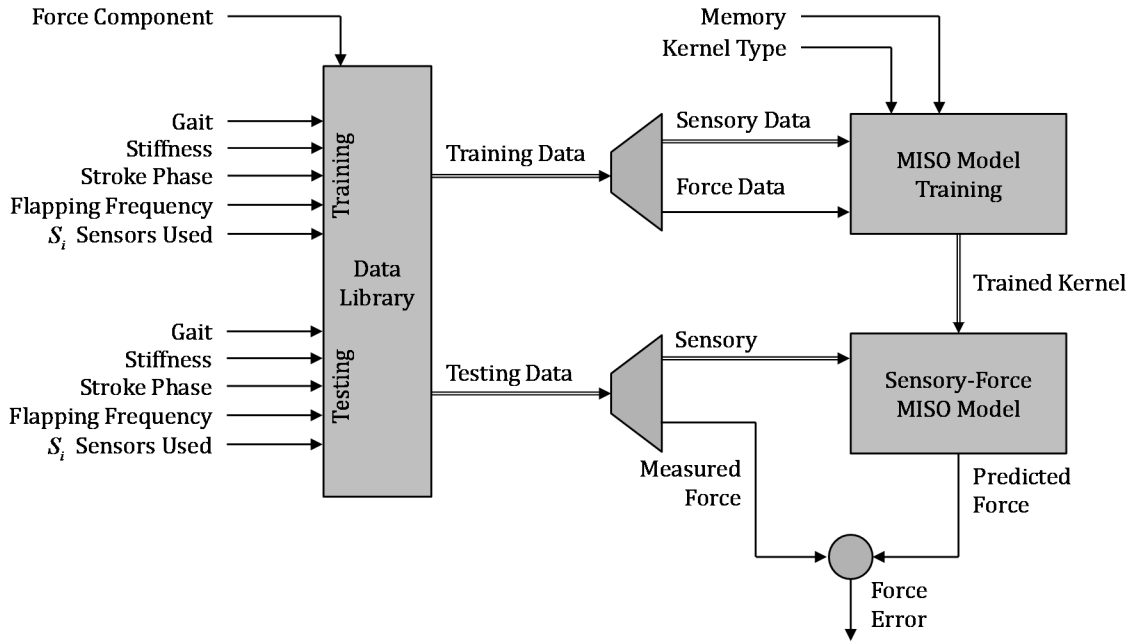


Figure 35. The process of developing a multi-input-single-output (MISO) Sensory-Force prediction model. The user assembles training and testing data from the Data Library by selecting experimental parameters of interest. The force component to be predicted is also selected (e.g. thrust force). Properties of the MISO model are chosen based on the desired complexity of the underlying model. A Trained Kernel is computed from the Training Data, and this kernel is used to predict forces from the Testing Data. Predicted forces are compared to measured forces to determine the error of the model.

4.7 Metrics of estimation performance

It is necessary to quantify and compare the performance of propulsive force models, so specific metrics of mean squared error (*MSE*), variance accounted for (*VAF*), Akaike information criterion (*AIC*), and model description length (*MDL*) are developed in detail below.

4.7.1 Sum of squared error (*SSE*) and mean squared error (*MSE*)

Mean squared error (*MSE*) is a metric that can be used to compare the performance of prediction models based on their error statistics. It is expressed as follows:

$$\begin{aligned}
MSE(y_k, \hat{y}_k) &= E[(y_k - \hat{y}_k)^2] \\
&= \frac{1}{N} \sum_{k=1}^N (y_k - \hat{y}_k)^2
\end{aligned} \tag{32}$$

where y_k is the data being estimated, \hat{y}_k is the estimate of the data, N is the number of data points in the series, and E is the expectation operator as expanded in (32).

If a direct comparison is possible between datasets of similar size, sum of squared error (SSE) is another useful metric to compare estimation models:

$$SSE(y_k, \hat{y}_k) = \sum_{k=1}^N (y_k - \hat{y}_k)^2 \tag{33}$$

Thus, MSE is simply a scaled version of SSE based on the number of data points in the series. It follows from the definition of SSE in (33) that it is unreasonable to compare the SSE of datasets of unequal size, as the sum of error for most models will accumulate over time.

Squaring the error has several implications, to name a few: 1) the operator is only concerned with the magnitude of the error, 2) errors less than magnitude 1 are deemphasized, and errors larger than 1 are amplified, 3) the operator is oblivious to the sign of the error. While this assumption is unlikely for most model estimation schemes in this thesis, the use of mean squared error as model metric is well suited to cases of least squares estimation, because this estimation algorithm is designed with the squared error as a cost function for optimization. Thus, in cases where the data to be estimated is well modeled by a linear system with Gaussian noise statistics, a zero MSE corresponds to a model that is optimal in squared error as a cost function.

4.7.2 Variance accounted for (VAF)

One measure for the goodness of a model fit that is commonly used is variance-accounted-for (*VAF*), which is a function of both the variance of the data and the variance of the model. It is given by:

$$VAF = \left(1 - \frac{\text{var}(y_k - \hat{y}_k)}{\text{var}(y_k)}\right) \cdot 100\% \quad (34)$$

where y_k is the data, \hat{y}_k is the estimate, and var is short for the variance function of the time series data. The fractional expression in (34) represents the variance of the estimation error over the variance of the source data. When the variance of the estimation error is very small relative to the variance of the data, or identically zero, the *VAF* is very high or close to 100%. However, when the variance of the estimation error is nearly as large or equal to the variance of the data, the *VAF* is very low or identically 0%.

Expanding the expression in (34) is useful to illustrate the utility of *VAF* as a metric:

$$\begin{aligned} \text{Let } \text{var}(y_k - \hat{y}_k) &\equiv \text{var}(e_k) \\ \frac{\text{var}(y_k - \hat{y}_k)}{\text{var}(y_k)} &= \frac{\text{var}(e_k)}{\text{var}(y_k)} = \frac{E[(e_k - \bar{e}_k)^2]}{E[(y_k - \bar{y}_k)^2]} \\ &= \frac{E[e_k^T e_k] - E[e_k]^2}{E[y_k^T y_k] - E[y_k]^2} = \dots = \frac{E[y_k^T y_k] + E[\hat{y}_k^T \hat{y}_k] - 2E[y_k^T \hat{y}_k]}{E[y_k^T y_k] - E[y_k]^2} \\ &= \frac{E[y_k^T y_k]}{E[y_k^T y_k] - E[y_k]^2} + \frac{E[\hat{y}_k^T \hat{y}_k]}{E[y_k^T y_k] - E[y_k]^2} - \frac{2E[y_k^T \hat{y}_k]}{E[y_k^T y_k] - E[y_k]^2} \\ &\equiv \alpha + \beta + \chi \end{aligned} \quad (35)$$

The denominator of all three expressions, $E[y_k^T y_k] - E[y_k]^2$, is the variance of the data, which is an expression of the distance from the mean squared data points from the

squared mean. The first expression, α , is the ratio of the mean squared values of the data to the variance of the data. This expression will always be greater than or equal to one, unless the data is zero mean (unbiased), then it is identical to one. The second expression, β , is the ratio of the mean squared values of the estimate to the variance of the data. If the data mean is zero, it simplifies to the ratio of mean squared values for both data sets. The last expression, χ , is the ratio of the expected value of the product of the data and the estimate to the variance of the data. Again, if the mean of the data is zero, then the last expression simplifies further. To summarize, if $E[y_k] = 0$, (35) will simplify:

$$\frac{\text{var}(y_k - \hat{y}_k)}{\text{var}(y_k)} = 1 + \frac{E[\hat{y}_k^T \hat{y}_k]}{E[y_k^T y_k]} - \frac{2E[y_k^T \hat{y}_k]}{E[y_k^T y_k]} \quad (36)$$

And we can see in the zero-mean data case, given by (36), there are several ways that this expression can reduce to zero, making the VAF will equal 100%. This will occur specifically when

$$E[y_k^T y_k] + E[\hat{y}_k^T \hat{y}_k] = 2E[y_k^T \hat{y}_k] \quad (37)$$

From this expression in (37), specific to the zero-mean data case, that the sum of expectations of squared data and squared estimates should equal twice the expectation of the product of the data and its estimate. When this occurs, the variance accounted for will be maximized.

In some cases where the modeling scheme is particularly ill-suited to the estimation task, the estimation scheme can introduce more variance into the estimation error than the original, and the fractional expression in (34) is greater than unity. In these cases, the *VAF* is a negative percentage and should alert the user that another metric (such

as mean squared error or sum of squared error) may be necessary to describe the goodness of fit.

4.7.3 Akaike information criterion (AIC)

The Akaike information criterion (AIC) is a relative metric to compare representations of data in terms of their amount of information measured against the cost of representing the information. It has been used historically for statistical model selection, where one of the goals of a statistical model is to accurately represent a process with a minimal number of terms (e.g. *degrees of freedom*) of the model. While many measures of success of a model are measured on an absolute scale, AIC was designed to be a relative metric between sets of models, the value it computes has no absolute meaning outside of the context of the source data that the models are based upon.

The canonical AIC was first written as

$$AIC(\hat{\theta}) = -2 \log(ML_{\hat{\theta}}) + 2k \quad (38)$$

where $\hat{\theta}$ is a parameterized model of a time series process, $ML_{\hat{\theta}}$ is the maximum likelihood (or in some cases, an estimate of the maximum likelihood value), k is the number of independently adjusted parameters to obtain $\hat{\theta}$ [107].

Since AIC is a relative metric, it can also be customized to a designer's goals of optimality; for instance, if there are discontinuities in the cost function for parameters it may be reasonable to have a piecewise AIC that is used to compare the same datasets. This flexibility makes it an excellent relative metric for local optimization of models. In Akaike's words, "when the maximum likelihood is identical for two models the [AIC] is the one defined with the smaller number of parameters." [107]

For models of time-series data, such as regression models, the canonical AIC can be modified to account for the required parameters. For a robot, which can be instrumented with multiple types and numbers of sensors, part of the k independently-varying parameters could be number of sensors. In addition, the number of sensor samples used to construct an estimate (i.e. model *memory*) is another component of k . Akaike's work anticipated and suggested this type of modification as a way to adapt the metric to specific model identification applications.

AIC can be modified for applications in regression and least squares estimation, such that low model error is rewarded and high numbers of parameters is penalized. These modifications are summarized in work by Hu [108]:

$$AIC_{LSE} = n \log \left(\frac{RSS}{n} \right) + 2k \quad (39)$$

where RSS is the error residual between the model fit and the measured data, n is the number of data points for regression, and k is the number of model parameters. A major limiting assumption of this case is that the errors are independent and independently distributed (*i.i.d.*) on normal distributions.

4.7.4 Minimum description length (MDL)

One type of cost function that was used to determine the appropriate number of model parameters was the minimum description length (MDL)

$$MDL(M) = \left(1 + \frac{M \log(N)}{N} \right) \sum_{t=1}^N (y(t) - \hat{y}(t, M))^2 \quad (40)$$

where M is the number of model parameters, N is the length of the data in samples, $\hat{y}(t, M)$ is the estimate of the output when only the M model parameters is used, and

$y(t)$ is the true value of the output. The series summation is equivalent to the sum of squared error (introduced earlier in 4.7.1; *SSE*), and therefore the *MDL* increases as either *SSE* increases or as the number of model parameters M increases. Thus, a low *MDL* is desirable such that a low number of parameters are used to achieve a low error.

Chapter 5. Estimation of propulsive forces from intrinsic sensory data

5.1 Chapter summary

The objective of the work presented in this chapter is to understand the estimation and prediction of propulsive forces from distributed, heterogeneous sensors in the robotic pectoral fin as the fin executes multiple swimming gaits.

Chapter 5 is comprised of two published reprints: (1) a journal paper published in *Bioinspiration & Biomimetics*, Volume 10, Number 3, June 2015 and (2) a conference paper published in the *IEEE International Conference on Robotics and Automation (ICRA) 2016*. Both studies were conducted to understand the use of distributed, heterogeneous sensors in a robotic fin for prediction of propulsion forces.

The first study found that linear MISO models of fin-intrinsic sensory data could be used to predict propulsive force magnitudes at multiple speeds and when fin stiffness was changed. Propulsive force magnitudes could be predicted with approximately 100ms of sensory data. MISO model performance was gait- and stroke-dependent in that performance varied significantly between steady swimming, maneuver, and ventral steady swimming gaits and performance varied significantly between the gait's outstroke and instroke phases. Models formed with bending sensor data typically outperformed models formed with pressure sensor data, and the optimal subsets of sensors for prediction always included at least one bending sensor. Despite high model performance on individual gaits and stroke phases, a single model could not predict the forces of multiple gaits and stroke phases.

The second study built upon the first by analyzing the structure and performance of nonlinear MISO models to predict propulsive force components (thrust and lateral) as

well as to validate important results of the linear study. Nonlinear Volterra-series MISO models could be used to predict propulsive forces very well across changes to gait, stroke phase, and fin parameters. Nonlinear models tended to have both a lower implementation cost and higher performance than linear models in the same fin conditions. This study validated that, for both linear and nonlinear models, models formed from bending data outperformed those formed from pressure data. This study compared performance differences between cases where thrust and lateral components of the force were predicted. Thrust forces were generally best predicted using a nonlinear model of the fin bending data, whereas lateral forces were best predicted using a linear model of fin pressure data.

5.2 Paper 3: Predicting propulsive forces using distributed sensors in a compliant, high DOF, robotic fin

5.2.1 Abstract

Engineered robotic fins have adapted principles of propulsion from bony-finned fish, using distributed compliance and complex kinematics to produce and control the fin's propulsive force through time. While methods of force production are well understood, few models exist to predict the propulsive forces of a compliant, high DOF, robotic fin as it moves through fluid. Inspired by evidence that the bluegill sunfish (*Lepomis Macrochirus*) has bending sensation in its pectoral fins, the objective of this study is to understand how sensors distributed within a compliant robotic fin can be used to estimate and predict the fin's propulsive force. A biorobotic model of a bluegill sunfish pectoral fin was instrumented with pressure and bending sensors at multiple locations. Experiments with the robotic fin were executed that varied the swimming gait, flapping frequency, stroke phase, and fin stiffness to understand the forces and sensory measures that occur during swimming. A convolution-based, multi-input-single-output (MISO) model was selected to model and study the relationships between sensory data and propulsive force. Subsets of sensory data were studied to determine which sensor modalities and sensor placement locations resulted in the best force predictions. The propulsive forces of the fin were accurately predicted using the linear MISO model on intrinsic sensory data. Bending sensation was more effective than pressure sensation for predicting propulsive forces, and the importance of bending sensation was consistent with several results in biology and engineering studies. It was important to have a spatial distribution of sensors and multiple sensory modalities in order to predict forces across

large changes to dynamics. The relationship between propulsive forces and intrinsic sensory measures is complex, and good models should allow for temporal lags between forces and sensory data, changes to the model within a fin stroke, and changes to the model through gait transitions.

Inspired by the swimming capabilities of fish, robotic fins have evolved from rigid flapping foils to compliant, multiple degree of freedom (DOF) fins with advanced propulsive capabilities. Studies over decades have investigated the roles of compliance and kinematics in producing propulsive force in fins. Many studies have used flexible foils as simplified, physical models to study the effects of kinematics and mechanical properties on fin propulsive forces [54]. Flapping foil experimental studies have investigated the effects of stiffness [38], flapping frequency [42; 44], heaving amplitude, propulsor shape [20], drag coefficients [30], and ground effect [39] on hydrodynamics and propulsive force outputs. A recent study demonstrates that flexible foils may serve as sufficient models of force production for caudal fin swimming as seen in two types of bony finned fish [44]. Further studies of fish have shown that complex kinematics and bending play a significant role in producing useful propulsive forces [26; 27], so biologically-inspired robotic fins have become more complex to achieve the performance of biological systems. Biologically-inspired robotic fins have been engineered to match the kinematics, mechanical properties, and hydrodynamics of their biological counterparts and can achieve advanced capabilities [24; 40]. A compliant robotic pectoral fin with multiple degrees of freedom, derived from knowledge of the bluegill sunfish (*Lepomis macrochirus*), can create thrust through an entire fin beat [25; 37; 51], even as the fin is driven into flow. The same fin can be used to create the time-varying thrust and

lift forces of a steady forward swimming gait [25; 37], the strong lateral and drag forces of a yaw turn maneuver [14], and the forces that balance a fish body during hovering [22]. Study of the ghost knifefish's (*Apteronotus albifrons*) propulsive strategies has enabled researchers to design a robot with an undulatory propulsor that uses counter-propagating waves to hover in place or jet upward rapidly [5]. In general, these studies validate that complex 3d kinematics and bending enable the creation of diverse and useful propulsive forces.

However, as robotic fins become more complex, the dynamics of force production are difficult to model and closed-loop control of force is challenging. Most biologically-inspired robotic fins execute kinematics in open-loop, and closed-loop control of individual kinematics has not been addressed, because modeling of an underactuated, multi-DOF, compliant, underwater robot is a major challenge. Few mathematical models exist that capture the nonlinear dynamics of the fluid structure interaction of a compliant fin in water, and those that model fin forces well are confined to single swimming gaits at fixed speeds [9; 35; 48], let alone the kinematics of each DOF. These numerical modeling methods have high computational and time costs, making them infeasible for real-time deployment on robotic platforms. Without a model of the propulsive forces, the available techniques for controlling the propulsive force are limited.

Prediction of the propulsive force is an essential challenge if we are to ultimately control the propulsive forces of compliant, high DOF, robotic fins; and sensors within the fins are likely to provide useful information for control of forces. To execute good prediction in the absence of force models, sensory measurements must capture the underlying force dynamics. Existing approaches to sensing and control of underwater

vehicles have focused on extrinsic sensing, such as inertial measurement units and magnetometers, which only measure the effects of propulsive force on the dynamics of the robot body. These methods are appropriate when the dynamics are well modeled, such that propulsive force is easily controlled and updated based on a desired body trajectory. However, when good models of propulsor dynamics do not exist (which is the case for compliant, multi-DOF fins), extrinsic measures cannot be used to determine how propulsive force is being created. With only extrinsic sensors of body forces, there are few direct ways to update local kinematics of a fin. Distributed sensors that are intrinsic to fins have the potential to capture distributed measures of the propulsive force that are created locally. Using local information about force production, the propulsive force can be controlled more precisely through updates to local kinematics. Thus, intrinsic sensors can be used to monitor force production, and to provide more direct sensory feedback for control of kinematics.

The approach of sensing in fins has direct connections to new discoveries in the biology and neuroanatomy of fishes. Recent work has shown that the fins of bony-finned fish may act as sensory systems, though the use of sensation during swimming is not well understood. Bluegill sunfish (*Lepomis macrochirus*, a model bony finned fish) pectoral fins are densely innervated with afferent nerve endings that respond to bending stimuli [15; 58]. Bending and force are directly related in flexible propulsors [33], and changes to the amount of stiffness of fins affect the force trajectory, magnitude, and direction [2; 12; 26; 51]. The sunfish uses its compliant pectoral fins to create complex propulsive forces during hovering [22], low speed maneuvers [14], and steady forward swimming [37]. The fish is able to vary the speed and flexural rigidity of its fins in order to change the

propulsive force [51]. Since changes to fin bending significantly affect the fin's propulsive force, it is likely that sensory measures of bending and other mechanical phenomena could be useful for predicting the propulsive force of the fin through time. Biologists have suggested that these afferent nerves may very likely be used to tune motor output of fins [37; 58], which could include the production of propulsive force.

If intrinsic sensing is used for prediction of fin propulsive forces, many practical considerations arise relating to the placement, modality, and number of sensors. In other words: 1) where should sensors be placed?, 2) what sensory modalities should be used?, 3) how many sensors are needed?, and 4) how do best modalities, locations, and numbers of sensors change as the fin dynamics change?. These questions must be addressed so that engineers know how to use intrinsic sensors to estimate outputs (such as propulsive force). While mechanisms of propulsion have been studied in detail, there have been few studies that investigate the use of sensing within fins. Several studies using IPMCs have suggested the use of embedded strain sensing within polymer fins to provide bending information for force control of fins [28; 50]. These sensors have been used to estimate the curvature of fins during flapping and heaving motions. Robotic models of a bluegill sunfish pectoral fin have been instrumented with bending and pressure sensors within the fin in preliminary work [22; 37; 52], and general trends have been identified that relate sensory measures to propulsive forces. However, these sensory measures have not been used to directly predict propulsive forces and it is not known what type of sensor (e.g. bending, pressure) is most useful for the task. Also, sensor placement optimization is a common problem in underwater sensing, but most techniques require system, sensor, and noise models [46]. Methods exist for experimentally selecting an optimal sensor

distribution to maximize observability of a state variable [7; 47; 55], though all require a numerical simulation and a sensor model for optimization. However, many compliant robots that interact with a complex environment do not have readily available state-space formulations or a priori equations of motion.

The objective of the work presented in this study is to understand how heterogeneous sensors, distributed within a compliant fin, can be used to estimate and predict the fin's propulsive force. This objective is based on the goal of using robotic fins to create and control propulsive forces, and the idea that intrinsic sensors could be valuable for controlling force. This study provides an assessment of the feasibility of propulsive force prediction from distributed sensors on a compliant robotic pectoral fin with complex kinematics and no a priori dynamical model. A robotic model of a bluegill sunfish pectoral fin [37] is instrumented with distributed pressure and bending sensors and programmed to execute multiple swimming gaits while sensory data and propulsive forces are measured. Force prediction is evaluated during gaits using complex 3D kinematics on a robotic fin with multiple underactuated degrees of freedom and the ability to change flexural rigidity and flapping frequency. Analyses are conducted to determine the best combinations of sensors, the best placement locations for sensors, and the best model parameters for the goal of predicting the propulsive force. A multi-input-single-output (MISO) convolution model is used to predict fin output forces because it allows for direct assessment of each sensor's contribution to a prediction, and subsets of sensory data can easily be substituted in this framework.

The remainder of this paper is structured as follows. Section 2 describes the methods, including the instrumented robotic fin (2.1.1), the experimental testing

environment (2.1.2) and the experiments executed with the fin (2.2). Section 2.3 describes the multi-input-single-output (MISO) convolution model and its use for mapping sensory data to propulsive forces. Sections 2.4-2.6 describe the use of the model for estimation and prediction, the performance metrics for the model, and the evaluation of prediction results to determine best sensor instrumentation practices. Section 3 presents the results, where the MISO model's performance is evaluated for force estimation and prediction as model parameters and robotic system parameters are varied (3.1). Lastly, measures of the model variance accounted for (VAF), model mean squared error (MSE), and an Akaike information criterion [1] are used to determine best sensors and model parameters under changing conditions on the fins (3.2-3.5).

5.2.2 *Methods*

5.2.2.1 *Experimental equipment*

The fins of the bluegill sunfish (*Lepomis macrochirus*; a bony-finned fish) have been studied over multiple years using robotic models of the caudal [18] and pectoral fins [5, 17, 32, 109] as they execute complex propulsive behaviors. A robotic pectoral fin, modified from [32], was instrumented with sensors and programmed to execute swimming gaits as sensory data and forces were measured in a quiescent water tank. The robotic platform and testing environment are described below.

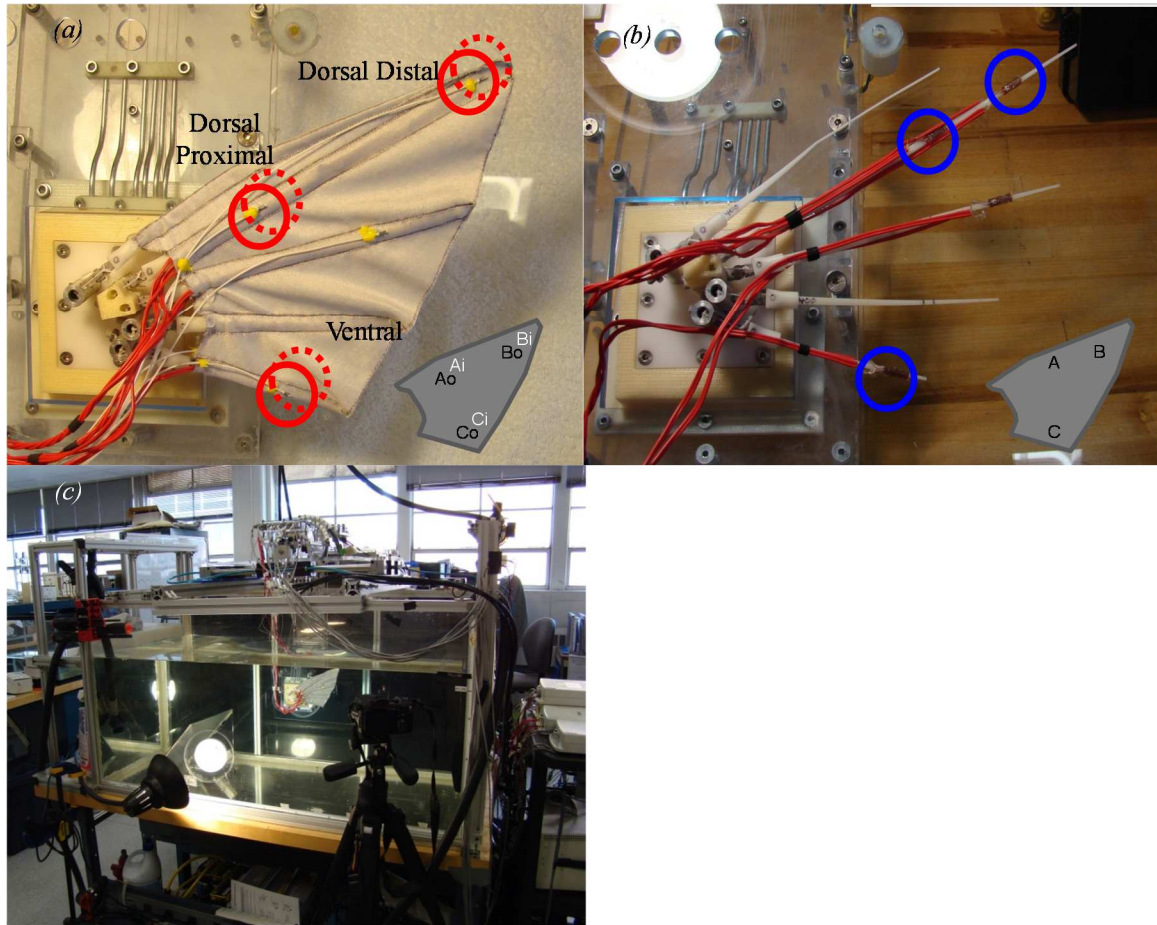


Figure 36. Sensory instrumentation and experiments with robotic pectoral fin. Catheter style pressure sensors (a) measured local pressures on both sides of fin webbing and half-bridge strain gages (b) measured local strains (bending). Propulsive forces were measured in the thrust and lateral directions while the fin executed complex kinematic trajectories in experiments (c).

A robotic fin was modeled on the pectoral fin of a bluegill sunfish and was designed to approximate the kinematics, mechanical properties, and hydrodynamics of the pectoral fin during steady swimming motions [37]. The robotic fin has five fin rays that are actuated in the sweep direction, and three of the fin rays can be actuated laterally, for a total of eight actuated degrees of freedom. The flexural rigidity of the robotic fin can be changed by replacing the fin rays between trials. The fin rays are sewn into

stretchable and compliant webbing (80% polyester, 20% elastane). More details of the robotic platform can be found in [37].

For descriptive purposes, three regions of the fin are referred to in this work. The dorsal region of the fin refers to the upper region of the fin formed by the first two fin rays and the webbing between them (Figure 1(d)). The medial region of the fin refers to the middle region of the fin formed by the second through fourth fin rays and the webbing between them. The ventral region of the fin refers to the bottom region of the fin formed by the fourth and fifth fin rays and the webbing between them. The fin's dorsal leading edge refers to the upper edge of the fin, and the ventral leading edge refers to the lower edge of the fin. For convenience, the long dorsal region is divided into dorsal proximal and dorsal distal regions.

The robotic fin was instrumented with distributed, heterogeneous sensors for use in propulsive force prediction. Eight pressure sensors (SPR-524, Millar Instruments, Houston, TX) and six bending sensors (KFG-5-120, Omega, Stamford, CT) were distributed over the robotic pectoral fin in dorsal and ventral regions. Pressure sensors were bonded to the fin webbing above the fin rays (Figure 1(d)), and bending sensors were affixed directly to the fin rays (Figure 36(e)). Sensors were placed along the dorsal leading edge at proximal and distal locations and the ventral leading edge (Figure 36(a,b) inset), as these areas corresponded to regions of strong vortex development [27], high density of sensory afferents [53; 56; 58], and which robotic and numerical studies have identified as important areas of force production during steady swimming [9; 35; 51]. Preliminary experiments using pressure sensors on the robotic fin showed dorsal sensors trending with thrust force and ventral sensors trending with lateral forces [22]. Pressure

sensors were bonded to the fin webbing at dorsal proximal, dorsal distal, medial, and ventral locations (OmniBond, Glu-Stix, Oldsmar, FL). Pre-wired strain gages were bonded to printed plastic fin rays (Accura 25, Quickparts, Atlanta, GA) in half bridge configurations using instant adhesive (Loctite 401, McMaster-Carr, 74765A63) at dorsal proximal, dorsal distal, and ventral locations. Strain gages were coated in silicone adhesive (McMaster-Carr, 73325A21) for flexible waterproofing.

Motor control and sensor measurement were conducted using a dedicated real time controller (PXI8106, National Instruments, Austin, TX) and acquisition cards (NI6229) with custom software in LabVIEW. Strain signals were amplified, measured, and conditioned on a slave chassis (NI9227 module, NI9144 EtherCAT Chassis, National Instruments, Austin, TX) and transferred to the real time controller. Digital servomotors (HSR-5990TG, HITEC RCD USA, Poway, CA) were driven using open loop trajectories at a 50Hz update rate. Sensory data were collected at 100Hz.

Experiments with the biorobotic fin were executed in a static water tank (1.8x0.9x0.9m). Oscillations created by the fin wake reflected off of tank walls were damped using a mesh (Vinyl Coated Polyester Scrim, 85695K2, McMaster-Carr, Robbinsville, NJ) aft of the fin over the tank cross section, which showed a 20% average magnitude reduction of the low frequency noise in the force sensors.

The fin's propulsive forces were measured using S-beam load cells (Futek LSB200, Futek Advanced Sensor Technology, Inc., Irvine, CA) oriented in thrust and lateral directions. The biorobotic fin was affixed to a low-friction air bearing carriage (New Way S301301, New Way Air Bearings, Aston, PA) to enable force measurement.

5.2.2.2 Experiments

Experiments were conducted to understand the relationship between propulsive forces and sensory data as kinematics and mechanical properties of the fin were varied. Experiments were executed that varied the fin gait (Figure 37), flexural rigidity, stroke phase, and flapping frequency over values consistent with the bluegill sunfish pectoral fin during swimming. To ensure statistical significance of results, over 40 trials were executed for each combination of the 81 fin conditions (Table 5), resulting in over 3200 trials. A description of the experimental parameters is provided below.

Table 5. Experimental conditions tested using the biorobotic pectoral fin.

Fin Parameter	Experimental Conditions
Gait	{Steady Swimming (SS), Maneuver (M), Ventral Steady Swimming (VSS)}
Stroke Phase	{Outstroke (OUT), Instroke (IN), Full Stroke (FULL)}
Flapping Frequency (Hz)	{0.65, 1.00, 1.30}
Flexural Rigidity	{400x, 600x, 800x}

5.2.2.2.1 Gaits

The robotic fin was programmed to execute three swimming gaits, using kinematics based on the kinematics of sunfish steady swimming [32], a sunfish yaw turn maneuver [5], and a modified ventral steady swimming (Figure 37). *Ventral steady swimming* was developed specifically for this study to investigate the effect of introducing a region-specific component of steady swimming. During the ventral steady swimming gait, the

ventral region of the fin executed the same kinematics used in steady swimming. The dorsal region of the fin was not actuated during the stroke, and only moved passively due to fluidic events. Steady swimming, yaw turn maneuver, and ventral steady swimming gaits are abbreviated in later sections (SS,M,VSS).



Figure 37. Picture summary of all gaits and stroke phases executed by the biorobotic pectoral fin in experiments. Gaits of steady swimming (SS; a), ventral steady swimming (VSS; b), and maneuver (M; c) were divided into outstroke (OUT, abduction) and instroke (IN, adduction) phases. Subsequent pictures were captured at time intervals of $T/8$, where T was the sum of the outstroke and instroke execution times.

5.2.2.2.2 Stroke Phase

The fin beat for each gait was divided into outstroke (abduction) and instroke (adduction) in order to study forces during each part of the fin stroke. The mechanisms of force production are significantly different between the outstroke and the instroke (c.f. [70]) so it was expected that a different model would be needed for each stroke phase. In experiments, the fin executed the outstroke trajectory of the gait, paused for >5s to allow for transient effects (e.g. reflected waves observed in forces and sensory data) to dissipate, and then executed the instroke trajectory of the gait. Trials were executed that tested the full fin beat. Outstroke, instroke, and full strokes are abbreviated in later sections (OUT,IN,FULL).

5.2.2.2.3 Effective Flapping Frequency

The execution speed of the fin beat was varied in experiments. Gaits were tested at flapping frequencies of 0.65, 1.00, and 1.30 Hz in accordance with values used from previous studies of the robotic fin and fish [32]. Since gaits were split into outstroke and instroke kinematics with a time delay in between, effective flapping frequency f_e was computed as

$$f_e = \frac{1}{t_{out} + t_{in}} \quad (41)$$

where t_{out} and t_{in} are the time duration of the outstroke and instroke, respectively.

5.2.2.2.4 Stiffness

The stiffness of the fins was varied by changing the flexural rigidity of fin rays. Flexural rigidities were selected to achieve similar bending to biological pectoral fins,

correspondingly, flexural rigidities of 400, 600, and 800 times the flexural rigidity of the biological fin rays were tested [17].

5.2.2.3 MISO Convolution Model

A convolution-based multi-input-single-output (MISO) model was selected to map the relationship between sensory measures and fin forces, as in (42), because it provides a clear way to link features of force production identified in previous preliminary studies [23, 32]. The MISO model allows for time delays between sensory measures on the fin and propulsive forces (seen in [23]). It allows for evaluation of single sensors and groups of sensors in their prediction performance, and the MISO model clearly indicates the weights $w_{i,j}$ of individual sensors and their time lags. The model has the benefit of a simple linear mapping between time-shifted sensory data S_i and force data F_k , so that an operator can study the effects of choosing a subset of sensors (e.g. $S_{1:4}$), the effects of changing the memory of the system (e.g. $[a,b]=[-4,0]$ ms), and even the effects of using weights trained on one data set to predict the forces of another data set (e.g. $F_k^{(2)} = \sum_i \sum_j S_i^{(2)} w_{i,j}^{(1)}$). Other methods, such as artificial neural networks [110] and supervised machine learning approaches [111] were considered for this application, but the transparency of the model relationships between sensory data and force data was preferred for this application. Further, the lack of an *a priori* system model or sensor model, due to complexities in the fluid structure interaction, prevented the use of model-based estimation schemes [112].

The relationship between estimated force F and sensory data S in this framework is:

$$F_k(a, b) = \sum_{i=1}^N \sum_{j=a}^b S_i(k - j\Delta t) w_{i,j} \quad (42)$$

Where F_k is the 2D force magnitude at discrete time k , N is the number of sensors used in the model, j is the discrete time window $[a, b]$ prior to discrete time k . $S_i(k - j\Delta t)$ is the i -th sensor's value at a delay of $j\Delta t$, and $w_{i,j}$ is the weighting sequence description for sensor i [100]. Δt is the sampling time, which was fixed at 1/100 s, for the 100Hz sampling rate used in this study.

Based on previous studies, only the magnitude components of the forces and sensory data were used in the MISO convolution model (42). This choice was made based on several studies with the robotic fin that have examined force magnitudes as kinematics and mechanical properties were changed [5, 23, 32]. This choice also enabled the use of single output regression to compute the weights, which was simpler for a first analysis of the relationships between forces and sensory measures. Force magnitudes were computed element-wise from the thrust and lateral components, such that at discrete time k :

$$\|F\|_k = \sqrt{F_{thrust_k}^2 + F_{lateral_k}^2} \quad (43)$$

5.2.2.4 Force estimates and predictions

Data from multiple experimental conditions were joined to form an input-output set with dynamics from a rich set of fin inputs and outputs, and these data were used to develop a force prediction model. A typical input-output set on which the model was developed included data from fins using flapping frequencies of 0.65Hz, 1.00Hz and 1.30Hz at 400x, 600x, and 800x fin stiffness. The fin gait was fixed for each input-output set. There were at least three trials used for each experimental condition, and all trials were

randomly selected. Model parameters (N, a, b) were selected and the weighting sequence description w_{ij} was computed using the Moore-Penrose pseudoinverse [113], which minimized squared error between the estimate of force and the measured force. Model-based *estimates* of the output data, that had been used to determine the model, were made by convolving the measured inputs with the model. The performance of the model was assessed by *MSE* and *VAF* performance metrics on the model estimates. The model was then used to predict output data from data sets that had not been used to form the model. These are referred to as model *predictions*, and these were also evaluated using *MSE* and *VAF* metrics.

The performance of each model was assessed by predicting data from experiments that: a) had the same experimental conditions as the experiments from which the model was made (*prediction*), b) had a different gait than the experiments from which the model was made (*prediction across gait*), or c) had a different stroke phase than the experiments from which the model was made (*prediction across stroke*).

5.2.2.5 Model performance and optimization

Performance of the model was assessed using calculations of mean squared error (*MSE*) and percent of variance accounted for (*VAF*) between estimated/predicted forces (\hat{F}) and measured forces (F).

$$VAF(F, \hat{F}) = \left(1 - \frac{SSE(F, \hat{F})}{SST(F)} \right) \times 100 \quad (44)$$

$$MSE(F, \hat{F}) = \frac{SSE(F, \hat{F})}{N} \quad (45)$$

$$SSE(F, \hat{F}) = \sum_k (\hat{F}_k - \bar{F})^2 \quad (46)$$

$$SST(F) = \sum_k (F_k - \bar{F})^2 \quad (47)$$

In this framework, VAF was negative if the sum of squared error (SSE) was greater than the total sum of squares (SST). In this case, the prediction was considered *failed* for analysis purposes and MSE was used as a performance metric.

The parameters of the convolution model were optimized using an Akaike information criterion (AIC) for least squares estimation [108]. AIC is a metric that increases linearly as the number of parameters increases and logarithmically as the model error (SSE) increases. By comparing the AIC of different models and sensor subsets, an optimized choice of sensors and model parameters can be made. The AIC is given by:

$$AIC = N \log_{10} \left(\frac{SSE}{N} \right) + 2k \quad (48)$$

where N is the number of data points used in the regression, and k is the number of model parameters, such that:

$$k = N_s (b - a) \quad (49)$$

where N_s is the number of sensors and $[a, b]$ is the window of sensory data delays used in the convolution. For comparison among samples, AIC was normalized within the sample. Prediction performance was evaluated statistically using a variant on the Welch's t-test for unequal variances [114].

To determine principles for selecting good model parameters, the effect of varying MISO model parameters on the prediction performance was studied. To determine the optimized time window for prediction, the time window size ($b - a$) and the time window

values (a,b) were varied as performance was evaluated. Single time delays ($a = b$) were evaluated from 0-200ms prior to force data to determine if the MISO model could be used to predict forces in advance. Performance was evaluated for each discrete, 1ms time window between 0 and 200ms inclusive.

5.2.2.6 *Sensor selection*

The data of specific sensors was used to form prediction models to determine which sensor modalities (e.g. bending vs. pressure) and placement locations (e.g. dorsal vs. ventral) resulted in the best force predictions. The performance of models developed using only pressure data and models using only bending data were compared as gait and stroke phase were varied. The performance of models developed using sensor data at one location were compared with models developed at other sensor locations to identify useful sensor placement locations as gait and stroke were varied.

To determine the best subsets of sensors for force prediction, model performance was computed as the number of available sensors (N) was varied. Prediction models were developed and tested for every subset of sensors ($2^9 - 1 = 511$ total subsets) for each of the fin conditions tested. With a fixed number of sensors available, the best subset of that size was chosen based on *MSE*. This process was repeated for all gait/stroke combinations with the number of available sensors allowed to vary between 1 and 9 sensors, and best subsets of sensors were identified as fin conditions changed. These best subsets of sensors were studied to identify performance trends in pressure sensors versus bending sensors.

5.2.3 *Results*

5.2.3.1 Evaluation of MISO model

Evaluation of the MISO convolution model involved testing of the model performance for the tasks of *estimation* and *prediction* of force data using sensory data (as described in section 2). Metrics of variance accounted for (*VAF*) and mean squared error (*MSE*) between estimated/predicted force and measured force were computed as the fin gait, flapping frequency, stiffness, and stroke phase were varied.

The MISO convolution model *estimated* the 2D propulsive forces produced by the robotic pectoral fin very well, such that the estimate accounted for as much as 94% of the variance (figure 3). Individual models for steady swimming gait were able to estimate outstroke forces very well (91% VAF, 2.2mN^2 MSE), instroke forces nearly as well (85% VAF, 4.0mN^2 MSE), and forces of the full fin beat with some accuracy (42% VAF, 11mN^2 MSE). Models for the yaw turn maneuver gait could be used to estimate its outstroke (70% VAF, 3.8mN^2 MSE), instroke (74% VAF, 2.8mN^2 MSE), and full fin beat forces (26% VAF, 5.7mN^2 MSE). Models for the ventral steady swimming gait could be used to estimate forces during its outstroke (69% VAF, 1.5mN^2 MSE) and instroke (62% VAF, 2.1mN^2 MSE), but not effectively during the full fin beat (negative VAF, 5.2mN^2 MSE). The model was able to estimate the forces of the outstroke with greater VAF than the forces of the instroke in both ventral steady swimming and steady swimming gaits (figure 3(b)). In all cases, the model estimated the forces of the outstroke better than the forces of the instroke (lower *MSE*; figure 3(c)). The performance of the model was always worst (highest MSE, lowest VAF) when the model was used to estimate the forces of a full fin beat (both outstroke and instroke combined; figure 3(b-c)).

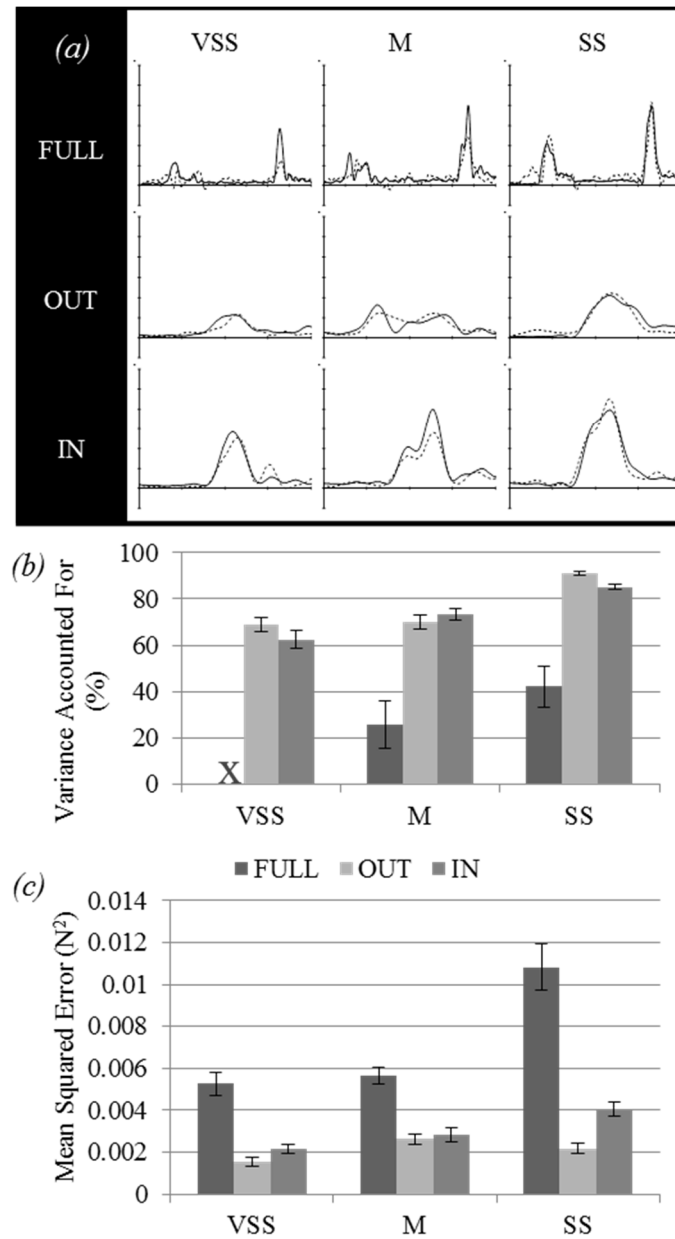


Figure 38. Force estimation performance of the MISO convolution model. Full stroke (FULL), outstroke (OUT), and instroke (IN) forces estimated for ventral steady swimming (VSS), maneuver (M), and steady swimming (SS) gaits (a). Performance metrics of variance accounted for (b) and mean squared error (c) were computed across conditions. “X” markers on the bar graph indicate that variance accounted for was negative in that case. Representative force magnitudes are shown with $f=1.0\text{Hz}$ at $600\times$ stiffness. Force data were low pass filtered at 7 Hz for clarity and displayed with 0.2N/division in force and 0.2s/division in time.

The MISO convolution model *predicted* the 2D propulsive forces produced by the robotic pectoral fin well, with performance of the model typically ranging from 65 to 85% VAF (Figure 39). A model that was trained on data from a range of flapping frequencies and stiffnesses (e.g. Steady Swimming Outstroke at $f=\{0.65,1,1.3\}Hz$ with $EI=\{400,600,800\}x$) could be used to predict forces with the same range of parameters (Figure 42). The propulsive forces of multiple gaits and stroke phases were successfully predicted with this model. Predictions of force during steady swimming gaits typically accounted for more than 80% of the variance of the measured force, yaw turn maneuver predictions accounted for more than 75% of the variance, and ventral steady swimming predictions accounted for more than 60% of the variance. The propulsive forces of different phases of the fin stroke were successfully predicted, such that prediction performance of the outstroke phase ranged from having 65 to 90% VAF and instroke-phase performance from having 70 to 90% VAF (Figure 41).

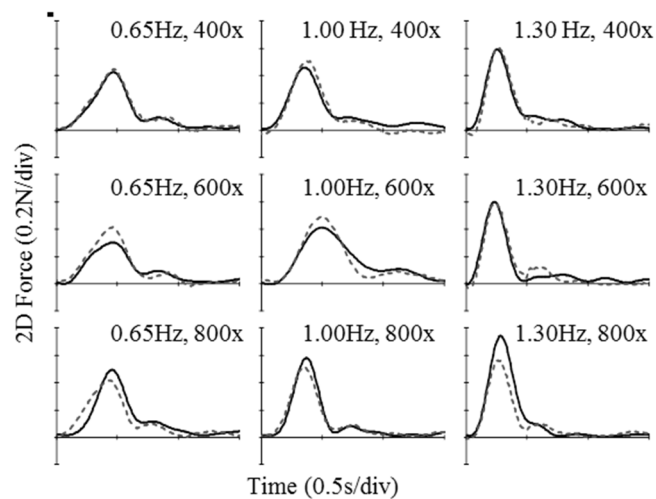


Figure 39. Force prediction across fin parameter changes. Experimental 2D propulsive force magnitudes can be predicted across changing conditions to flapping frequency (0.65Hz, 1.00Hz, 1.30Hz; left to right) and mechanical properties (400x, 600x, 800x flexural rigidity; top to bottom) without changing sensory model weights. Forces and predictions are shown for steady swimming outstrokes (SS OUT) and are representative of trends in the fin system

when gait and stroke phase are held constant. Sensory model weights were trained with delays from $[-200,0]$ ms. Data were low pass filtered at 7 Hz for clarity.

Performance of the MISO model improved as the length of the time window was increased, though optimal quality could be achieved using a short time window of sensory data. For optimal performance in VAF, time windows of $[-200,0]$ ms performed best, but optimal model performance in AIC was always obtained using a window of sensory data from 0 to 110ms prior (Figure 44(a)). The selection of the optimal time window (by AIC) was dependent on the fin's swimming gait and the stroke phase. The optimal time window parameters (AIC) during steady swimming outstrokes and instrokes were both equal to $[-30,0]$ ms, maneuver outstrokes and instrokes were $[-70,-60]$ ms and $[-40,0]$ ms, and ventral steady swimming outstrokes and instrokes were $[-20,0]$ ms and $[-100,0]$ ms. In most cases, the optimal time window for a full stroke model was longer in duration than the optimal windows for the outstroke or instroke models. The optimal time window for outstroke models had a short duration (10-20ms), and the optimal time window for instroke models was typically longer (20-100ms). Model performance was not strongly affected by the optimization method; optimization using VAF, AIC, or a full window ($[-200,0]$ ms) all produced similar model performance (Figure 44(b-c)), and using AIC as an optimization criterion always reduced the length of the time window required for optimality.

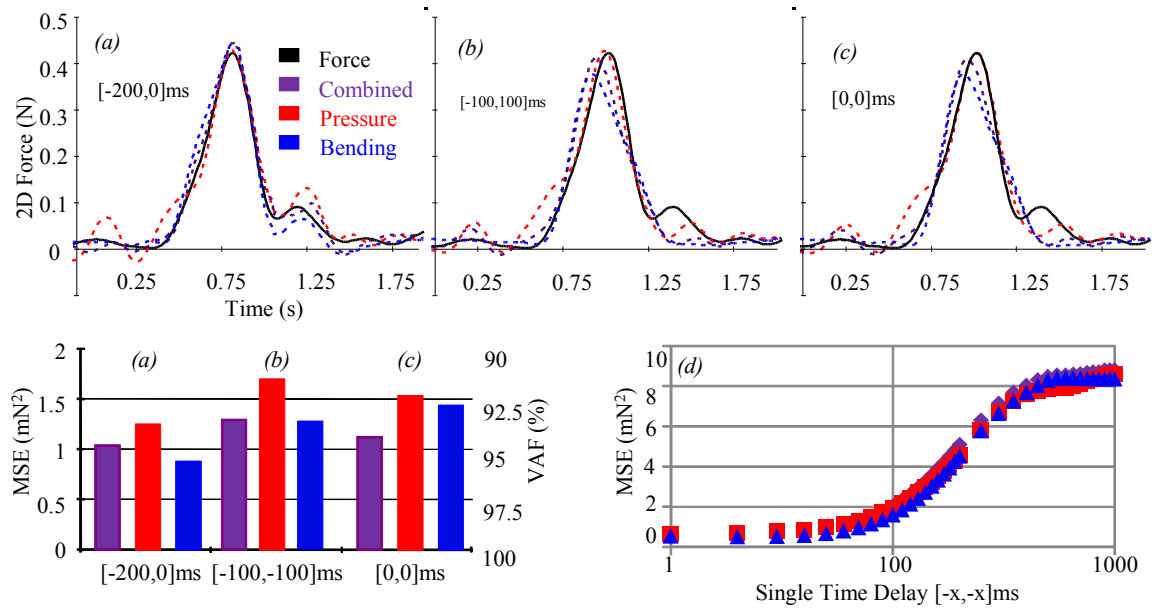


Figure 40. Effects of MISO model time window parameters on force prediction performance. Representative experimental 2D propulsive force and the predicted force from combined (pressure and bending-based models), pressure-based, and bending-based models are shown as the number and value of delay elements are varied in the MISO convolution model (a-c, top) and MSE is computed for these cases (a-c, bottom). Time series predictions are shown for steady swimming outstrokes at 0.65Hz. Mean squared error is shown as the delay (ms) of a single time lag is increased (d). Time series data were low pass filtered at 7 Hz for clarity.

Predictions of force could be made using sensory data at a single time lag ($a = b$). A 0ms time lag (i.e. $a, b = 0$) of sensory data relative to force data yielded the best performance out of all single time lags (where $a - b = 1$). As the time between force data and sensory data was increased, MSE increased monotonically (Figure 40(d)). Predicted forces could approximate measured forces for small time lags (<200 ms), but at high time lags (>200 ms) predictions were poor approximations for measured forces and had high MSE and low VAF.

Performance of the MISO model was highly sensitive to the sensors used to form the input dataset, and increasing the number of available sensors did not always increase performance (Figure 43). Although all sensors were used to acquire data during experiments, the performance of force predictions was studied with sensory data from

subsets of sensors. Steady swimming forces could be predicted using a single bending sensor (approximately 80% VAF), while at least two sensors were required for the model to predict maneuver and ventral steady swimming forces. Acceptable performance (more than 50%VAF) for maneuver and steady swimming force prediction was achieved using 4 and 5 sensors, respectively (Figure 43). Predictions of force were best during steady swimming was achieved using data from four sensors during the outstroke and seven sensors during the instroke. Predictions of force were best during maneuver using data from eight sensors in the outstroke and data from six sensors during the instroke. Predictions were best during ventral steady swimming using data from eight sensors during the outstroke and data from all nine sensors during the instroke. Thus, in almost all cases, the optimal number of sensors for prediction was less than the full set of nine sensors.

5.2.3.2 *Force prediction*

Forces were predicted best when the model used for prediction was developed using data from the same gait (Figure 42; $P < 0.001$, $N = 217$), though in some cases a model trained on data from one gait could be used to predict the forces of another gait. Prediction performance was highest for steady swimming models (more than 75% VAF), slightly less for maneuver models (more than 65% VAF), and least for ventral steady swimming models (more than 50% VAF). Significant differences in the model's performance (as measured by *MSE*) were found between force prediction of steady swimming and ventral steady swimming models (Table 7; $P < 0.001$, $N = 138$), maneuver and ventral steady swimming models ($P < 0.001$, $N = 109$), but not between steady swimming and maneuver models ($P < 0.3$, $N = 106$). In some cases, a MISO model trained on one gait could be used

to predict the propulsive force of another gait. Models that had been trained on steady swimming forces were unable to predict the forces of other gaits (Figure 42(b), negative VAF). However, when maneuver-trained models were used to predict the forces of other gaits, predictions of steady swimming outstroke forces had 69.5% VAF and ventral steady swimming forces had 45.5% VAF (Figure 42). Instroke-trained models had 78.0 and 32.4% VAF on similar conditions. When models trained on ventral steady swimming data were used to predict the forces of other gaits, predictions ranged from 0 to 49% VAF. The predictions of models trained on maneuver data had significantly lower MSE when predicting the forces of other gaits than models trained on steady swimming data ($P < 0.005$, $N = 76$). Further, predictions from models trained on steady swimming data had significantly lower MSE when predicting the forces of other gaits than models trained on ventral steady swimming data ($P < 0.001$, $N = 76$).

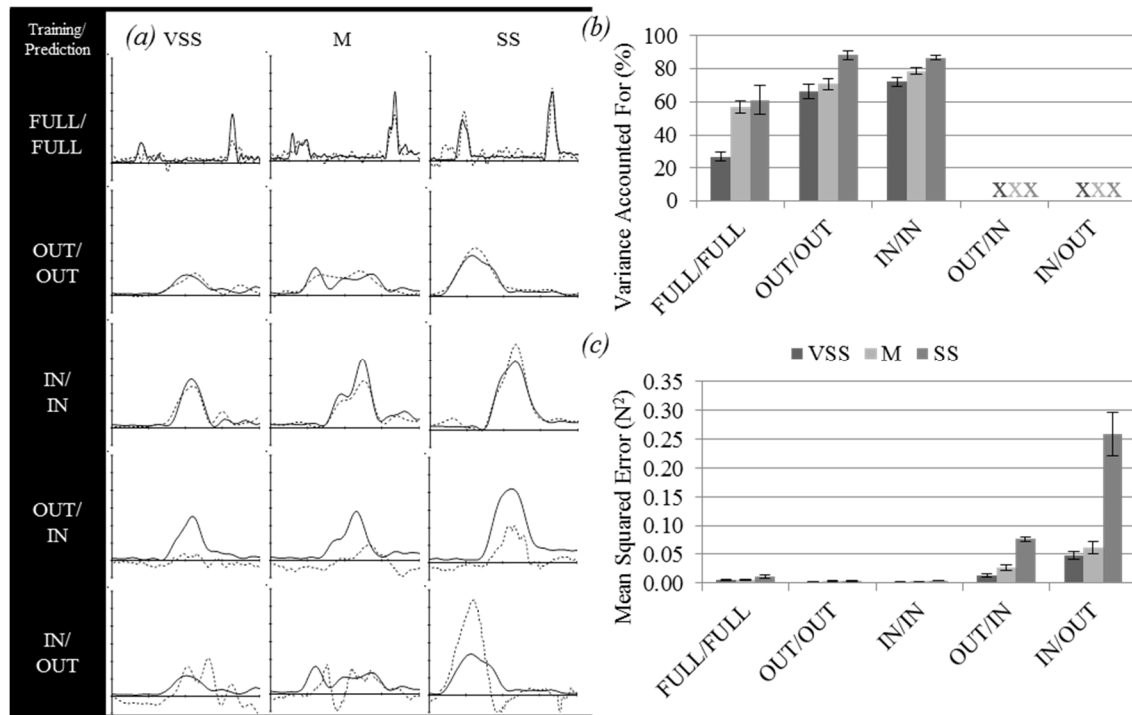


Figure 41. Force prediction across changes to stroke phase. Full stroke (FULL), outstroke (OUT), and instroke (IN) forces predicted for ventral steady swimming (VSS), maneuver (M), and steady swimming (SS) gaits (a). Performance metrics of variance accounted for (b) and mean squared error (c) were computed across conditions. “X” markers on the bar graph indicate that variance accounted for was negative in that case. Representative force magnitudes are shown with $f=1.0\text{Hz}$ at $600\times$ stiffness. Data were low pass filtered at 7 Hz for clarity and displayed with 0.2N/division in force and 0.2s/division in time.

Forces were predicted best when the model used for prediction was developed using data from the same stroke phase (Figure 41; Table 6; $P<0.001$, $N=97$). For prediction of forces created during the outstroke, prediction performance was highest when models trained on outstroke data were used, having 67 to 89% VAF. For instroke force magnitudes, prediction performance was highest when models trained on instroke data were used with 72 to 87% VAF. Models that had been trained on instroke forces were unable to predict outstroke forces, and vice-versa (less than 0% VAF). Predictions were best when separate models were developed for each of the instroke and outstroke phases ($P<0.001$, $N=32$).

Table 6. Prediction performance for different sensory systems on the robotic fin.^a

#	Reference Name	Bending			Pressure						Fin Gait/Stroke Combination: VAF(%)					
		A	B	C	Ao	Bo	Co	Ai	Bi	Gi	SS OUT	SS IN	M OUT	MIN	VSS OUT	VSS IN
1	All Sensors (Baseline)										86.44	85.96	60.76	75.06	51.79	66.95
2	Bending Only										81.92	82.00	5.87	63.34	X	56.99
3	Pressure Only										83.71	76.55	46.71	58.88	38.01	X
4	Dorsal Only										83.30	85.33	37.57	64.79	24.92	52.07
5	Ventral Only										83.59	61.21	29.70	17.32	30.74	X
6	Dorsal Proximal Only										79.79	79.87	X	27.23	X	11.50
7	Dorsal Distal Only										72.14	74.88	7.96	45.83	X	X
8	Outer Pressure Only										80.63	71.58	X	45.80	30.41	X
9	Inner Pressure Only										40.82	X	X	X	X	X
10	Bending and Outer Pressure										84.96	84.73	52.16	73.18	52.23	65.80

^a Comparing the performance of user-defined sensor selection strategies (rows 2-10) to the baseline performance of all sensors (row 1). Each row shows the average force magnitude prediction performance obtained with a group of sensors for each fin gait/stroke combination. Cells are crossed out (X) where force magnitudes could not be predicted (VAF<0%). Performance was assessed on data from flapping frequencies of 0.65, 1, 1.3Hz and fin stiffnesses of 400, 600, and 800x. Force predictions were made using sensory data weighted at delays ranging from 0 to 200ms (inclusive) to account for timing differences.

5.2.3.3 Sensor selection

The best subsets of sensors used to form the model were highly sensitive to which fin gait was being executed (Figure 43), and operator-defined sensor choices often resulted in poor predictions of force. The prediction of ventral steady swimming forces required the largest subsets of sensors for good performance. No single sensor was suitable to predict the forces of ventral steady swimming (negative VAF using 1 sensor), and performance above 50% VAF could not be obtained until multiple sensors were used (5 sensors for outstroke forces, 3 for instroke forces). Predictions of ventral steady swimming forces had 27 to 72% VAF, and predictions frequently failed across changes to gait and stroke

phase. Operator-defined sensor placements (Table 6) were often insufficient to predict outstroke and instroke forces of ventral steady swimming. For example, using specific strategies of “bending only”, “pressure only”, “ventral only”, ventral steady swimming forces could not usually be predicted (less than 0% VAF for these cases). The prediction of steady swimming forces had the lowest complexity cost of any gait tested. Using only the dorsal proximal bending sensor to predict forces in steady swimming, performances of greater than 78% VAF were typical. Optimal prediction performance was obtained using less than the maximal number of sensors for both outstroke and instroke (4 and 7 sensors, respectively).

The best subsets of sensors were also highly sensitive to which stroke phase the fin was executing (outstroke versus instroke; Figure 43). The prediction of instroke forces required smaller subsets of sensors for good predictions than the prediction of outstroke forces did. Instroke forces were better predicted than outstroke forces, and full fin beat forces were predicted worse than either instroke or outstroke forces (Table 6). Predictions of the instroke forces had significantly lower MSE than predictions of the full fin beat ($P < 0.001$, $N = 64$), and had margins of more than 20% VAF between them. Outstroke predictions had significantly lower MSE than predictions of the full fin beat ($P < 0.001$, $N = 32$), and margins of VAF were greater than 10%. Predictions of the full fin stroke typically had 26 to 61% VAF. Steady swimming full stroke forces were the easiest to predict ($61.3 \pm 8.8\%$ VAF) and ventral steady swimming full stroke forces the hardest to predict ($26.7 \pm 2.6\%$ VAF) among conditions tested. Predictions of steady swimming outstroke and instroke forces had comparable MSE and VAF, predictions of maneuver outstroke forces had significantly worse MSE than predictions of instroke forces, and

predictions of ventral steady swimming outstroke forces had significantly lower MSE than predictions of instroke forces. Differences in prediction MSE were largest in the stroke phases of the maneuver gait, which suggests a large complexity difference between outstroke and instroke dynamics.

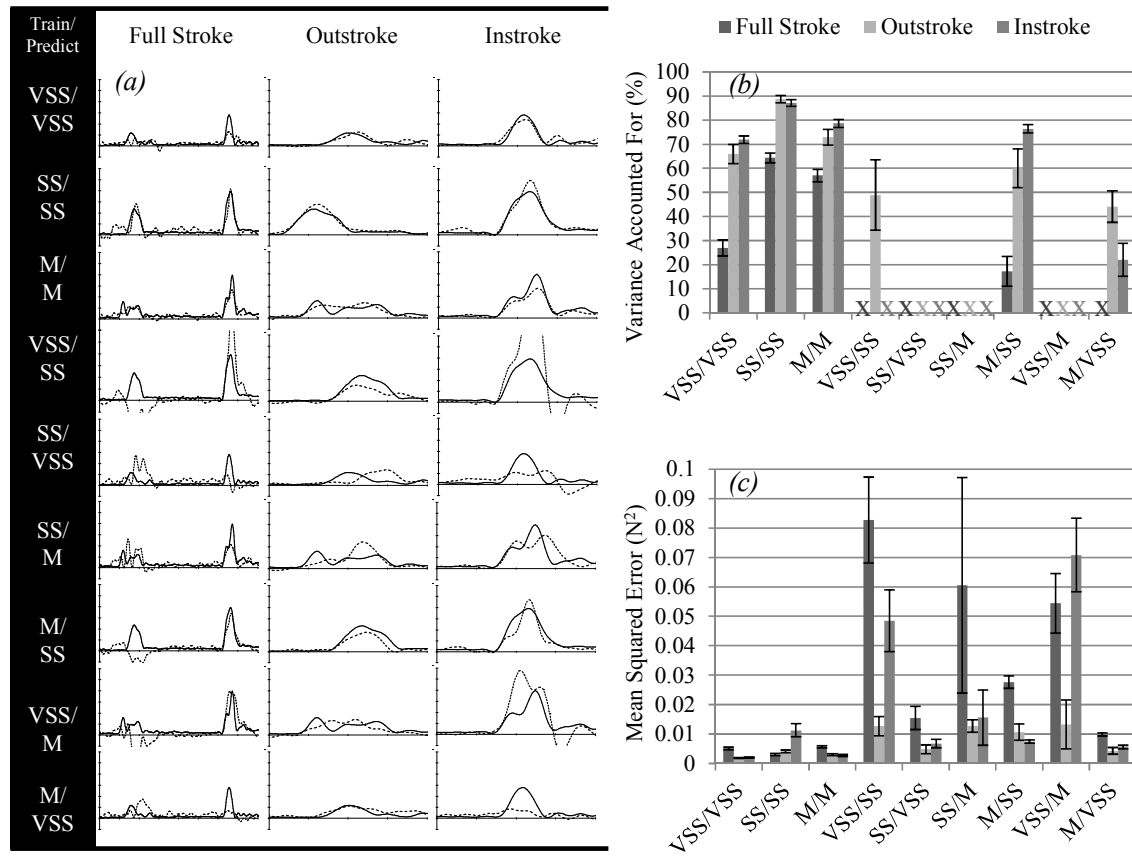


Figure 42. Force prediction across changes to fin gait. Ventral steady swimming (VSS), steady swimming (SS), and maneuver (M) gait forces are predicted for fin full strokes, outstrokes, and instrokes individually (a). Performance metrics of variance accounted for (b) and mean squared error were computed across conditions (c). “X” markers on the bar graph indicate that variance accounted for was negative in that case. Representative peaks are shown with $f=1.0\text{Hz}$ at $600\times$ stiffness. Data were low pass filtered at 7 Hz for clarity and displayed with 0.2N/division in force and 0.2s/division in time.

Best subsets of sensors varied significantly depending on which gait the fin executed, and the best subsets often changed from outstroke to instroke (Figure 43). In a

steady swimming gait (Figure 37(a)), models that used dorsal region sensors had the highest prediction performance and sensors from the dorsal region were used most frequently in best subsets. During the outstroke of the gait, models that used the dorsal proximal bending sensor alone had 79.51% VAF and the dorsal distal outer pressure sensor was used more often than any other sensor in best fits (8/9 cases). Adding this sensor to the single dorsal proximal bending sensor resulted in an increase of 4.87%, yielding 84.38% VAF. During the instroke, models that used the dorsal proximal bending sensor alone had 78.46% VAF and this sensor was used more often in best fits than any other sensor (9/9 cases = 100%). In a maneuver gait (Figure 37(b)), data from both dorsal and ventral region sensors were needed for best predictions. During the outstroke, models that used dorsal distal bending and ventral outer pressure sensors had 23.65% VAF. These two sensors were also used in all eight cases in best fits. The addition of a dorsal proximal bending sensor to the model improved VAF by 20.75%, yielding 44.40% VAF. During the instroke, models that used the dorsal distal outer pressure sensor alone had best fits (14.58% VAF). The dorsal distal outer pressure sensor was also used most often in best fits (8/8 cases). Performance increased by 47.02% when the dorsal distal and ventral bending sensors were used instead. In a ventral steady swimming gait (Figure 37(c)), models that used the ventral region sensors had best predictions on the outstroke, and models that used the dorsal bending sensors had best predictions on the instroke. During the outstroke, models that used ventral sensors alone were the optimal selection when only two sensors were used. Ventral bending and ventral outer pressure sensors were used more often than any other sensors in best fits (8/8 cases for each sensor, tied for best performance). The addition of the dorsal distal outer pressure sensor to the model

increased VAF by 23.26%. During the gait instroke, models that used the dorsal proximal and dorsal distal bending sensors provided the best fit (2 sensors permitted, 36.58% VAF) and these two sensors were the most frequently used in best fits (8/8 cases, tied). Adding the ventral bending sensor's data to the model caused an increase in instroke prediction performance by more than 20%, yielding 56.99% VAF.

5.2.3.4 *Sensor modality*

The use of both pressure and bending sensory data to form the model typically resulted in better force predictions than using either sensor's data alone (Figure 40(a-c)). Models that used bending sensor data to predict forces performed better than models that used pressure sensor data, and models that used both pressure and bending data performed comparably or better than models that used bending data. The performance of these models was affected by the time lags used. Regardless of the number of time lags used, using both pressure and bending sensory data in a model led to better performance than using pressure or bending data alone. Adding time lags typically increased the model performance for pressure-based, bending-based, and pressure and bending-based models. In estimation and prediction, models that used both pressure and bending data typically outperformed pressure-based or bending-based models by margins greater than 5% VAF (Table 6).

Bending-based models performed better than pressure-based models, but data from both sensors were required to form models that could predict the forces of multiple gaits and stroke phases. Bending-based models outperformed pressured-based models across changes to fin gait and stroke phase (Table 6). Bending sensors were used more prevalently than pressure sensors in best predictions when the number of available

sensors was fixed (Figure 43). A bending sensor was always one of the sensors used in the best predictions (Figure 43; 268/268 cases). Further, bending sensors were among the most frequently used sensors in a best fit with (1) Ventral Bending at 14.9% usage (40/268 cases), (2) Dorsal Distal Bending at 13.8% usage (37/268 cases), and (3) Dorsal Proximal Bending at 13.4% usage (36/268 cases). The best performing single sensor for any given gait/stroke pair was most frequently a bending sensor (in 7/8 cases), and when the number of sensors was allowed to vary (from 1 to 9 sensors), the top used sensor for a gait/stroke pair was typically a bending sensor (7/8 cases). For successful force prediction across fin conditions, using “pressure only” or “bending only” were not suitable strategies (Table 6). Using only pressure sensors, ventral steady swimming outstrokes could not be predicted and maneuver outstroke predictions decreased in performance by more than 50% VAF. Using only bending sensors, ventral steady swimming instrokes could not be predicted and prediction performance typically decreased by more than 5% across gait/stroke conditions.

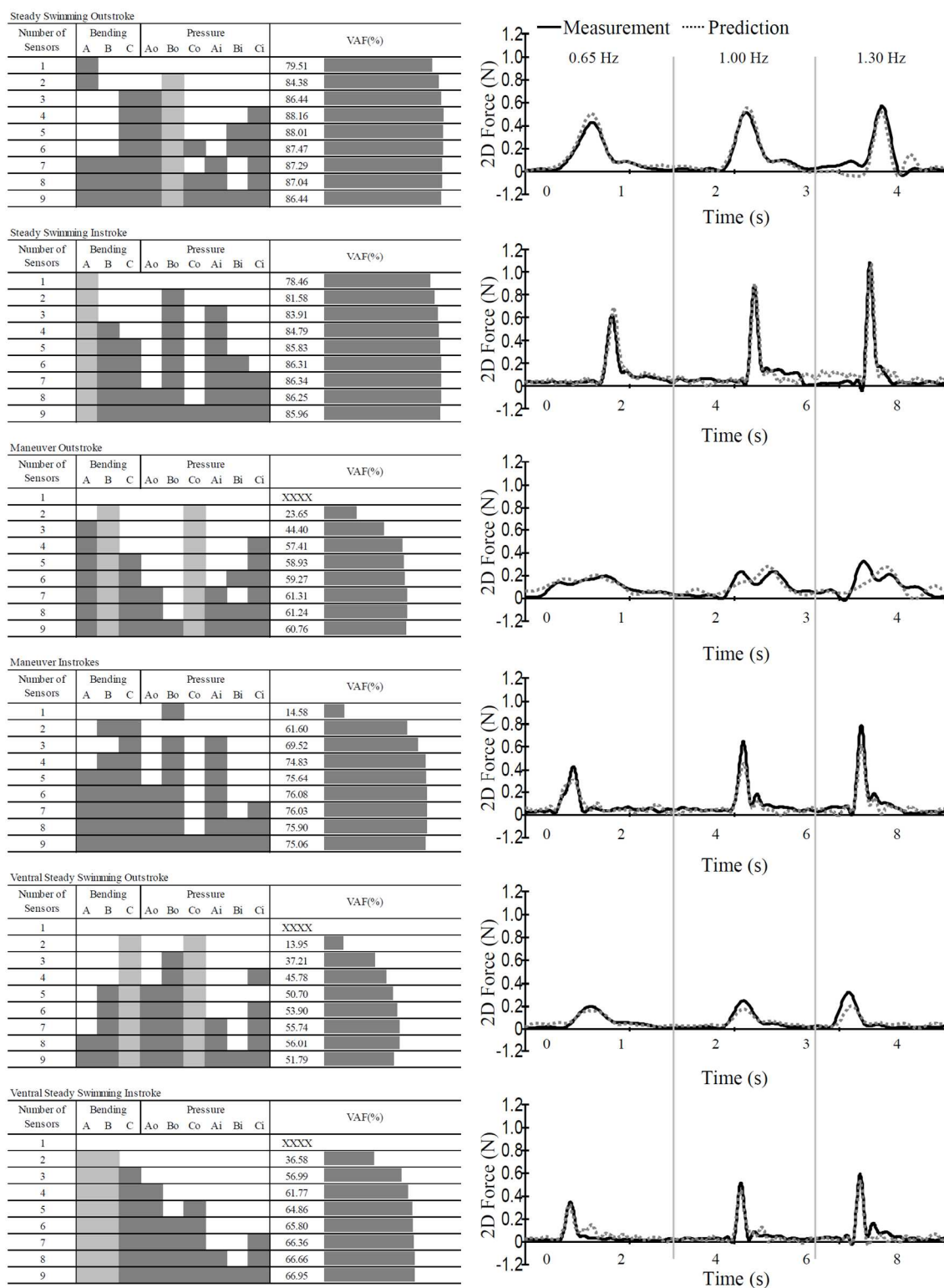


Figure 43. Optimal sensor combinations for a fixed number of sensors as fin gait and stroke phase are varied. Shaded cells indicate the sensors used in the force magnitude predictions (see Figure 1 for sensor locations). Variance accounted for was computed as a performance metric for each subset of sensors tested on data from fins at 400, 600,

and 800x stiffness and 0.65, 1, and 1.3Hz flapping frequency. VAF was averaged for each subset across ten or more trials. Representative fits are shown across changes to flapping frequency (force magnitude peaks at 0.65, 1.00, 1.30 Hz shown; right column). Model time windows of 0 to 20ms (inclusive) were used in fits. Force data were low pass filtered at 5 Hz for clarity.

5.2.3.5 *Sensor location*

Best predictions of propulsive force occurred when sensory data was sampled from multiple fin regions and used to form the prediction model, rather than data sampled from a single region. There was no single sensor location of those tested (i.e. “dorsal proximal”, “dorsal distal”, or “ventral”) whose data could be used in a model to predict forces across fin conditions (Table 6, rows 5-7). Use of “dorsal distal only” data had 79% VAF for outstroke/instroke of steady swimming, but these models failed to predict maneuver and ventral steady swimming outstroke forces (less than 0% VAF). “Dorsal proximal only” models predicted steady swimming forces with 72.14/74.88% VAF, maneuver forces with 7.96/45.83% VAF, but failed to predict ventral steady swimming forces. “Ventral only” models predicted steady swimming forces with 83.59/61.21% VAF, maneuver forces with 29.70/17.32% VAF, and failed to predict ventral steady swimming forces. “Dorsal only” models had a large range of 25 to 85% VAF. Using “dorsal only” models, prediction of maneuver outstroke forces and ventral steady swimming instroke forces decreased significantly from the baseline of using models developed on data from all locations. When “ventral only” models were used, ventral steady swimming instroke forces could not be predicted and performances decreased from baseline by as much as 58% VAF. Not all of the data that was gathered was particularly useful in creating good prediction models. For instance, using data from pressure sensors on the inner face (body facing side) of the fin did not significantly

improve prediction performance when added to the model (Table 6, row 9). Removing the data from these inner face sensors by using a “bending and outer pressure” model (Table 6, row 10) did not significantly impact performance (less than 5% decrease in VAF from baseline), except in the prediction of maneuver outstrokes (9% decrease in VAF). Using “inner pressure only” models resulted in failed predictions for almost all fin conditions (Table 6, row 9).

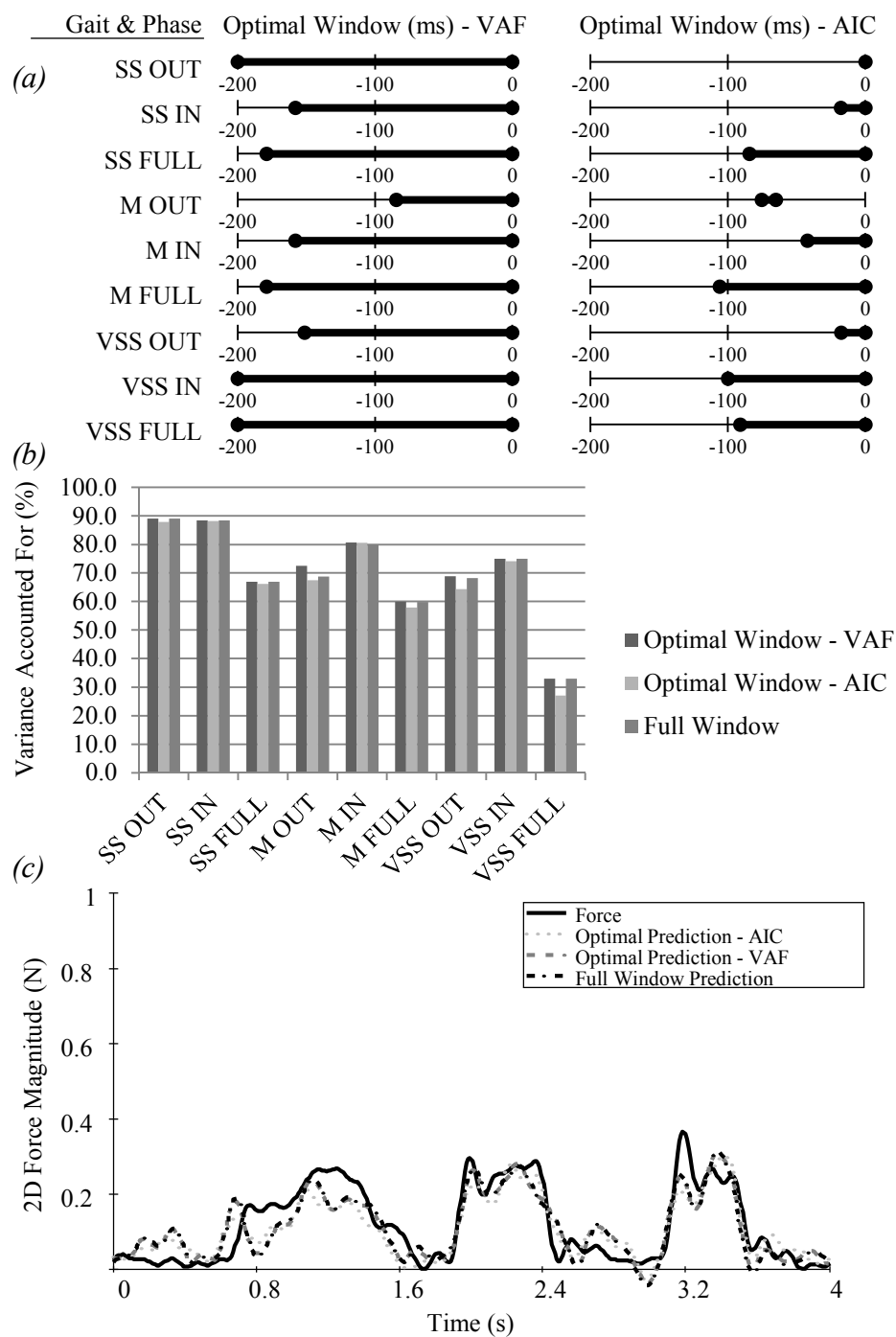


Figure 44. Optimization of model time windows for a fixed gait/stroke combination (a). 1D plots show the optimal time window of sensory weights when variance accounted for (left) and Akaike information criterion are used as optimization criteria. Model performance is compared when VAF and AIC are used as metrics against a baseline of a full 200ms window (b). Force magnitude predictions are compared using these three approaches (c).

Table 7. Hypothesis testing to evaluate model prediction performance across fin gait and fin stroke timing.

Hypothesis			Significance	Trials (#)
P(SS)	>	P(MAN)	>0.1	106
P(SS)	>	P(VSS)	<0.001	138
P(M)	>	P(VSS)	<0.001	109
P(Same Gait)	>	P(Different Gaits)	<0.001	217
P(Same Stroke Phase)	>	P(Different Stroke Phases)	<0.001	97
P(IN)	>	P(OUT)	<0.001	64
P(OUT)	>	P(FULL)	<0.001	32
P(Mwt)	>	P(SSwt)	<0.005	76
P(SSwt)	>	P(VSSwt)	<0.001	76
P(INwt)	>	P(OUTwt)	<0.001	32
P(Bending)	>	P(Pressure)	<0.001	138

^a “P(SS)>P(M)” means that the prediction performance on steady swimming (SS) forces was greater than prediction performance on maneuver (M) forces.

^b “P(Mwt)>P(SSwt)” means that weights trained on maneuver forces had better prediction performance than weights trained on steady swimming forces.

^c MSE statistics of predictions in each category were used to determine significance levels with a two-sided T-test.

5.2.4 Discussion

The MISO convolution model was effective for understanding how to predict of propulsive force from a compliant, multiple degree of freedom robotic fin with complex dynamics. It was effective for prediction of forces from sensory data and provided insight into the underlying relationships between sensor parameters and forces. The MISO model structure allowed for an in depth analysis of the roles of individual sensors, the memory of the system, and the performance effects of changing multiple parameters. The underlying model could be further improved using basic knowledge of robot behavior (e.g. which gait and stroke phase are being executed). The evaluation methods used, including MISO for prediction and AIC for sensor and parameter selection, suggest a framework with which to optimize sensor selection and placement for intrinsic robotic sensory systems without *a priori* models. This could be more broadly applicable to other

research areas, including: multi-modal tactile sensing in perception research [84, 115], grasping studies of in-hand manipulation [116, 117], and proprioceptive robotic systems for measurement of human body forces and kinematics [118]. The empirical techniques presented here could be used to validate optimal sensor modalities and optimal sensor placements for many other sensing challenges in robotics, especially where the dynamics of the system are challenging to model mathematically but feasible to model with bio-inspired robotic platforms [119]. These techniques could be valuable to the study of animal systems, where compliance, complex dynamics, and environmental effects all contribute significantly to the performance of particular behaviors.

Complex changes to the fin kinematics required more complex sensing and modeling strategies. When small changes were made to the fin dynamics, by changing flapping frequency or fin stiffness, the same model could be used to predict forces across these conditions (Figure 39). But when the entire swimming gait changed, the model trained on one gait could not be used to predict the forces of another gait. For instance, models trained on steady swimming forces were unsuccessful at predicting the forces of ventral steady swimming (Figure 42), even though ventral steady swimming has the same ventral edge kinematics as steady swimming (Figure 37). Sensing strategies also had to change as gaits changed. The best sensors subsets for each gait differed, as best predictions of ventral steady swimming forces were achieved with $S=\{C,C_O,A,B\}$ and best predictions of steady swimming forces were achieved with $S=\{B_O,A\}$. The fluid structure interaction that produces propulsive forces involves multiple fin regions and the energetic exchange of their interactions [70, 120], and so large changes to kinematics can change the fundamental mechanisms of force production. Thus, in order to have a

sensory system that can reliably predict forces when swimming gaits change, multiple sensors and models are needed. This may have implications for robots that execute complex gaits and gait changes with compliant control surfaces, such as elastomer-based soft robots that crawl and undulate [121], fish-inspired robots that use compliant fins to execute multiple swimming gaits [33, 109, 122], and bipedal robots with compliant joints that shift from walking to jogging [123]. Robots that engage in multi-modal locomotion (e.g. aquatic to terrestrial [124, 125], terrestrial to aerial [126], aerial to scansorial [127]) may also benefit from multi-modal, distributed sensory systems; because as the physics of the environment change, the underlying sensor modes and distributions may have to change accordingly.

The best sensory modalities were related to known dynamics of compliant fins. Bending sensation was more useful for force prediction than pressure sensation in the compliant, multi degree of freedom, robotic fin (Table 7). Bending and compliance have been shown to play a major role in force production in fins, and good estimation of the forces occurred using distributed strain measurements. Past study of bending and curvature in sunfish pectoral fins show that the fish can modulate fin stiffness [16, 17]. Since stiffness control is a major mechanism of force production in fins [17], it is reasonable that bending would be highly useful for force prediction, as demonstrated above empirically. The importance of bending measures in fins is consistent with behavioral biology studies [3] and neurobiological evidence [6]. Theories of haptic function have argued that local strain measures may be more informative for contact sensing than pressure measures and may be what is more commonly found in biological systems [128]. Thus, an understanding of the important sensors and underlying physics

from computational biology, neurobiology, and haptics disciplines can provide insight into sensory instrumentation in robotic systems. However, in this study, bending data alone was not sufficient to predict propulsive forces in all robotic swimming modes (Table 6), so propulsive force prediction may perform best using multiple sensory modalities, such as: fin ray bending, fin pressure, membrane stretch, and further components of the strain.

The placement of sensors is important for force prediction. Good placement may agree with the areas responsible for force production in animal and robotic models. Sensors along the dorsal leading edge, both bending and pressure sensors, were essential for good prediction of propulsive forces. The importance of the dorsal leading edge in thrust force production has been well documented in study of bony-finned fishes [11, 32]. Since sensor placement was determined primarily by study of steady swimming modes [70], it was consistent that model performance was highest for predicting force magnitudes during steady swimming. Further, biological evidence suggests that free nerve afferents in sunfish pectoral fins innervate multiple regions of the fin and have relatively high density in the dorsal and ventral leading edges [6, 19, 20]. In this way, engineers may be able to look at simulation data and biological studies of relevant animal gaits in order to determine initial locations for sensors on their biologically-derived robots.

Distributed, heterogeneous sensors in fins can serve multiple roles in the control of propulsive force: they can be used for forming accurate predictions of the force (Figure 39), can serve as direct inputs to kinematic controls, and can be exploited for more robust control with redundancies. In some cases, the sensory data could be used to predict the

propulsive force in advance (60-70ms; Figure 44), which could be useful in a feedforward control framework. While sensory data can be fused to predict forces, the individual sensor components are still available to the operator and can be used in a control framework for fast updates to kinematics. *Intrinsic* sensors provide information about the strain and pressure distributions across the fin's control surface, which can aid in understanding the components of the propulsive force; whereas this local information about force is largely unavailable to a single *extrinsic* sensor (such as a force sensor at the fin-body interface). Having access to local components of the propulsive force (local strains, pressures) can be exploited by a controller that updates local kinematics according to these measures. Using both the force predictions and the sensory data directly provides more feedback pathways in a control framework. *Intrinsic* sensors provide redundant information due to the mechanical coupling created by the fin webbing. Redundant sensors can be used to help localize contact with an obstacle (as in terrestrial examples of whisking [65, 66]), to compensate for a sensor failure by sampling from surrounding sensors, or to provide weighted estimates of the force that improve on estimates from single sensors or single modalities (c.f. robotics research in hyperacuity [84]). The redundancy gained by through intrinsic, distributed, heterogeneous sensors can be exploited for more robust estimates and more robust control. These advantages are ripe for exploration in future work with biologically-inspired robots.

5.2.5 Conclusion

This study demonstrates successful prediction of propulsive forces on a robotic fin using sensors distributed within the fin and practices for sensor and model parameter selection depending on robot behavior. The effectiveness of a MISO convolution framework is

demonstrated in a complex force prediction scenario: prediction of propulsive forces using a distributed, multimodal sensory system on a compliant robot underwater. Weighted sensory data were utilized to successfully predict propulsive forces across changes to fin flapping frequency and stiffness. Sensory contributions to the force estimate were easily assessed and temporal relationships between the sensory data and forces were discovered. The linear, time-varying assumption of the framework was sufficient for this application and low numbers of model parameters were usable to achieve high prediction performance.

It is important to have a broad spatial distribution of sensors and multiple sensory modalities for propulsive force prediction. No single modality or sensor sampling region was appropriate for predicting forces across conditions. An analysis of best fits for fixed cost revealed that force prediction quality improved when an appropriate subset of sensors was used, and this subset varied significantly depending on swimming conditions. Thus, choosing a fixed subset of sensors had significant costs to performance, as many operator-selected sensory subsets performed significantly worse than baseline measures. Having a broad spatial distribution of sensors was important even within a single fin beat, as some subsets were preferable to predict outstroke forces and other subsets for instroke forces of the same gait. While the study reveals which subsets were best for force prediction, future work will identify best sensor arrangements for other biologically-relevant behavioral tasks such as characterizing contact with obstacles [3].

The relationship between sensory measures and propulsive forces on a high-DOF robotic pectoral fin is complex. A good model relating the two would likely allow for: a) temporal lags between forces and sensory data, b) changes to the model within a fin

stroke, and c) changes to the model through gait transitions. The degree of required model complexity varied from gait to gait, though the problem of mapping between sensors and forces was tractable using the MISO model. Fin-intrinsic sensory information may have different utility depending on robot behavior and swimming modes, as outstroke forces were more easily predicted than instroke forces and steady swimming forces were more easily predicted than maneuver forces.

5.3 Paper 4: Distributed sensing and nonlinear MISO models for predicting the propulsive forces of flexible, multi-DOF robotic fins

5.3.1 Abstract

Fish are capable of producing a wide repertoire of 3D propulsive forces using their fins, and have inspired the development of compliant, multiple-DOF, robotic fins with similar capabilities. Most of these robotic fins are under open-loop control on propulsive force because the forces are challenging to model. Understanding how to predict propulsive forces for these types of fins would significantly advance the state of the art towards closed-loop control of forces. Distributed sensors within robotic fins have been used to predict propulsive forces using linear models, but these models fail to predict forces when fin kinematics become more complex. The objective of the work presented herein is to understand the use of nonlinear, multiple-input-single-output (MISO) Volterra series models between intrinsic sensory measurements and propulsive forces of a flexible robotic fin. Techniques in nonlinear system identification are used to address model conditioning. Nonlinear models predict the propulsive forces well, capturing features of both thrust and lateral forces. Nonlinear models significantly outperformed linear models both in cost of implementation and performance. The best sensor sampling practice was to sample from multiple locations with both pressure and bending modalities. Distributed sensing paired with nonlinear Volterra series models was successful for predicting the forces created by flexible robotic fins with complex kinematics and multiple degrees of freedom.

5.3.2 Introduction

The fins of bony fish are capable of producing a wide repertoire of 3D propulsive forces, and have inspired the development of compliant, multiple degree of freedom (DOF), robotic fins with similar capabilities of force production [1]. These robotic fins typically have multiple underactuated degrees of freedom and their fins are flexible so as to improve the production of desired forces. The hydrodynamics of these fins are complex, as multiple regions of the fin interact with the fluid to form vortices and jets that are shed to produce forces [2]. Relationships between kinematics and propulsive forces are complex, and do not account for known mechanisms of force production, which are related to the fluid-structure interaction of the fin with the surrounding fluid [3, 4]. This is in contrast to the large number of force models of low-DOF flapping foils and ribbon fins. Most current control schemes are closed-loop control on the kinematics, but open-loop control on the forces such that forces are not predicted or controlled. Understanding how to predict propulsive forces for these types of fins would significantly advance the state of the art towards closed-loop control of propulsive forces.

The fusion of data from sensors distributed within fins is a natural way to estimate the fin's propulsive force. Studies of bony-finned fish and robotic models have identified the importance of bending within fins, both as a sensory measure and as a physical phenomenon related to the production of propulsive forces. Bluegill sunfish (*Lepomis macrochirus*) have distributed, heterogeneous sensory afferents in their pectoral fins that respond to bending on a broad frequency band [5], and sunfish use their pectoral fins to contact obstacles underwater in sensory-deprived conditions [6]. During propulsion, bony-finned fish can actively modulate the stiffness of their fins [7], which changes the amount of bending in their fins and results in varied propulsive forces during swimming

[8]. Robotic models of the sunfish's pectoral fin have been instrumented with distributed bending and pressure sensors and were used to predict the magnitude of propulsive forces [9].

But distributed sensory measurements from within robotic fins are correlated with one another due to the mechanical interactions of the fin and the fluid. Thus, the identification of an input-output model that relates sensory measurements to propulsive forces is a significant challenge. Correlations between inputs typically result in a numerically ill-conditioned modeling problem [10]. While linear multi-input-single-output (MISO) convolution models between sensory measurements and forces are excellent during simple gaits (e.g. steady forward swimming [11]), linear models predict forces poorly when gait kinematics become more complex (e.g. turns and maneuvers [12]) or as the fin changes direction from outstroke to instroke. The forces created by changing gaits or transitioning from outstroke to instroke may be better captured by nonlinear models of sensory data, but this hypothesis had not been evaluated previously. Techniques from physiological system identification [13, 14] may be useful for characterizing the complex relationship between sensory measurements and propulsive forces, while also addressing the numerical issues of correlated inputs.

The objective of the work presented herein is to understand the use and optimization of nonlinear, multiple-input-single-output (MISO) Volterra series models between the intrinsic sensory measurements (inputs) and propulsive force (output) of a compliant, robotic pectoral fin during multiple swimming gaits. This work builds upon linear analyses of the sensory-force relationships [9, 15], and evaluates the performance of nonlinear Volterra series models for prediction of forces from sensory data. The

appropriate model order is identified by evaluating model performance across changing kinematics and mechanical properties of a biologically-derived robotic (biorobotic) fin. Best practices are assessed for selecting sensor placement locations and sensor modalities for force prediction during different gaits and stroke phases, and best practices are also validated against results of linear models. By understanding the best sensor locations and modalities (i.e. pressure versus strain) and the nonlinear relationships between sensory measurements and forces, principles are extracted for modeling the complex propulsive forces of a robotic fin.

5.3.3 *Methods*

5.3.3.1 *Biorobotic pectoral fin experiments*

A biologically-derived robotic (*biorobotic*) fin was programmed to execute multiple 3d kinematic patterns (called *gaits*) in order to create a rich set of sensory inputs and propulsive force outputs for the model identification study. The fin is comprised of flexible plastic beams called fin rays that are sheathed in elastic webbing (84/16% polyester/elastane), and is driven by servomotors on eight underactuated degrees of freedom with programmed nonlinear trajectories. The span of the longest fin ray is 150 mm. The fin rays are driven by motors in a tendon-pulley configuration about a small hinge joint (detailed in [32]). Steady swimming, yaw turn maneuver, and ventral steady swimming gaits (SS, M, VSS) were executed underwater by the robot as propulsive forces and sensor data were measured. The robot was fixed to a low friction air bearing carriage attached to S-beam load cells (LSB200, Futek Advanced Sensor Technology, LLC., Irvine, CA, USA) in the lateral and thrust directions in order to measure propulsive

forces (Figure 45a). Thousands of trials were executed as multiple gaits were executed using fin rays of three stiffnesses (400x, 600x, 800x) at three fin flapping frequencies (0.65Hz, 1Hz, 1.3Hz).

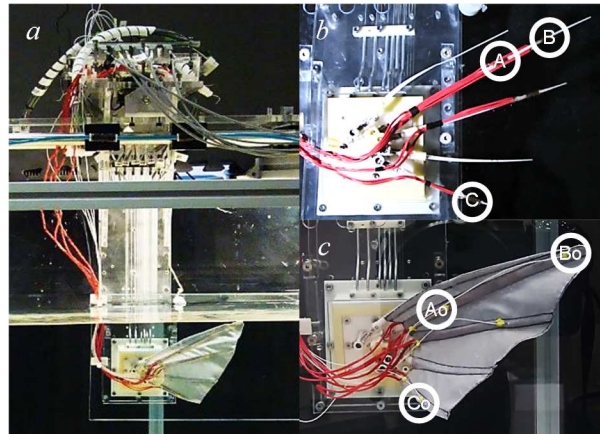


Figure 45. A biorobotic pectoral fin was submerged underwater (a) and instrumented with distributed strain sensors (b; A, B, C) and pressure sensors (c; outer sensors Ao, Bo, Co shown, inner sensors omitted). Intrinsic sensory measurements were used to predict the measured propulsive forces of the fin during multiple swimming gaits.

As described in prior work [23, 88], the robotic fin was instrumented with distributed pressure and bending sensors that took sensory measurements as the fin executed multiple swimming gaits. Catheter pressure sensors (SPR-524, A/D Instruments, Colorado Springs, CO, USA) were affixed to the fin webbing at dorsal-base (A), dorsal-tip (B), and ventral locations (C) and were affixed to inner (body-facing) and outer fin faces (Figure 45c). Strain gages (KFH-3-120, Omega Engineering, Swedesboro, NJ, USA) in half-bridge configurations were used as bending sensors and were placed at dorsal-base, dorsal-tip, and ventral locations and were affixed to the plastic fin rays inside the webbing (Figure 45b).

5.3.3.2 Volterra series MISO models

Multiple-input-single-output (MISO) convolution-based models were selected to map the sensory data inputs to the propulsive force outputs, with a weighted Volterra series as the underlying model. These models were selected because they allow for time delays between sensory measurements and forces, their model weights allow for assessment of the contribution of individual sensors and their delays, and linear MISO models have been successful in past studies at predicting propulsive forces under limited conditions.

The Volterra series for MISO models is a weighted series of time-shifted inputs whose weights are the model coefficients that are obtained through regression or learning. Volterra series with solely 1st, solely 2nd, and both 1st & 2nd order kernels were used in this study and are described herein. The 1st order Volterra series terms are given by

$$y^{(1)}(t) = \sum_{i=1}^m \left\{ \sum_{\tau=0}^{T-1} h_i^{(1)}(\tau) u_i(t-\tau) \right\} \quad (50)$$

such that there are m sensory signal inputs and T lag values in the discrete time convolution. Each sensory input u_i has its own kernel h_i such that each lagged value of the input is weighted. The 2nd-order Volterra series terms are given by

$$y^{(2)}(t) = \sum_{i=1}^m \left\{ \sum_{\tau_1=0}^{T-1} \sum_{\tau_2=0}^{T-1} h_{ii}^{(2)}(\tau_1, \tau_2) u_i(t-\tau_1) u_i(t-\tau_2) + \sum_{j=i+1}^m \sum_{\tau_1=0}^{T-1} \sum_{\tau_2=0}^{T-1} h_{ij}^{(2)}(\tau_1, \tau_2) u_i(t-\tau_1) u_j(t-\tau_2) \right\} \quad (51)$$

where there are self-terms which involve the same sensory input u_i , and cross-terms that involve different sensory inputs u_i and u_j .

Let $y(t)$ be the measured output (here the propulsive force) at time t such that:

$$\begin{aligned}
y(t) &= c + y^{(1)}(t) + y^{(2)}(t) + w(t) \\
\bar{y} &= \mathbf{X}\bar{h} + \bar{w}
\end{aligned} \tag{52}$$

where c is a constant, and $w(t)$ accounts for the noise of the system and any additional input effects, the horizontal bars signify column vectors, and h is a weighting vector applied to \mathbf{X} . \mathbf{X} is the following block-structured matrix (53):

$$\begin{aligned}
\mathbf{X} &= [\mathbf{X}_\alpha \mid \mathbf{X}_\beta \mid \mathbf{X}_\gamma] \\
\mathbf{X}_\alpha &= [\mathbf{X}_1 \quad \mathbf{X}_2 \quad \cdots \quad \mathbf{X}_N] \\
\mathbf{X}_\beta &= [\mathbf{X}_{1,1} \quad \mathbf{X}_{2,2} \quad \cdots \quad \mathbf{X}_{N,N}] \\
\mathbf{X}_\gamma &= [\mathbf{X}_{1,2} \quad \cdots \quad \mathbf{X}_{1,N} \quad \mathbf{X}_{2,3} \quad \cdots \quad \mathbf{X}_{2,N} \quad \cdots \quad \mathbf{X}_{N-1,N}]
\end{aligned} \tag{53}$$

\mathbf{X} is composed of three major component matrices: \mathbf{X}_α , \mathbf{X}_β , and \mathbf{X}_γ . \mathbf{X}_α represents the first-order Volterra series terms. \mathbf{X}_β represents the *same* terms of the second-order Volterra series where sensor values are squared, and \mathbf{X}_γ represents the *cross* terms of the second-order Volterra series where measurements from different sensors are multiplied (see [129]).

$$\mathbf{X}_i = \begin{bmatrix} x_i(1) & 0 & \cdots & 0 \\ x_i(2) & x_i(1) & \cdots & 0 \\ \vdots & \vdots & \ddots & \vdots \\ x_i(T) & x_i(T-1) & \cdots & x_i(T-M+1) \end{bmatrix} \tag{54}$$

$$\mathbf{X}_{i,j} = \mathbf{X}_i^T \mathbf{X}_j \tag{55}$$

Using these block structured matrices, models are formed by calculating the proper weights h that produce the desired force output y in (52). A pseudo-inverse method was used:

$$\begin{aligned}
\bar{y} &= \mathbf{X}\bar{h} \\
\mathbf{X}^T \bar{y} &= \mathbf{X}^T \mathbf{X} \bar{h} \\
\bar{h} &= (\mathbf{X}^T \mathbf{X})^{-1} \mathbf{X}^T \bar{y}
\end{aligned} \tag{56}$$

5.3.3.3 Assessing output contribution by SVD

Because of the significant correlations of the input sensory data, the block structured matrices \mathbf{X} of the inputs can result in ill-conditioned inversions and lead to poor performance in estimation and prediction. A method of assessing the contribution of individual inputs to the output signal was used to reduce the dimensionality of the input matrix prior to calculating the regression weights. The method is described in [130] and was applied to a case study of neural inputs and a motor output, improving the conditioning of the regression matrix \mathbf{X} in order to better estimate desired outputs. This method was originally applied with first-order Volterra series terms but has been extended in this work to a second-order Volterra series for nonlinear models with the above block-structured matrix \mathbf{X} .

5.3.3.4 Performance metrics

Two performance metrics were used to compare linear and nonlinear models in this study. Percent of variance accounted for ($\%VAF$) is an absolute performance metric that approaches 100% as the variance of the estimate approaches the variance of the measured output, and decreases as the variance of the estimate decreases relative to the variance of the measured output. Negative $\%VAF$ can occur if \mathbf{X} is ill-conditioned and the variance of the estimate is greater than the variance of the measured output [88]. $\%VAF$ is calculated by the following formula:

$$\%VAF(y, \hat{y}) = \left[1 - \frac{\sum_k (\hat{y}_k - y_k)^2}{\sum_k (y_k - \mu_y)^2} \right] \times 100 \quad (57)$$

where μ_y is the mean value of the true output y , and \hat{y}_k is the estimate of the output at discrete time k .

Minimum description length (*MDL*) is a cost functional that increases as: mean squared error increases, sum of squared error increases, and as the number of model parameters increases (c.f. 4.7.4). Thus models can have a high *MDL* cost if they perform with significant error or require significant numbers of parameters, but models will have a low *MDL* cost if they have low numbers of parameters and low error. *MDL* cost is calculated by the following:

$$MDL(M, N, y, \hat{y}) = \left[1 + \frac{M \log(N)}{N} \right] \sum_{t=1}^N [y(t) - \hat{y}(t, M)]^2 \quad (58)$$

where M is the number of model parameters (i.e. the length of \bar{h}), N is the sample length, y is the true output value, and \hat{y} is the estimate or prediction of the output value [129].

5.3.3.5 Analysis

Optimal model parameters were identified by developing models with a fixed set of parameters and validating them against unseen datasets. To predict propulsive forces from sensory data, sensory data were first sorted into the appropriate block structured matrix X . The output contribution (\mathcal{Y}_k) of individual matrix columns was computed by the methods in [16] and the model was expanded based on the D most significant columns according to output contribution. D was increased for each case until subsequent

increases resulted in a performance change of less than 1% VAF. After the most significant sensory data columns were selected, linear regression was performed using the pseudoinverse of the matrix formed by the most significant columns (56) [9]. The linear regression generated scalar weights for each matrix column. These weights were stored and could be used to predict propulsive forces using sensory data from unseen trial conditions. Individual models were developed for thrust force prediction, lateral force prediction, and force magnitude prediction for comparison of performance trends across different components of force.

Nonlinear models were evaluated for force prediction with all three fin gaits and both outstroke (OUT) and instroke (IN) stroke phases. Multiple trials' sensory and force data were concatenated to form training sets that were representative of the gamut of input-output conditions for the robotic fin. The performance of linear and nonlinear models were compared across changes in gait, stroke phase, flapping frequency, and flexural rigidity.

Analyses were executed to determine consistently good sensor placements regardless of the model structure, so best placement locations were analyzed as forces were predicted with both linear and nonlinear models. Optimal sensor placement was studied as the fin gaits and stroke phase were changed. These analyses were conducted to address the following questions: Where should sensors be placed for optimal performance? Are there consistently optimal locations regardless of the model structure?

Analyses were conducted to determine consistently good sensor modalities (i.e. pressure vs bending) for force prediction, regardless of model structure. Prior work identified that linear models using bending sensors performed better than those using

pressure sensors, but these results had not been validated for nonlinear models or evaluated using components of the propulsive force (i.e. thrust and lateral forces). The performance of models formed from individual modalities was studied across gaits, force components, and stroke phases.

There are situations where sensory resources may be limited (e.g. due to implementation cost) and so the optimal subsets of sensors were determined as the number of available sensors was varied. As in prior work [88], optimal subsets were determined by forming and evaluating models with data from every possible subset of sensors (9 sensors = 511 combinations). The results were sorted by performance and best subsets were selected for each sensor count (e.g. the best subset of 3 sensors based on %*VAF*). This process was repeated for models of thrust force, lateral force, and force magnitudes. Large datasets were formed using data from every fin stiffness, fin speed, stroke phase, and gait into to ensure generality of results.

5.3.4 Results

The results are divided into three major sections. First, results are given comparing the performance and implementation costs of linear and nonlinear models (A, Figure 46- Figure 48). Second, given a chosen model, the best sensor placement locations are presented for both linear and nonlinear models (B, Figure 49). Performance and cost are discussed for models formed with a single sensor (Figure 50) and for optimal subsets of sensors (Figure 51). Finally, the performance of models formed with bending sensors is compared to that of models formed with pressure sensors for both linear and nonlinear models (C, Figure 49).

5.3.4.1 *Optimal nonlinear prediction*

A single nonlinear model (1st & 2nd order kernel) could be used to predict forces well across all gait changes without changing parameters, whereas linear (1st order kernel) models performed poorly in this case (Figure 46). Nonlinear (1st & 2nd order kernel) models performed well at predicting both thrust and lateral components of the propulsive force as well as force magnitudes, even with a single model for all gaits and stroke phases (thrust: $61.2 \pm 1.5\%$ VAF, lateral: $79.7 \pm 1.7\%$ VAF, magnitude: $68.2 \pm 3.2\%$ VAF). Linear models performed poorly at predicting thrust force and force magnitudes. The largest errors in force occurred during large peaks of thrust during steady swimming and maneuver gaits. Thrust forces were poorly predicted ($21.6 \pm 2.4\%$ VAF) and force magnitudes were also poorly predicted ($23.0 \pm 5.9\%$ VAF) by models with 1st order kernels. However, lateral forces were typically well predicted by linear models ($73.9 \pm 1.5\%$ VAF), with only slightly lower performance than nonlinear models.

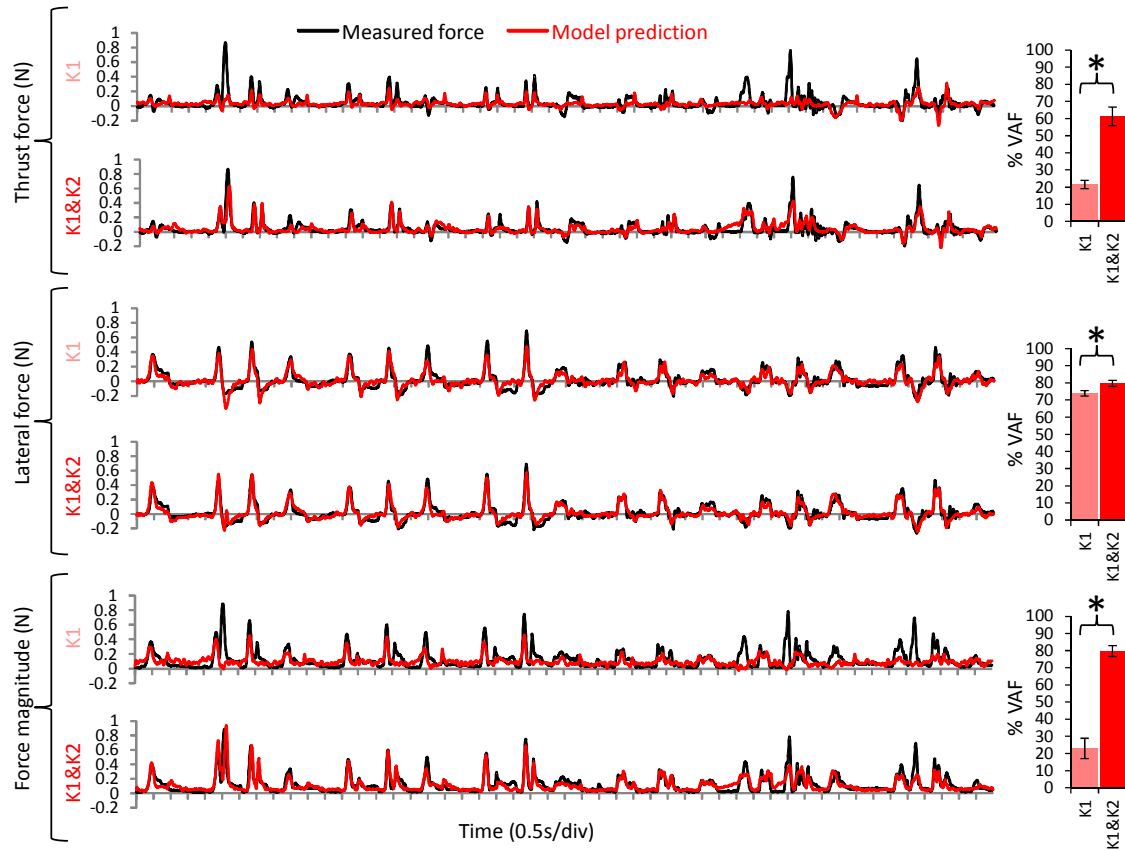


Figure 46. Comparison of model performance with linear (K1) and nonlinear (K1&K2) kernels for prediction of full stroke forces across multiple swimming gaits. Representative time series force data and model predictions are shown for thrust forces, lateral forces, and force magnitudes. Percent of variance accounted for (%VAF) is shown with statistics for each case. Error bars show one standard deviation from the sample mean (N=5 trials) and asterisks indicate significant differences in %VAF ($P < 0.005$).

Models with kernels of both 1st & 2nd order generally outperformed models that used only 1st or 2nd order kernels. When a 1st & 2nd order kernel was used, thrust force and force magnitude were well predicted (60-70%VAF), and lateral force was very well predicted (75-80%VAF). Using only a 1st order kernel, thrust force and force magnitude were poorly predicted (25-40%VAF typical). When only a 2nd order kernel was used, thrust force was poorly predicted (10-40%VAF range), but both lateral force and force magnitude were well predicted. Significant differences in performance (measured by %VAF differences, with $P < 0.005$) were found between linear and nonlinear models. The

largest difference in performance was for the prediction of force magnitudes (Figure 46), where models with 1st order kernels performed poorly and models with 1st & 2nd order kernels performed very well, and the differences were highly significant ($P < 10^{-6}$). Similarly large differences were found for predictions of thrust forces ($P < 10^{-5}$), and less significant differences were found for predictions of lateral forces ($P < 0.005$).

Nonlinear models were more (MDL) cost-effective than linear models, despite having significantly more model parameters. MDL cost was lower for models with kernels of both 1st & 2nd order than those with kernels of only 1st or only 2nd order (Figure 49, Figure 51). When prediction was done across changes to stroke phase (i.e. the fin moves from outstroke to instroke while gait is fixed), a model with a 1st & 2nd order kernel always had the lowest MDL cost regardless of the force component being predicted (Figure 47). When prediction was done across gait changes (e.g. switching from steady swimming to ventral steady swimming without changing the model), the best choice of kernel varied. The 1st & 2nd order kernel had the lowest MDL cost for thrust force prediction, but cost was comparable to each of the 1st and 2nd order kernels for lateral and force magnitude prediction.

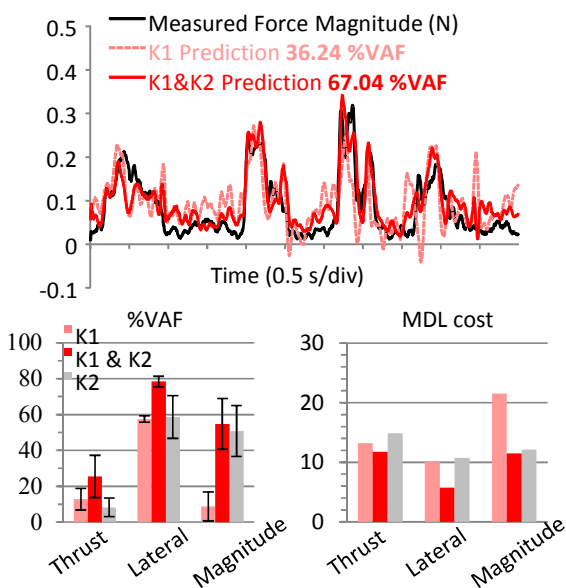


Figure 47. Prediction of propulsive forces across outstroke and instroke. Performance is shown for time-series data, percent of variance accounted for (%VAF), and MDL cost. Data shown are representative of general trends. Data were filtered at 10Hz.

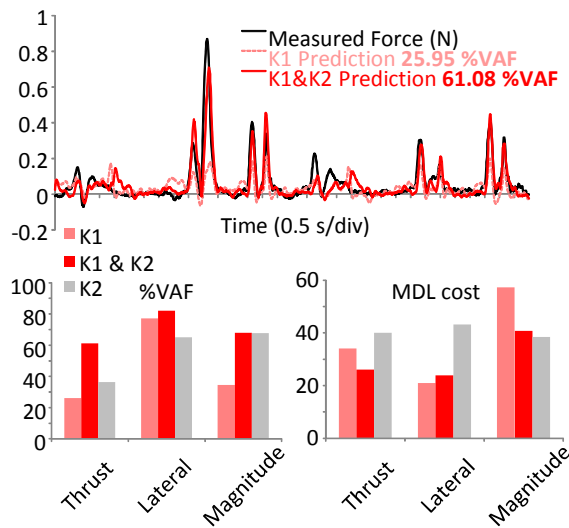


Figure 48. Prediction of propulsive forces across multiple swimming gaits with linear (K1) and nonlinear (K1&K2, K2) models. The performance of a model trained on multiple gaits, tested on unseen trial data from similar swimming gaits. Performance is shown for time-series data (top), percent of variance accounted for (%VAF, bottom left), and MDL cost (bottom right). Data shown are representative of general trends. Data were filtered at 10Hz for clarity.

Using nonlinear models (both 1st & 2nd order kernels), good predictions were achieved with significantly lower numbers of sensors than with models with only 1st or 2nd order kernels. For thrust force prediction, forces were somewhat well predicted with only two sensors and a nonlinear model (B,C; 51.4%VAF; Figure 51), but were poorly predicted with a linear model (B,C; 13.1%VAF) using the same number of sensors. MDL cost was significantly lower for models with 1st & 2nd order kernels than for models with 1st order kernels in this case, which meant that the cost of adding sensors did not significantly improve performance of the models (Figure 51). Even with all nine sensors for thrust force prediction, linear models were unable to achieve the performance of a nonlinear model with just one sensor (linear, 9 sensors: 20.9%VAF; nonlinear, 1 sensor: 29.9%VAF; Figure 49, Figure 51). For lateral force prediction, forces were well predicted with only two sensors' data in a nonlinear model (B,C; 70.8%VAF), and less well predicted when a linear model was used (B,Bo; 60.5%VAF). Using data from all nine sensors for lateral force prediction, linear models were unable to achieve the performance of a nonlinear model with just four sensors by comparison (linear: 75.7%VAF; nonlinear, 4 sensors: 77.3%VAF).

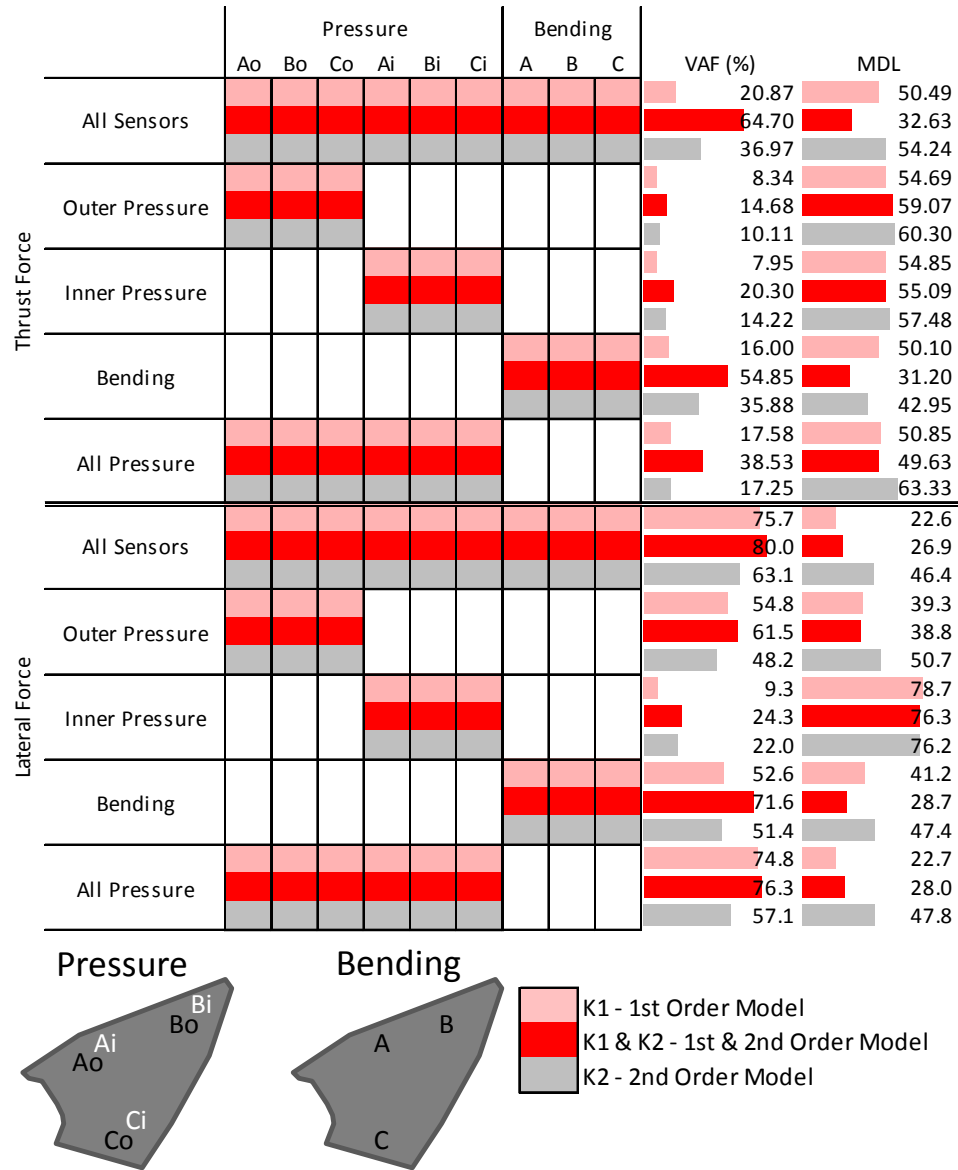


Figure 49. Comparison of prediction performance between models formed with pressure versus bending sensory data. Best performance (%VAF, MDL) was observed with a K1&K2 model using bending sensors, regardless of forces and fin conditions. Performance was compared between models formed from outer pressure data, inner pressure data, bending data, and all pressure data. Performance metrics were computed for all three model structures (K1,K1&K2,K2). Thrust force prediction and lateral force prediction are shown. Trial datasets were randomly selected for training and prediction.

5.3.4.2 Optimal sensor placement locations

The performance of models formed with individual sensors varied significantly, but the models that used data from dorsal-tip (Bo,Bi,B) sensors typically had the best

performance, and this effect was stronger for bending sensors than pressure sensors (Figure 50). Among models formed with bending sensors (A,B,C), best performance was achieved using models formed from dorsal-tip bending data (B; 26-56%VAF). Among models formed with outer pressure sensors (Ao,Bo,Co), ventral (Co) data yielded the best performance (10-22%VAF), with comparable performance from models with dorsal-tip sensors (Bo; 12-19%VAF), and low performance from models with dorsal-base sensors (Ao; 6-13%VAF). Among models formed with inner pressure sensor data (Ai,Bi,Ci), performance was poor (0.3-10%VAF), with best performance from models formed with ventral pressures (Ci; 5-10%VAF). However, a single sensor was usually inadequate to predict forces well regardless of model structure (0-56%VAF range).

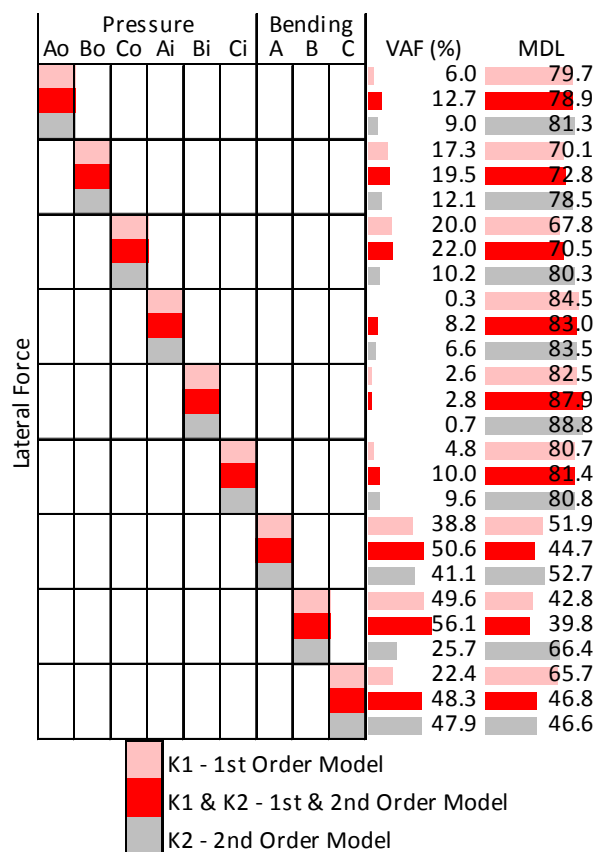


Figure 50. Force prediction performance compared with data from individual sensors. Performance was compared between models formed from each of the individual sensors (Ao,...,C). Performance metrics were computed for all three model structures (K1,K1&K2,K2). Lateral force prediction is shown as representative of general trends.

The sensor that contributed most to MISO model performance was the dorsal-tip bending sensor (B). Of models formed with individual sensors' data, a model formed using B performed the best (56%VAF for lateral force, 31%VAF for thrust force, and 40%VAF for force magnitude prediction with nonlinear kernels). The optimal subset of sensors always included the dorsal-tip bending sensor (B) when a nonlinear model was used (Figure 51), and it was often selected as the best sensor for linear models. The sensors that contributed least to model performance were the inner pressure sensors (Ai,Bi,Ci) which had a poor range of performance individually (failure-28%VAF) and as a full group performed just as poorly (Figure 5; 8-24%VAF). These sensors were

uncommon in optimal subsets of sensors (Figure 7) and did not typically increase performance when added to the sensor pool.

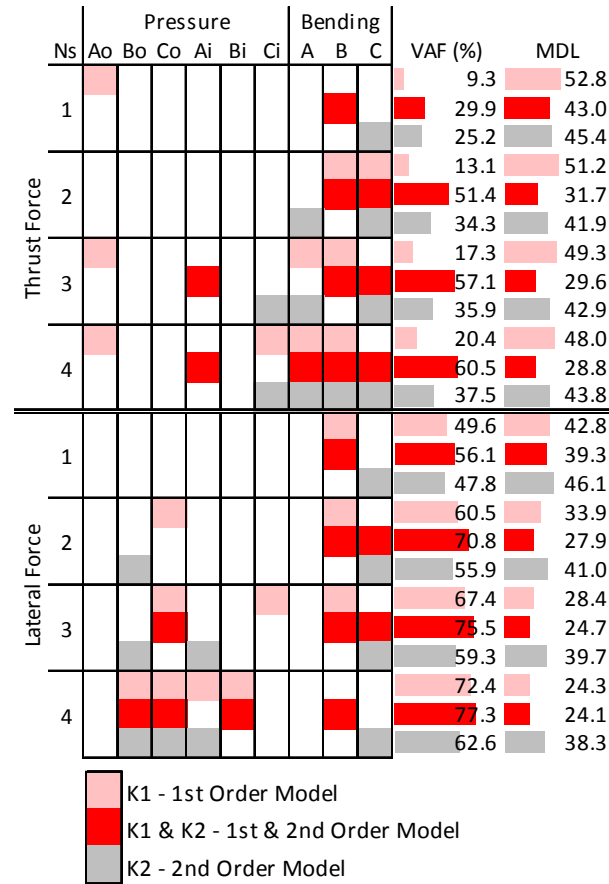


Figure 51. Optimal subsets of sensors as the number of sensors (Ns) is varied. For example, if thrust forces are predicted, only 2 sensors are used, and a K1&K2 kernel is used, then the optimal sensor choice is (B,C), resulting in 51.39%VAF and an MDL cost of 31.71. Optimal subsets were chosen based on %VAF and were computed for all three model types (K1, K1&K2, K2). Thrust force and lateral force prediction results are shown for predictions across both gait and stroke phase.

5.3.4.3 Optimal sensor modalities

Nonlinear models that used exclusively bending data performed better than models that used exclusively pressure data, which was consistent with prior results for linear models [88]. Regardless of the kernel used, models formed with *only* outer pressure sensors

(Ao,Bo,Co) and models formed with *only* inner pressure sensors (Ai,Bi,Ci) performed poorly at prediction of forces (5-40%*VAF* typical). In some cases, models that used only pressure sensors failed to predict the propulsive force (%*VAF*<0). Even when all six pressure sensors' data were used to form the model, failures occurred and performance was less than the performance of models formed with *only* bending sensory data. In some cases, the use of three bending sensors' data to form the model resulted in lower *MDL* cost than using all nine sensors' data to form the model (e.g. thrust force).

Models that used bending sensors generally outperformed those that used pressure sensors, but pressure sensors were specifically useful for predicting lateral forces. In optimal subsets of sensors for force prediction, high performing subsets often included outer pressure sensors for linear and nonlinear models. For instance, the best subsets of sensors for predicting lateral forces often included the Bo and Co sensors with significant improvements to performance (increases of 3-7%*VAF*) and lower *MDL* cost. Including the inner pressure sensors' data (i.e. Ai, Bi, Ci) in a model did not significantly improve performance of force prediction for any of the components.

Prediction of thrust forces and lateral forces required different sensor pools for good performance. Thrust forces could be well predicted using only bending sensors in many cases and were poorly predicted using only pressure sensors. Thrust forces were very poorly predicted using outer pressure sensors' data (8-15%*VAF*) and inner pressure sensors (8-20%*VAF*), but were somewhat well predicted using bending sensors' data (16-55%*VAF*). Even using all six pressure sensors' data resulted in performance worse than using only three bending sensors (38.5% versus 54.8%*VAF*, respectively). Lateral forces were well predicted with bending sensors (53-72%*VAF*) but performance was best with

either all six pressure sensors (57-76%*VAF*) or a combination of pressure and bending sensors (63-80%*VAF*).

5.3.5 Discussion and Conclusion

Nonlinear Volterra series MISO models predicted the propulsive forces of a biorobotic pectoral fin very well, capturing features of both thrust and lateral force components and significantly outperforming linear models. Nonlinear models could be used to predict forces across changes to gait and stroke phase, whereas linear models were gait- and stroke-specific. Regardless of the force components being predicted, nonlinear models typically had a lower *MDL* cost and higher %*VAF* performance than linear models. Nonlinear models achieved the same performance of linear models while using data from fewer sensors, which could be exploited to reduce the manufacturing, financial, and monitoring costs of sensory instrumentation. Additionally, the use of the output contribution method [130] to reduce the dimensionality of the input matrix was successful in keeping the *MDL* cost low for both linear and nonlinear models.

Some sensor sampling locations were better than others, though the best practice was to sample optimally from several locations. Models formed using sensory data from the dorsal-tip performed best (B,Bo,Bi locations), which was consistent with previous findings and knowledge of pectoral fins. The best sensor to sample from was usually on the dorsal tip, regardless of model structure. If only a few sensors are available, placing them in this region will improve performance. The dorsal tip is responsible for the majority of thrust force production in sunfish pectoral fins [4], and the thrust component of force is typically large during steady swimming motions [3]. However, sampling from

a single sensor location was rarely a good strategy for force prediction, as it was necessary to sample from at least two locations for adequate prediction performance.

Selecting the best sensory modality was dependent on both: (a) the force component being predicted and (b) whether the model used was linear or nonlinear. Distributed bending data was more useful than distributed pressure data for obtaining accurate predictions of propulsive force, though pressure data was useful for modeling lateral forces. Prior to the introduction of nonlinear models, thrust forces were very poorly predicted [15], and including the nonlinear components of bending data improved these predictions significantly. However, linear models that used only pressure data predicted lateral forces well, often better than nonlinear models. Thus, careful consideration of the sensor modality, force component, and model structure was important for achieving accurate force prediction. For example, to predict both thrust and lateral forces well it would be prudent to use a distribution of outer pressure sensors (Bo,Co) and the leading edge bending sensor (B). Simpler models, such as the 1st or 2nd order Volterra kernels, may require more sensors and multiple modalities for good prediction. However, the use of more complex models (e.g. 1st & 2nd order Volterra series) allowed for the use of only bending sensory data for predictions.

Distributed sensing paired with nonlinear Volterra series MISO models provides a method for predicting the forces created by flexible robotic fins with complex kinematics and multiple degrees of freedom. This could ultimately be used to predict forces produced by specific regions of a fin, which could provide local feedback on force production. Force control could be achieved by updating the kinematics of portions of the fin within the fin beat, as sunfish do during hovering [23]. Closed loop control of force

can be done to correct for changes to the fin (damage) or changes in the environment. Using distributed, heterogeneous sensing and nonlinear MISO models brings engineers closer to predicting and controlling the propulsive forces of complex, flexible fins during unsteady maneuvers.

Chapter 6. Biologically-inspired control framework for fin-intrinsic sensing

6.1 Chapter summary

Prior chapters examined the use of fin intrinsic sensation for prediction of propulsive forces and for understanding underwater touch using robotic fins.

The objective of the work presented in this chapter is to propose a biologically-inspired control framework in which to utilize the results of force prediction and of classifying contact with obstacles.

The bluegill sunfish (*Lepomis macrochirus*) serves as the biological inspiration for much of this work, and the control strategies it uses during hovering to produce forces serve directly to inform the proposed control framework. The kinematics of hovering animals have been studied from a steady swimming perspective, where stereotypical motions are analyzed and dominant forces are identified, but hovering in sunfish is a highly dynamic behavior where kinematics change from stroke to stroke and often change within a stroke. The rapid changes to hovering kinematics within a stroke suggest that the fin kinematics are under sensory-mediated control, and therefore hovering is an important fish behavior to study in the context of fin-intrinsic sensation and its uses. A conference paper reprint, from *IEEE International Conference on Intelligent Robots and Systems (IROS) 2012*, is included in the chapter to detail several qualitative aspects of sunfish hovering that contribute to the proposed control framework.

Since the parameter space of a multiple degree-of-freedom (DOF), flexible fin is very large and has many possible kinematic patterns, work has been done to *evolve* kinematics to optimize a given force performance criterion. In this way, new gaits can be learned online to better control propulsive forces by switching. This chapter includes a

reprint of that work, published in the *IEEE International Conference on Intelligent Robots and Systems (IROS) 2013*.

Drawing from the elements of force prediction, underwater touch, sunfish hovering, and evolving gaits, a detailed control framework is proposed for controlling the propulsive forces of an underwater vehicle driven by multi-DOF, flexible, robotic fins. This work is in revision for submission to a special issue of the *Bioinspiration and Biomimetics* Journal.

6.2 Paper 5: Hover kinematics and distributed pressure sensing for force control of biorobotic fins

6.2.1 Abstract

A comprehensive understanding of the ways in which fish create and control forces is fundamental to engineering underwater vehicles that maneuver with the agility of fish. In this study the sunfish is selected as a biological model from which to understand pectoral fin motions and forces during hover. The kinematic patterns of the biological fin were identified and implemented on a biorobotic model of the fin. The effects of fin patterns and mechanical properties on force were evaluated. Pressure was measured at multiple points on the fin's surface and assessed for use in the closed loop control of fin force. The study revealed that a wide range of motions are used during hover, and that forces are significantly different from those found previously for steady swimming. However as fin speeds increase, the fin's dynamic motions, and the magnitude and direction of the forces become more similar to those of steady swimming. Collective measures of pressure over the fin's surface exhibited trends that correlated well with fin force, while measures of pressure at individual points reflect force for particular sections of the fin. This suggests strongly that distributed measures of pressure are useful for force prediction and control.

6.2.2 Introduction

Bony fish are extraordinary agile swimmers and can serve as biological models for understanding how hydrodynamic forces are created and controlled with fins. Their agility comes from an ability to control their movements with multiple fins, and this

agility often far exceeds that of engineered underwater vehicles [131]. These fins create forces on the body through repeated kinematic patterns, or gaits. These gaits are used to produce characteristic forces that drive the locomotive behavior of fish (e.g. a steady swimming gait is primarily thrust producing for swimming forward in flow). The bluegill sunfish (*Lepomis macrochirus*) uses its pectoral fins to produce a variety of gaits, such as steady forward swimming, yaw turn maneuvers, and hovering in place. Hover is an interesting gait from a force production standpoint because the sunfish is dynamically unstable; constant force production is necessary to keep the fish center of mass balanced atop the center of buoyancy. Whereas motions such as steady swimming and turning maneuvers rely on a dominant pattern to produce characteristic forces, hover has a wide repertoire of fin motions used to maintain posture dynamically that vary significantly in trajectory, velocity, and direction.

Greater levels of fish agility emerge through the control of properties within a particular gait. Within a particular gait, the fish can modulate forces by actively changing the kinematics and mechanical properties of its fins. By varying mechanical stiffness through co-contraction of muscles, the fin changes the magnitude of the time varying forces. Increasing the velocity of the fin will change the magnitude and direction of forces. Slight changes in trajectory are also observed and likely allow the fish to "fine-tune" the forces produced through a particular cycle. These beat-to-beat differences in fin motions suggest that sensory feedback is used in controlling forces [132]. The wide repertoire of hover motions observed further supports this hypothesis (Figure 52). Neurobiological studies are just beginning to address how this sensory feedback works in aquatic vertebrates. The nature of the feedback (i.e. cell body types, physical phenomena

transduced) is largely unknown, though sensory nerve fibers densely innervate the pectoral fins in regions crucial to the development of forces [20].

To the authors' knowledge, there have been no biological studies that address the kinematics or forces of hovering fish. Pectoral fin use in steady forward swimming [4], varied fin maneuver motions, and escape reflexes [133] have all received kinematic and force analysis through modeling and physical testing. Behavioral biology work has long documented the value of hovering as a means for foraging, hunting, socialization, and nest guarding behaviors [134], but the role of specific pectoral fin motions to produce hover forces is a novel consideration.

Robotics studies have developed hovering vehicles, and have significantly analyzed forces on engineered hover motions ([135, 136]), but have not implemented a biologically-derived hover motion on a robotic platform with flexible fins. And further, despite neurobiological evidence in aquatic and terrestrial vertebrates, few robotics studies have considered distributed measurements along the limbs and surfaces responsible for propulsion. Biologically derived distributed sensory systems have been considered, notably including an artificial lateral line for measurements of body pressure [137] and electroreceptive sensors to model ghost knifefish sensation [138], but few studies have examined fin-intrinsic sensation on robotic fin models [32].

Previous experiments with a flexible biorobotic model of the sunfish fin have evaluated a steady swimming gait [32] and a yaw turn maneuver [5] and how kinematic and mechanical properties affect force production through these modes [139]. Studies using computational fluid dynamics have also verified the fin mechanisms of force production [4]. Prior work with the biorobotic fin has addressed fin bending as a sensory

measure for estimation of forces, but found that bending alone could not be used to estimate the magnitude of force produced [32].

In this paper, we first present an analysis of the pectoral fin motions used by sunfish during hover. Secondly, we evaluate the forces produced during hover using a biorobotic model of a sunfish pectoral fin. Third, the influence of the fin's kinematics and mechanical properties on these forces is determined. Lastly, distributed measures of pressure over the robotic fin's surface are assessed as a means to predict the time-varying force for closed loop fin control.

6.2.3 *Methods*

6.2.3.1 *Biological hover motions*

Studies of bluegill sunfish hovering were conducted in a 600 L flow tank with a 26cm by 26cm by 80cm working volume, as in previous research [140, 141]. Three synchronized high-speed video cameras (Photron USA, San Diego, CA, USA) were positioned to record simultaneously the fish swimming in the lateral (XY plane), posterior (YZ plane) and ventral (XZ plane) views. Videos of the fish hovering were filmed at 250 frames s⁻¹ with 1024 by 1024 pixel resolution.

Ethogram techniques developed from [142] were employed to classify and organize the fin patterns observed through hover videos. Following the identification of a frequently occurring cycle of hover, video of this fin beat were calibrated in three dimensions using direct linear transformation of a custom 20-point calibration frame and digitized using a program written for MATLAB 7 (MathWorks, Natick, MA, USA) by

Ty Hedrick [143]. Points along the biological fin were fit to the robotic fin base using a least squares regression to fit the three base points of each digitized fin ray to a line segment. These line segments were extended through a center of rotation on the robot. Angles of rotation were calculated for the available robot degrees of freedom and these angles through time formed the trajectories of the programmed hover motion. Individual fin-ray trajectories were fit to eighth-order sinusoidal basis functions that were tuned to capture relevant visual features of the hover motion as determined by ethogram.

6.2.3.2 Biorobotic hover and fin pressure studies

The biorobotic pectoral fin was supported by an air bearing carriage (New Way S301301, New Way Air Bearings, Aston, PA) and fixed against two s-beam load cells (LSB200, FUTEK, Irvine, CA) to measure force in thrust and lateral directions. More details of the setup are described in [32, 144]. The pectoral fin membrane (80% polyester, 20% elastane) was sewn from a 4x scaled pattern of a sunfish pectoral fin. Previous work used this material untreated but this porous material confounds pressure measurements between outer and inner fin faces [33]; therefore the fin was coated with two thin coats of latex paint (Liquid Latex Body Cosmetic, Maximum Impact, Langhorne, PA) and cured for waterproofing between fin faces.

High precision catheter-style pressure sensors (SPR-524, Millar Instruments, Houston, TX) were placed on the fin at areas with high sensory innervation in the sunfish (as in [20]). These sensors were used to measure pressure on the inner and outer faces of the fin along the dorsal and ventral leading edges. The sensors were oriented orthogonally to the fin face, and affixed to the webbing using the aforementioned latex paint.

To evaluate the force production of hover and to determine if on-fin pressure measurements are predictive of the magnitude of forces through varied swimming conditions, the pectoral fin was programmed to execute hover trajectories with full factorial experiments varying fin ray stiffness (200,400,600,800,1000x) and fin beat period ($T = 4.00, 2.00, 1.54, 0.77, 0.62$ s) as on-fin pressure data were taken with 8 pressure sensors at the dorsal and ventral leading edges of the fin. Sensors were oriented on inner (facing body) and outer (facing water) faces, and at locations proximal and distal to the fin base. Force, sensor, and position data were taken at 100Hz using real-time data acquisition software programmed in LabVIEW and compiled on a dedicated hardware controller (LabVIEW 2010 and PXI-8106, National Instruments, Austin, TX).

6.2.4 Results

6.2.4.1 Biological hover motions

The analysis of fin motions revealed that sunfish use a range of kinematic patterns during hover. Certain motion patterns occur much more frequently than others, but unlike the repeated gait used during steady swimming [17], the hover gait cannot be characterized as a single motion program. Instead, the ethogram analysis characterized pectoral fin motions during hover into twelve motion patterns: six for the fin's outstroke from the body, two for the fin's instroke to the body, and four for the transition from outstroke to instroke (Figure 52).

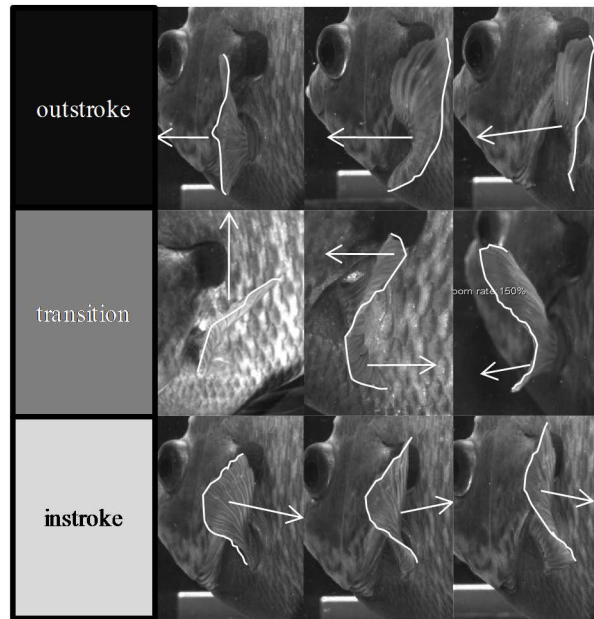


Figure 52. Some of the diverse fin motions associated with hover, classified as outstroke (TOP), transitional (MIDDLE), and instroke (BOTTOM) features. Each column represents an observed fin motion from top to bottom. E.g. Column one shows a “flat plate” outstroke with little temporal lag between fin segments, a “upward push” as the transition feature, and a “lift and drop” instroke where the fin rotates downward to meet the body.

Six characteristic motion patterns were identified for the outstroke of the fin from the body, three of which accounted for 71% of the outstroke motions analyzed. The most common motion pattern ($P = 25\%$) was an asymmetric cupping of the fin about its centerline (from proximal root to distal end) with the cupping led by the fin’s ventral edge (ventral led cupping, Figure 53). The second characteristic pattern ($P = 23\%$) was a symmetric cupping motion (cupping), which was led approximately equally by the dorsal-and ventral-most fin rays. In both the “cupping” and the “ventral led cupping” patterns, the cupped shape of the fin extended from the fin’s proximal root to the fin’s distal edge. These two cupping patterns are similar to the cupping and sweep motion that dominates the pectoral fin’s motion during steady swimming [17]. The third most common outstroke pattern ($P=21\%$, cupping with flat plate) was defined by a more

moderate cupping of the fin at its base with a flattening of the fin towards its distal edge. There was almost no phase difference between the fin rays at their distal ends and this resulted in the fin appearing flat as it moved through the water. Three additional motion patterns were observed less frequently. These were descriptively named “dorsal lead” ($P = 10\%$), “flat plate” ($P = 10\%$), and “half stroke” ($P = 9\%$).

Instroke motions were characterized by two patterns. The most frequent ($P = 83\%$) was a motion where the fin moved as a flat plate, but did not follow a straight trajectory back to the body. The fin moved toward the body and dorsally during the first half of the instroke, and toward the body and ventrally during the second half of the instroke (flat plate lift and drop, Figure 53). Much less frequent ($P = 17\%$) was an instroke pattern that was led by the dorsal-most fin ray and that had linearly increasing phase lag between subsequent fin rays.

Transition motions were short duration movements that allowed the fin to transition from the outstroke to the instroke pattern. These motions usually included either a sudden deceleration or change in direction of groups of fin ray. Most common ($P = 55\%$) was an “s-undulation” (Fig. 1)) of the rays where the ventral half of the fin changed direction rapidly and the dorsal segment moved toward the midline and before changing direction, inward, producing an “S” shape. Three more observed transition patterns occurred much less frequently than the “s-undulation” These were descriptively named “inversion” ($P = 15\%$), “spread” ($P = 15\%$), and “upward flap” ($P = 15\%$, Figure 52).

6.2.4.2 *Biorobotic hover fin motions*

The biorobotic fin was programmed to execute the “ventral led cupping” pattern for its outstroke, the “flat plate lift and drop” for its instroke, and no transition between the

outstroke and instroke (Figure 53). This motion program represented the most frequent pattern exhibited by the sunfish during hover. The robotic pectoral fin captures major components of the biological fin's motion when the robot's fin rays were scaled between 200 and 1000 times the flexural rigidity of the biological fin rays. In general, as the fin moved away from the body in the outstroke (Fig. 2; $t = 0.0, 0.4$ s), the ventral region of the fin remained stiff as it led the motion, followed by the dorsal leading edge. The robotic fin motion experienced significant bending at the distal tips of the dorsal leading edge and the overall curvatures were consistent with the sunfish's fin curvatures. As the "ventral led cupping" pattern continued, the ventral edge lifted up toward the dorsal leading edge to bring the distal fin tips closer together. Through this time period, the robotic fin did not have as much dorsal movement as the biological fin in the medial rays. This was due to having only a single degree of freedom in medial fin rays as compared to two degrees of freedom in ventral and dorsal rays.

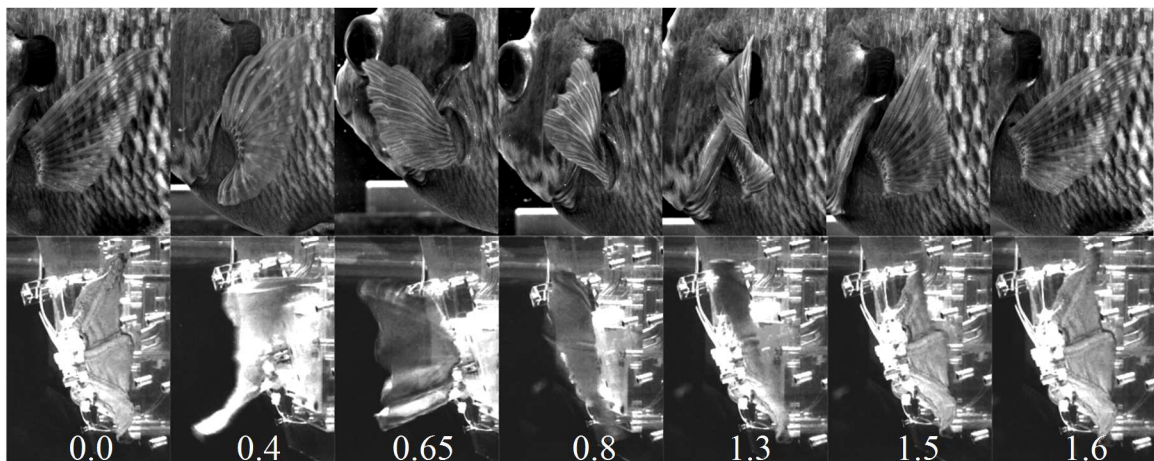


Figure 53. Sunfish (TOP) and biorobotic fin (BOTTOM) executing the dominant hover motion of "Ventral led cupping" outstroke to "Flat Plate Lift and Drop" instroke. Robotic fin trajectories were derived by point and velocity tracking of the fin segments through 3D high speed video and mapping of trajectories to the degrees of freedom on the robot. Robotic trajectories were consistent with sunfish fins through time varying curvature and velocities of fin regions.

Beginning the outstroke "flat plate lift and drop motion", the ventral edge started to drop downward (Fig. 2; $t=0.65, 0.8$ s), leading the motion and creating a flattened appearance along the edge of the fin with some bending at dorsal and medial fin tips. At low flexural rigidities (200x, 400x, 600x), the curvature of the robot visually matched the fish fin curvature but at higher rigidities (800x, 1000x), pockets tended to form in the fin webbing that caused the fin edge to appear wavy rather than flat. As the instroke completed, the ventral edge met the body (Fig. 2; $t=1.3$ s) before the dorsal edge (Figure 53; $t=1.5$ s) in both robot and fish. The motion completed with a very slight rotation of both the dorsal and ventral segments downward. This last part of the motion was more irregular in the robot than the fish, as medial fin rays could not rotate about the appropriate axis to move downward. The final "drop" of the motion was approximated by the downward rotation of the dorsal and ventral fin rays in the robot.

Though some limitations were encountered with the robot's degrees of freedom in the medial fin rays, the motions matched biological motions consistently through biologically relevant rigidities and fin beat periods and thus the programmed hover motion was validated visually as a model of sunfish hovering.

6.2.4.3 *Biorobotic hover forces*

A dominant hover force profile was identified over the conditions tested. During the "cupping with ventral lead" outstroke, the fin produced drag and a strong contra-lateral force (Figure 54A). As the fin transitioned from outstroke to instroke, the magnitude of the force decreased. Through the "flat plate lift and drop" instroke, the fin produced strong thrust and ipsi-lateral force. The average lateral forces were typically balanced

through the fin beat such that the mean lateral force was close to zero. Mean thrust forces through the beat were typically close to zero or slightly positive depending on test conditions. The magnitude, direction, and time varying courses of the force varied as fin beat frequency and mechanical stiffness were modulated. Application of characteristic forces to the fish body would result in a backward and contra-lateral movement through the outstroke, forward and ipsi-lateral movement through the instroke, and a slight net forward movement of the body from the starting position (Figure 54B). When coupled with the wide repertoire of other motions associated with sunfish hovering, this net result of slight forward movement and balanced lateral movement is relevant to hover behaviorally. Further, since hover motions are executed on two pectoral fins and multiple body fins, it's reasonable to assume that the contra-lateral pectoral fin and could employ a fin beat to correct for the thrust force generated.

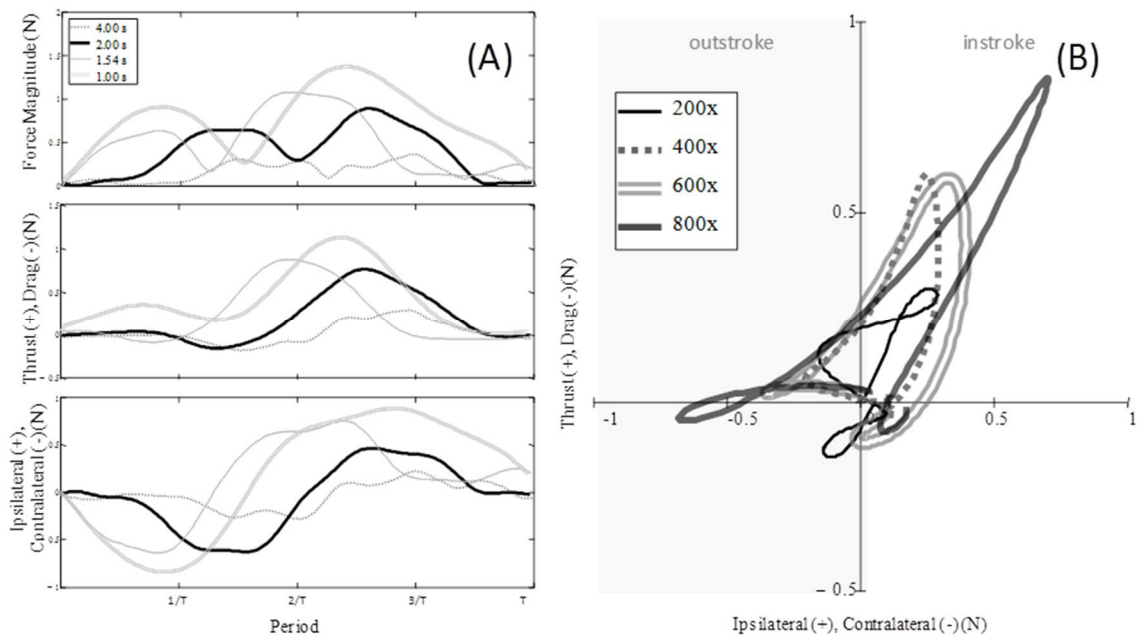


Figure 54. Characteristic forces of hover in the thrust-lateral directions. 2D magnitude of force (A.TOP), thrust force (A.MIDDLE), and lateral force (A.BOTTOM) are graphed as fin beat period is varied from 1-4 s in duration. Forces

representative of hover in the biology would typically be executed over 1 s (highlighted) and slower. Forces shown in the thrust-lateral plane (B) through varied stiffness show the characteristic representative forces through one fin beat (outstroke to instroke) and allow envisioning of body movement in the thrust-lateral plane. Through the outstroke a strong force is mostly directed laterally, whereas the instroke motion creates strong forces in the thrust and lateral directions. Data are representative of a six-cycle average of the forces and were low-pass filtered at 5Hz for clarity.

When fin stiffness was held constant, varying the fin beat period affected the magnitude, direction, and time course of fin forces. For slow and moderate fin speeds ($T=4, 2, 1.54$, and 1 s), the mean magnitude of the 2d forces increased as the duration of the fin beat was reduced and the fin's velocity increased (Figure 55). Effects on forces were also largely dependent on whether the fin was in the outstroke or instroke of the fin beat. At the fastest fin speeds ($T=1.54, 1.00$ s) thrust, not drag, was produced during the outstroke (Fig. 3A). The shift from drag to thrust is not, however, surprising. At faster fin speeds, the fin bends back and directs flow backwards. This behavior is consistent with steady swimming fin beat patterns, which take advantage of the bending to produce thrust during the outstroke. During the instroke, decreasing the period increased the average lateral forces significantly, leading to larger and longer duration ipsi-lateral forces (Figure 54A). Thrust means in the instroke also increased with decreasing beat period. The increase of thrust and contra-lateral components drove up the magnitude forces during the instroke. Changes in the fin beat period also change fish body movements. Increasing the fin beat period leads to more balanced thrust-drag components of the force and would lead to a motion in which the fish starts and ends the beat in the same global position. At shorter beat durations, the motion would tend to move the fish forward and ipsi-laterally as a net result.

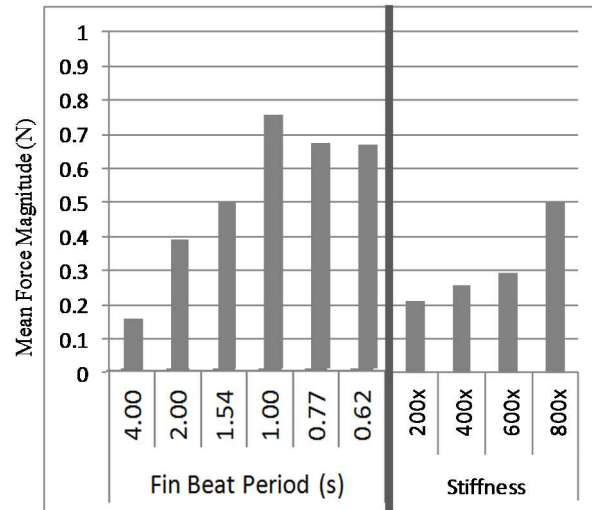


Figure 55. Hover mean 2d forces (thrust-lateral plane) over one fin beat. Mean force magnitudes increase monotonically as fin beat periods are decreased. Increasing stiffness increases mean magnitudes monotonically. For varied frequencies, data are shown from an 800x fin; for varied stiffness, 0.65Hz flapping frequency data were used. These data are representative of general trends through varied frequencies and stiffness.

When fin beat period was held constant, increasing the stiffness tended to increase mean 2d forces, change the direction of thrust forces in the outstroke, and increase mean lateral force magnitudes. As stiffness increased, the strong drag and contra-lateral forces of the outstroke became slight thrust and contra-lateral forces (Figure 54B; 200x, 400x traces). Through the instroke, increasing stiffness tended to increase the mean thrust and contra-lateral forces, without impacting direction. At very high stiffness (Figure 54B; 800x trace) the outstroke contra-lateral and thrust forces were significantly greater than other stiffnesses. Increasing stiffness tended to cause instroke thrust and magnitudes to develop earlier in the period (Figure 54A), but did not affect the rate of development of lateral forces. Applying forces to the fish body as fin stiffness increased would tend to move the fish more laterally during the instroke and outstroke and more forward during the instroke due to increased thrust.

6.2.4.4 *Distributed fin pressure sensing*

The magnitudes of the pressures measured on the fin webbing tracked well with the rise and fall of the 2d fin force. Differences in the magnitude and timing of the pressure signals at distinct points on the fin reflected the development of forces at specific fin regions. Relationships between pressure measures and forces were dependent on the phase of the fin beat period (instroke vs. outstroke) and the side of the fin webbing the pressure sensor was affixed to (outer vs. inner face). During the outstroke, pressure sensors on the outer surface of the fin tracked well with forces, while inner sensors reported predominantly noise. During the instroke, pressure sensors on the inner surface of the fin tracked well with forces, while outer sensors reported predominantly noise. Sensors more proximal to the fin base tended to have lower mean pressure magnitudes than their more distal counterparts. Sensors on the ventral edge of the fin webbing tended to trend consistently with the 2d fin force regardless of instroke or outstroke.

During an outstroke, the fin's ventral edge leads the fin's movement into the water (Figure 53; 0.4s), and correspondingly, pressure is sensed there first (Figure 56F). As the outstroke continues and strong contra-lateral force is created, the pressure measured by the sensors on the ventral edge outer face (Figure 56F) increases with the force. As the outstroke progressed, the dorsal leading edge left the body after the ventral leading edge, causing further increase in contra-lateral forces. Pressures on the outer dorsal leading edge rose significantly (Figure 56D) following the movement of the dorsal leading edge of the fin. Pressure development in this region also lagged ventral edge pressure development just as the dorsal edge lags the ventral edge in the outstroke. The inner dorsal leading edge (Figure 56E) shows an oscillation in the pressure from negative to

positive that corresponds temporally with the thrust force oscillations (Figure 56B). Trends between the thrust force and the inner dorsal leading edge were more visible through slower speeds ($T = 4, 2, 1.54$ s) where more drag was created during the outstroke. As pressure magnitudes on the outer face increased with force production, mean pressure magnitudes for outer face proximal sensors were always less than those of distal sensors (Figure 56D,F).

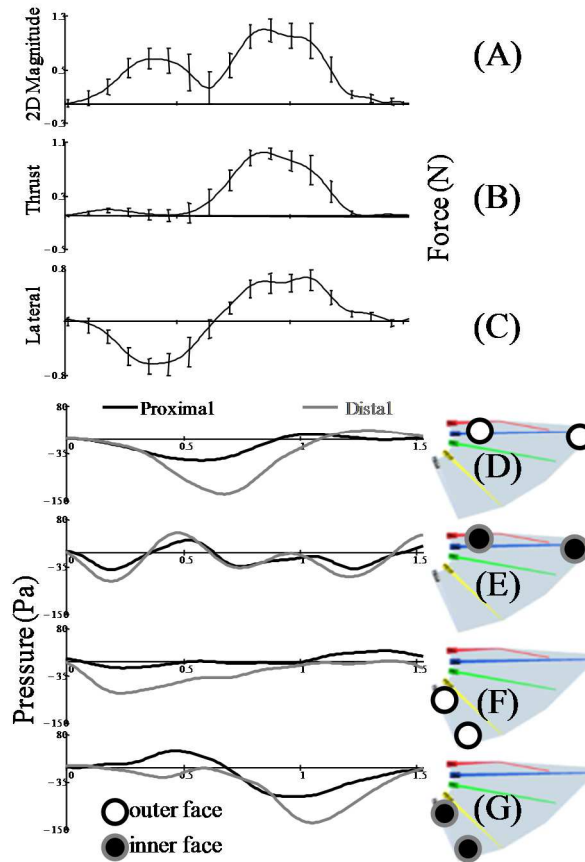


Figure 56. Distributed pressure measurements on the biorobotic fin during hover motion are good estimates of the magnitude and direction of forces during swimming. Trends are representative across testing conditions. Data are grouped in proximal (black) and distal (grey) measures along the dorsal and ventral leading edges on both inner (black circle, grey outline) and outer (white circle, black outline) fin faces. Data shown at fin beat period of $T = 1.54$ s with an 800x fin.

Individual pressure measurements on the inner face of the fin webbing also followed trends in magnitude and direction through the instroke. As the fin was flapped toward the body through the "flat plate lift and drop" instroke, strong ipsi-lateral and thrust forces developed just as the inner ventral leading edge (Figure 56G) pressures increased. As fin completes its instroke, the dorsal edge slightly lags the ventral leading edge (Figure 53; 1.3 s) before coming to rest on the body, and correspondingly, pressures along the inner dorsal leading edge develop as the fin reaches the body. During the instroke, along the inner ventral leading edge pressure sensors, proximal pressure magnitudes consistently increased before distal pressure magnitudes. This trend did not hold for the inner dorsal leading edge pressure measures, as they measured more noise and oscillations. The outer dorsal leading edge pressures (Figure 56E) oscillated at low magnitudes and did not provide clear information about forces. Outer ventral pressures increased as force magnitudes increased (Figure 56F) despite being on the outer face of the fin.

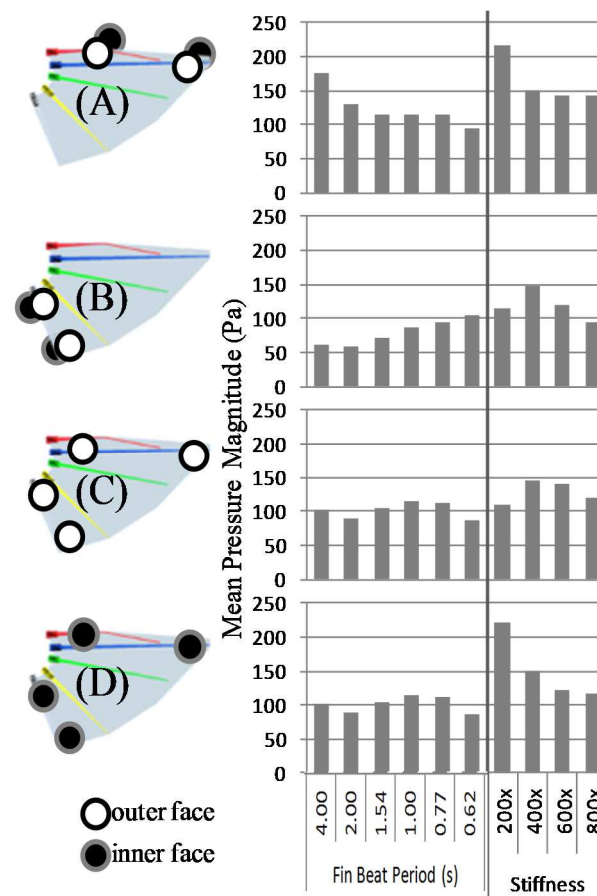


Figure 57. Distributed pressure means through hover with varied fin beat periods and stiffness are useful predictors of two-dimensional force magnitudes. Time varying pressure magnitudes from indicated points were added over the course of one fin beat of hover and then averaged (e.g. (A) shows the mean pressures that result from the sum of all dorsal leading edge pressure signals on the inner and outer faces). Distributed pressures on the ventral leading edge (B) increased monotonically as fin beat period decreased. Pressures on the outer and inner faces of the fin (C), (D) generally increased and pressures on the inner face (D) showed monotonic decrease as fin stiffness increased.

In order to compare larger scale trends in the pressure measurements taken on the fin, time varying pressure signals were added together over the course of a fin beat to see the mean pressure magnitudes over a region of the fin. For instance, to evaluate the pressure along the dorsal leading edge, four time varying pressure signal magnitudes (outer proximal dorsal, outer distal dorsal, inner proximal dorsal, inner distal dorsal) were added together over a cycle and the mean was computed. This mean was used to represent the mean pressure sensed along a region of the fin through a fin beat cycle for

comparison with average force magnitudes. This process was repeated as fin stiffness and fin beat period were varied for full comparison to the mean 2d magnitudes of hover (Figure 57).

Summing and averaging pressure magnitudes over fin regions provided information about the mean 2d forces through the fin beat. In general, decreasing fin beat period and increasing flapping velocity caused consistent decreases in summed and averaged pressure measures as well as mean 2d forces. Additionally, increasing the fin stiffness caused increase mean 2d force magnitudes but decreased summed and averaged pressure magnitudes. However, decreasing fin beat period tends to increase mean 2d forces until $T=1$ s, at which point decreasing the period reduces mean 2d forces. As fin beat period was decreased and the fin velocities increased, mean pressure magnitudes over the ventral leading edge (Figure 57B) increased monotonically with the force magnitudes until $T=1$ s. Mean pressure magnitudes also generally increased as fin beat period increased over the summed outer (Figure 57C) and inner faces (Figure 57D), and at short fin beat periods decreased as forces decreased ($T=0.77, 0.62$ s). Increasing mean 2d forces monotonically by increasing stiffness (Figure 55) caused corresponding monotonic decreases in the summed and mean pressure measures over the dorsal leading edge (Figure 57A), the inner face means (Figure 57D), and overall decrease in ventral leading edge means (Figure 57B) and outer face means (Figure 57C). This was consistent across summed and averaged pressure sensor data over other regions (all sensors, proximal sensors, distal sensors).

6.2.5 Conclusion

Sunfish pectoral fin hovering was analyzed and a repertoire of hover motions were extracted using ethogram techniques. A significant result was the evidence that hover is executed with much more stroke-to-stroke variation than other gaits, and this has significant bearing for engineers of finned robotic systems and aquatic bio-inspired designs that have often relied on consistent, dominant motions to produce forces. Even though the forces of "hover" were considered through varying kinematic and mechanical properties and clear trends were identified, hovering is a much more complex behavior with multiple patterns of outstroke, transition, and instroke that serve to maintain fish body balance and position. These beat-to-beat variations are also highly indicative of a sensory based control that regulates motion patterns within hover. Future work will address the specific roles of these patterns and how they contribute to the fine tuning of forces and closed-loop control of the fish body.

A frequently occurring pattern of sunfish hovering was evaluated on a biorobotic pectoral fin platform for the first time and dominant patterns of forces were identified in the thrust-lateral planes. The developed gait produced consistent forces that can be varied with kinematic and mechanical properties to produce patterns of force consistent with the biological behavior of hovering. This result opens pathways for further research in gait-based closed loop force control of fins and expands the testable repertoire of motions and resulting forces for the pectoral fin robot. Future studies will utilize the hover motion with a multiple fin fish robot and with paired robotic pectoral fins to consider interactions between fins during the complex gait. Further analysis of the motion's effects on body movement will allow for further validation of the hover motion between robot and fish.

Lastly, a distributed fin-intrinsic pressure system was instrumented on a biorobotic pectoral fin and tested through varied fin kinematics and mechanical properties, showing direct relationships to the fin's propulsive forces. Expanding on experiments with single pressure measures [33], this study showed how individual sensors could be used to estimate instantaneous forces on the body and that multiple sensors could be used to estimate mean force magnitudes through an entire cycle. Trends observed showed promising results for the closed-loop control of fins as gaits, mechanical properties, and kinematics vary during swimming. Measuring distributed pressures on force producing surfaces is likely to be a valuable for force estimation in many other types of robotic systems and could be a possible link to understanding fish strategies of sensory input. On fin pressure sensors will be used in future studies with other known gaits (steady swimming, yaw turn maneuver) to more completely evaluate their potential to estimate propulsive forces.

6.3 Paper 6: Application of a micro-genetic algorithm for gait development on a bio-inspired robotic pectoral fin

6.3.1 Abstract

Biologically-inspired robotic (biorobotic) platforms have been successfully adapted for engineering use, but it is difficult to extend these platforms' locomotive gaits to meet optimization goals. The gait spaces of biorobotic platforms can be very large, with multiple local optima and intractable numerical models. Further, the time cost of empirical exploration is often prohibitive. Micro-genetic algorithms have been successful in developing inverse kinematics in simulation, optimizing in spaces with numerous local optima, and working quickly to optimize with low numbers of trials, but have not yet been evaluated for online robotic gait development. To address the problem of engineering gait development in a biorobotic space, a micro-genetic algorithm (μ GA) is evaluated on a biorobotic pectoral fin platform. The μ GA effectively optimizes in the gait space with low time costs, discovering new gaits that optimize thrust force production on the swimming fin. The μ GA also reveals parameter tuning strategies for changing propulsive forces. Overall, the μ GA framework is shown to be effective at online optimization in a large, complex biorobotic gait space.

6.3.2 Introduction

Researchers in biologically-inspired locomotion have successfully used robotic platforms to understand and approximate complex animal gaits [145, 146] [147-149]. Biorobotic platforms have also been adapted to meet specific engineering goals [150-152], but it is difficult to optimize these platforms for force production over their broad gait spaces (the

high dimensional spaces formed by the kinematic parameters). By design, most studies evaluate a small region of the space near the biological behavior of interest. Optimization over the broader gait space could extend the range of behavior possible with bio-inspired platforms.

However, the gait spaces of bio-inspired robots are frequently large and complex due to many actuated degrees of freedom [153], compliant mechanisms[154], and non-linear dynamics, making broad optimization challenging. Optimization can be even more difficult without a numerical system model, making simulation infeasible and local optima hard to identify. Even if a model exists, generalized numerical modeling is often infeasible beyond the gaits and behaviors of interest. These gait spaces are usually too large for empirical evaluation; new gait development strategies must be employed to optimize for engineering goals.

Genetic algorithms, or heuristic approaches that “evolve” a population of solutions based on a fitness function, can successfully optimize in large parameter spaces without a numerical model, but fall short in online implementation. A few studies have evolved behaviors with the use of simulated robot teams [155, 156] and in simulated optimization of gait parameters [157, 158]. However, traditional genetic algorithms can converge too quickly to local optima [159], exploring small regions of the solution space with a depth-first approach. Genetic algorithms can be time-consuming for online implementation in large spaces, where the evaluation of each solution requires an experimental trial. These factors make the basic genetic algorithm a good choice for simulated robotic gait development, but a poor choice for online biorobotic gait development where spaces are complex and fewer general models exist.

Micro-Genetic algorithms (μ GAs) present a framework to optimize in large parameter spaces by identifying and evolving diverse local optima, but they have yet to be evaluated in online robotic platforms. Recent work by Hedrick et al. developed a micro genetic algorithm μ GA for the inverse kinematic problem of hawkmoth flight [160], evolving simulated wing gaits to approximate force trajectories in live moths. Work by Doorly et al. used a general genetic algorithm in online framework to test the evolutionary principle of selection with robots [161]. Theoretical work developing μ GAs demonstrates their effectiveness in finding near-optimal solutions in landscapes with multiple local optima [162]. These developments suggest that μ GAs could be effective for generating optimized gaits for bio-inspired robots, though to the authors' knowledge μ GAs have not been evaluated for this application.

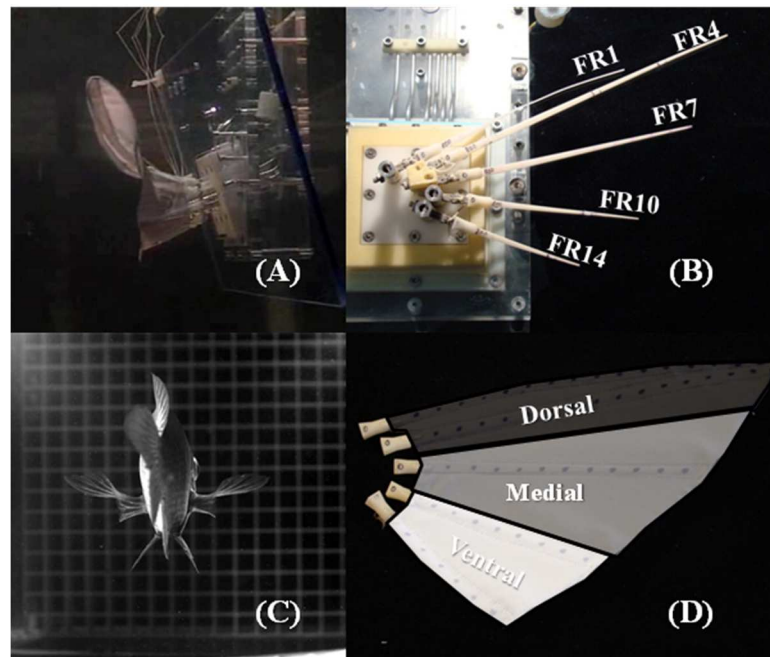


Figure 58. In this study, a biologically-inspired pectoral fin platform was used to test the effectiveness of a micro-genetic algorithm for developing gaits in large kinematic spaces. The biorbotic fin (A) matches the kinematics, mechanical properties, and hydrodynamics of the steady swimming gait of a bluegill sunfish (C). The fin is composed of 5 fin rays (B) connected by a flexible webbing (D) that is driven by a servo tendon system to produce forces underwater. The kinematics of the first DOF ("cupping") were labeled FR1, FR4, FR7, FR10, and FR14; these indices refer to their biological counterparts. The kinematics of the second DOF ("sweeping") were labeled FR1b, FR10b, and FR14b. The fin was functionally divided into segments. The long, flexible *dorsal leading edge* is formed by the fin rays and webbing of FR1 and FR4; the *ventral leading edge* formed by the shorter length FR10, FR14 and webbing; the *medial area* formed by FR7 and webbing. Sunfish image (C) used with permission of George V. Lauder.

A biologically-inspired robotic model of a bluegill sunfish pectoral fin (Figure 58A) is an excellent candidate for evaluation in the μ GA framework. The platform was designed to study the mechanisms of pectoral fin force production during swimming. It approximates the kinematics, mechanical properties, forces, and hydrodynamics of the fish fin and has been used to study the gaits of steady forward swimming [17, 32], yaw turn maneuvers [5], and hovering in place [23]. Engineering (non-biological) gaits have been developed by modifying a steady swimming gait [163], though no broad gait optimization has been conducted. Researchers have developed low order numerical models of sunfish steady swimming [164] and yaw turn maneuvers [165] and validated

these models against robot performance. But given the variable fin stiffness, non-linear dynamics, and complex vorticity, a general numerical model of kinematics and forces is currently infeasible [70]. The lack of a numerical model, the complexity and size of the gait space, and the empirical nature of the platform make it appropriate for μ GA evaluation.

To address the problem of gait optimization in large biorobotic parameter spaces, a μ GA is evaluated on the biorobotic pectoral fin platform. The μ GA develops swimming gaits that optimize for thrust production. Contributions include the development of methods for implementing a μ GA on a robotic platform, μ GA discovery of engineered gaits for swimming fins, detailed understanding of the parameter space and outputs for fin gaits and propulsive forces, and the comparison of known fish swimming gaits with those found in the μ GA framework.

6.3.3 *Methods*

To evaluate the effectiveness of a μ GA in a large, complex parameter space, the μ GA was applied to an existing biologically-inspired robotic (biorobotic) pectoral fin. The μ GA was developed based on the methods described in [160] and included the genetic operators of roulette-wheel selection, bit-wise mutation, and crossover of parameters to evolve candidate gaits. Successive generations of candidate swimming gaits were tested with propulsive force measurement on the biorobotic platform. The fitness of a gait was determined experimentally by the average thrust produced through a stroke.

6.3.3.1 Micro-genetic algorithm

A μ GA works by testing a large population of random gaits, sampling quality gaits from the population to form a sub-population, and evolving multiple sub-populations with the use of genetic operators. The μ GA first generated a random population (P) of candidate solutions of fixed size (N). This entire random population P was tested with force measurement and fitnesses were computed for each candidate gait. At each major iteration, a fixed number of gaits (i) were sampled from P , forming an sub-population P_i (Figure 59). The sub-population was then evolved iteratively.

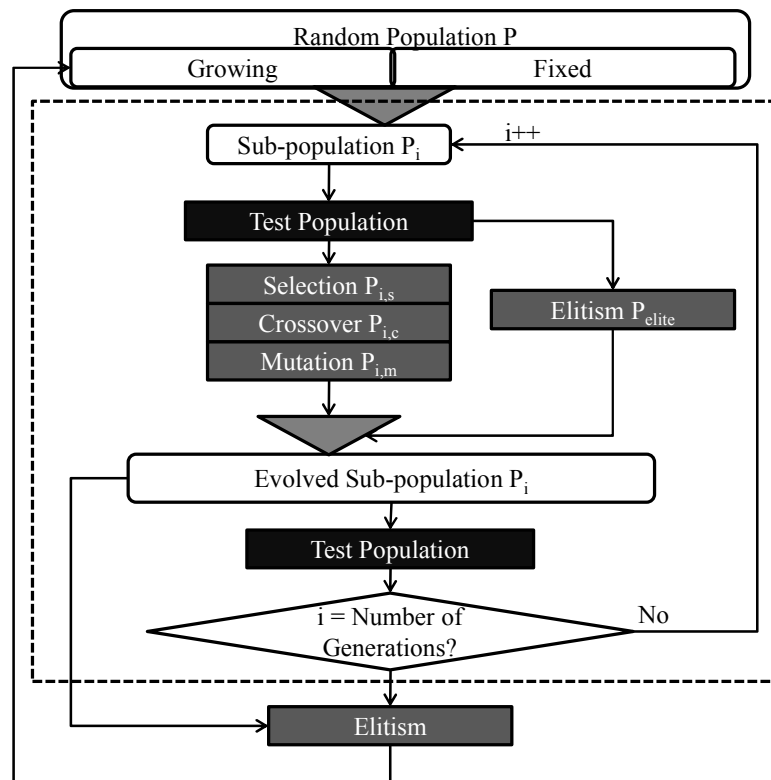


Figure 59. A block diagram shows the steps of the live testing μ GA - a genetic algorithm that tests small populations and allows for reinitialization of the evolving population. The fitness of candidate gaits was determined through testing when the random population was first generated, and at the generation of each new population (shaded blocks). The main program iterated (dotted line) and tested generations of initial populations until the convergence criterion was reached. Convergence was determined by number of generations per iteration. Diagram modified from [166].

At each loop iteration, genetic operators were used to improve the fitness of gaits in the sub-population P_i . For each generation, elitism was applied to P_i , selecting the first non-dominated vector of the population, P_{elite} . Elitism preserved the genetic information of the best solutions. Next, selection was applied, where $i-1$ candidate solutions were sampled from a fitness-weighted distribution, forming the selected population $P_{i,s}$. The probability of an individual candidate solution's selection $p(X_i = CG_i)$ was given a normalized weight of its fitness as in (59). Following selection, crossover was applied between randomly generated pairs of candidate gaits, in which their genetic information was swapped at a random index, forming two offspring candidate gaits and creating $P_{i,c}$. Crossover shares genetic information of high-fitness gaits, forming offspring of paired gaits. Bit-wise mutation was applied to the members of $P_{i,c}$ with a fixed probability $p(m)$, forming $P_{i,m}$. Mutation added randomness to the search by inverting bits of the candidate gait binary representation. The non-dominated solution P_{elite} and the mutated solutions $P_{i,m}$ were merged into a new population P_i , completing one iteration of the μ GA. The fitness of the new population P_i was established through force testing. Following testing, when the planned number of generations was reached, the loop terminated.

$$p(X_i = CG_i) = \frac{CG_{i,fitness}}{\sum CG_{fitness}} \quad (59)$$

After loop termination, all elite candidate gaits from the evolved sub-population were saved to the growing portion of the random population. These filtered gaits could be re-sampled in future iterations during the sampling stage. The use of a growing random population is unique to μ GAs and typically produces a diverse distribution of solutions along a near-optimal front [167].

6.3.3.2 Biorobotic fin implementation

The biorobotic fin was developed to approximate the kinematics, mechanical properties, and hydrodynamics of a swimming sunfish pectoral fin (see [23, 32], Figure 58). The biorobotic fin was composed of multiple fin rays enclosed in a fabric webbing; a servo-tendon system driving up to two degrees of freedom (DOF) on each fin ray to produce gaits (Figure 58A,B). The five fin rays independently execute kinematic patterns along a “cupping” DOF (FR1,4,7,10,14), and three of them along an additional “sweep” DOF (FR1b,10b,14b). The fin is divided into dorsal, medial, and ventral regions for results discussion (Figure 58D). The *outstroke* of a kinematic pattern refers to the time duration when the gross movement of the fin is moving away from the body, the *instroke* when it is moving toward the body.

To apply a μ GA to the biorobotic fin, the components of a gait were parametrized and represented in a genetic algorithm framework. To parametrize kinematic trajectories for each actuated fin ray DOF, the underlying kinematic trajectory of steady swimming ([32]) was used and the amplitude (A; degrees), phase offset (P; fraction of period T), and flapping frequency (F; Hz) were varied, forming the range of kinematic patterns (Table 8). Changes in fin mechanical properties require time-consuming swaps of fin equipment so fin ray flexural rigidity was fixed at a stiffness with known strong thrust production

(EI = 800 times the biological rays; [17]). Parameter values were selected so as to avoid damage to the platform, by restricting phase lags between segments and limiting flapping frequency. The kinematics of an individual fin ray were represented by a binary array of 18 elements, and thus the kinematics of an entire fin were represented using 144 binary elements, forming a “candidate gait” for the genetic algorithm. The solution space specified by the kinematic parameters contains over 2 million possible fin trajectories, so brute force search of the space was not feasible.

Each candidate gait was represented by a data cluster containing the kinematic parameters (see Table 8), the servo trajectories, the measured propulsive forces in thrust and lateral planes, and the fitness (or quantitative measure of solution quality). The kinematic parameters and servo trajectories were selected by the μ GA, while forces and fitness were determined through testing. Average thrust (N) through a fin beat period was used as the fitness criterion to explore basic forward swimming. The fitness landscape was a 25-dimensional space, formed by the {Amplitude, Phase, Frequency} parameters of each of the candidate gaits and the fitness of their forces.

Table 8. Parameter space of fin ray kinematics

	Amp. (A;°)	Phase (P;T)	Freq. (F;Hz)
Minimum	0	0.00	0.25
Maximum	63	0.31	1.52
Increment	1	0.01	0.01
$2^{\#bits}$	2^6	2^5	2^7

6.3.3.3 Experiments

Candidate gaits were tested in real time on the biorobotic platform with measurement of force and execution of μ GA-specified kinematic patterns. All force and kinematic data were sampled at 100 Hz on analog input channels and stored in a single delimited log file. The trials were filmed at 60 frames per second (Exilim FX-1, Casio, JP) to observe gaits and fin bending underwater. Experiments were carried out through use of a custom robot graphical user interface in the LabVIEW programming environment (National Instruments, Austin, TX, U.S.A.) that drove servo kinematics on the robot (described in [32]). The robot was mounted onto a low-friction air bearing carriage (New Way Air Bearings, Aston, PA, USA) and propulsive forces were measured in the thrust and lateral directions (LSB200, Futek Advanced Sensor Technology, LLC., Irvine, CA, USA) in a standing water tank.

μ GA trial parameters were tuned to reduce trial time, obtain diverse elite gaits, and evaluate a simple fitness criteria. Each trial had a random population P of 50 candidate gaits, a total of 10 iterations of sub-populations P_i , 5 generations per sub-population, and 5 candidate gaits per generation, leading to a testing of 300 candidate gaits per trial. A total of 5 trials were conducted, each lasting approximately 50 minutes. Fitness was calculated as the average thrust force through the fin stroke. After each generation, elite candidate gait data were streamed to file, including parameters, force, and fitness measures. Each candidate gait took between 4 and 10 seconds to test and save, and genetic operator run-times were negligible.

6.3.4 Results and Discussion

The μ GA was effective at identifying diverse, locally-optimal gaits for the optimization of thrust in the large biorobotic parameter space. The μ GA developed new gaits that extended existing strategies of thrust production on the biorobotic fin. The μ GA identified a new non-biological gait for thrust production with comparable force production to the bio-inspired steady swimming gait. This gait, termed “ μ GA-bimodal” (see Figure 60), used a high-amplitude, early-deployment, rapid dorsal edge movement ($A_{FR1,4} = [40, 50]^\circ$, $P_{FR1,4} \cong 0T$, $F_{FR1,4} = [1.0, 1.3] Hz$) in combination with a high-amplitude, late-deployment, slow ventral edge movement (see Figure 60). These kinematics caused a thrust-producing instroke followed by a burst of thrust in the later outstroke, something not documented before in fish or the robotic platform.

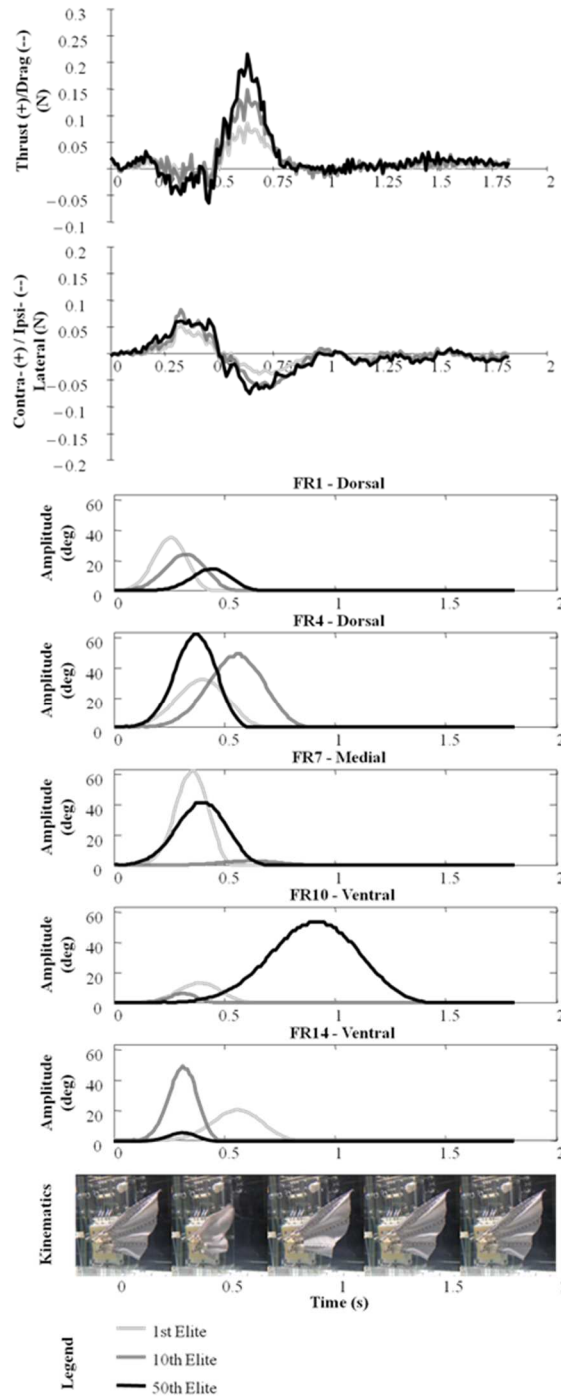


Figure 60. The μ GA evolved a new non-biological swimming gait for thrust production. Evolution of the “bimodal” candidate gait over fifty generations in a local optima region shows the improvement of thrust production (A). The evolution of kinematics (B) show an increase of amplitude on the dorsal leading edge fin rays, causing increase in thrust production through the outstroke ($t=[0,0.25]$ s) and instroke ($t=[0.75,1.25]$ s). “Bimodal” gaits evolved to employ a delayed movement of the ventral kinematics to produce slight thrust in the late instroke ($t=[1.0,1.5]$ s). Data were low pass filtered at 7Hz for clarity.

Elite gaits (local optima) of the μ GA approximated the kinematics and force production of known bio-inspired gaits of steady swimming and hovering. One elite solution generated matched closely the kinematic parameters of steady swimming (Figure 61), following the typical pattern of: low or no amplitude along the second degree of freedom fin rays ($A_{FR7,10,14} \rightarrow 0^\circ$), high amplitudes along the dorsal leading edge ($A_{FR1,4} \rightarrow 60^\circ$), and little phase lag between segments ($P_{all} \cong 0T$). μ GA solutions typically produced between 80 and 90% of the average thrust of a bio-inspired steady swimming gait.

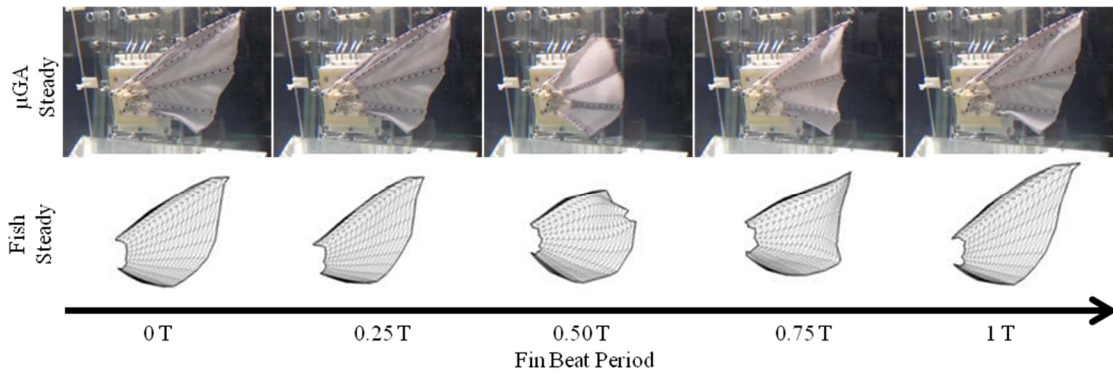


Figure 61. Elite gaits (local optima) of the μ GA approximated the kinematics and force production of known bio-inspired gaits of steady swimming and hovering (not shown). A comparison of an elite (i.e. locally optimal) candidate gait of the μ GA (TOP) to a sunfish steady swimming gait (BOTTOM). Small phase differences in the μ GA solution led to near-optimal performance of the gait. Steady swimming in both the evolved gait and the biology produces a strong thrust force using the dorsal leading edge segment of the fin with little phase lag between fin segments. μ GA solutions typically produced between 80 and 90% of the average thrust of a biologically-inspired steady swimming gait. Steady swimming images modified from [5].

Another elite solution generated, “ μ GA-hover,” closely matched the kinematics used by the sunfish in hovering, typified by: early deployment of the dorsal leading edge ($P_{FR1,4} \cong 0.0T$), late deployment of the ventral leading edge ($P_{FR7,10,14} \rightarrow 0.3T$), and late, high-amplitude, deployment of the second DOF along the ventral leading edge (

$A_{FR10b,14b} \cong 30^\circ$; “lift and drop” pattern detailed in [23]). Typical bio-inspired hover gaits produce nearly balanced lateral and thrust forces (Force Means $\cong 0N$), but when hover was executed at high speeds ($F \cong 1.0Hz$) and with stiff fins ($EI = 800x$), it was a strong thrust producing mode [23].

Local optima were quickly reached in μ GA execution. The “ μ GA-bimodal” gait converged (less than 1% change in solution quality between generations) after 50 total gaits were tested (Figure 60), “ μ GA-hover” after 23 gaits, and “ μ GA-steady” after 10 gaits (each in their respective trials). With trial times ranging on 4-10s, this meant that local optima convergence was obtained on the order of minutes.

The μ GA revealed fine-tuning strategies for improving the thrust production of the biorobotic fin. Changes to individual fin ray parameters affected the fitness of candidate solutions (Figure 62). Fitness was negatively affected by large differences in phase lag between fin rays, except in the case where the ventral rays and dorsal rays were deployed at similar lags respectively (i.e. $P_{FR1} \cong P_{FR4}$ and $P_{FR10} \cong P_{FR14}$), where fitness was positively affected by similar phase lags among segments. Fitness increased as phase lags approached zero ($P_{FR1,4,7,10,14} \rightarrow 0.0T$). Fitness increased as first DOF amplitudes ($A_{FR1,7,10,14}$) increased, excepting fin ray 4, which produced high fitness at lower amplitudes ($A_{FR10} = [10,20]^\circ$). Increasing the flapping frequency of FR4 tended to increase fitness. Increasing the flapping frequency on other fin rays had no consistent effects on fitness.

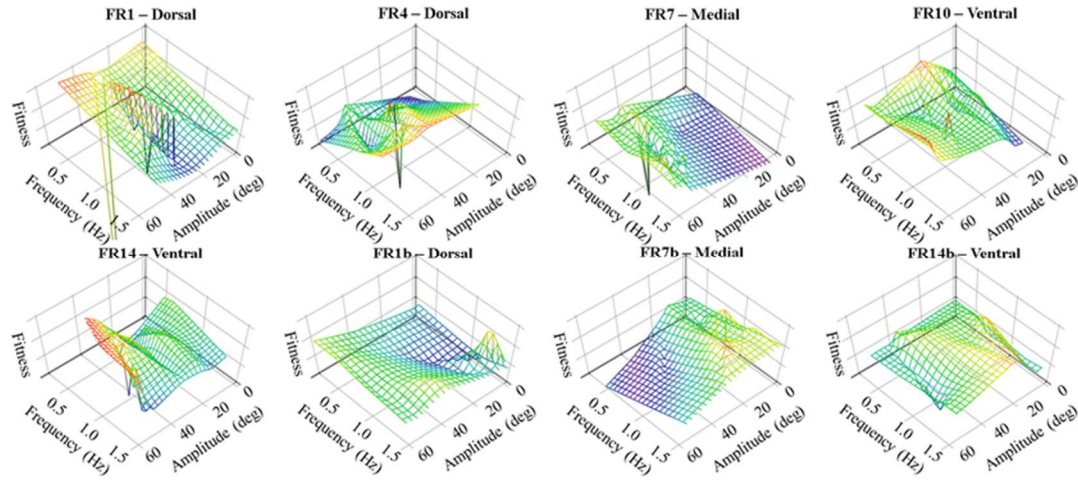


Figure 62. The μ GA revealed fine tuning strategies for fin ray degrees of freedom (DOF) in the biorobotic platform. The kinematic parameters of “Amplitude” and “Frequency” are varied along each of the DOF. “Phase” variations had unclear impacts on fitness and are excluded from these figures. Landscapes were constructed by meshing of 300 candidate solution fitnesses over the broad range explored in one trial of the μ GA.

μ GA parameters required tuning to determine trial conditions that would produce diverse, high-fitness gaits. Consistent with simulation results in [162], increasing the number of generations per iteration (beyond 5) did not significantly affect the quality of solutions found, and increasing the generation size resulted in a linear increase in testing time. Increasing the size of the starting random population (P) tested was the most effective way to improve the quality of solutions found without significantly adding to testing time. Increasing the number of iterations only improved quality of solutions when the random population was sufficiently large (above 50 solutions), but was a very costly linear operation. Increasing the number of iterations often resulted in exploration of the same solution spaces without adding to diversity. Increasing the bit-wise mutation rate beyond 5% did not have a significant impact on solution quality.

6.3.5 Conclusions

Overall, this study demonstrated that a μ GA framework is effective for optimizing in biorobotic gait spaces. Several diverse gaits were developed for thrust production that were comparable in quality to previous bio-inspired gaits. The μ GA discovered new gaits that extended the capabilities of the biorobotic platform in short numbers of experiments. The μ GA identified gaits approximating the biological gaits of steady swimming and hovering, and both were local optima in the gait space. The μ GA gait space also provided insight into the effects on fitness of tuning individual parameters in the robot degrees of freedom. μ GA parameter tuning was straightforward.

Future work can be done to improve the quality and diversity of gaits developed in the μ GA framework. While regions of local optima were explored, precise local optima were not determined in this study. For future work, a simplex algorithm could be used to better explore the space of local optima with hill climbing, using methods from [168]. The μ GA could be modified to produce better solution diversity without increasing trial time with the technique of “niching,” with methods from [169].

The μ GA framework will be used in future study with the biorobotic fin platform to develop new gaits that optimize for other useful engineering goals. Simple changes could optimize for balanced forces through the fin stroke, strong lateral forces to produce maneuver behaviors, or the inverse kinematics problem. For instance, the μ GA framework could be used to search for gaits that minimize the mean square error between a desired force trajectory and the observed, developing inverse kinematics for force trajectories. In similar ways, the μ GA can extend the effectiveness of biorobotic platforms.

6.4 Biologically-inspired control framework for closed-loop control of propulsive force using fin-intrinsic sensing

6.4.1 *Sensory feedback and control architecture*

Force is the control target. To control the body of an underwater vehicle, the forces of its propulsors must be controlled. When there is a simple relationship between propulsive force and propulsor inputs (e.g. multi-DOF propeller systems), an optimal force (and often an optimal force trajectory) can be computed, and an inverse relationship can be used to compute the input necessary to create that desired force. Controllability may still be an issue for underwater vehicles, with many unstable states and nonlinearities, but the relationships between forces and control inputs has been explored for many systems of this type [170-172].

The mapping from desired propulsive force to fin kinematics and mechanical properties is complex, and is not unique. Finned systems have many underactuated degrees of freedom, and have a very large space of input parameters to produce propulsive forces. The system is time varying and the mechanisms of force production are nonlinear. Given a desired force, or behavioral objective, there may be many sets of mechanical and kinematic parameters that optimize it. More specifically, given a desired force trajectory through a fin beat, there is not likely a unique set of fin kinematics to generate the trajectory. Thus the mapping from forces to kinematics is not one-to-one.

The fluid environment locally and globally changes the propulsive forces produced by the fin. An underwater vehicle can be subject to many diverse perturbations from the surrounding fluid. The fins can be subject to local flow perturbations which

cause time-varying changes to the propulsive forces. Thus, the propulsive force of the fin is also highly dependent on the local flow conditions in addition to fin's properties.

Sensory input can modulate the fin's kinematics in the middle of a stroke. Sunfish hovering involves updates to the kinematics in the middle of a fin stroke, suggesting that the kinematics can be modified after initial execution, depending on sensory input. For the robotic platform, there are a number of ways that force can be modulated

Given a desired force, what kinematics and mechanical properties should be used? This is more of a motion planning problem where a solution could take the form of a set of kinematics and mechanical properties that produce a desired force trajectory, or a net force through a stroke. This problem is tractable as long as a number of solutions are known or can be estimated. To find a solution, the operator must define a cost functional and then search a known space of trajectories to identify the closest trajectory that best satisfies the cost functional.

The approach taken by this work has two levels of control. At a high level, the gait and subset of kinematics is chosen through an optimization algorithm that decides which motions to make on a stroke-to-stroke basis. The high level controller takes a force trajectory, or net force, as an input, and the output is the kinematic patterns for the motors. The low level controller deals with updating the kinematics based on sensory inputs from the fin during the stroke. The low level controller has multiple inputs, including the desired force, and the sensory signals from the fin (position measures and intrinsic sensory measures). The output of the low level controller is a modulated set of desired kinematics for the fin.

The fin-intrinsic sensory data is essential to multiple sections of this loop. It is used to predict the total propulsive force of the fin through time and to weight the force estimate in order to predict local forces. This inner loop that modulates the desired kinematics x_{des} , allows for fast update of kinematics and tuning of the propulsive force that would not be achievable with other measures of force. Without sensory data, there is no direct way to modulate the local kinematics of the robot without significant modeling of the relationship between kinematics and force. At a high level, the planning and control operates in the following way:

1. Initialize the fish body model
 - a. Specify initial states
 - b. Specify process and measurement error statistics
 - c. Choose environmental input sequence
2. Initialize the planner sequence
 - a. Search for force-optimal strokes for first outstroke, transition, and instroke
 - b. Concatenate outstroke, transition, instroke strokes
3. Run the controller
 - a. Compute desired force for the stroke based on body dynamics
 - b. Compare desired stroke force to current plan.
 - i. If plan exceeds error threshold, update plan with changes to future strokes.
 - ii. If in outstroke and error threshold is exceeded, determine if adding a transition will decrease error.

- c. Modulate stroke kinematics using sensory feedback in an inner local force control loop
 - i. Compare plan force to estimated force
 - ii. Update control signal based on error

Learning can also be introduced by repeating a particular initialization of the fish body model and attempting small perturbations to the kinematics until a better solution is obtained. The perturbations can be associated to a particular DMP so that the database of gaits has DMPs that have general functions and each has been explored to give specific behaviors that modulate on the functions. This tree-like structure can be searched more efficiently.

Control of propulsion begins with a set of desired body dynamics, which includes the position, velocity, and acceleration of the robot body ($\bar{X}_d, \dot{\bar{X}}_d, \ddot{\bar{X}}_d$; Figure 63). The actual body dynamics ($\bar{X}_a, \dot{\bar{X}}_a, \ddot{\bar{X}}_a$) arise as the result of a fluid structure interaction between the sunfish body and the fluid environment. The difference between desired and actual body dynamics is the error in body dynamics, \bar{e}_x . This error is fed into an inverse body model that maps errors in dynamics to a desired force \bar{F}_d to act on the body from the propulsors.

Stroke kinematics are selected or evolved by comparison of the desired forces with forces in a reference library of kinematic patterns and their associated forces. Kahn and Tangorra have detailed how to use a micro-genetic algorithm (μGA ; c.f. Figure 63) to evolve gaits in order to optimize a desirable force criterion. A dynamics model that maps desired forces (\bar{F}_d) to stroke kinematics could be used in substitution of the selection and

evolution process for kinematics (dashed box, Figure 63), though a general dynamical model has not been developed for these types of flexible, multi-DOF, robotic fins.

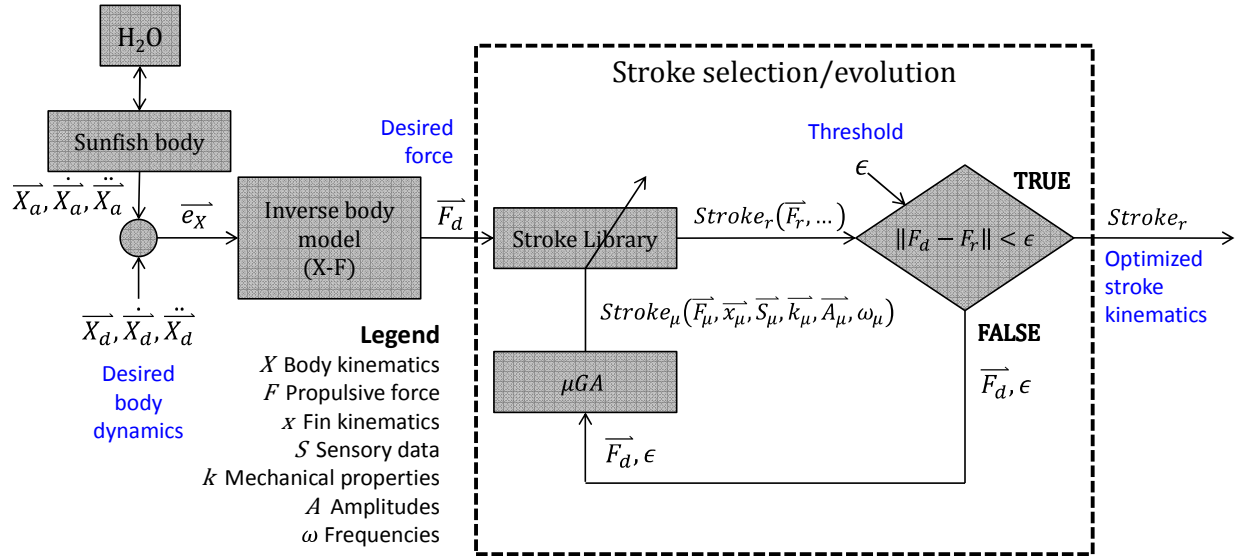


Figure 63. Block diagram showing the mapping from desired robot body dynamics to optimized stroke kinematics. Stroke kinematics are selected from a reference library or evolved using a search algorithm in order to optimize forces to a reference criterion.

Based on prior research, there are multiple ways to build up a control framework for closed loop control of forces for future work, all of which take advantage of the use of distributed, heterogeneous, fin-intrinsic sensing in the fins of a robotic fish. A few strategies are presented below, in order of increasing complexity.

At a baseline, feedback control can be executed on the fin kinematics (Figure 64), where errors in kinematics $e_{x_i} = x_{i,r} - x_{i,m}$ are fed into a controller (e.g. PID or PD type) that sends commands to the motors in the robotic fin. This type of control is likely necessary to ensure that the desired kinematics match the measured kinematics. No fin-intrinsic sensing is required for this strategy, as measurement of fin ray position is taken

at the motors. This strategy also does not control forces directly, but attempts to track the reference kinematics of a particular stroke.

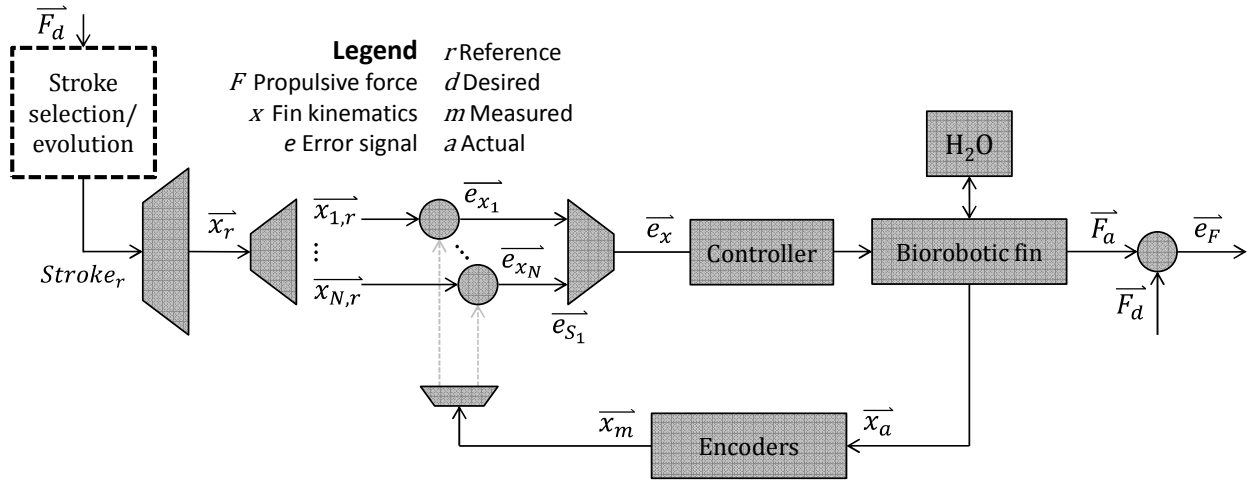


Figure 64. Block diagram of feedback control on fin ray kinematics. Measured kinematics are compared to reference kinematics and the error is fed into a controller which modulates the kinematics of the biorobotic fin. The fin produces forces which are compared to desired forces in order to determine the error in forces. The stroke selection/evolution block is detailed in Figure 63.

Just as the fish will switch its kinematic patterns during a fin beat, a similar switching control strategy can be used to enable the robot to switch its desired kinematics multiple times within a fin beat (Figure 65). At a high level, the desired forces from multiple regions of the fin are compared to the estimated forces from multiple regions of the fin. If the error is sufficiently high, a stroke selection algorithm is used to select a new set of kinematics to execute that is expected to better match the desired forces. In this case, the fin-intrinsic sensors play a key role in estimating the local forces in different regions of the fin.

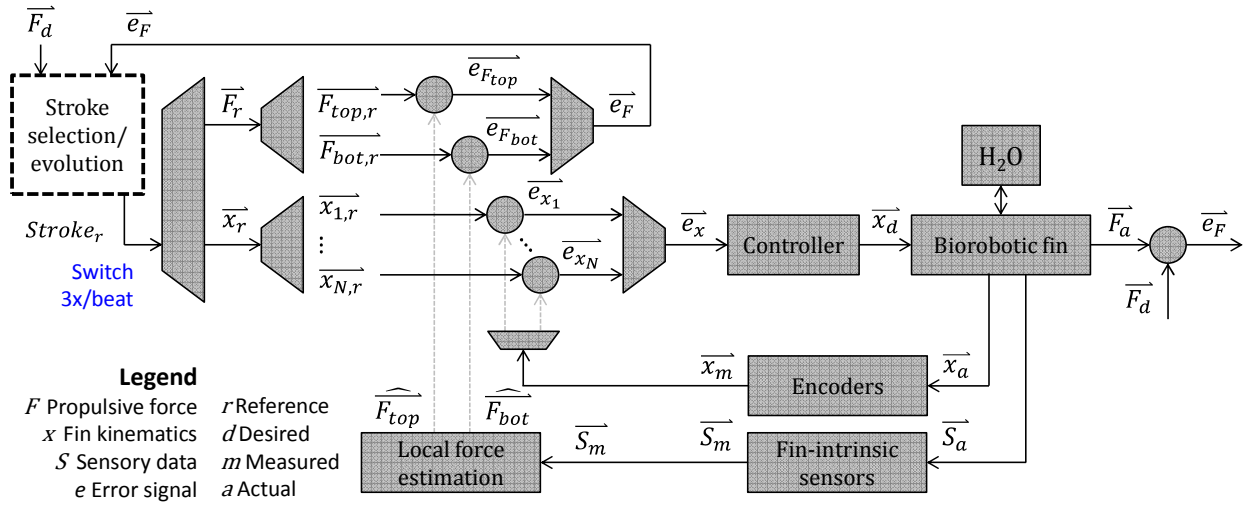


Figure 65. Block diagram of switching control of propulsive forces. The inner loop executes feedback control on fin ray kinematics (c.f. Figure 64) while the outer loop uses fin-intrinsic sensors to estimate forces from the top and bottom sections of the fin and compares force estimates to force reference signals. Inspired by the bluegill sunfish, the stroke kinematics can switch multiple times per fin beat in order to modulate forces.

When the sunfish is hovering, for instance, there are sometimes significant variations in the kinematics in the middle of a stroke, which suggests closed-loop-control of the fin forces. This strategy can be adapted to the robotic fin by feeding the errors in local forces directly to a real time controller (Figure 66). In this case, the estimates of force from the fin-intrinsic sensors are used in real time to modulate the kinematics of the fin.

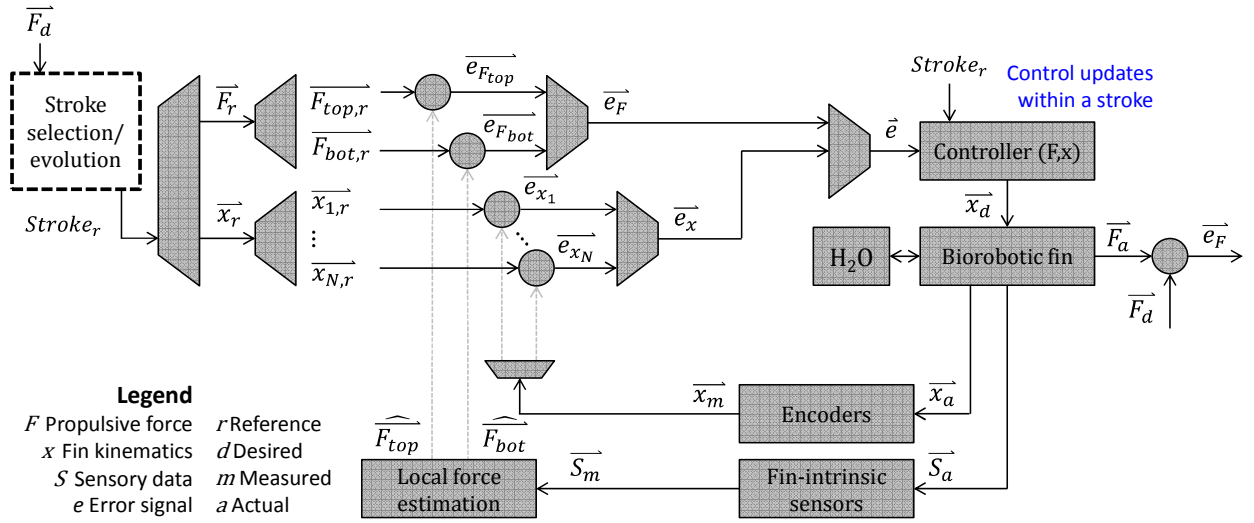


Figure 66. Block diagram of control updates within a swimming stroke. Errors in local force and kinematics are used to update the stiffness and kinematic control of the biorobotic fin using an inverse kinematic model that maps from force errors and current kinematics to modified kinematics mid-stroke.

Lastly, a hybrid approach can be used to allow for both switching of strokes and modulation of kinematics within a stroke. This is consistent with sunfish behavior, and employs the force estimates from the fin-intrinsic sensors in two closed paths to control forces.

Fin-intrinsic sensation can also be used directly in a feedback path to alter robot behavior by triggering events. An additional sensory path is used for detecting touch events during swimming. Study of the sensory signals associated with touch can allow for the triggering of a sensory event that could consist of a stereotyped motion or body-level response to the stimuli.

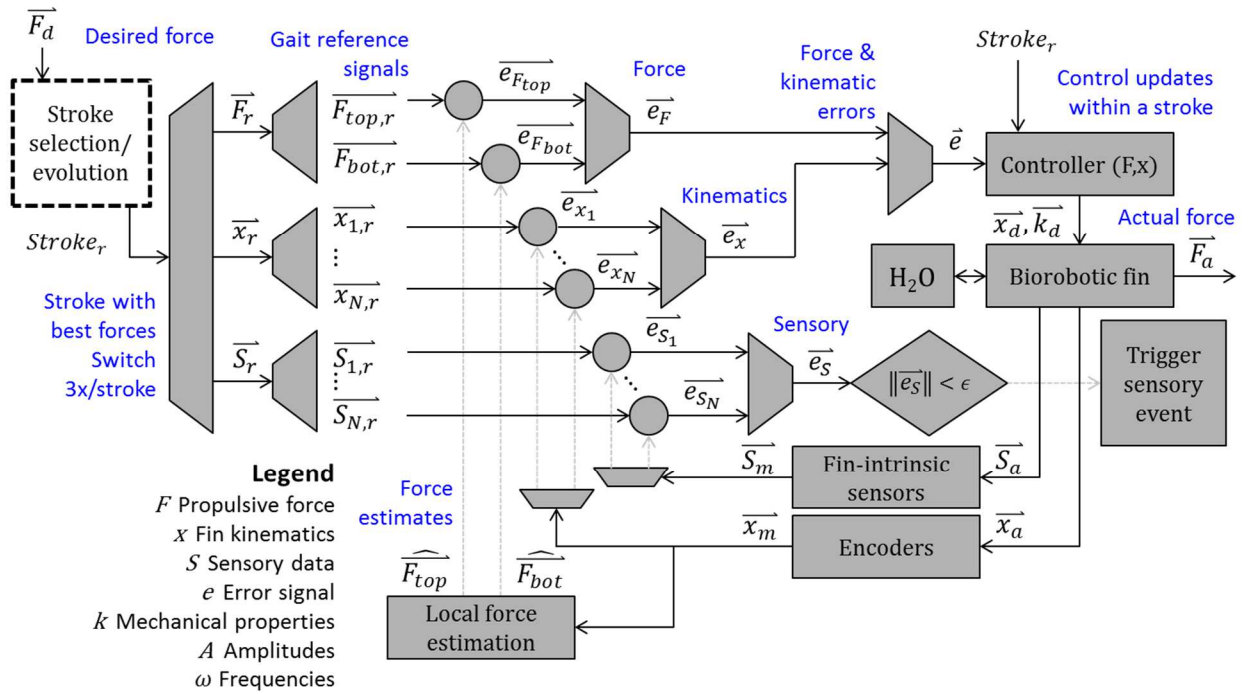


Figure 67. Block diagram of a hybrid control approach for controlling propulsive forces, including force control within a stroke, switching control of kinematics, and triggered sensory events based on fin-intrinsic sensory data.

Chapter 7. Conclusions

Fin intrinsic sensing can be used in a MISO convolution framework to effectively predict the forces of a compliant, multiple DOF, robotic fin. Even with a basic linear MISO convolution model, small numbers of sensors with short time windows of data were used to predict forces of a single gait. Using linear models, good prediction performance was achieved when the stiffness and the speed of the fins were changed. This generalization of low-order models suggests that the sensory data captures the important aspects of the underlying sensory-force mapping. The fins tested had a four-fold range in stiffness, and a two-fold range in speed. The gaits tested were representative of two very different approaches to generating forces (steady, forward swimming and yaw turn maneuvering) in the output space. The fin tested had a high number of underactuated degrees of freedom and produced complex 3d propulsive forces. Prediction could be done in advance, such that forces could be predicted 60-70ms prior to their development in most cases. With this much lead time, real-time control approaches are likely feasible with low computational requirements.

Bending sensory data was generally more useful than pressure sensory data in forming models for force prediction with the fin tested. This could be seen in multiple ways in the data analysis and from a practical instrumentation perspective. Firstly, models formed using only bending data significantly outperformed those using only pressure data. This meant that instrumenting this fin with only bending sensors would yield better force predictions than using twice the amount of pressure sensors in these same locations. Secondly, when the number of available sensors was fixed (i.e. only $N=3$ sensors are permitted), the best sensor subsets always included a bending sensor. This

was consistent regardless of the gait, stiffness, speed, and stroke phase being tested. This effect was also found to be statistically significant ($P < 0.001$). Thirdly, the financial cost of instrumenting and amplifying a bending sensor was significantly less per sensor for a bending sensor relative to a pressure sensor (\$440 vs. \$1900), making it an obvious pragmatic choice for instrumentation. Bending sensors were also cheaply replaced when damaged compared to pressure sensors (unit cost to replace: \$40 vs. \$900).

Choosing good sensor placement locations was important for performance and these locations depend highly on the underlying dynamics of force production. Placing a sensor in the wrong location could result in very poor model performance. This was seen in that the pressure sensors on the inner (body-facing) side of the fins did not significantly contribute to prediction performance and adding their data to the model often degraded performance. In study of optimal sensor placement locations, clear trends emerged for the location of sensors based on which gait was being executed. For instance, during steady swimming, the best placement locations were along the dorsal leading edge and in areas of high bending (on dorsal proximal sensors). This was consistent with CFD analysis of the biological gait that indicates that at least 90% of the thrust forces arise from the dorsal tip of the pectoral fin. During maneuver, best sensors were on both dorsal and ventral leading edges and were generally more distributed over the surface of the fin. This was consistent with the use of both dorsal and ventral edges to produce forces during the gait.

The memory of the sensory-force system was small, such that short time windows of sensory data could be used to predict forces. In most cases, less than 100ms of sensory data was necessary for good predictions. Increasing the window size beyond 100ms

typically had little payoff for performance when linear models were used, and in the case of nonlinear models made the computation of weights cost-prohibitive. Using less than 100ms of sensory data was effective as long as the right windows of data were selected, and these effects were most sensitive to gait. For nonlinear models, window lengths of 50ms or less were often sufficient (5 or less samples) and gave best cost-performance tradeoffs. In some special cases, a single sample (at 100Hz) was sufficient to predict the forces from sensory data.

Nonlinear models of the sensory-force system had better performance and lower implementation cost than linear models and were better suited for force prediction from distributed sensors. By both performance metrics ($\%VAF$, MSE) and cost functionals (MDL , AIC), nonlinear models outperformed linear models for the majority of tested cases. This effect was insensitive to gait, stroke phase, stiffness, and speed. However, changes to the target output, i.e. propulsive force component (thrust vs. lateral), led to changes in the performance. Linear models were slightly more cost effective than nonlinear models for predicting lateral forces during steady swimming gaits, for example.

Fin intrinsic strain sensors could be used to effectively discriminate between fluidic loading and contact loading during an underwater contact with a rigid obstacle. With data from a single strain sensor, or using simple arithmetic operations on multiple sensors' data, it was possible to discriminate between fluidic loading and contact loading. At low speeds underwater, thresholding based on a constant value of strain worked well, but major changes to speed and stiffness made discrimination more difficult with basic strain and strain rate thresholding methods. At high speeds and high fin ray compliance, more sensors and strain differencing techniques were required to discriminate between

fluidic loading and contact loading. Taking the difference between proximal and distal sensors revealed the instants where tip loading (distal) exceeded base loading (proximal), a direct feature of contact with distal objects.

Fluidic loading significantly affected the strain experienced by fins and beams during approach and contact with obstacles underwater. The experiments executed in this thesis highlighted the loading differences experienced by fins during different phases of the contact experiment. The phases identified, which can be used descriptively in future experiments and in those with more complexity, included *acceleration*, *constant velocity*, *approach*, *contact*, and *relaxation*. The *constant velocity* phase would likely vary depending on the kinematics of the robot and the characteristics of the fluidic environment. The phases of the contact experiment were affected by the structure-fluid-structure-interaction (*SFSI*) where the fin and the object both interacted through the medium of the fluid. The loading experienced by the fin during early phases of the experiment affected the loading of later phases of the experiment. The initial *acceleration* phase typically caused the fin to bend prior to contact, which meant that it contacted the obstacle in a deformed state. This changed the dynamics of contact and created a strong effect during the *relaxation* phase after *contact* when the fin settled to a less deformed state. At low initial accelerations, or when fins are very stiff, this effect was less pronounced. Fluidic loading, and the variables that affect its presence, was an important consideration for the sensing of underwater contact, in contrast to most experiments in air.

Common techniques for contact detection in air were not as effective when used underwater due to the effects of fluidic loading through multiple stages of the contact

experiment. Thresholding, and often rate thresholding, are common methods of detecting contact in air and result in reliable estimation of the onset and duration of contact. In the underwater environment, analysis showed that detecting the onset and duration of contact was confounded by the multiple effects of fluidic loading during phases of the experiment. The first feature of the input data was the loading experience at the onset of the *acceleration* phase and during the *constant velocity* phase that made detection by thresholding difficult, delaying the predicted onset of contact or confusing the ramp in strain due to acceleration with the ramp in strain due to contact with an obstacle. Even at low speeds, a very flexible fin ray could deform sufficiently or oscillate enough to trigger many false positives of contact detection. The *approach* phase also tended to see a small magnitude, sharp increase in strain and strain rate that could be falsely detected as contact loading.

The technique of strain differencing was effective in the classification of onset and contact duration in the underwater environment, and required multiple, distributed sensors. While strain differencing may be unnecessary or even perform poorly for contact discrimination in the air, it was a simple and valuable technique to reliably discriminate between fluidic loading and contact loading underwater. This technique makes use of distributed sensors and exploits the spatial strain relationships across the surface of the flexible fin. Onset of contact was easily determined by the zero crossing of the difference in proximal and distal strain signals.

Chapter 8. Future work

Distributed, intrinsic sensing could be of benefit to sensing in compliant, robotic systems. Unlike centralized multifunctional sensors, distributed intrinsic sensors can be used to assess the performance of multiple aspects of a joint or control surface. Local forces can be estimated, damage to the system can be localized, and failures can be inferred from data. Assessing failures and damage make compensatory control possible. Distributed, intrinsic sensors can also fail individually without compromising perception completely. For instance, the loss of a single bending sensor did not make predicting propulsive forces impossible, it merely degraded performance, often by less than 10% VAF. Compliant robots are also very hard to model, and as was demonstrated with the robotic fin, an *a priori* model was not necessary to predict forces across a variety of conditions using distributed sensors. As manufacturing techniques outstrip the development of mathematical models of soft and flexible robots, distributed sensors and simple convolutional algorithms can enable prediction and control of key outputs such as locomotive forces.

Physics-based mathematical models of flexible, multi-DOF fins would be valuable to the underwater robotics community, and would widen the range of techniques usable for force control of these types of fins. Being able to model the kinematics and resulting forces of a general flexible, multipanel fin would enable optimization of force production through simulation to design robotic fins for specific control applications. Further, model-based control techniques for nonlinear systems could be employed given a kinematic-force model and its inverse. Distributed sensing and force prediction would still be necessary to verify that actual forces tracked desired forces, but the selection of

gaits and gait parameters could be executed with significantly less testing. Rather than rely on a library of gaits, where optimization is done empirically, it could be done ahead of time computationally. Further, if the operating envelope of the system was known, the nonlinear space could be simplified through parameterization, for example.

In both touch and propulsive force prediction, more general methods are needed to determine best sensor placements for predicting forces and contact state. Until computationally-feasible CFD methods are developed that can simulate many fin geometries, more experimental studies with simplified, lower-DOF fins are needed to understand how to instrument a general fin based on its geometry and actuated degrees of freedom. This is an open question for symmetric and asymmetric fin shapes and a thoughtful study of geometry and sensing would be valuable. For contact prediction, multiple sensor placements along a symmetric fin and study of the resulting data would increase our understanding of what mechanosensory information develops during contact. Study of these data would also give clues as to how to interpret the information for perception of robot self and obstacles.

Fin-intrinsic sensation may provide a useful input for feed-forward control of the propulsive force. For instance, if intrinsic strain data can be used to predict propulsive forces in advance (up to 100ms in our previous work [88]), a feed-forward controller could use the strain data to modulate kinematics in response to a disturbance. Feed-forward control can also be viewed as system inversion [173], where a kinematic trajectory is desired as output, and a feed-forward controller takes the desired trajectory as input and computes the necessary inputs to the plant to produce the desired output.

Understanding how touch is perceived underwater is an open research area. Firstly, there are still major questions as to what should be measured to perceive touch underwater. The work in this thesis focused on strain along the axis of movement in a flexible fin, but there are many other biologically-relevant phenomena that can be measured. Even in the testing example where a flexible fin is rotated into contact with a rigid plate obstacle, strain could be measured in two directions perpendicular to the axis of rotation of the fin. The planar strain (i.e. stretch) can be measured in the webbing of fins. Vibration within the fins can be measured. Each of these mechanosensory phenomena are likely to differ between air and underwater environments in ways that have not been studied, quantified, and characterized. Understanding their characterization will yield a better understanding of how to use sensing for underwater touch. The structure of the probing system (e.g. fin or finger) can be varied. The fin in this thesis is non-jointed, but instrumentation of jointed robots may increase the complexity of sensory signals, and could introduce a need for measurement of additional sensory phenomena such as joint angle and “tendon” strain. The complexity of the SFSI could increase with a jointed platform such that a hand, for example, may interact with itself and the target object through the fluid forces.

The manufacturing process of instrumented robotic fins could be refined through automatic processes that rely less on skilled hands and more on precise equipment. Instrumenting strain sensors, even when pre-wired, takes time, skill, and training to execute reliably and prevent sensor failure. Likewise, casting or sewing the robotic fins is time-consuming and subject to large variations in mechanical properties depending on manufacturing skill. Co-design of instrumentation and manufacturing would likely result

in more reliable prototypes from mechanical and sensory perspectives. Approaches in shape deposition manufacturing, where mechanisms and sensors are simultaneously fabricated and assembled, may prove useful in future designs of instrumented fins and rays. Additionally, approaches in layering techniques and pop-up MEMS may enable co-manufacturing of sensory and performance layers of the fin structure. For instance, a rigid fin ray layer could be sandwiched between a flexible membrane layer that forms the fin panels, while a sensory layer is embedded with traces and strain sensing patterns on flexible printed circuit board. Design and experimental testing is needed with these technologies to advance the state of the art for robotic fins. In all of the mentioned cases, waterproofing all electrical components can be a significant but necessary challenge and design constraint.

With an increase in sensors comes an increase in cabling for power and communications, which can change the mechanical properties and dynamics of flexible robots. There are several approaches to addressing the effects of cabling on flexible robot dynamics, either in manufacturing and design, or in software. In truly flexible or soft robots, it is undesirable to have cabling and sensors that are many orders of magnitude stiffer than the control surfaces of a limb or appendage. Increasing the flexibility of sensors and their cabling can be done by sensor design and development and use of different design choices. For instance, flexible strain sensors have been developed using fluidic conductive traces embedded in polymers. Approaches like this, while more sophisticated from a design and manufacturing perspective, only minimally affect the stiffness of flexible and soft robots. If the manufacturing approach is infeasible, it is possible to model the effects of adding sensors on the kinematics and dynamics of the

robot on which they are instrumented. For model-based control techniques, this may be especially necessary. In this case, approaches in nonlinear system identification may be appropriate. However, with low numbers of sensors, the effect of cabling may be negligible.

Biologically-inspired gaits could be further optimized to track desirable force trajectories, especially through algorithmic techniques in search and machine learning. Micro-genetic algorithms provided a good solution to search a very large parameter space, but do not necessarily map out the full state space. Search techniques which simultaneously explore and parameterize the state space (e.g. affine linear meshes [174]) may be of great utility in obtaining precise control of propulsive forces. Techniques in reinforcement learning may also be used where output forces are measured and used as training data. If performance is more desirable than model clarity, neural networks with multiple hidden layers may be used to generate accurate mappings between kinematics and propulsive forces with high performance on large sets of training data. If physics-based or intuitive models are sought, techniques in nonlinear system identification may be best for future work.

Hand-tracking of points on biological systems is extremely time consuming and laborious, but these data have immense value in the analysis of biological systems. Automating tracking would significantly increase the speed of data harvesting from biological gaits to develop robotic gaits. Automation could be enhanced by improving software and hardware design. On software, local feature detection in complex and repetitive body patterns is a major challenge. Estimating points in the presence of temporary occlusions (self or environment) is also necessary for many videos of animals.

More development is needed to advance the perception of underwater touch, and research in air can serve as a roadmap for advancement. Strain differencing should be studied under a variety of testing conditions where the duration and location of contact are varied to better understand the limitations of the technique. Obstacles of different shapes and compliances should be presented to the platform and the effects on sensing should be studied. Following an active touch sensing approach, the kinematics of fins and beams should be optimized to understand how to probe obstacles to infer properties such as geometry, compliance, and dynamics. Or, in an obstacle avoidance framework, predictive methods could be studied to anticipate contact and respond reflexively to the *approach* strain prior to *contact*.

Propulsive forces created by fins vary in magnitude and in 3d direction through time. Local regions of the fin also create local forces that then interact nonlinearly with one another and sum to create the total force of the fin. Propulsive force is thus a function of multiple fluid structure interactions, kinematics of multiple fin rays, dynamics of the webbing and fluid, etc. A useful model that relates sensory data to propulsive forces should be able to relate local sensors to local estimates of force. Using these local estimates, an estimate of total force can be obtained. If the total force is estimated, there is no natural way to understand how to modulate local kinematics to control the total force. However, if local force is estimated along with total force, it is easy to understand how to change local kinematics to change local force, and in turn change total force. Thus, models are mapped to local sensory measures to local forces, and a further model that maps local force to total force.

Bibliography

- [1] M. L. Latash, *Neurophysiological basis of movement*, 2nd ed.: Human Kinetics, 2008.
- [2] P. M. Kennedy and J. T. Inglis, "Distribution and behaviour of glabrous cutaneous receptors in the human foot sole," *The Journal of Physiology*, vol. 538, pp. 995-1002, 2002.
- [3] B. E. Flammang and G. V. Lauder, "Pectoral fins aid in navigation of a complex environment by bluegill sunfish under sensory deprivation conditions," *The Journal of experimental biology*, vol. 216, pp. 3084-3089, 2013.
- [4] G. V. Lauder, P. G. Madden, R. Mittal, H. Dong, and M. Bozkurtas, "Locomotion with flexible propulsors: I. Experimental analysis of pectoral fin swimming in sunfish," *Bioinspiration & biomimetics*, vol. 1, p. S25, 2006.
- [5] J. R. Gottlieb, J. L. Tangorra, C. J. Esposito, and G. V. Lauder, "A biologically derived pectoral fin for yaw turn manoeuvres," *Applied Bionics and Biomechanics*, vol. 7, pp. 41-55, 2010.
- [6] R. Williams IV, N. Neubarth, and M. E. Hale, "The function of fin rays as proprioceptive sensors in fish," *Nature communications*, vol. 4, p. 1729, 2013.
- [7] R. Williams and M. E. Hale, "Fin ray sensation participates in the generation of normal fin movement in the hovering behavior of the bluegill sunfish (*Lepomis macrochirus*)," *Journal of Experimental Biology*, vol. 218, pp. 3435-3447, 2015-11-01 00:00:00 2015.
- [8] K. N. Lucas, N. Johnson, W. T. Beaulieu, E. Cathcart, G. Tirrell, S. P. Colin, *et al.*, "Bending rules for animal propulsion," *Nature communications*, vol. 5, 2014.
- [9] G. V. Lauder and P. G. Madden, "Learning from fish: kinematics and experimental hydrodynamics for roboticists," *International journal of automation and computing*, vol. 3, pp. 325-335, 2006.
- [10] G. V. Lauder and E. G. Drucker, "Morphology and experimental hydrodynamics of fish fin control surfaces," *Oceanic Engineering, IEEE Journal of*, vol. 29, pp. 556-571, 2004.
- [11] E. G. Drucker and G. V. Lauder, "Locomotor forces on a swimming fish: three-dimensional vortex wake dynamics quantified using digital particle image velocimetry," *The Journal of Experimental Biology*, vol. 202, pp. 2393-2412, 1999.

- [12] T. J. Ehlinger and D. S. Wilson, "Complex foraging polymorphism in bluegill sunfish," *Proceedings of the National Academy of Sciences*, vol. 85, pp. 1878-1882, March 1, 1988 1988.
- [13] B. C. Jayne, A. F. Lozada, and G. V. Lauder, "Function of the dorsal fin in bluegill sunfish: motor patterns during four distinct locomotor behaviors," *Journal of Morphology*, vol. 228, pp. 307-326, 1996.
- [14] E. G. Drucker and G. V. Lauder, "Function of pectoral fins in rainbow trout: behavioral repertoire and hydrodynamic forces," *Journal of Experimental Biology*, vol. 206, pp. 813-826, March 1, 2003 2003.
- [15] G. V. Lauder, P. Madden, I. Hunter, J. Tangorra, N. Davidson, L. Proctor, *et al.*, "Design and performance of a fish fin-like propulsor for AUVs," in *Proceedings of 14th International Symposium on Unmanned Untethered Submersible Technology*, Durham, NH, 2005.
- [16] S. Alben, P. G. Madden, and G. V. Lauder, "The mechanics of active fin-shape control in ray-finned fishes," *Journal of The Royal Society Interface*, vol. 4, pp. 243-256, 2007.
- [17] J. L. Tangorra, G. V. Lauder, I. W. Hunter, R. Mittal, P. G. Madden, and M. Bozkurtas, "The effect of fin ray flexural rigidity on the propulsive forces generated by a biorobotic fish pectoral fin," *The Journal of Experimental Biology*, vol. 213, pp. 4043-4054, 2010.
- [18] C. J. Esposito, J. L. Tangorra, B. E. Flammang, and G. V. Lauder, "A robotic fish caudal fin: effects of stiffness and motor program on locomotor performance," *The Journal of experimental biology*, vol. 215, pp. 56-67, 2012.
- [19] M. W. Westneat, D. H. Thorsen, J. A. Walker, and M. E. Hale, "Structure, function, and neural control of pectoral fins in fishes," *IEEE Journal of Oceanic Engineering*, vol. 29, pp. 674-683, 2004.
- [20] D. H. Thorsen and M. E. Hale, "Neural development of the zebrafish (*Danio rerio*) pectoral fin," *Journal of Comparative Neurology*, vol. 504, pp. 168-184, 2007.
- [21] M. Hale and R. Williams, "Pectoral fins as sensors: Spatial distribution of sensory input to the pectoral fins of the bluegill sunfish," in *INTEGRATIVE AND COMPARATIVE BIOLOGY*, 2012, pp. E71-E71.
- [22] R. Williams IV and M. E. Hale, "Fin ray sensation participates in the generation of normal fin movement in the hovering behavior of the bluegill sunfish (*Lepomis macrochirus*) " *Journal of Experimental Biology*, 2015-09-07 2015.

- [23] J. C. Kahn, B. E. Flammang, and J. L. Tangorra, "Hover kinematics and distributed pressure sensing for force control of biorobotic fins," in *2012 IEEE/RSJ International Conference on Intelligent Robots and Systems (IROS)*, Vilamoura, Portugal, 2012, pp. 1460-1466.
- [24] M. S. Triantafyllou, A. H. Techet, and F. S. Hover, "Review of experimental work in biomimetic foils," *IEEE Journal of Oceanic Engineering*, vol. 29, pp. 585-594, 2004.
- [25] P. Prempraneerach, F. Hover, and M. Triantafyllou, "The effect of chordwise flexibility on the thrust and efficiency of a flapping foil," in *Proc. 13th Int. Symp. on Unmanned Untethered Submersible Technology: special session on bioengineering research related to autonomous underwater vehicles*, New Hampshire, 2003.
- [26] R. M. Shelton, P. Thornycroft, and G. V. Lauder, "Undulatory locomotion of flexible foils as biomimetic models for understanding fish propulsion," *The Journal of experimental biology*, p. jeb. 098046, 2014.
- [27] L. Schouveiler, F. Hover, and M. Triantafyllou, "Performance of flapping foil propulsion," *Journal of Fluids and Structures*, vol. 20, pp. 949-959, 2005.
- [28] P. Jifeng and A. Silas, "Effects of shape and stroke parameters on the propulsion performance of an axisymmetric swimmer," *Bioinspiration & Biomimetics*, vol. 7, p. 016012, 2012.
- [29] S. Licht, V. Polidoro, M. Flores, F. S. Hover, and M. S. Triantafyllou, "Design and projected performance of a flapping foil AUV," *IEEE Journal of Oceanic Engineering*, vol. 29, pp. 786-794, 2004.
- [30] D. B. Quinn, G. V. Lauder, and A. J. Smits, "Flexible propulsors in ground effect," *Bioinspiration & Biomimetics*, vol. 9, p. 036008, 2014.
- [31] I. D. Neveln, Y. Bai, J. B. Snyder, J. R. Solberg, O. M. Curet, K. M. Lynch, *et al.*, "Biomimetic and bio-inspired robotics in electric fish research," *The Journal of Experimental Biology*, vol. 216, pp. 2501-2514, July 1, 2013 2013.
- [32] C. Phelan, J. Tangorra, G. Lauder, and M. Hale, "A biorobotic model of the sunfish pectoral fin for investigations of fin sensorimotor control," *Bioinspiration & biomimetics*, vol. 5, p. 035003, 2010.
- [33] J. L. Tangorra, A. P. Mignano, G. N. Carryon, and J. C. Kahn, "Biologically derived models of the sunfish for experimental investigations of multi-fin swimming," in *2011 IEEE/RSJ International Conference on Intelligent Robots and Systems (IROS)*, San Francisco, CA, USA, 2011, pp. 580-587.

- [34] R. M. Eustice, H. Singh, J. J. Leonard, and M. R. Walter, "Visually mapping the RMS Titanic: Conservative covariance estimates for SLAM information filters," *The international journal of robotics research*, vol. 25, pp. 1223-1242, 2006.
- [35] R. M. Eustice, H. Singh, and J. J. Leonard, "Exactly sparse delayed-state filters for view-based SLAM," *IEEE Transactions on Robotics*, vol. 22, pp. 1100-1114, 2006.
- [36] J. M. Sáez, A. Hogue, F. Escolano, and M. Jenkin, "Underwater 3D SLAM through entropy minimization," in *Robotics and automation, 2006. ICRA 2006. Proceedings 2006 IEEE international conference on*, 2006, pp. 3562-3567.
- [37] P. M. Newman, J. J. Leonard, and R. J. Rikoski, "Towards constant-time SLAM on an autonomous underwater vehicle using synthetic aperture sonar," in *Robotics Research*, ed: Springer, 2005, pp. 409-420.
- [38] D. Ribas, P. Ridao, J. D. Tardós, and J. Neira, "Underwater SLAM in man-made structured environments," *Journal of Field Robotics*, vol. 25, pp. 898-921, 2008.
- [39] S. Williams and I. Mahon, "Simultaneous localisation and mapping on the great barrier reef," in *Robotics and Automation, 2004. Proceedings. ICRA'04. 2004 IEEE International Conference on*, 2004, pp. 1771-1776.
- [40] J. R. Solberg, K. M. Lynch, and M. A. MacIver, "Active electrolocation for underwater target localization," *The International Journal of Robotics Research*, vol. 27, pp. 529-548, 2008.
- [41] Z. Fan, J. Chen, J. Zou, D. Bullen, C. Liu, and F. Delcomyn, "Design and fabrication of artificial lateral line flow sensors," *Journal of Micromechanics and Microengineering*, vol. 12, p. 655, 2002.
- [42] F. D. Lagor, L. D. DeVries, K. M. Waychoff, and D. A. Paley, "Bio-inspired flow sensing and control: Autonomous rheotaxis using distributed pressure measurements," *Journal of Unmanned System Technology*, vol. 1, pp. 78-88, 2013.
- [43] Y. Silverman, L. M. Miller, M. A. MacIver, and T. D. Murphey, "Optimal planning for information acquisition," in *Intelligent Robots and Systems (IROS), 2013 IEEE/RSJ International Conference on*, 2013, pp. 5974-5980.
- [44] R. Grant, S. Wieskotten, N. Wengst, T. Prescott, and G. Dehnhardt, "Vibrissal touch sensing in the harbor seal (*Phoca vitulina*): how do seals judge size?," *Journal of Comparative Physiology A*, vol. 199, pp. 521-533, 2013.
- [45] R. Kastelein and M. Van Gaalen, "The sensitivity of the vibrissae of a Pacific walrus (*Odobenus rosmarus divergem*) Part," *Aquatic Mammals*, vol. 14, pp. 123-133, 1988.

- [46] G. Dehnhardt, B. Mauck, and H. Bleckmann, "Seal whiskers detect water movements," *Nature*, vol. 394, pp. 235-236, 1998.
- [47] G. Dehnhardt, B. Mauck, W. Hanke, and H. Bleckmann, "Hydrodynamic trail-following in harbor seals (*Phoca vitulina*)," *Science*, vol. 293, pp. 102-104, 2001.
- [48] N. Levermann, A. Galatius, G. Ehlme, S. Rysgaard, and E. W. Born, "Feeding behaviour of free-ranging walrus with notes on apparent dexterity of flipper use," *BMC ecology*, vol. 3, p. 9, 2003.
- [49] C. J. Sullivan, B. Mitchinson, M. J. Pearson, M. Evans, N. F. Lepora, C. W. Fox, *et al.*, "Tactile discrimination using active whisker sensors," *Sensors Journal, IEEE*, vol. 12, pp. 350-362, 2012.
- [50] J. H. Solomon and M. J. Hartmann, "Extracting object contours with the sweep of a robotic whisker using torque information," *The International Journal of Robotics Research*, vol. 29, pp. 1233-1245, 2010.
- [51] P. V. y Alvarado, V. Subramaniam, and M. Triantafyllou, "Design of a bio-inspired whisker sensor for underwater applications," *Proc. IEEE Sensors, Taipei, Taiwan*, 2012.
- [52] T. Rooney, M. Pearson, J. Welsby, I. Horsfield, R. Sewell, and S. Dogramadzi, "Object localisation using active whiskers on underwater autonomous walking robot," in *Field Robotics: Proceedings of the 14th International Conference on Climbing and Walking Robots and the Support Technologies for Mobile Machines*, Paris, France, 2011, pp. 190-195.
- [53] J. C. Kahn, D. Peretz, J. Tangorra, and Y. Visell, "Touch sensing in a robotic fish fin," in *Living Machines*, London, UK, 2013.
- [54] H. S. Stuart, S. Wang, B. Gardineer, D. L. Christensen, D. M. Aukes, and M. Cutkosky, "A Compliant Underactuated Hand with Suction Flow for Underwater Mobile Manipulation."
- [55] J. Lemburg, P. Kampmann, and F. Kirchner, "A small-scale actuator with passive-compliance for a fine-manipulation deep-sea manipulator," in *OCEANS 2011*, 2011, pp. 1-4.
- [56] D. J. O'Brien and D. M. Lane, "Force and slip sensing for a dextrous underwater gripper," in *Robotics and Automation, 1998. Proceedings. 1998 IEEE International Conference on*, 1998, pp. 1057-1062.
- [57] X. Tan, "Autonomous robotic fish as mobile sensor platforms: Challenges and potential solutions," *Marine Technology Society Journal*, vol. 45, pp. 31-40, 2011.

- [58] K. K. Leang, Y. Shan, S. Song, and K. J. Kim, "Integrated sensing for IPMC actuators using strain gages for underwater applications," *IEEE/ASME Transactions on Mechatronics*, vol. 17, pp. 345-355, 2012.
- [59] J. C. Kahn and J. L. Tangorra, "Application of a micro-genetic algorithm for gait development on a bio-inspired robotic pectoral fin," in *Intelligent Robots and Systems (IROS), 2013 IEEE/RSJ International Conference on*, 2013, pp. 3784-3789.
- [60] D. Barrett, M. Grosenbaugh, and M. Triantafyllou, "The optimal control of a flexible hull robotic undersea vehicle propelled by an oscillating foil," in *Autonomous Underwater Vehicle Technology, 1996. AUV '96., Proceedings of the 1996 Symposium on*, 1996, pp. 1-9.
- [61] A. J. Ijspeert, "Central pattern generators for locomotion control in animals and robots: A review," *Neural Networks*, vol. 21, pp. 642-653, 5// 2008.
- [62] G. N. Carryon and J. L. Tangorra, "Biologically-inspired adaptive control of compliant foils using a neural-based oscillator (in press)," presented at the ASME 2014 Dynamic Systems and Control Conference, San Antonio, TX, USA, 2014.
- [63] Z. Chunlin and K. H. Low, "Design and Locomotion Control of a Biomimetic Underwater Vehicle With Fin Propulsion," *IEEE/ASME Transactions on Mechatronics*, vol. 17, pp. 25-35, 2012.
- [64] S.-J. Chung and M. Dorothy, "Neurobiologically inspired control of engineered flapping flight," *Journal of guidance, control, and dynamics*, vol. 33, pp. 440-453, 2010.
- [65] J. H. Solomon and M. J. Hartmann, "Biomechanics: Robotic whiskers used to sense features," *Nature*, vol. 443, pp. 525-525, 10/05/print 2006.
- [66] M. Kaneko, N. Kanayama, and T. Tsuji, "Active antenna for contact sensing," *Robotics and Automation, IEEE Transactions on*, vol. 14, pp. 278-291, 1998.
- [67] A. Eberle, P. Reinhall, and T. Daniel, "Fluid–structure interaction in compliant insect wings," *Bioinspiration & biomimetics*, vol. 9, p. 025005, 2014.
- [68] A. Kancharala and M. Philen, "Study of flexible fin and compliant joint stiffness on propulsive performance: theory and experiments," *Bioinspiration & biomimetics*, vol. 9, p. 036011, 2014.
- [69] H. Dong, M. Bozkurtas, R. Mittal, P. Madden, and G. Lauder, "Computational modelling and analysis of the hydrodynamics of a highly deformable fish pectoral fin," *Journal of Fluid Mechanics*, vol. 645, pp. 345-373, 2010.

- [70] R. Mittal, H. Dong, M. Bozkurtas, G. Lauder, and P. Madden, "Locomotion with flexible propulsors: II. Computational modeling of pectoral fin swimming in sunfish," *Bioinspiration & biomimetics*, vol. 1, p. S35, 2006.
- [71] E. J. Kim, M. Wolf, V. M. Ortega-Jimenez, S. H. Cheng, and R. Dudley, "Hovering performance of Anna's hummingbirds (*Calypte anna*) in ground effect," *Journal of The Royal Society Interface*, vol. 11, September 6, 2014 2014.
- [72] B. Erin and V. L. George, "Swimming near the substrate: a simple robotic model of stingray locomotion," *Bioinspiration & Biomimetics*, vol. 8, p. 016005, 2013.
- [73] T. Rooney, A. G. Pipe, S. Dogramadzi, and M. J. Pearson, "Towards Tactile Sensing Applied to Underwater Autonomous Vehicles for Near Shore Survey and De-mining," in *Advances in Autonomous Robotics*, 2012, pp. 463-464.
- [74] C. Intartaglia, L. Soria, and M. Porfiri, "Hydrodynamic coupling of two sharp-edged beams vibrating in a viscous fluid," *Proceedings of the Royal Society A: Mathematical, Physical and Engineering Science*, vol. 470, p. 20130397, 2014.
- [75] H. S. Stuart, S. Wang, B. Gardineer, D. L. Christensen, D. M. Aukes, and M. Cutkosky, "A Compliant Underactuated Hand with Suction Flow for Underwater Mobile Manipulation," in *IEEE International Conference on Robotics and Automation*, Hong Kong, China, 2014.
- [76] D. M. Lane, J. B. C. Davies, G. Robinson, D. J. O'Brien, J. Sneddon, E. Seaton, *et al.*, "The AMADEUS dextrous subsea hand: design, modeling, and sensor processing," *Oceanic Engineering, IEEE Journal of*, vol. 24, pp. 96-111, 1999.
- [77] W. J. Stewart, A. Nair, H. Jiang, and M. J. McHenry, "Prey fish escape by sensing the bow wave of a predator," *The Journal of Experimental Biology*, vol. 217, pp. 4328-4336, December 15, 2014 2014.
- [78] J. C. Montgomery, C. F. Baker, and A. G. Carton, "The lateral line can mediate rheotaxis in fish," *Nature*, vol. 389, pp. 960-963, 10/30/print 1997.
- [79] S. Vogel, *Life in moving fluids: the physical biology of flow*: Princeton University Press, 1996.
- [80] A. M. Dollar and R. D. Howe, "The Highly Adaptive SDM Hand: Design and Performance Evaluation," *The International Journal of Robotics Research*, vol. 29, pp. 585-597, April 1, 2010 2010.
- [81] A. V. Oppenheim, R. W. Schaffer, and J. R. Buck, *Discrete-time signal processing*. Upper Saddle River, N.J: Prentice Hall, 1999.
- [82] C. H. K. Williamson and R. Govardhan, "Vortex-induced vibrations," *Annual Review of Fluid Mechanics*, vol. 36, pp. 413-455, 2004.

- [83] B. W. Quist, V. Seghete, L. A. Huet, T. D. Murphey, and M. J. Z. Hartmann, "Modeling Forces and Moments at the Base of a Rat Vibrissa during Noncontact Whisking and Whisking against an Object," *The Journal of Neuroscience*, vol. 34, pp. 9828-9844, July 23, 2014 2014.
- [84] N. F. Lepora, U. Martinez-Hernandez, H. Barron-Gonzalez, M. Evans, G. Metta, and T. J. Prescott, "Embodied hyperacuity from Bayesian perception: Shape and position discrimination with an iCub fingertip sensor," in *2012 IEEE/RSJ International Conference on Intelligent Robots and Systems (IROS)*, Vilamoura, Portugal, 2012, pp. 4638-4643.
- [85] N. F. Lepora, U. Martinez-Hernandez, M. Evans, L. Natale, G. Metta, and T. J. Prescott, "Tactile Superresolution and Biomimetic Hyperacuity," *Robotics, IEEE Transactions on*, vol. PP, pp. 1-14, 2015.
- [86] B. Delhay, V. Hayward, P. Lefèvre, and J.-L. Thonnard, "Texture-induced vibrations in the forearm during tactile exploration," *Frontiers in Behavioral Neuroscience*, vol. 6, 2012-July-6 2012.
- [87] R. Cholewiak and A. Collins, "Vibrotactile localization on the arm: Effects of place, space, and age," *Perception & Psychophysics*, vol. 65, pp. 1058-1077, 2003/10/01 2003.
- [88] J. C. Kahn, D. J. Peretz, and J. L. Tangorra, "Predicting propulsive forces using distributed sensors in a compliant, high DOF, robotic fin," *Bioinspiration & Biomimetics*, vol. 10, p. 036009, 2015.
- [89] Y.-L. Park, C. Majidi, R. Kramer, P. Bérard, and R. J. Wood, "Hyperelastic pressure sensing with a liquid-embedded elastomer," *Journal of Micromechanics and Microengineering*, vol. 20, p. 125029, 2010.
- [90] J. C. Kahn and J. L. Tangorra, "The effects of fluidic loading on underwater contact sensing with robotic fins and beams," *IEEE Transactions on Haptics*, vol. PP, pp. 1-1, 2015.
- [91] N. Ueno, M. M. Svinin, and M. Kaneko, "Dynamic contact sensing by flexible beam," *Mechatronics, IEEE/ASME Transactions on*, vol. 3, pp. 254-264, 1998.
- [92] D. Kim and R. Möller, "Biomimetic whiskers for shape recognition," *Robotics and Autonomous Systems*, vol. 55, pp. 229-243, 3/31/ 2007.
- [93] T. N. Clements and C. D. Rahn, "Three-dimensional contact imaging with an actuated whisker," *Robotics, IEEE Transactions on*, vol. 22, pp. 844-848, 2006.

- [94] M. J. Pearson, B. Mitchinson, J. C. Sullivan, A. G. Pipe, and T. J. Prescott, "Biomimetic vibrissal sensing for robots," *Philosophical Transactions of the Royal Society of London B: Biological Sciences*, vol. 366, pp. 3085-3096, 2011-11-12 00:00:00 2011.
- [95] C. L. Schroeder and M. J. Z. Hartmann, "Sensory prediction on a whiskered robot: A tactile analogy to "optic flow"," *Frontiers in Neurorobotics*, vol. 6, 2012-October-22 2012.
- [96] A. E. Schultz, J. H. Solomon, M. A. Peshkin, and M. J. Hartmann, "Multifunctional Whisker Arrays for Distance Detection, Terrain Mapping, and Object Feature Extraction," in *Robotics and Automation, 2005. ICRA 2005. Proceedings of the 2005 IEEE International Conference on*, 2005, pp. 2588-2593.
- [97] S. Visa, B. Ramsay, A. L. Ralescu, and E. van der Knaap, "Confusion Matrix-based Feature Selection," in *MAICS*, 2011, pp. 120-127.
- [98] X. He and H. Asada, "A New Method for Identifying Orders of Input-Output Models for Nonlinear Dynamic Systems," in *American Control Conference, 1993*, 1993, pp. 2520-2523.
- [99] L. Ljung, *System identification*: Springer, 1998.
- [100] J.-N. Juang, *Applied system identification*: Prentice-Hall, Inc., 1994.
- [101] W. H. Press, S. A. Teukolsky, W. T. Vetterling, and B. P. Flannery, *Numerical recipes: the art of scientific computing*, 3rd Edition ed.: Cambridge University Press, 2007.
- [102] J. Hill, H. Bart-Smith, C. Barbier, and J. Humphrey, "Investigation of a Bioinspired Whisker-Like Fluid Motion Sensor," in *ASME 2006 International Mechanical Engineering Congress and Exposition*, 2006, pp. 375-381.
- [103] T. Ogunfunmi, *Adaptive nonlinear system identification: The Volterra and Wiener model approaches*: Springer, 2007.
- [104] M. Korenberg and I. Hunter, "The identification of nonlinear biological systems: Volterra kernel approaches," *Annals of Biomedical Engineering*, vol. 24, pp. 250-268, 1996/03/01 1996.
- [105] A. Watanabe and L. Stark, "Kernel method for nonlinear analysis: identification of a biological control system," *Mathematical Biosciences*, vol. 27, pp. 99-108, // 1975.

- [106] M. J. Korenberg, S. B. Bruder, and P. J. McLlroy, "Exact orthogonal kernel estimation from finite data records: Extending Weiner's identification of nonlinear systems," *Annals of Biomedical Engineering*, vol. 16, pp. 201-214, 1988/03/01 1988.
- [107] H. Akaike, "A new look at the statistical model identification," *IEEE Transactions on Automatic Control*, vol. 19, pp. 716-723, 1974.
- [108] S. Hu, "Akaike information criterion," 2007.
- [109] G. V. Lauder, E. J. Anderson, J. Tangorra, and P. G. A. Madden, "Fish biorobotics: kinematics and hydrodynamics of self-propulsion," *Journal of Experimental Biology*, vol. 210, pp. 2767-2780, August 15, 2007 2007.
- [110] R. P. Lippmann, "An introduction to computing with neural nets," in *IEEE ASSP Magazine* vol. 4, ed, 1987, pp. 4-22.
- [111] M. Schmidt and H. Lipson, "Distilling free-form natural laws from experimental data," *Science*, vol. 324, pp. 81-85, 2009.
- [112] D. Simon, *Optimal state estimation: Kalman, H infinity, and nonlinear approaches*: John Wiley & Sons, 2006.
- [113] R. Penrose, "A generalized inverse for matrices," *Mathematical Proceedings of the Cambridge Philosophical Society*, vol. 51, pp. 406-413, 1955.
- [114] K. K. Yuen, "The two-sample trimmed t for unequal population variances," *Biometrika*, vol. 61, pp. 165-170, 1974.
- [115] N. Wettels, J. Fishel, Z. Su, C. Lin, and G. Loeb, "Multi-modal synergistic tactile sensing," *Tactile sensing in humanoids—Tactile sensors and beyond workshop, 9th IEEE-RAS international conference on humanoid robots*, 2009.
- [116] H. Yousef, M. Boukallel, and K. Althoefer, "Tactile sensing for dexterous in-hand manipulation in robotics—A review," *Sensors and Actuators A: Physical*, vol. 167, pp. 171-187, 6// 2011.
- [117] R. D. Howe, "Tactile sensing and control of robotic manipulation," *Advanced Robotics*, vol. 8, pp. 245-261, 1993.
- [118] Y. Menguc, Y.-L. Park, E. Martinez-Villalpando, P. Aubin, M. Zisook, L. Stirling, *et al.*, "Soft wearable motion sensing suit for lower limb biomechanics measurements," in *2013 IEEE International Conference on Robotics and Automation (ICRA)*, Karlsruhe, Germany, 2013, pp. 5309-5316.

- [119] J. W. Bahlman, S. M. Swartz, and K. S. Breuer, "How wing kinematics affect power requirements and aerodynamic force production in a robotic bat wing," *Bioinspiration & biomimetics*, vol. 9, p. 025008, 2014.
- [120] M. Bozkurttas, J. Tangorra, G. Lauder, and R. Mittal, "Understanding the hydrodynamics of swimming: From fish fins to flexible propulsors for autonomous underwater vehicles," *Advances in Science and Technology*, vol. 58, pp. 193-202, 2008.
- [121] R. F. Shepherd, F. Ilievski, W. Choi, S. A. Morin, A. A. Stokes, A. D. Mazzeo, *et al.*, "Multigait soft robot," *Proceedings of the National Academy of Sciences*, vol. 108, pp. 20400-20403, December 20, 2011 2011.
- [122] K. H. Low, C. Zhou, and Y. Zhong, "Gait planning for steady swimming control of biomimetic fish robots," *Advanced Robotics*, vol. 23, pp. 805-829, 2009.
- [123] A. Seyfarth, F. Iida, R. Tausch, M. Stelzer, O. von Stryk, and A. Karguth, "Towards bipedal jogging as a natural result of optimizing walking speed for passively compliant three-segmented legs," *The International Journal of Robotics Research*, vol. 28, pp. 257-265, 2009.
- [124] A. J. Ijspeert, A. Crespi, D. Ryczko, and J.-M. Cabelguen, "From Swimming to Walking with a Salamander Robot Driven by a Spinal Cord Model," *Science*, vol. 315, pp. 1416-1420, March 9, 2007 2007.
- [125] B. B. Dey, S. Manjanna, and G. Dudek, "Ninja legs: Amphibious one degree of freedom robotic legs," in *Intelligent Robots and Systems (IROS), 2013 IEEE/RSJ International Conference on*, 2013, pp. 5622-5628.
- [126] M. A. Woodward and M. Sitti, "Design of a miniature integrated multi-modal jumping and gliding robot," in *Intelligent Robots and Systems (IROS), 2011 IEEE/RSJ International Conference on*, 2011, pp. 556-561.
- [127] A. L. Desbiens, A. Asbeck, and M. Cutkosky, "Hybrid aerial and scansorial robotics," in *Robotics and Automation (ICRA), 2010 IEEE International Conference on*, 2010, pp. 72-77.
- [128] V. Hayward, "Is there a 'plenhaptic' function?," *Philosophical Transactions of the Royal Society B: Biological Sciences*, vol. 366, pp. 3115-3122, 2011.
- [129] D. T. Westwick and R. E. Kearney, *Identification of nonlinear physiological systems* vol. 7: John Wiley & Sons, 2003.
- [130] D. T. Westwick, E. A. Pohlmeier, S. A. Solla, L. E. Miller, and E. J. Perreault, "Identification of Multiple-Input Systems with Highly Coupled Inputs: Application to EMG Prediction from Multiple Intracortical Electrodes," *Neural Computation*, vol. 18, pp. 329-355, 2006/02/01 2006.

- [131] P. R. Bandyopadhyay, "Maneuvering Hydrodynamics of Fish and Small Underwater Vehicles," *Integrative and Comparative Biology*, vol. 42, pp. 102-117, February 1, 2002 2002.
- [132] D. H. Thorsen, J. J. Cassidy, and M. E. Hale, "Swimming of larval zebrafish: fin-axis coordination and implications for function and neural control," *Journal of Experimental Biology*, vol. 207, pp. 4175-4183, 2004.
- [133] P. Domenici and R. Blake, "The kinematics and performance of fish fast-start swimming," *The Journal of Experimental Biology*, vol. 200, pp. 1165-1178, 1997.
- [134] R. W. BLAKE, "The Energetics of Hovering in the Mandarin Fish (*Synchropus Picturatus*)," *The Journal of Experimental Biology*, vol. 82, pp. 25-33, 1979.
- [135] N. Kato and M. Furushima, "Pectoral fin model for maneuver of underwater vehicles," in *Autonomous Underwater Vehicle Technology, 1996. AUV '96., Proceedings of the 1996 Symposium on*, 1996, pp. 49-56.
- [136] P. E. Sitorus, Y. Y. Nazaruddin, E. Leksono, and A. Budiyo, "Design and Implementation of Paired Pectoral Fins Locomotion of Labriform Fish Applied to a Fish Robot," *Journal of Bionic Engineering*, vol. 6, pp. 37-45, 3// 2009.
- [137] Y. Yingchen, N. Nam, C. Nannan, L. Michael, T. Craig, H. Huan, *et al.*, "Artificial lateral line with biomimetic neuromasts to emulate fish sensing," *Bioinspiration & Biomimetics*, vol. 5, p. 016001, 2010.
- [138] M. A. MacIver, E. Fontaine, and J. W. Burdick, "Designing future underwater vehicles: principles and mechanisms of the weakly electric fish," *IEEE Journal of Oceanic Engineering*, vol. 29, pp. 651-659, 2004.
- [139] J. L. Tangorra, C. J. Esposito, and G. V. Lauder, "Biorobotic fins for investigations of fish locomotion," in *2009 IEEE/RSJ International Conference on Intelligent Robots and Systems*, 2009, pp. 2120-2125.
- [140] B. E. Flammang and G. V. Lauder, "<div xmlns='Speed-dependent intrinsic caudal fin muscle recruitment during steady swimming in bluegill sunfish, Lepomis macrochirus</div>," *Journal of Experimental Biology*, vol. 211, pp. 587-598, 2008.
- [141] B. E. Flammang and G. V. Lauder, "Caudal fin shape modulation and control during acceleration, braking and backing maneuvers in bluegill sunfish," *Journal of Experimental Biology*, vol. 212, p. 277, 2008.

- [142] J. A. Mather, U. Griebel, and R. A. Byrne, "Squid dances: an ethogram of postures and actions of *Sepioteuthis sepioidea* squid with a muscular hydrostatic system," *Marine and Freshwater Behaviour and Physiology*, vol. 43, pp. 45-61, 2010.
- [143] L. H. Tyson, "Software techniques for two- and three-dimensional kinematic measurements of biological and biomimetic systems," *Bioinspiration & Biomimetics*, vol. 3, p. 034001, 2008.
- [144] J. L. Tangorra, S. N. Davidson, I. W. Hunter, P. G. A. Madden, G. V. Lauder, H. Dong, *et al.*, "The Development of a Biologically Inspired Propulsor for Unmanned Underwater Vehicles," *Oceanic Engineering, IEEE Journal of*, vol. 32, pp. 533-550, 2007.
- [145] S. Floyd, T. Keegan, J. Palmisano, and M. Sitti, "A Novel Water Running Robot Inspired by Basilisk Lizards," in *2006 IEEE/RSJ International Conference on Intelligent Robots and Systems*, 2006, pp. 5430-5436.
- [146] A. Lussier Desbiens, A. T. Asbeck, and M. R. Cutkosky, "Landing, perching and taking off from vertical surfaces," *The International Journal of Robotics Research*, January 20, 2011 2011.
- [147] S. Sefati, I. Neveln, M. A. MacIver, E. S. Fortune, and N. J. Cowan, "Counter-propagating waves enhance maneuverability and stability: A bio-inspired strategy for robotic ribbon-fin propulsion," in *Biomedical Robotics and Biomechatronics (BioRob), 2012 4th IEEE RAS & EMBS International Conference on*, 2012, pp. 1620-1625.
- [148] S. H. Suhr, Y. S. Song, S. J. Lee, and M. Sitti, "Biologically Inspired Miniature Water Strider Robot," in *Robotics: Science and Systems*, 2005, pp. 319-326.
- [149] K. Karakasiliotis and A. J. Ijspeert, "Analysis of the terrestrial locomotion of a salamander robot," in *Intelligent Robots and Systems, 2009. IROS 2009. IEEE/RSJ International Conference on*, 2009, pp. 5015-5020.
- [150] E. Moore, D. Campbell, F. Grimmering, and M. Buehler, "Reliable stair climbing in the simple hexapod 'RHex'," in *Robotics and Automation, 2002. Proceedings. ICRA'02. IEEE International Conference on*, 2002, pp. 2222-2227.
- [151] U. Saranli and D. E. Koditschek, "Back flips with a hexapedal robot," in *Robotics and Automation, 2002. Proceedings. ICRA'02. IEEE International Conference on*, 2002, pp. 2209-2215.
- [152] A. T. Asbeck, S. Kim, M. R. Cutkosky, W. R. Provancher, and M. Lanzetta, "Scaling hard vertical surfaces with compliant microspine arrays," *The International Journal of Robotics Research*, vol. 25, pp. 1165-1179, 2006.

- [153] A. Crespi and A. J. Ijspeert, "Online optimization of swimming and crawling in an amphibious snake robot," *Robotics, IEEE Transactions on*, vol. 24, pp. 75-87, 2008.
- [154] R. Altendorfer, N. Moore, H. Komsuoglu, M. Buehler, H. B. Brown Jr, D. McMordie, *et al.*, "RHex: a biologically inspired hexapod runner," *Autonomous Robots*, vol. 11, pp. 207-213, 2001.
- [155] J. B. Pollack, H. Lipson, S. Ficici, P. Funes, G. Hornby, and R. A. Watson, "Evolutionary techniques in physical robotics," in *Evolvable Systems: from biology to hardware*, ed: Springer, 2000, pp. 175-186.
- [156] H. Lipson, J. C. Bongard, V. Zykov, and E. Malone, "Evolutionary Robotics for Legged Machines: From Simulation to Physical Reality," in *IAS*, 2006, pp. 11-18.
- [157] D. Marbach and A. J. Ijspeert, "Online optimization of modular robot locomotion," in *Mechatronics and Automation, 2005 IEEE International Conference*, 2005, pp. 248-253.
- [158] L. Yang, C.-M. Chew, A. N. Poo, and T. Zielinska, "Adjustable bipedal gait generation using genetic algorithm optimized Fourier series formulation," in *Intelligent Robots and Systems, 2006 IEEE/RSJ International Conference on*, 2006, pp. 4435-4440.
- [159] R. Salomon, "Evolutionary algorithms and gradient search: similarities and differences," *Evolutionary Computation, IEEE Transactions on*, vol. 2, pp. 45-55, 1998.
- [160] T. Hedrick and T. Daniel, "Flight control in the hawkmoth *Manduca sexta*: the inverse problem of hovering," *The journal of experimental Biology*, vol. 209, pp. 3114-3130, 2006.
- [161] N. Doorly, K. Irving, G. McArthur, K. Combie, V. Engel, H. Sakhtah, *et al.*, "Biomimetic evolutionary analysis: robotically-simulated vertebrates in a predator-prey ecology," in *Artificial Life, 2009. ALife'09. IEEE Symposium on*, 2009, pp. 147-154.
- [162] K. Krishnakumar, "Micro-genetic algorithms for stationary and non-stationary function optimization," in *1989 Advances in Intelligent Robotics Systems Conference*, 1990, pp. 289-296.
- [163] J. L. Tangorra, G. V. Lauder, P. G. Madden, R. Mittal, M. Bozkurtas, and I. W. Hunter, "A biorobotic flapping fin for propulsion and maneuvering," in *Robotics and Automation, 2008. ICRA 2008. IEEE International Conference on*, 2008, pp. 700-705.

- [164] M. Bozkurtas, R. Mittal, H. Dong, G. Lauder, and P. Madden, "Low-dimensional models and performance scaling of a highly deformable fish pectoral fin," *Journal of Fluid Mechanics*, vol. 631, pp. 311-342, 2009.
- [165] S. Ramakrishnan, M. Bozkurtas, R. Mittal, and G. V. Lauder, "Thrust production in highly flexible pectoral fins: a computational dissection," *Marine Technology Society Journal*, vol. 45, pp. 56-64, 2011.
- [166] C. A. C. Coello and G. T. Pulido, "Multiobjective optimization using a micro-genetic algorithm."
- [167] E. Zitzler and L. Thiele, "Multiobjective evolutionary algorithms: a comparative case study and the strength Pareto approach," *evolutionary computation, IEEE transactions on*, vol. 3, pp. 257-271, 1999.
- [168] J. Yen, J. C. Liao, B. Lee, and D. Randolph, "A hybrid approach to modeling metabolic systems using a genetic algorithm and simplex method," *Systems, Man, and Cybernetics, Part B: Cybernetics, IEEE Transactions on*, vol. 28, pp. 173-191, 1998.
- [169] S. W. Mahfoud, "Niching methods for genetic algorithms," *Urbana*, vol. 51, pp. 62-94, 1995.
- [170] S. Bhattacharyya and H. H. Asada, "Control of a compact, tetherless ROV for in-contact inspection of complex underwater structures," in *Intelligent Robots and Systems (IROS 2014), 2014 IEEE/RSJ International Conference on*, 2014, pp. 2265-2272.
- [171] J. Yuh, "Design and Control of Autonomous Underwater Robots: A Survey," *Autonomous Robots*, vol. 8, pp. 7-24, 2000/01/01 2000.
- [172] N. E. Leonard, "Stability of a bottom-heavy underwater vehicle," *Automatica*, vol. 33, pp. 331-346, 3// 1997.
- [173] S. Devasia, "Should model-based inverse inputs be used as feedforward under plant uncertainty?," *Automatic Control, IEEE Transactions on*, vol. 47, pp. 1865-1871, 2002.
- [174] A. D. Buchan, D. W. Haldane, and R. S. Fearing, "Automatic identification of dynamic piecewise affine models for a running robot," in *2013 IEEE/RSJ International Conference on Intelligent Robots and Systems*, 2013, pp. 5600-5607.
- [175] P. Yong-Jai, J. Useok, L. Jeongsu, K. Seok-Ryung, K. Ho-Young, and C. Kyu-Jin, "Kinematic Condition for Maximizing the Thrust of a Robotic Fish Using a Compliant Caudal Fin," *Robotics, IEEE Transactions on*, vol. 28, pp. 1216-1227, 2012.

- [176] L. DeVries and D. A. Paley, "Observability-based optimization for flow sensing and control of an underwater vehicle in a uniform flowfield," in *American Control Conference (ACC), 2013*, 2013, pp. 1386-1391.
- [177] E. Gillies, "Multiple sensor control of vortex shedding," *AIAA journal*, vol. 39, pp. 748-750, 2001.
- [178] V. Roberto, A. Otari, V. Francesco, J. Jaas, D. C. Lily, T. Gert, *et al.*, "Hydrodynamic pressure sensing with an artificial lateral line in steady and unsteady flows," *Bioinspiration & Biomimetics*, vol. 7, p. 036004, 2012.
- [179] B. T. Hinson and K. A. Morgansen, "Observability-Based Optimal Sensor Placement for Flapping Airfoil Wake Estimation," *Journal of Guidance, Control, and Dynamics*, pp. 1-10, 2014.
- [180] S. Coombs, "Smart Skins: Information Processing by Lateral Line Flow Sensors," *Autonomous Robots*, vol. 11, pp. 255-261, 2001/11/01 2001.
- [181] Y. Yang, J. Chen, J. Engel, S. Pandya, N. Chen, C. Tucker, *et al.*, "Distant Touch Hydrodynamic Imaging with an Artificial Lateral Line," *Proceedings of the National Academy of Sciences of the United States of America*, vol. 103, pp. 18891-18895, 2006.
- [182] J. H. Solomon and M. J. Z. Hartmann, "Extracting Object Contours with the Sweep of a Robotic Whisker Using Torque Information," *The International Journal of Robotics Research*, vol. 29, pp. 1233-1245, August 1, 2010 2010.
- [183] V. Hayward, "Is there a 'plenhaptic' function?," *Philosophical Transactions of the Royal Society B: Biological Sciences*, vol. 366, pp. 3115-3122, November 12, 2011 2011.
- [184] P. Pourcelot, F. Audigé, C. Degueurce, D. Geiger, and J. M. Denoix, "A method to synchronise cameras using the direct linear transformation technique," *Journal of Biomechanics*, vol. 33, pp. 1751-1754, 12// 2000.
- [185] B. E. Flammang, S. Alben, P. G. Madden, and G. V. Lauder, "Functional morphology of the fin rays of teleost fishes," *Journal of morphology*, 2013.
- [186] R. Ruiz-Torres, O. M. Curet, G. V. Lauder, and M. A. MacIver, "Kinematics of the ribbon fin in hovering and swimming of the electric ghost knifefish," *The Journal of Experimental Biology*, vol. 216, pp. 823-834, March 1, 2013 2013.
- [187] Y. C. Liang, H. P. Lee, S. P. Lim, W. Z. Lin, K. H. Lee, and C. G. Wu, "Proper orthogonal decomposition and its applications—Part 1: Theory," *Journal of Sound and Vibration*, vol. 252, pp. 527-544, 5/2/ 2002.

Appendix A Supplemental Written Materials

8.1 Scope of the Thesis

There are many ways in which distributed, heterogeneous, fin-intrinsic sensing could be used in robotic fins, including:

- a) For sensory mediated control of high speed propulsion.
- b) For characterization of the fluid environment.
- c) For sensory mediated control of low speed maneuvers and hovering.
- d) For touch sensing and interaction with obstacles.

However, to address all four would be beyond the scope of a single thesis as these areas straddle multiple disciplines in engineering and several research programs in biology. All four of these areas have some relevance to biological systems and have implications for engineering applications. Two of the four identified areas were selected for the dissertation work and were deemed appropriate for the scope of the core research question.

There were three primary criteria that were used to evaluate whether a particular use of fin-intrinsic sensing was appropriate for inclusion in this thesis. The first criterion was that the use of fin-intrinsic sensing *requires a distributed and heterogeneous sensor pool*. A primary feature of intrinsic sensing in the fish is that the sensors are distributed throughout tissue, and in many other biological systems, a diverse set of sensory cell bodies are used to measure mechanical phenomena. In cases where a single sensor could do the job of a set of sensors, engineers will continue to use a single sensor rather than

consider multiple distributed sensors. Thus, if a use of fin-intrinsic sensing could rely on a single sensor or one sensor type, it was eliminated from consideration. The uses for fin-intrinsic sensation should only be evaluated if there is not an existing engineering approach. The second criterion was that the use of fin-intrinsic sensing be *biologically relevant to the fish*, either behaviorally or neurologically. The goal of biologically-inspired engineering should be to actually learn from nature before adapting it to human applications. If features of biological systems are adapted to engineering systems before being well understood, the role of these features may be misinterpreted and then the engineering research has no utility for biologists seeking deeper knowledge. Thus, if a use of fin-intrinsic sensing was not directly relevant to the fish, it was eliminated from consideration. The last criterion was that the use of fin-intrinsic sensation be *novel, without significant research being pursued in the area*. In this way, the research pursued in this thesis can make novel contributions to the state of the art in biologically-inspired robotics and underwater sensing.

8.1.1 For sensory mediated control of high speed propulsion.

It has been shown that the degree of bending in a flexible fin significantly affects its force production, and therefore intrinsic bending sensation can provide feedback for force control of fins. A recent engineering study by the author's colleagues showed that bending feedback could enable a flexible foil to drive at its mechanical resonance, maximizing the thrust force of the foil [62]. Distributed bending sensation may be enable further optimization of propulsive forces, as a recent study identified that bending at the distal tips of fins/wings of multiple animal taxa seems to occur at the same location and to the same magnitude when the animal is engaged in steady state locomotion [8]. Recent

work with robotic, compliant caudal fins suggests that maintaining a fixed phase difference between the base and tip of a fin may maximize its thrust production [175], which provides a strong argument for monitoring bending during steady state propulsion. Thus, fin intrinsic sensation of the base and the tips of propulsors may be of significant benefit for control of high speed propulsion.

However, even though some distributed measurement may be important to characterize forces in high speed locomotion, the kinematic modes of high speed motions are relatively simple and do not require many sensors to characterize. For instance, in work by the author, it was shown that steady swimming forces could be predicted accurately (>80% accuracy) using only two bending sensors. Pressure sensors (a second sensing modality) were not often even required to predict propulsive force in these cases. Complex motions that involved the movement of multiple fin regions (such as yaw turn maneuvers and customized swimming gaits) required high sensor counts and multiple sensor types. However, high speed propulsion does not rely on multiple fin regions or complex kinematic patterns, so it is unlikely that the use of fin-intrinsic sensing during high speed propulsion would require distributed or heterogeneous sensors.

Therefore, fin intrinsic sensation in high speed propulsion is not of primary importance to this thesis because it may not require a significantly *distributed* or *heterogeneous* sensor pool. Further, this area is not of major focus to this thesis because it is currently being addressed by colleagues in other funded research that focuses on the closed-loop control of high-speed propulsion [62].

8.1.2 *For characterization of the fluid environment.*

Many researchers examine the role of sensors to characterize properties of the fluid environment. Fluidic properties of interest have included flow speed [176], direction of flow [42], wakes of upstream objects [177], and properties of vortex streets [178]. During swimming, fluidic properties have been estimated such as vortex wake from a foil [179]. It has been demonstrated that flow characterization is sensitive to sensor orientation, spatial distributions of sensors, and the spectral sensitivities of the set of sensors [41, 180].

Much of what is known about characterizing the underwater environment with sensors is from research into the fish lateral line sensory system. Engineers and biologists have investigated the role of the lateral line of fish, a sensory system comprised of spatially distributed flow sensors on their bodies [78]. Research of the biological lateral line has shown that the lateral line responds to low frequency stimuli in water, which include near-field moving objects, the animal's own movements, and movements of surrounding fluid [180]. To characterize flows, researchers have constructed artificial lateral line arrays [41]. Research with artificial, engineered, lateral lines has shown that these sensory systems can be used to localize a fluidic dipole source [181], and even a crayfish's natural vibrations [137].

However, there is no strong biological evidence that fin intrinsic sensation in the sunfish is being used to sense fluidic phenomena in the environment. In the same way that researchers have said that a fish's lateral line may provide a sense of "distant touch" to objects through their wakes [181], it could be that fin-intrinsic sensation is useful in mediating schooling behavior, detecting the wakes of prey or predators, or identifying flow properties, but there is currently little behavioral or neurobiological evidence to

support these assertions. It is presumable that fin intrinsic sensation could be used to measure and characterize coherent structures in flow, but the lack of biological evidence and the presence of strong existing approaches to this type of sensing (with artificial lateral lines) led the author to focus on more biologically-relevant, less-explored uses of fin intrinsic sensation in robotic fins.

8.1.3 *For sensory mediated control of low speed maneuvers and hovering.*

We expect that fin-intrinsic sensation should be most useful when trying to precisely control the 3d propulsive force at low speeds. The author has shown that prediction of propulsive forces of multiple gaits requires distributed bending and pressure sensors, and the complexity of kinematics increases, the number of sensors and types of sensors must increase to predict forces well. This is strong evidence that fin intrinsic sensing should be *distributed* and *heterogeneous* especially during low speed maneuvers and hovering, where kinematics are complex and varied.

For the bluegill sunfish, fin kinematics must be more complex and varied at lower swimming speeds than at higher speeds. Sunfish are statically unstable due to their body's center of buoyancy being located below its center of gravity [9]. This means that at low swimming speeds, or when the fish is hovering in place, it must create and control its 3d propulsive force through time to avoid rolling or pitching over. This requires complex pectoral fin kinematics, and the author has shown that the sunfish executes multiple (10-12) distinct kinematic patterns during hovering [23]. Further, the sunfish pectoral fin kinematics are frequently updated mid stroke, such that the fin will start a stroke by executing one pattern and then switch to another pattern before completing the fin beat. These complex behaviors seen during hovering suggest that local fin regions are

under closed-loop control and this control occurs at an update rate faster than one fin beat.

Hovering is a task where fin intrinsic sensation could be very useful. If multiple regions of the fin are executing 3d kinematics, then the propulsive forces are the result of a complex, nonlinear interaction between those fin regions and the fluid. We expect that in order to control the forces coming from each region, it could be helpful to have mechanical measures from these fin regions. An extrinsic measure, such as an inertial sensor in the fish body, or a reaction force measure at the fin base, cannot recover the local forces created by the fin. For example, if multiple regions of the fin can produce thrust, and an extrinsic sensor sees that thrust force is low during a behavior, there is no immediate way to know which region of the fin is responsible, or how to update the kinematics to correct this issue. But with distributed bending sensors, the fin can observe when the bending of a particular fin region is incorrect and the control can provide a feedback to the fin region to increase the thrust force. In this way, having local measures of bending, pressure, stretch, or curvature of the fin can inform the control of the many degrees of freedom the fin has.

Therefore, the primary focus of the thesis is to understand the use of fin intrinsic sensation during low speed maneuvers and hovering, because the application likely requires a distributed and heterogeneous sensor pool, and due the biological evidence of tighter closed-loop control during these modes of swimming.

8.1.4 For touch sensing and interaction with obstacles.

It is expected that fin-intrinsic sensation could be useful in sensing contact with obstacles in the underwater environment.

Since fluidic loading affects the dynamics of fins and the dynamics of obstacles, it is expected that heterogeneity and distribution of sensors are both important characteristics for this use of fin-intrinsic sensing. In work with terrestrial whisker sensors, it has been shown that torque measurements from a cantilever beam can be used to estimate the shape of a target object by striking that object multiple times at different points [182]. However, unlike whisker sensing, where in most cases the probe is less rigid than the target object [183], fins are generally more rigid than the fluid medium and could be more or less rigid than the objects they contact. In order to estimate the propulsive forces of complex fins, distributed and heterogeneous sensors are needed, and thus multiple sensors are required for understanding contact before the fin strikes its target object. Unlike a whisker sensor, multiple parts of a fin may contact an object at the same time and so data from a distribution of sensors could help resolve the shape of an object, whereas data from a single sensor may not be sufficient. Heterogeneous sensors may also be necessary in order to distinguish between fluidic loading and contact forces, which arise from different physical phenomena.

Since obstacle contact with pectoral fins is a behavior observed in the sunfish and it likely requires distributed and heterogeneous sensing, the secondary research area of this thesis is to understand the use of fin-intrinsic sensing during obstacle contact to discriminate contact loading from fluidic loading. Fish use their pectoral fins to contact obstacles so this behavior (and the use of fin-intrinsic sensing) has direct biological relevance. Additionally, very little attention has been devoted to this topic in engineering research, so it has significant potential for advancing the state of the art of contact sensing in underwater environments using robots.

8.2 Tracking of fins

The analysis of sunfish fins typically begins with calibrated high speed video of the sunfish executing a behavior of interest. The fins of sunfish are very thin, highly deformable, and highly flexible and reliable marker-based tracking methods have not been developed. The goal from an engineering standpoint is to use high speed video to obtain an accurate representation of the kinematics of the pectoral fin and sunfish body. The video is planar, whereas the kinematics of fins are three dimensional, so transform techniques have been developed to map from the image coordinates to the object coordinates. One of the most popular methods in biological systems analysis is the direct linear transform (DLT). The equations of the DLT are typically given by (as in [184]):

$$x + \delta x = \frac{L_1 X + L_2 Y + L_3 Z + L_4}{L_9 X + L_{10} Y + L_{11} Z + 1} \quad (60)$$

$$y + \delta y = \frac{L_5 X + L_6 Y + L_7 Z + L_8}{L_9 X + L_{10} Y + L_{11} Z + 1} \quad (61)$$

where (x, y) are the coordinates of the point in the image, $(\delta x, \delta y)$ are the errors associated with the coordinates, (X, Y, Z) are the coordinates of the object in space, and $(L_1, L_2, \dots, L_{11})$ are unknown the DLT parameters of each camera. The errors $(\delta x, \delta y)$ are typically optical errors with the camera and are often nonlinear functions of the lens distortion.

The unknown DLT parameters are desired in order to map from image coordinates to object coordinates. In this application, they are obtained using camera calibration methods and least-squares regression.

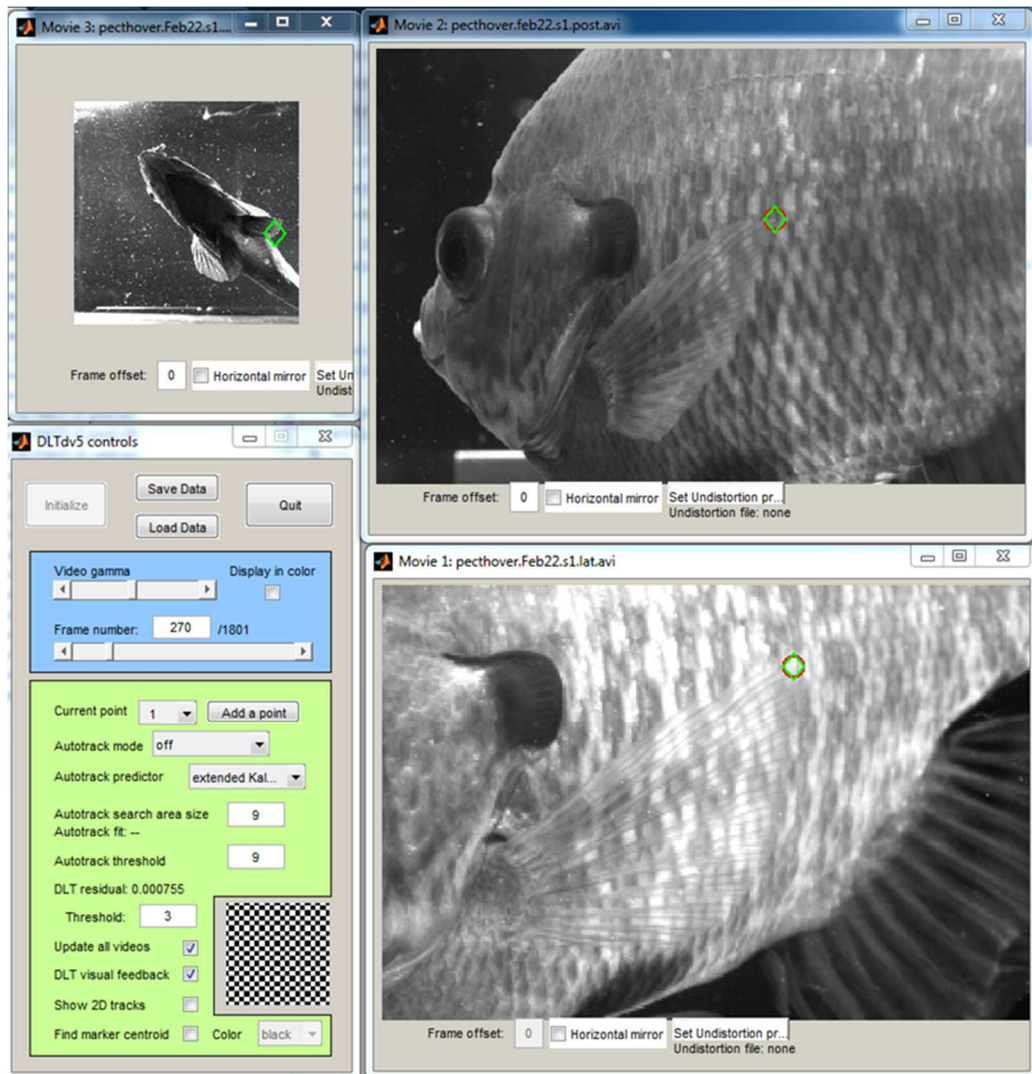


Figure 68. Interface of DLTdv5 tracking program during tracking of points on sunfish pectoral fin. Points along the pectoral fins were assigned by subdividing major fin rays into ten equal components. Tracking was performed by hand based on visual features in the fins.

8.2.1 Implementation of kinematics on biorobotic fin

The tracked 3D points were shifted from the global image frame to a local coordinate frame with the origin on a rigid segment of the body of the fish (Figure 69). Thus, fin kinematics were computed relative to a moving body frame on the fish.

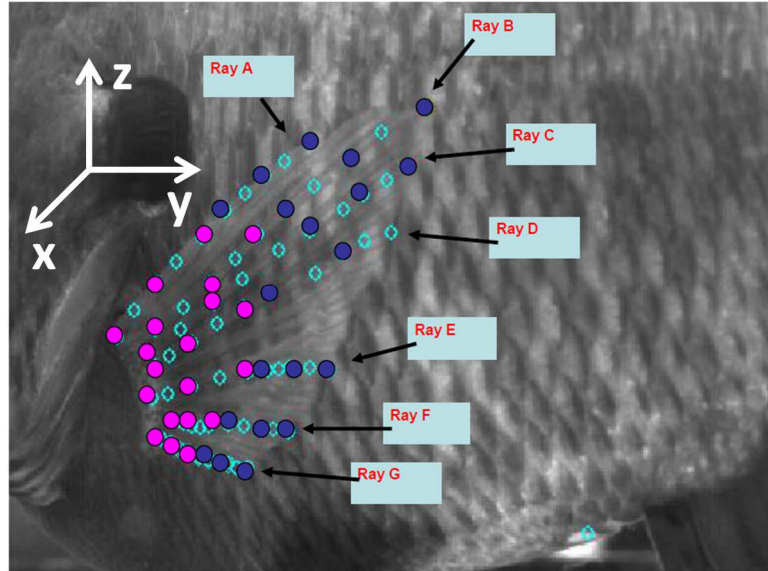


Figure 69. Tracking points along fictive rays A through G and the local coordinate frame on body of the bluegill sunfish.

Points along the fin are grouped into fictive *rays* (labeled *ray A* through *ray F*), where each ray starts at the proximal base of the pectoral fin and terminates at the distal tip of the fin. This tracking convention is typical in similar work [18, 69, 164, 185, 186] because it is not feasible to precisely track all 14 fin rays with current methods [143].

Each fictive *ray* (A-F) is then mapped to a ray on the biorobotic fin. Details of this process can be found in prior work [17], but the methods are summarized here. First, the fin points are rotated such that the most proximal points on *ray A* and *ray F* lie in the yz -plane. Then the fin points are rotated to minimize the mean-square distance between all other points and the yz -plane at the first time instant.

After rotations of the fin points, the center of rotation is determined for each fin ray about both the z - and x -axes. This is done by first projecting the ray points through

time onto each of the yz - and xy -planes. At each time instant, the three proximal-most points are fit by a linear regression and this process is repeated to generate a series of lines. A best-fit intersection point is identified (by *MSE*) and the *center of rotation* is identified. This process is repeated to identify a *center of rotation* for both z - and x -axis rotations, which correspond to the flap and sweep degrees of freedom of the robotic fin rays. A *center of rotation* is identified for all rays *A-G*, and is used to compute rotation vectors through time for each of the fin rays. These rotation vectors are then mapped to the degrees of freedom of the robot in the flap and sweep directions of actuation.

8.2.2 Kinematic Analysis of fish fins with POD/PCA

Point tracking is a very labor-intensive process that produces a high order representation of the kinematics of the sunfish pectoral fin. In prior work, as many as 63 [23] or over 100 points [70] are tracked by hand over several dozen image frames per point in order to describe the kinematics of the fin membrane. The combination of several, lower-order processes may be sufficient to capture the important aspects of the kinematics without requiring perfect fidelity to the biological system. The goal of this section is to explain how to obtain lower order representations of the kinematics that can be evaluated to identify the mechanisms of force production in the pectoral fins.

Principle component analysis (PCA) is a data analysis technique that seeks to obtain a reduced-dimensional representation of a high-dimensional process or dataset. This technique falls under the category of proper orthogonal decomposition (POD) methods including Karhunen-Loève decomposition and singular value decomposition (SVD) [187]. The fundamental idea of these methods is to find a set of orthonormal basis vectors such that data can be expressed sub-optimally using a reduced number of basis

vectors. Mean squared error (MSE) is frequently used as an optimality metric for PCA, such that:

$$E\left[\|x - x(l)\|^2\right] \leq E\left[\|x - \hat{x}(l)\|^2\right] \quad (62)$$

Where E is the expected value function, $x(l)$ approximates a random vector x using the first l orthonormal basis vectors of x and $\hat{x}(l)$ approximates x using arbitrary l basis vectors. In short, the mean squared error of the space spanned by l ordered basis vectors should be less than that of the MSE for l arbitrary basis vectors. These orthonormal basis vectors are often referred to as the *modes* of the data.

The method, as applied to the pectoral fin data, is carried out using the following procedure:

1. Construct a matrix of displacements from the x,y,z triples of the tracking data, using (63)
2. Compute the SVD of the displacement matrix and obtain singular values, using (64)
3. Arrange the singular values of the SVD by magnitude from largest to smallest
4. Determine the kinematic modes associated with largest singular values and their combinations

In summary, after multiple points (x,y,z triples) are tracked on the fin, a displacement matrix (63) is analyzed for each kinematic pattern observed.

$$\Delta X = \begin{bmatrix} \Delta x_1(t_1) & \Delta y_1(t_1) & \Delta z_1(t_1) & \cdots & \Delta x_m(t_1) & \Delta y_m(t_1) & \Delta z_m(t_1) \\ \Delta x_1(t_2) & \Delta y_1(t_2) & \Delta z_1(t_2) & \cdots & \Delta x_m(t_2) & \Delta y_m(t_2) & \Delta z_m(t_2) \\ \vdots & \vdots & \vdots & \ddots & \vdots & \vdots & \vdots \\ \Delta x_1(t_n) & \Delta y_1(t_n) & \Delta z_1(t_n) & \cdots & \Delta x_m(t_n) & \Delta y_m(t_n) & \Delta z_m(t_n) \end{bmatrix} \quad (63)$$

A singular value decomposition (SVD) of the above displacement matrix is given by:

$$\Delta X_{n \times 3m} = U_{n \times n} \Sigma_{n \times 3m} V_{3m \times 3m}^T \quad (64)$$

where U and V are orthogonal unitary matrices; n is the number of time steps in the flapping cycle, and m is the number of surface points on the pectoral fin. The singular values identified in the Σ matrix can be compared between kinematic patterns. This analysis is used to determine a reduced order (modal) description of the kinematics seen in swimming gaits and which features may be common among gaits.

Appendix B Equipment datasheets

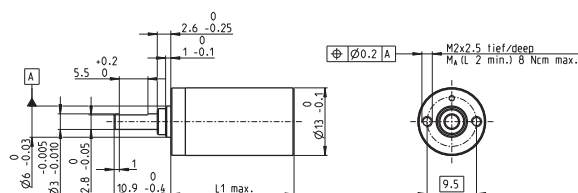
8.3 Major Equipment

8.4 Actuators

B1. Touch fin motor gearhead

Planetary Gearhead GP 13 A 13 mm, 0.2 - 0.35 Nm

maxon gear



M 1:1

Technical Data

Planetary Gearhead	straight teeth
Output shaft	stainless steel, hardened
Bearing at output	sleeve bearing
Radial play, 6 mm from angle	max. 0.055 mm
Axial play	0.02 - 0.10 mm
Max. permissible axial load	8 N
Max. permissible force for press ts	100 N
Sense of rotation, drive to output	=
Recommended input speed	< 8000 rpm
Recommended temperature range	-40 ... +100°C
Number of stages	1 2 3 4 5
Max. radial load, 6 mm from angle	8 N 12 N 16 N 20 N 20 N

- ☒ Stock program
☐ Standard program
☐ Special program (on request)

Order Number

Gearhead Data	110313	110314	110315	110316	110317
1 Reduction	4.1 : 1	17 : 1	67 : 1	275 : 1	1119 : 1
2 Reduction absolute	57/14	3249/100	185193/2744	10556001/38410	601692007/337824
3 Max. motor shaft diameter	mm 1.5	1.5	1.5	1.5	1.5
Order Number	352365	352366	352367	352368	352369
1 Reduction	5.1 : 1	26 : 1	131 : 1	664 : 1	3373 : 1
2 Reduction absolute	66/13	4354/169	281496/2197	18814736/28561	1252332576/371293
3 Max. motor shaft diameter	mm 1.5	1.5	1.5	1.5	1.5
4 Number of stages	1	2	3	4	5
5 Max. continuous torque	Nm 0.20	0.20	0.30	0.30	0.35
6 Intermittently permissible torque at gear output	Nm 0.30	0.30	0.45	0.45	0.53
7 Max. efficiency	% 91	83	75	69	62
8 Weight	g 11	14	17	20	23
9 Average backlash no load	" 1.0	1.2	1.5	1.8	2.0
10 Mass inertia	gcm ² 0.025	0.015	0.015	0.015	0.015
11 Gearhead length L1*	mm 16.0	19.9	23.7	27.6	31.4

*for A-max 12 and RE-max 13 L1 is + 0.3 mm



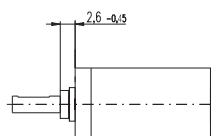
maxon Modular System

+ Motor	Page	+ Sensor/Brake	Page	Overall length [mm] = Motor length + gearhead length + (sensor / brake) + assembly parts				
RE 13	57/59			35.4	39.3	43.1	47.0	50.8
RE 13, 0.75 W	59	MR	255-257	42.5	46.4	50.2	54.1	57.9
RE 13, 0.75 W	59	MEnc 13	274	43.2	47.1	50.9	54.8	58.6
RE 13	61/63			47.6	51.5	55.3	59.2	63.0
RE 13, 2 W	63	MR	255-257	54.7	58.6	62.4	66.3	70.1
RE 13, 2 W	63	MEnc 13	274	55.4	59.3	63.1	67.0	70.8
RE 13, 1.5 W	65/67			38.5	42.4	46.2	50.1	53.9
RE 13, 1.5 W	67	MR	255-257	44.6	48.5	52.3	56.2	60.0
RE 13, 1.5 W	67	MEnc 13	274	46.5	50.4	54.2	58.1	61.9
RE 13, 3 W	69/71			50.7	54.6	58.4	62.3	66.1
RE 13, 3 W	71	MR	255-257	56.8	60.7	64.5	68.4	72.2
RE 13, 3 W	71	MEnc 13	274	58.7	62.6	66.4	70.3	74.1
A-max 12	87/88			37.6	41.5	45.3	49.2	53.0
A-max 12, 0.5 W	88	MR	255-257	41.7	45.6	49.4	53.3	57.1
RE-max 13	115/116			36.9	40.8	44.6	48.5	52.3
RE-max 13, 0.75 W	116	MR	255-257	41.6	45.5	49.3	53.2	57.0
RE-max 13	117/118			47.9	51.8	55.6	59.5	63.3
RE-max 13, 2 W	118	MR	255-257	52.6	56.5	60.3	64.2	68.0
EC 13, 6 W	141			37.4	41.3	45.1	49.0	52.8
EC 13, 12 W	142			49.6	53.5	57.3	61.2	65.0

Option Ball Bearing

Order Number

Technical Data



Gearhead length: L1 + 0.2 mm

4.1 : 1	144300	131 : 1	352393
5.1 : 1	352391	275 : 1	144303
17 : 1	144301	664 : 1	352394
26 : 1	352392	1119 : 1	144304
67 : 1	144302	3373 : 1	352395

Planetary Gearhead	straight teeth
Output shaft	stainless steel, hardened
Bearing at output	preloaded ball bearings
Radial play, 6 mm from angle	max. 0.04 mm
Axial play at axial load	< 5 N 0 mm
	> 5 N max. 0.04 mm
Max. permissible axial load	8 N
Max. permissible force for press ts	25 N
Sense of rotation, drive to output	=
Recommended input speed	< 8000 rpm
Recommended temperature range	-15 ... +100°C
Extended range as option	-35 ... +100°C
Number of stages	1 2 3 4 5
Max. radial load, 6 mm from angle	10 N 15 N 20 N 20 N 20 N
Gearhead values according to sleeve bearing version	

B3. *Touch fin motor general specifications and encoder settings*

Combination data

Nominal voltage	V	9
No load speed	min-	104
Max. continuous torque	Nm	0.3
Stall torque	mNm	0.45

Motor data

Article No.	118635	
Program	RE 13 13 mm, Graphite Brushes, 3 Watt	
Assigned power rating	W	3
Nominal voltage	V	9
No load speed	min-	13500
Stall torque	mNm	10.2
Max. continuous torque	mNm	2.22
Speed / torque gradient	min- / mNm-	1390
No load current	mA	62.5
Starting current	A	1.69
Terminal resistance	Ohm	5.32
Max. permissible speed	min-	16000
Nominal current (max. continuous current)	A	0.424
Max. efficiency		63.5
Torque constant	mNm / A-	6.06
Speed constant	min- / V-	1580
Mechanical time constant	ms	7.66
Rotor inertia	gcm	0.528
Terminal inductance	m	0.164
Thermal resistance housing-ambient	KW-	7
Thermal resistance winding-housing	KW-	33
Thermal time constant winding	s	4.76
Motor length	mm	34.5
Weight	g	27

Gear data

Article No.	352393	
Program	Planetary Gearhead GP 13 A 13 mm, 0.2 - 0.35 Nm, Metal Version, Ball Bearing	
Reduction		131:1
No. of stages		3
Max. continuous torque	Nm	0.3
Intermittently permissible torque at gear output	Nm	0.45
Sense of rotation, drive to output		=
Max. efficiency		75
Average backlash no load	°	1.5
Mass inertia	gcm	0.015
Gearhead length L1	mm	23.88
Weight	g	17
Max. motor shaft diameter	mm	1.5

Sensor data

Article No.	323054	
Program	Encoder MR, Type S, 64 - 256 CPT, 2 Channels, with Line Driver	
Counts per turn		256
Number of channels		2
Max. operating frequency	k	2.8125
Operating temperature range	°C	-25...
Weight	g	0
Shaft diameter	mm	0

B4. Servomotor for pectoral fin

8.5 Sensors

8.5.1 Strain gages for instrumented pectoral fin



PRE-WIRED STRAIN GAGES

PRECISION LINEAR PATTERN

KFH Series

- 2- or 3-Wire Models
- 120 or 350 Ω
- 0.6 to 20 mm Grid Lengths
- U Pre-Wired for Fast Installation
- U No Soldering at Measurement End
- U Broad Temperature Range
- U 2- or 3-Wire Models
- U Clear Alignment Marks








- U Bonds with Hot or Cold Cure Adhesives
- U PTFE Wire at Attachment End Prevents Sticking During Installation

Linear pattern precision gages with miniature and medium length grids are for general purpose and stress analysis applications. Available with either two 1-meter leads or three 3-meter leads and 120 or 350 Ω resistance. All models are compensated for steel.



Strain gage shown larger than actual size.

To Order Visit omega.com/kfh for Pricing and Details

GAGE PATTERN Leads not shown	MODEL NO. Pkg of 10	NOM. RESIS- TANCE (Ω)	DIMENSIONS mm (inch)				MAX V* (Vrms)	TEMP COMP	TERMINATION AND LEAD LENGTH
			GRID		CARRIER				
			A	B	C	D			
	0.3 mm GRID								
	KFH-03-120-C1-11L1M2R	120	0.3 (0.012)	1.96 (0.077)	4.5 (0.18)	3.9 (0.15)	1.5	ST	Two 1 m leads
	KFH-03-120-C1-11L3M2R	120					1.5	ST	Three 3 m leads
	0.6 mm GRID								
	KFH-06-120-C1-11L1M2R	120	0.6 (0.024)	1.1 (0.043)	4.8 (0.19)	3.9 (0.15)	1.5	ST	Two 1 m leads
	KFH-06-120-C1-11L3M3R	120					1.5	ST	Three 3 m leads
	1.5 mm GRID								
	KFH-1.5-120-C1-11L1M2R	120	1.5 (0.059)	1.5 (0.059)	5.8 (0.23)	3.9 (0.15)	2.5	ST	Two 1 m leads
	KFH-1.5-120-C1-11L3M3R	120					2.5	ST	Three 3 m leads
Shown actual size, 3 mm 	3 mm GRID								
	KFH-3-120-C1-11L1M2R	120	3.0 (0.118)	2.0 (0.079)	7.4 (0.29)	3.9 (0.15)	4	ST	Two 1 m leads
	KFH-3-120-C1-11L3M3R	120					4	ST	Three 3 m leads
	KFH-3-350-C1-11L1M2R	350					9	ST	Two 1 m leads
	KFH-3-350-C1-11L3M3R	350					9	ST	Three 3 m leads
Shown actual size, 6 mm 	6 mm GRID								
	KFH-6-120-C1-11L1M2R	120	6.0 (0.24)	2.0 (0.079)	10.5 (0.41)	3.9 (0.15)	8	ST	Two 1 m leads
	KFH-6-120-C1-11L3M3S	120					8	ST	Three 3 m leads
	KFH-6-350-C1-11L1M2R	350					15	ST	Two 1 m leads
	KFH-6-350-C1-11L3M3R	350					15	ST	Three 3 m leads
Shown actual size, 10 mm 	10 mm GRID								
	KFH-10-120-C1-11L1M2R	120	10 (0.39)	3.0 (0.12)	14.8 (0.58)	4.8 (0.19)	14	ST	Two 1 m leads
	KFH-10-120-C1-11L3M3R	120					14	ST	Three 3 m leads
Shown actual size, 20 mm 	20 mm GRID								
	KFH-20-120-C1-11L1M2R	120	20 (0.79)	3.0 (0.12)	25.2 (0.99)	4.8 (0.19)	7	ST	Two 1 m leads
	KFH-20-120-C1-11L3M3R	120					7	ST	Three 3 m leads

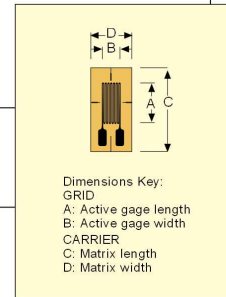
ACCESSORIES

MODEL NO.	DESCRIPTION
TT300	Complete heat cure adhesive kit
SG496	1 oz methyl-based cyanoacrylate (approximately 750 gages)
SG401	0.1 oz ethyl-based cyanoacrylate (approximately 50 gages)

* Maximum permitted bridge energizing voltage (Vrms)

Ordering Examples: KFH-1.5-120-C1-11L1M2S, a linear 1.5 mm grid, 120 Ω , with two 1 m leads.
KFH-3-350-C1-11L3M3S, a linear 3 mm grid, 350 Ω , with three 3 m leads per grid.

SPECIFICATIONS		
Strain Gage Construction		Foil strain gage with embedded measuring grid
Measuring Grid		
Material		Constantan
Thickness	μm (microinch)	3.8 or 5 (150 or 197), depending upon strain gage type
Carrier		
Material		Polyimide
Thickness	μm (microinch)	45 ± 10 (1.772 ± 394)
Connections		PTFE wire, Ø - 0.051 mm ² , approximately 50 mm long, connected to AWG 28 ribbon cables (PVC insulated) through solder sleeves in 2- or 3-wire configurations
Nominal Resistance ¹	Ω	120 or 350 depending upon gage
Resistance Tolerance ¹	%	±0.35
with 0.6 mm and 1.5 mm grid length	%	±1
Gage Factor		approximately 2 (stated on package)
Gage Factor Tolerance	%	±1
with 0.6 mm and 1.5 mm grid length	%	±1.5
Temperature coefficient of gage factor	1/K [1/°F]	(115 ± 10) × 10 ⁻⁶ [(64 ± 5.5) × 10 ⁻⁶]
Nominal value of gage factor temperature coefficient		Specified on each package
Reference Temperature	°C (°F)	23
Operating Temperature Range		PTFE cable
for static measurement (zero point related)	°C (°F)	-10 to 155 (-14 to 320)
for dynamic measurement (not zero point related)	°C (°F)	-10 to 155 (-14 to 320)
Transverse Sensitivity for linear 3 mm 120Ω gage	%	±0.2
Temperature Response		Specified on each package
Temperature response as required, adapted to coefficient of thermal expansion		
a for aluminum	1/K [1/°F]	10.8 × 10 ⁻⁶ (6.0 × 10 ⁻⁶)
a for plastic material	1/K [1/°F]	23 × 10 ⁻⁶ (12.8 × 10 ⁻⁶)
a for austenitic steel	1/K [1/°F]	65 × 10 ⁻⁶ (36.1 × 10 ⁻⁶)
a for titanium	1/K [1/°F]	16 × 10 ⁻⁶ (8.9 × 10 ⁻⁶)
a for molybdenum	1/K [1/°F]	9 × 10 ⁻⁶ (5.0 × 10 ⁻⁶)
a for quartz	1/K [1/°F]	5.4 × 10 ⁻⁶ (3.0 × 10 ⁻⁶)
Tolerance of temperature response	°C (°F)	0.05 × 10 ⁻⁶ (0.3 × 10 ⁻⁶)
		-10 to 120 (-14 to 248)
Mechanical Hysteresis		
1) at reference temperature and strain $\epsilon = 1000 \mu\text{m/m}$ (microstrain) on linear 3 mm 120Ω gage		
at 1 st load cycle and adhesive SG496	μm/m (microstrain)	1
at 3 rd load cycle and adhesive SG496	μm/m (microstrain)	0.5
Maximum Elongation		
at reference temperature on linear 3 mm 120Ω gage		
Absolute strain value for positive direction	μm/m (microstrain)	20,000 ± 2%
Absolute strain value for negative direction	μm/m (microstrain)	25,000 ± 2.5%
Fatigue Life		
at reference temperature on linear 3 mm 120Ω gage		
Achievable Number of Load Cycles N_w at Alternating Strain $\epsilon_w = \pm 1000 \mu\text{m/m}$ and zero point variation ≤ 300	μm/m (microstrain)	>1 × 10 ⁷ (test was stopped)
zero point variation ≤ 30	μm/m (microstrain)	5 × 10 ⁶
Minimum Radius of Curvature, Longitudinal and Transverse, at Reference Temperature		
within measuring grid area	mm (inch)	0.3 (0.012)
within solder tab area	mm (inch)	10 (0.394)
Applicable Bonding Materials		
Cold Cure Adhesives		SG496, SG401
Heat Cure Adhesives		TT300



8.5.2 *Pressure sensors for instrumented pectoral fin*

World Headquarters

Millar Instruments, Inc.
 6001-A Gulf Freeway
 Houston, Texas 77023-5417 USA
 Phone: 832.667.7000 or 800-669-2343 (in the USA)
 Fax: 832.667.7001
 Email: info@millarmail.com
 Web site: www.millarinstruments.com

Millar Worldwide Distribution

Millar Instruments, Inc. has a network of Authorized Distributors in most countries around the world. For information on the Millar distributor in your country, please contact the Millar Customer Service Department at our headquarters in Houston.

European Authorized Representative

FMI Föhr Medical Instruments GmbH
 In der Grube 13
 D-64342 Seeheim/Ober Beerbach
 Germany
 Telephone: +49 (0) 62 57 - 96 22 60
 Fax: +49 (0) 62 57 - 96 22 62 + 8 20 17
 Email: info@fmigmhbh.de



0086



Sensors.Systems.Solutions.®

Mikro-Tip® Catheter Pressure Transducer

Animal Use Only

Instructions for Use

© 2007 Millar Instruments, Inc. All rights reserved.
 Millar, Mikro-Tip and Sensors.Systems.Solutions. are registered trademarks of Millar Instruments, Inc.
 Products and company names used are the trademarks or trade names of their respective companies.
 Models referred to herein are protected by USA and International patents.

M.I. P/N: 004-2129 Rev. E


Table of Contents

RECOMMENDED ACCESSORIES.....	1
DEVICE DESCRIPTION	1
INTENDED USE/INDICATIONS	2
WARNINGS	2
PRECAUTIONS	2
MAINTAINING DEVICE EFFECTIVENESS.....	2
STORAGE	2
PLASTIC DOME FITTING.....	2
ROUTINE INSPECTION AND TESTING.....	2
CATHETER.....	2
PRESSURE SENSOR(S).....	3
CONNECTOR(S) AND CABLE(S).....	3
TRANSDUCER VERIFICATION AND SETUP	3
OPERATING INSTRUCTIONS.....	3
OPERATIONAL NOTES	4
HIGH-SPEED INJECTION CATHETERS	4
SPECIAL FLUSHING INSTRUCTIONS PRIOR TO INJECTION.....	4
CATHETERS FOR USE WITH GUIDE WIRES.....	4
PHONOCARADIOGRAM RECORDING	4
HANDLING PRECAUTIONS FOR MIKRO-TIP CATHETERS	5
TROUBLESHOOTING AND CORRECTIVE MAINTENANCE	5
CLEANING.....	5
APPROVED CLEANERS AND DISINFECTANTS	5
WATER RESISTANT CONNECTOR CAPS	6
CLEANING PROCEDURE.....	6
DISINFECTION	7
RINSING AFTER DISINFECTION.....	7
METHOD OF STERILIZATION FOR CATHETERS AND EXTENSION CABLES (OPTIONAL).....	7
ETHYLENE OXIDE STERILIZATION CYCLE PARAMETERS.....	8
SENSOR SPECIFICATIONS	9
SCHEMATICS.....	10
FIGURES.....	11
SERVICE PROVISION.....	13
MILLAR LIMITED WARRANTY	13


Recommended Accessories

M.I. P/N: 851-5918, Model TC-510 Control Unit, No patient isolation
M.I. P/N: 880-0129, Model PCU-2000 Control Unit with Patient Isolation
M.I. P/N: 850-1118, Model TEC-5C Extension Cable
M.I. P/N: 850-1108, Model TEC-10C Extension Cable
M.I. P/N: 850-1308, Model TEC-10D Extension Cable
M.I. P/N: 850-5088, Model PEC-1.5C Extension Cable to PCU-2000
M.I. P/N: 850-5089, Model PEC-10C Extension Cable to PCU-2000
M.I. P/N: 850-5103, PEC-4D Extension Cable to PCU-2000
M.I. P/N: 850-5090, PEC-10D Extension Cable to PCU-2000
Monitor Input Cables as appropriate for monitor.
All accessories sold separately.

Definition of Symbols



Attention, consult accompanying documents




Date of Manufacture

REF


Catalog Number

SN


Serial Number




Batch Code



Use By Date



Electrostatic Sensitive Device



EU Declaration of Conformity

Device Description

Mikro-Tip catheters consist of an ultra-miniature pressure sensor(s) at the distal end of a catheter, as shown in Figure 1, with an electrical connector(s) at the proximal end. The pressure sensor produces an electrical output signal, which varies in direct proportion to the magnitude of sensed pressure.

Mikro-Tip catheters are intended for multiple uses. Experience has proven that the instruments are safe and effective for extended service if proper handling, cleaning, and sterilization procedures are followed.

Immediately upon receipt of the catheter, and prior to its initial cleaning, sterilization, and use, the customer should verify that the catheter is operational.

Flexible extension cables are available for connection between the pressure connector and the pressure control unit. These flexible cables facilitate maneuvering the catheter during recording. They may be sterilized to permit connection of the transducer to a Millar control unit outside the sterile field.

Service Provision

Consult web site below for service information:

www.millarinstruments.com

Millar Limited Warranty

Millar Instruments, Inc. (Millar) warrants that at the time of sale to the original purchaser, the device was free from defects in both materials and workmanship. For a period of 365 days (1-year) from the date of original shipment to the original purchaser, Millar will, at no charge and at its option, either repair or replace any Mikro-Tip transducer found to have been shipped with defects in either materials or workmanship. Our warranty does not cover damage to the product from alterations, misuse, abuse, negligence, or accident. The SPR-524 is warranted for a period of 30 days from the date of original shipment to the original purchaser. The SPR-524 is non-repairable.

Millar hereby excludes all warranties not herein stated, whether express or implied by operation of law or course of dealing or trade usage or otherwise, including but not limited to any implied warranties of fitness or merchantability.

Since handling, storage, cleaning and sterilization of the product, as well as factors relating to patient diagnosis, treatment, catheterization procedures, and other matters beyond Millar's control, directly affect the product and the results obtained from its use, Millar shall not be liable for any incidental or consequential loss, damage, or expense arising directly or indirectly from the use of this product.

The user shall determine suitability for use of these medical devices for any surgical or clinical procedure. Therefore, the user accepts these devices subject to all the terms hereof. Further, Millar makes no warranty regarding device efficacy after three (3) years from the date of manufacture.

Intended Use/Indications

The use of Mikro-Tip catheter is indicated when physiological pressures are to be measured.

For cardiovascular applications, Mikro-Tip catheters may be introduced into the cardiovascular system percutaneously or through the wall of a surgically exposed artery or vein.

With the aid of fluoroscopy or echocardiography, the transducer may be advanced from the introduction site to the desired location.

Warnings

- Mikro-Tip transducer catheters are shipped with a plastic or foam dome fitting over the pressure sensor. The dome should be in place during handling.
- Do not allow any body fluids to collect under protective covering on catheter connector; otherwise, sterilization cannot be assured.

Precautions

Use of Mikro-Tip catheters should be restricted to specialists who are familiar with, and have been trained to perform, the catheterization procedures for which the device is intended.

- Inspect the Mikro-Tip catheter for damage (cracking, kinks, etc.) prior to each use.
- Clean the Mikro-Tip catheter immediately after each use (see Cleaning).
- Store Mikro-Tip catheters in a dark, cool, dry place.
- Do not touch the sensor area with sharp objects. Do not make sharp bends in the catheter.
- Refrain from applying direct pressure to the sensor area with instruments such as forceps or tweezers.
- When handling the catheter with either fingertips or surgical instruments, always grip several millimeters (5-10 mm) proximal to the sensor area. The sensor area contains very fragile wires which may be damaged or broken if the catheter is gripped too close to the sensor.
- Avoid electrostatic discharge to the Mikro-Tip sensor. Do not touch the sensor element while the catheter is disconnected from monitoring equipment.

Maintaining Device Effectiveness

Storage

Store the catheter in the plastic tray provided. Make sure the catheter has a plastic or foam dome fitting over each pressure sensor.

Plastic Dome Fitting

All catheters are shipped with a protective tubing(s) and/or plastic dome fitting over the pressure sensor(s) to protect the sensor from damage. Plastic Domes **ARE NOT** interchangeable.

When using the plastic dome fitting, the tip of the pressure sensor should be positioned inside the plastic dome fitting as shown in Figure 2.

Routine Inspection and Testing

CAUTION: If damage is found during inspection, DO NOT use the catheter. Contact Millar Instruments or authorized distributor.

Catheter

Inspect each catheter thoroughly before and after each use. Carefully examine the catheter for defects.

Pressure Sensor(s)

Examine the pressure sensor active surface (diaphragm) for blood or materials not removed by cleaning. A dirty sensor may cause short-term baseline drift. Follow cleaning directions in this IFU.

Connector(s) and Cable(s)

The connector(s) should be routinely inspected for corrosion or bad contacts. Liquid entering the connector(s) can cause electrical hazard, erratic operation and components corrosion.

Transducer Verification and Setup

CAUTION: DO NOT handle or squeeze the pressure transducers during catheter manipulation!

Each transducer is calibrated for a standardized sensitivity of **5µV/V/mmHg (37.6 µV/V/kPa)**. To verify system outputs, apply a reference pressure signal to adjust sensitivity or to specific monitor requirement. Use a mercury manometer or pressure reference device, as shown in Figure 3a or 3b. Apply a known pressure to the Millar catheter and verify the signal at the monitor. Follow the instructions for the Millar pressure control unit being used. Set up the mercury manometer as shown in 3a or 3b and compare the 100 mmHg (13.3 kPa) output produced using the mercury manometer with the electrical 100 mmHg (13.3 kPa) produced by the control unit. Reading errors at or near the 0 mmHg (0kPa) manometer indication can be minimized by offsetting the manometer zero indication to 20 mmHg (26.6 kPa) and using the 100 mmHg (133 kPa) increments from the 20-120 mmHg (26.6 – 160 kPa) pressure indication rather than the 0-100 mmHg (0-133 kPa) pressure indication. Errors due to inconsistent meniscus shape between consecutive readings can be minimized by adjusting the pressure at each reading to maintain a consistent curve at the top of the meniscus. These errors may be avoided by using an electronic pressure meter as shown in Figure 3b.

Operating Instructions

When Using a Millar Pressure Control Unit (see Control Unit's IFU)

- 1. Soak the sensor in room-temperature sterile water or sterile saline for 30 minutes prior to use to minimize drift.
- 2. Connect the Millar pressure control unit to the monitor.
- 3. Turn the pressure control unit function switch to STANDBY 0 and adjust the monitor to zero baseline.
- 4. Turn the pressure control unit function switch to 100 mmHg and adjust the monitor sensitivity.
- 5. Connect the extension cable to the pressure control unit.
- 6. Connect the catheter to the extension cable.
- 7. Turn the pressure control unit function switch to TRANSDUCER. Shield the sensor from light. Adjust the TRANSDUCER BALANCE CONTROL to zero baseline. LOCK the catheter balance.
- 8. The catheter system is now ready for use.

Monitor ZERO-REFERENCE can be verified by setting the Millar pressure control unit selector switch to STANDBY 0 to reproduce the original zero baseline. Monitor zero baseline adjustment can be performed at this time if required. Monitor GAIN can then be verified by setting the selector switch to the 100 mmHg (13.3 kPa) position on the control unit. Monitor GAIN adjustments can be made at this time if required.

CAUTION: The “zero” output produced by placing the control unit function switch in the STANDBY 0 position is an electrical zero, not an atmospheric zero!

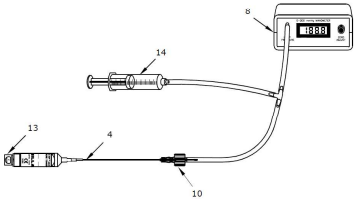
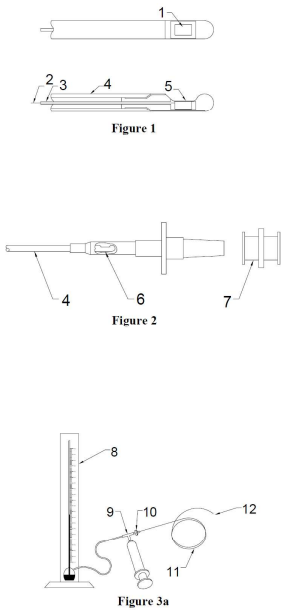


Figure 3b

Figure Legend

1. Pressure Sensing Area	7. Luer Fitting
2. Wires to Connector	8. Mercury Manometer
3. Vent to Connector	9. Tee Fitting
4. Catheter	10. Plastic Dome
5. Silicone Rubber Diaphragm	11. Pressure Transducer Catheter
6. Pressure Sensor	12. To Recorder

Figures



Operational Notes

- CAUTION: Use appropriate size introducer for catheter being used.
- CAUTION: Consider use of systemic heparinization.

High-speed Injection Catheters

Use catheters only for injection of contrast media and short-term pressure measurements. For Renografin 76, 7F single sensor pressure transducer rate is typically 10-15 ml/sec at 1000 psi (6895 kPa) and 8F is 20-25 ml/sec. 8F dual pressure sensor transducer rate is typically 10 ml/sec at 1200 psi (8274 kPa). Priming volume is approximately 1.6 ml (7F) and 2.4 ml (8F).

Special Flushing Instructions Prior to Injection

- A saline drip will not adequately irrigate the tip of high-speed injection side-hole catheters with a pigtail tip or extension. To prevent air emboli formation:
1. Fill the lumen and tip or extension with saline before introducing the catheter. Cover the side holes during filling to ensure that the tip or extension is filled.
 2. Keep the catheter lumen filled with flushing solution or contrast medium while in use.
 3. Flush the catheter with 10-15 ml saline every two minutes, or as needed.

Catheters for Use with Guide Wires

All guide wire catheters are designed to be inserted and advanced over a guide wire. The distal pigtail extension may fold and buckle if the catheter is advanced without the guide wire in position. Never advance the guide wire against resistance.

- CAUTION: Verify maximum guide wire outside diameter before use. Do not handle or squeeze the pressure sensors when inserting the guide wire.

A “J” guide wire should not be inserted or advanced from the hub end of a catheter with side openings for high-speed injection. If a straight guide wire is inserted or advanced from the hub end of one of these catheters, care should be taken to ensure that the guide wire does not exit through the lumen side openings. Remove guide wire immediately after use.

Flush catheter immediately after use. During flushing, intermittently occlude lumen side openings to ensure complete flushing of the distal catheter extension.

Phonocardiogram Recording

Mikro-Tip catheters have pressure sensors with a sufficiently high frequency response to sense heart sounds. These transducers detect sounds simultaneously from many sources in a localized fashion. Heart sounds visible on the pressure waveform can be amplified and clearly displayed on a separate channel. Heart sounds less than the noise of the display system will display only that noise.

Handling Precautions for Mikro-Tip Catheters

	DO:	DO NOT:
Pressure Sensor	Clean immediately after use	Clean with stiff-bristled brush
		Clean with high pressure water jet
	Protect with dome when not in use	Tap the sensor against a rigid surface
	Disconnect during electrical defibrillation or electrosurgery	Apply excessive force to the sensor surface
Catheter & Pigtail	Clean immediately after use	Expose to excessive pressure
		Cut, crease, knot, fold, kink, or crush with forceps or clamps of any kind
Connector & Cables	Protect connectors from fluid	Immerse connectors in liquid
Lumen	Clean immediately after use	Over pressurize
	Flush during use	Use Teflon-coated guide wires.
		Use cleaning wires or guide wires on models not designed for guide wires
Cleaning	Keep catheter, lumen, and sensor wet until cleaning	Expose to alcohol, cresols, phenols, mercury compounds, hypochlorites, acetone, peroxide, silicone chloride, sylvanes, trichloroethylene, or freon
	Clean thoroughly with approved enzymatic cleanser immediately after use	Use ultrasonic cleaner.
		Immerse electrical connector
Sterilizing	Dry catheter and lumen before sterilizing	Autoclave, irradiate (gamma/e-beam), plasma, peroxide or formaldehyde vapor solutions
	Remove plastic dome from catheter	Use Sporox or Cidex PA solutions

Troubleshooting and Corrective Maintenance

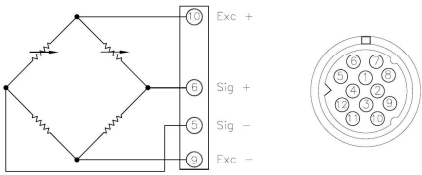
Problem	Probable Cause	Corrective Action
Excessive Drift	Deposit of foreign material on the diaphragm of the pressure sensor.	Follow Cleaning Instructions. If problem persists, contact Millar.
Transducer will not balance (zero)	Moisture in the connector, damage to wires in the catheter, or fractured strain gauge within pressure sensor system.	Follow Operating Instructions or substitute a transducer known to be operating properly into the recording system.

Cleaning

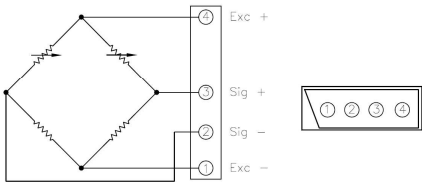
Approved Cleaners and Disinfectants

Type	Trade Name	Manufacturer	Active Ingredient	Soak Time/Temperature
Enzymatic Detergent	Enzol® (in UK: Cidezyme®)	Advanced Sterilization Products (J&J)	Propylene Glycol	15 minutes / room temperature
	Endozime®	Ruhoff Corporation	Propylene Glycol	15 minutes / room temperature
	Terg-A-Zyme®	Alconox	Sodium Dodecylbenzene	15 minutes / room temperature
High-level Disinfectant	Cidex Activated Dialdehyde Solution	Advanced Sterilization Products (J&J)	Glutaraldehyde	1-2 hours / 25 °C (77°F)
High-level	Cidex® OPA	Advanced	Ortho-	16-30 minutes / 20

Schematics



Sensor & Viking Connector



Sensor & Low Profile Connector

Sensor Specifications

	2F Catheter	≥3F Catheter
Type of Sensor	Diffused Semiconductor, piezoresistive	
Pressure Range	-50 to + 300 mmHg (-6.7 to 40 kPa)	
Overpressure	+4000 mmHg (+530 kPa), -760 mmHg (100 kPa)	
Rated Excitation*	2.5-7.5 V _{DC} or V _{AC} rms	
Sensitivity	5 μV/V/mmHg, nominal (37.6 μV/V/kPa)	
Temperature Error Band at Zero Pressure	±3 mmHg (± 0.4 kPa) BSL, 23 ± 38 °C	±1.5 mmHg (±0.2 kPa), BSL, room temperature to body temperature [3 mmHg (0.4 kPa) maximum shift, approximately 23-38 °C]
Linearity and Hysteresis	±1%, BSL of full scale	±0.5%, BSL of full scale
Drift**	<6 mmHg (0.8 kPa) in 12 hours	
Natural Frequency	≥10 kHz	
Bridge Resistance	1000 ohms, nominal	
Reference Pressure	Atmosphere	
Electrical Leakage	< 10 μA at 180 V _{DC} 10 μA at 120 V _{AC}	< 10 μA at 600 V _{DC} 10 μA at 120 V _{AC}
Zero Offset	< ±50 mmHg (± 6.7 kPa)	

* Performance specifications are for 5 V_{DC}. Transient voltages up to 20 volts will not damage the transducer.

** Based on 30 minute presoak.

Type	Trade Name	Manufacturer	Active Ingredient.	Soak Time/Temperature
Disinfectant		Sterilization Products (J&J)	phthalaldehyde	°C (68°F)
	MetriCide®	Metrex	Glutaraldehyde	1-2 hours / 25 °C (77°F)

DO NOT USE:

- Glutaraldehyde solutions containing surfactants (e.g., Cidex 7 or Cidex Plus 28 Day)
- Solutions containing hydrogen peroxide (e.g. Sporox)
- Cidex PA solution

Water Resistant Connector Caps

Each catheter has water-resistant caps to protect electrical pins and circuitry. Place caps over the open end of the connectors before cleaning and disinfecting. Remove caps prior to sterilization. Save and reuse these caps each time the catheter is cleaned and disinfected.

Cleaning Procedure

CAUTION:	DO NOT submerge the wye junction or connectors. This will damage the catheter and void its warranty! Wipe with cleaner and gauze.
CAUTION:	Use only the listed cleaners for the times/temperatures indicated.
CAUTION:	Delays in rinsing greatly reduce cleaning effectiveness!

1. Wipe catheter with wetted gauze and flush catheter lumen with water immediately after use to remove bulk contaminants. During flushing, intermittently occlude lumen side openings to ensure complete flushing of the catheter tip.
2. Submerge only the distal contaminated portion of the catheter in room-temperature water (DO NOT use hot water) up to the wye junction, or the connector's strain relief.
3. If applicable, flush the lumen with water until the effluent is clear. Wipe the proximal outer surface of the catheter (including wye junction, and connector(s)) with soft gauze.
4. Clean the interior of the lumen hub with a wet Q-tip.
5. Prepare cleaning solution. Place the distal portion of the catheter in the cleaning solution.
6. If applicable, use a 15 cc syringe to flush the lumen with cleaning solution until no air bubbles are seen coming from the lumen. Leave the syringe attached so that the cleaner will continue to fill the lumen.
7. Wet soft surgical gauze with the cleaning solution. Wipe the outer surface of the catheter with gauze.
8. Soak distal portion of the catheter in a cleaning solution for the time specified, and then remove.
9. If applicable, remove syringe, clean the interior of the lumen hub with Q-tips soaked in cleaning solution. Drain the cleaner from the lumen of the catheter. Gently wipe the catheter and sensor clean with a soft, wet gauze or tissue.
10. Immediately rinse the catheter and sensor(s) at least three times with sterile, pyrogen-free water. Do not reuse the water from each rinse, as it will contain residuals from the cleaner.
11. If applicable, immerse catheter lumen distal openings in sterile, pyrogen-free water and aspirate at least 150 cc through the lumen. Flush lumen with sterile, pyrogen-free water at least three times.
12. Dry the outside of the catheter with soft gauze. Dry the lumen with at least fifteen 60-cc syringes of air, filtered air (900 cc), or carbon dioxide.

- 13. Package for sterilization. It is crucial that the lumen be dried completely.
- 14. Failure to clean and sterilize according to directions may void catheter warranty.

Disinfection

- 1. The catheter must be cleaned, rinsed and dried prior to disinfection. Soil, debris, proteins, and water can interfere with the effectiveness of the following procedure, posing a risk to the patient and the user. Note that some disinfectants have a limited usable life after activation or opening the container. Failure to heed such warnings can inhibit the effectiveness of the disinfection process.
- 2. Prepare the disinfectant according to the manufacturer’s instructions.
- 3. Fill a 10cc syringe with the disinfectant.
- 4. Connect the syringe to the lumen hub of the catheter.
- 5. Submerge all of the catheter’s lumen vents in a bath of the disinfectant. Submerge the catheter into the disinfectant up to the junction (dual-sensor or lumen models) or the connector strain relief (single-sensor/no-lumen models). Do not submerge the junction or the connector as it will damage the transducer and void the warranty.
- 6. Forcefully inject the contents of the syringe into the lumen and observe the disinfectant leaving the vents. If the disinfectant leaving the vents is not bubble free, a larger syringe will be needed. Make sure that there are no bubbles on the surface of the catheter. The disinfectant must be in contact with all surfaces that need to be disinfected.
- 7. With the syringe still connected and the lumen vents still submerged, forcefully draw 3cc of disinfectant back into the syringe.
- 8. Force the disinfectant back through the lumen and observe the disinfectant leaving the vents to confirm that it is bubble-free.
- 9. Perform at least three cycles of inject/draw/inject. It is important to remove all bubbles from the lumen to ensure that all surfaces of the lumen are disinfected. Leave the syringe connected to the lumen hub so that the disinfectant will continue to completely fill the lumen.
- 10. Soak the transducer in the disinfectant at the temperature and time intervals listed.

Rinsing after Disinfection

- 1. Drain the disinfectant from the lumen of the catheter.
- 2. Rinse the device by submerging all exterior disinfected surfaces in sterile pyrogen-free water. The volume of the water should be at least two gallons (7.6 liters) and the soak time should be at least one minute.
- 3. At least three separate rinses are required. Do not reuse any of the water used for rinsing since it will be contaminated with the disinfectant.
- 4. During each rinse, inject 120cc of sterile pyrogen-free water through the lumen.

Method of Sterilization for Catheters and Extension Cables (Optional)

CAUTION: DO NOT sterilize by autoclaving, radiation (gamma or e-beam), plasma, peroxide or formaldehyde vapor solutions.

Catheters must be completely cleaned and dried before sterilization. Aerate at room temperature or in a heated aeration cabinet. (max. 145 °F, 63 °C) Catheters may be sterilized in the white plastic shipping tray. The foam dome and connector caps must be removed and placed alongside the catheter inside the pouch during sterilization. The caps should be saved and reused each time the catheter is cleaned.

The tray, with lid, should be placed in a breathable polyethylene pouch (e.g., 3M™ Steri-Lok™).

CAUTION: The catheter should be completely dry before sterilization.

Ethylene Oxide Sterilization Cycle Parameters

Preheat phase:	Starting Temperature 110 °F (43°C) min. Duration 30 minutes
Initial Vacuum:	6.0 inHgA (20.3 kPa) Rate: 3 minutes
Nitrogen Flush: 2 cycles	
Nitrogen Addition to:	28.0 ± 0.5 inHgA (94.8 ± 1.7 kPa)
Rate:	1.4 ± 0.5 inHgA/min. (4.7 ± 1.7 kPa/min.)
Evacuation:	6.0 ± 0.5 inHgA (20.3 ± 1.7 kPa)
Rate:	1.0 ± 0.5 inHgA/min. (3.4 ± 1.7 kPa)
Conditioning	
Humidification:	1.5 ± 0.5 inHgA (5.1 ± 1.7 kPa)
Steam Conditioning:	10 min.
Humidity Dwell:	30 ± 5 min. at 7.5 ± 0.5 inHgA (25.4 ± 1.7 kPa)
Relative Humidity:	15-70%
Ethylene Oxide Concentration:	500 ± 50 mg/L
Dwell Pressure:	16.5 ± 1.0 inHgA (55.8 ± 3.4 kPa)
Dwell Time:	2 hours
Temperature:	110-130 °F (43-54 °C)
Relative Humidity:	30-70% (35-44% nominal)
After Vacuum	
Vacuum:	6.0 ± 0.5 inHgA (20.3 ± 1.7 kPa)
Rate:	1.0 ± 0.5 inHgA/min. (3.4 ± 1.7 kPa)
Vacuum Hold:	10 min.
Gas Wash A:	4 cycles (minimum)
Release:	30.0 inHgA/min. (94.8 ± 1.7 kPa)
Rate:	1.4 ± 0.5 inHgA/min. (4.7 ± 1.7 kPa)
Vacuum	6.0 ± 0.5 inHgA (20.3 ± 1.7 kPa)
Rate:	1.0 ± 0.5 inHgA/min. (3.4 ± 1.7 kPa)
Release (Filtered Air):	28.0 ± 0.5 inHgA (94.8 ± 1.7 kPa)
Rate:	2.0 ± 0.5 inHgA/min. (6.6 ± 1.7 kPa)
Aeration (Hot Cell)	
Duration:	At least 8 hours
Temperature:	110 ± 10 °F (43 °C)

CAUTION: The Mikro-Tip transducer should not be used earlier than 5 days after sterilization.

8.5.3 *Pressure sensor amplifier*

World Headquarters

Millar Instruments, Inc.
 6001-A Gulf Freeway
 Houston, Texas 77023-5417 USA
 Phone: 832.667.7000 or 800-669-2343 (in the USA)
 Fax: 832.667.7001
 Email: info@millarinc.com
 Web site: www.millarinstruments.com

Millar Worldwide Distribution

Millar Instruments, Inc. has a network of Authorized Distributors in most countries around the world. For information on the Millar distributor in your country, please contact the Millar Customer Service Department at our headquarters in Houston.

European Authorized Representative

FMI Föhr Medical Instruments GmbH
 In der Grube 13
 D-64342 Seeheim/Ober-Beerbach
 Germany
 Telephone: +49 (0) 62 57 - 96 22 60
 Fax: +49 (0) 62 57 - 96 22 62 + 8 20 17
 Email: info@fmigmbh.de



© 2003, 2005, 2007 Millar Instruments, Inc. All rights reserved.

Millar, Mikro-Tip and *Sensors.Systems.Solutions.* are registered trademarks of Millar Instruments, Inc.

Products and company names used are the trademarks or trade names of their respective companies.

Models referred to herein are protected by USA and International patents.

M.I. P/N: 004-2113 Rev. F



Sensors.Systems.Solutions.®

**MODEL PCU-2000****Pressure Control Unit with Patient Isolation****Instructions for Use (IFU)**

U.S.A. federal law restricts this device to sale by or on the order of a physician or other licensed practitioner, when used as a medical device.

Operating	50° to 104°F (10 to 40°C),
	30 to 75 % RH
Transport and Storage	-4° to 140°F (-20 to 65°C),
	30 to 75% RH
Safety Protection	
Fuse	Re-settable, 0.4A

Note: Specifications subject to change without notice.

Factory Repair






If repair or return is needed, contact your distributor. If you purchased the PCU-2000 or accessory directly from Millar Instruments, contact Millar's Customer Service Department to obtain a Return Material Authorization (RMA) number and specific instructions regarding the return of the PCU-2000 or accessory. All returns must have a RMA number. Millar contact information may be found on the back cover of this IFU.

Millar Limited Warranty

Millar Instruments, Inc. (Millar) warrants that at the time of sale to the original purchaser, the device was free from defects in both materials and workmanship. For a period of 365 days (1-year) from the date of original shipment to the original purchaser, Millar will, at no charge and at its option, either repair or replace this product if found to have been shipped with defects in either materials or workmanship. Our warranty does not cover damage to the product from alterations, misuse, abuse, negligence, or accident. Millar hereby excludes all warranties not herein stated, whether express or implied by operation of law or course of dealing or trade usage or otherwise, including but not limited to any implied warranties of fitness or merchantability.

Since handling, storage, cleaning and sterilization of the product, as well as factors relating to patient diagnosis, treatment, catheterization procedures, and other matters beyond Millar's control, may directly affect the product and the results obtained from its use, Millar shall not be liable for any incidental or consequential loss, damage, or expense arising directly or indirectly from the use of this product. The user shall determine suitability for use of these medical devices for any research or clinical procedure. Therefore, the user accepts these devices subject to all the terms hereof.

Table of Contents	
Definition of Symbols	1
Definitions	1
Device Description	1
Intended Use / Indications.....	3
Warnings	3
Precautions	3
Contraindications	3
Normal Use Operating Instructions.....	4
Repair, Cleaning, Preventative Maintenance and Inspection	6
Output Connector Wiring.....	7
Pressure Output Connection	7
Troubleshooting	8
Recommended Accessories	9
PCU-2000 Interface Cables.....	9
Power Supply Information	9
Interface and Adapter Cables.....	10
Safety and EMC Testing Standards.....	10
Electrical Safety	10
Electromagnetic Compatibility (EMC).....	10
PCU-2000 Specifications	14
Factory Repair.....	15
Millar Limited Warranty	15

Definition of Symbols	
	Attention, consult accompanying documents
	Date of Manufacture
REF	Catalog Number
SN	Serial Number
LOT	Batch Code
	Type CF Applied Part
	Double Insulated
CE	EU Declaration of Conformity
	Waste Electrical and Electronic Equipment

Definitions	
DC	Direct Current
IFU	Instructions for use
AC	Alternating Current
Transducer	Pressure tip catheter
AC Mains	Hospital Alternating Current Supply
RMA	Return Material Authorization
M.I.	Miller Instruments
RF	Radio Frequency
EMC	Electromagnetic Compatibility
EMI	Electromagnetic Interference

READ ALL INSTRUCTIONS, WARNINGS AND PRECAUTIONS
PRIOR TO USE

Device Description

The following information will provide data relating to the safe operation of the PCU-2000. The two-channel PCU-2000, M.I. P/N 880-0129, is an essential interface between one dual-pressure or two single-pressure Mikro-Tip catheters and a CE-approved data acquisition system or patient monitor. The unit is powered by a Miller-supplied external AC/DC power supply.

The PCU-2000 pressure inputs (input channel 1 and input channel 2) are electrically isolated for patient safety. These inputs are also protected against the effects of a cardiac defibrillator discharge. The discharge of a cardiac defibrillator has no effect on the operation of the PCU-2000.

The pressure outputs have a sensitivity of 1V/100mmHg, which is ideally compatible with most monitors and computer data acquisition systems. The amplifier provides bridge excitation voltage, separate balance (zero) controls and lighted push buttons for electronic calibrations of 0, 25, 100 or 125 mmHg for both channels.

PCU-2000 Specifications

Equipment Classifications	
Class	II (USA), IIb (EU), II (Canada)
Ingress Protection	IP20
Type	CF
Pressure Transducer Characteristics	
Transducer Sensitivity	5 μ V/V/mmHg, nominal
Bridge Excitation Load	1000 ohms, nominal
Resistance	350 ohms, minimum
Transducer Bridge Excitation	5.0 V _{DC} , nominal
Signal Input Resistance	50 megohm, nominal
Pressure Outputs	
Sensitivity	1 V/100 mmHg, nominal
Accuracy Error Band	$\leq \pm 1$ mmHg or 1 % of reading, whichever is greater
Frequency Response	DC to 1000 Hz (-3 Db), minimum
Output Resistance	1000 ohms, nominal
Noise	< 0.3 mmHg peak-to-peak
Zero-Offset Temperature	< 0.15 mmHg/ $^{\circ}$ C
Coefficient Gain Temperature	< 0.1 %/ $^{\circ}$ C
Coefficient Balance Adjustment Range	± 140 mmHg, nominal
Standby-Calibration Mode	
Zero Offset	$\leq \pm 1$ mmHg
Calibration Steps	0, 25, 100 and 125 mmHg
Calibration Accuracy	$\leq \pm 0.5$ mmHg
LED Bar Graphs	
Range	-25 to 200 mmHg in 10 steps
Resolution	25 mmHg
Out of Range	Top light stays on at high pressures Bottom light turns off at low pressures
Power Supply	
Input (Universal)	100 to 240 V _{AC} , 0.3A, 50/60 Hz
Output	5 V _{DC} /2.0 A, regulated ($\pm 5\%$)
Safety Approvals	EN 60601-1, CSA C22.2 No. 601.1
Mechanical	
Size	2.6 in. H x 6.1 in. W x 5.3 in. D 6.6 cm H x 15.5 cm W x 13.5 cm D
Weight	1.1 lbs. (0.5kg)
Environmental	

Recommended separation distances between portable and mobile RF communications equipment and the PCU-2000			
The PCU-2000 is intended for use in an electromagnetic environment in which radiated RF disturbances are controlled. The customer or the user of the PCU-2000 can help prevent electromagnetic interference by maintaining a minimum distance between portable and mobile RF communications equipment (transmitters) and the PCU-2000 as recommended below, according to the maximum output power of the communications equipment			
Rated maximum output power of transmitter W	Separation distance according to frequency of transmitter m		
	150 kHz to 80 MHz in ISM bands $d = 1.17\sqrt{P}$	80 MHz to 800 MHz in ISM bands $d = 1.17\sqrt{P}$	800 MHz to 2.5 GHz $d = 2.3\sqrt{P}$
0.01	0.117	0.117	0.23
0.1	0.37	0.37	0.73
1	1.17	1.17	2.3
10	3.7	3.7	7.3
100	11.7	11.7	2.3
For transmitters rated at a maximum output power not listed above, the recommended separation distance d in meters (m) can be estimated using the equation applicable to the frequency of the transmitter, where P is the maximum output power rating of the transmitter in watts (W) according to the transmitter manufacturer.			
NOTE 1 At 80 MHz and 800 MHz, the separation distance for the higher frequency range applies.			
NOTE 2 These guidelines may not apply in all situations. Electromagnetic propagation is affected by absorption and reflection from structures, objects and people.			
NOTE 3 An additional factor of 10/3 is used in calculating the recommended separation distance for transmitters in the ISM frequency bands between 150 kHz and 80 MHz and in the frequency range 80 MHz to 2.5 GHz to decrease the likelihood that mobile/portable communications equipment could cause interference if it is inadvertently brought into patient areas.			
NOTE 4 These guidelines may not apply in all situations. Electromagnetic propagation is affected by absorption and reflection from structures, objects and people.			

Medical electrical equipment such as the PCU-2000 needs special precautions regarding electromagnetic compatibility (EMC) and needs to be installed and put into service according to the EMC information provided in this document.

Portable and mobile radio frequency (RF) communications equipment can affect medical electrical equipment such as the PCU-2000.

The PCU-2000 should not be used adjacent to or stacked with other equipment. If adjacent or stacked use is necessary, the PCU-2000 should be observed to verify normal operation in the configuration in which it will be used.

The PCU-2000 allows selection of standby mode to verify zero and calibration. The output connectors are standard ¼-inch phone jacks. Output cables are not provided. See Output Connector Wiring section in this IFU for additional information.

Intended Use/Indications

The PCU-2000 Pressure Control Unit is intended for use with Millar Mikro-Tip® pressure catheters that have the standard medical sensitivity of 5 µV/mmHg. It is intended for use in monitoring diagnostic pressures, such as noninvasive or invasive blood pressures, intracranial pressures, gastrointestinal pressures, esophageal pressures, urinary tract pressures, intrauterine pressures, intraocular pressures and other physiological pressures with similar ranges. It is intended for use in critical care areas in a hospital and in diagnostic centers in hospitals or medical clinics. It is intended for use by trained clinicians or research personnel.

Warnings

EXPLOSION HAZARD! Do not operate this unit in the presence of flammable anesthetic mixtures with air or with oxygen or nitrous oxide.
ELECTRIC SHOCK HAZARD! Use only those power supplies and power cables recommended and approved by Millar Instruments. In addition, use only Millar catheters. See the RECOMMENDED ACCESSORIES section for replacement parts.
ELECTRIC SHOCK HAZARD! The PCU-2000 is not to be used in wet environments. Discontinue use of the PCU-2000 if it is suspected that liquid has entered the case. Contact Millar Instruments customer service immediately.
 No modification of this equipment is allowed.

DO NOT use the PCU-2000 during defibrillation. Disconnect all connections to the patient before defibrillation.

Precautions


DO NOT remove the cover. Refer servicing to qualified personnel.
 DO NOT use the PCU-2000 and transducers with or near high-frequency surgical equipment.
 DO NOT use the PCU-2000 in close proximity to high electrical noise-generating equipment, as this may cause interference with the signal. If interference occurs, move the PCU-2000 system away from the noise-generating device. Medical electrical equipment such as the PCU-2000 needs special precautions regarding electromagnetic compatibility (EMC) and needs to be installed and put into service according to the EMC information provided in this document. Portable and mobile radio frequency (RF) communications equipment can affect medical electrical equipment such as the PCU-2000.
 DO refer to the respective cardiac defibrillator manual prior to performing defibrillation if applicable.

Contraindications

Results obtained by using non-Millar catheters have not been validated.

Environmental protection

Disposal of this ME Equipment (PCU-2000 and all accessories) is to be performed following all governmental standards that may be applicable to your country and / or origin of use. There are no inherent risks to the user with the disposal of this ME Equipment.

Guidance and manufacturer's declaration – electromagnetic immunity			
The PCU-2000 is intended for use in the electromagnetic environment specified below. The customer or the user of the PCU-2000 should assure that it is used in such an environment.			
Immunity test	IEC 60601 test level	Compliance level	Electromagnetic environment – guidance
Conducted RF IEC 61000-4-6	3 Vrms 150 kHz to 80 MHz	3 V 3 V/m	<p>Portable and mobile RF communications equipment should be used no closer to any part of the EQUIPMENT or SYSTEM, including cables, than the recommended separation distance calculated from the equation applicable to the frequency of the transmitter.</p> <p>Recommended separation distance</p> <p>$d = 1.17\sqrt{P}$</p> <p>$d = 1.17\sqrt{P}$, 80 MHz to 800 MHz</p> <p>$d = 2.3\sqrt{P}$, 800 MHz to 2.5 GHz</p> <p>Where P is the maximum output power rating of the transmitter in watts (W) according to the transmitter manufacturer and d is the recommended separation distance in meters (m).</p> <p>Field strengths from fixed RF transmitters, as determined by an electromagnetic site survey,^a should be less than the compliance level in each frequency range.^b</p> <p>Interference may occur in the vicinity of equipment marked with the following symbol:</p> <p></p>
Radiated RF IEC 61000-4-3	3 V/m 80 MHz to 2.5 GHz		
NOTE 1 At 80 MHz and 8000 MHz, the higher frequency range applies.			
NOTE 2 These guidelines may not apply in all situations. Electromagnetic propagation is affected by absorption and reflection from structures, objects and people.			
^a Field strengths from fixed transmitters, such as base stations for radio (cellular/cordless) telephones and land mobile radios, amateur radio, AM and FM radio broadcast and TV broadcast cannot be predicted theoretically with accuracy. To assess the electromagnetic environment due to fixed RF transmitters, an electromagnetic site survey should be considered. If the measured field strength in the location in which the PCU-2000 is used exceeds the applicable RF compliance level above, the PCU-2000 should be observed to verify normal operation. If abnormal performance is observed, additional measures may be necessary, such as reorienting or relocating the PCU-2000.			
^b Over the frequency range 150 kHz to 80 MHz, field strengths should be less than [V/m] V/m			

Guidance and manufacturer's declaration – electromagnetic immunity			
The PCU-2000 is intended for use in the electromagnetic environment specified below. The customer or the user of the PCU-2000 should assure that it is used in such an environment.			
Immunity test	IEC 60601 test level	Compliance level	Electromagnetic environment – guidance
Electrostatic discharge (ESD) IEC 61000-4-2	±6 kV contact ±8 kV air	±6 kV contact ±8 kV air	Floors should be wood, concrete or ceramic tile. If floors are covered with synthetic material, the relative humidity should be at least 30%.
Electrical fast transient/burst IEC 61000-4-4	±2 kV for power supply lines ±1 kV for input/output Lines	±2 kV for power supply lines ±1 kV for input/output Lines	Mains power quality should be that of a typical commercial or hospital environment.
Surge IEC 61000-4-5	±1 kV differential mode ±2 kV common mode	±1 kV differential mode ±2 kV common mode	Mains power quality should be that of a typical commercial or hospital environment.
Voltage dips, short interruptions and voltage variations on power supply input lines IEC 61000-4-11	<5 % U/T (>95 % dip in U/T) for 0.5 cycle 40 % U/T (60 % dip in U/T) for 5 cycles 70 % U/T (30 % dip in U/T) for 25 cycles <5 % U/T (>95 % dip in U/T) for 5 sec	100%-0.5cycle and 250 cycles (Performance Criteria A & B), 60%-5 cycles (Performance Criteria A), 30%-25c (Performance Criteria A)	Mains power quality should be that of a typical commercial or hospital environment. If the user of the PCU-2000 requires continued operation during power mains interruptions, it is recommended that the PCU-2000 be powered from an uninterruptible power supply or a battery.
Power frequency (50/60 Hz) magnetic field IEC 61000-4-8	3 A/m	Not applicable	Power frequency magnetic fields should be at levels characteristic of a typical location in a typical commercial or hospital environment.
NOTE U/T is the a.c. mains voltage prior to application of the test level.			

Normal Use Operating Instructions

To minimize drift, presoak the catheter pressure sensor in sterile water or saline for 30 minutes prior to balancing.

Connect the PCU-2000 Control Unit to the monitor and insert the DC power plug into the DC IN jack on the rear panel. Plug the other end of the power cord into the AC mains connection. Refer to Fig. 2.

Connect the power cord to the external power supply.

Set the PCU-2000 mode switch to STANDBY and the power switch to ON. Ensure power switch LED is illuminated on the back panel. If power LED does not illuminate, see troubleshooting section for additional help.

Adjust the monitor for a zero baseline. Ensure the 25 and 100 mmHg calibration buttons are in the off position.

Press the 25 mmHg CALIBRATION button, the 100 mmHg CALIBRATION button, or both buttons to get a 125 mmHg calibration signal, according to the desired range, and then adjust the monitor sensitivity.

Connect the catheter and extension cable to the PCU-2000 pressure input(s) on back of unit; channel 1 or 2 or both (Fig. 2). Turn the PCU-2000 function switch located on the front panel (Fig. 1) to TRANSDUCER and, with the pressure sensor just below the surface of water or saline and shielded from ambient light, adjust the TRANSDUCER BALANCE control to the same zero baseline as in step 3.

Place the catheter balance locking mechanism in the LOCK position.

The catheter is now ready for use. Refer to the catheter IFU for additional information.

During sustained use, calibration can be checked without removal of the catheter from the subject by switching the PCU-2000 function switch to STANDBY, reproducing the original zero baseline.

Subsequently, calibration signals equivalent to 25 mmHg, 100 mmHg, or 125 mmHg (using both switches) can be obtained by selecting the corresponding buttons.

To remove the transducer connections after use, simply hold the outside collar of the connector and pull out. The Power Input Connection and the Output Monitor Connection can be removed by holding the connector body and pulling out. Do not pull the cable of any connection to remove it from the back panel. Always use the connector body.

Figures



Fig. 1. PCU-2000 Front Panel Controls



Fig. 2. PCU-2000 Rear Panel

Interface and Adapter Cables

To purchase interface and adapter cables to connect pressure transducers and monitors, please contact Fogg System Company, Inc.

Fogg System Company, Inc
15592 East Batavia Drive
Aurora, CO 80011 USA
Phone: 303.344.1883
Fax: 303.344.1780
Email: Sales@foggsystem.com
Web site: www.foggsystems.com

Safety and EMC Testing Standards

Electrical Safety

This device was tested for electrical safety and approved under the general standard EN 60601-1.

Electromagnetic Compatibility (EMC)

This device was tested for electromagnetic compatibility (EMC) under the EN 60601-1-2 standard.

Guidance and manufacturer's declaration – electromagnetic emissions		
The PCU-2000 is intended for use in the electromagnetic environment specified below. The customer or the user of the Model 001 should assure that it is used in such an environment.		
Emissions Test	Compliance	Electromagnetic environment – guidance
RF emissions CISPR 11	Group 1	The PCU-2000 uses RF energy only for its internal function. Therefore, its RF emissions are very low and are not likely to cause any interference in nearby electronic equipment.
RF emissions CISPR 11	Class B	The PCU-2000 is suitable for use in all establishments, including domestic establishments and those directly connected to the public low-voltage power supply network that supplies buildings used for domestic purposes.
Harmonic emissions IEC 61000-3-2	Class A	
Voltage fluctuations/ flicker emissions IEC 61000-3-3	Complies	

Recommended Accessories

Only Millar accessories are to be used with the PCU-2000. All accessories are sold separately. When used in Canada, all connecting cables must comply with Canadian Electrical Code, Part 1. The use of accessories, transducers, and cables other than those specified or supplied by Millar Instruments, Inc. may result in increased EMI emissions or decreased immunity to EMC.

PCU-2000 Interface Cables

Cable Model	M. I. Part Number	Cable Length	Catheter End Connector Type
PEC-1.5C	850-5088	1.5 ft. (46 cm)	Viking
PEC-10C	850-5089	10 ft. (305 cm)	Viking
PEC-4D	850-5103	4 ft. (122 cm)	Low Profile
PEC-10D	850-5090	10 ft. (305 cm)	Low Profile

Note: Viking connectors are round with 4 pins. Low Profile connectors are flat with 4 pins.
Note: The maximum length of interface cables is 10ft. EMC testing has not been performed with longer cables.

Power Supply Information

Item	M. I. Part Number	Description	Connectors
Power Supply	249-2365 * GlobTek GTM21089-1305-T3	Power Supply	C14
North American Power Cord	850-5117	Power Cord	Hospital Grade NEMA 5/15 and C13
European Power Cord	850-5118	Power Cord	Type CEE 7/7 and C13

* This unit must be purchased from Millar Instruments. The separate power supply is considered part of this ME Equipment.
Power cords for locations other than North America and continental Europe may be acquired directly from Feller GmbH. Cords used in other regions will require a C13 connector for the power supply connection and the appropriate regional plug for connection to the power source. The cord must be SJT, 18AWG, and rated for at least 10 amperes at the appropriate regional voltage. The maximum power cord length is 8.2 feet or 2.5m.
You may contact Feller directly at the numbers listed below.

Web: www.feller-at.com	Austria	(+43) 256/6232
Feller GmbH	Great Britain	(+44) (191) 455 1048
Feller (UK) Ltd.	Hungary	(+36) (94) 512 730
Feller KFT	Hong Kong	(+852)280 68166
Feller-Neumayer LTD	USA	(732) 247-7333
Feller US Corp.		

Since monitors have different input wiring requirements, a control unit with a specified monitor input cable should be used only with same make and model of monitor for which it is supplied, even if the connector fits another monitor.
Millar does not assume responsibility for calibration of external monitors.

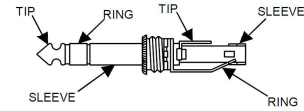
CAUTION: The bar graph pressure displays in Fig. 1 are intended for use in set-up and operation of the unit. The displays are intended to show a presence of signal. They are NOT intended to supply quantitative or qualitative signal information for use in diagnosis of patient condition.

Repair, Cleaning, Preventative Maintenance and Inspection

There are no user-serviceable parts inside the PCU-2000 or its accessories. If the unit or accessory is found to be defective, it MUST be returned to Millar Instruments for repair or replacement. The user must call Millar Instruments Customer Service to obtain a Return Material Authorization (RMA) number and specific instructions regarding the return of the PCU-2000 or accessory. All returns must have a RMA number.
The PCU-2000 should be cleaned periodically with a damp cloth and mild detergent, if needed. Disconnect the power connection from the unit before cleaning. Care should be taken to prevent excessive water from entering the case during cleaning. A 70/30 alcohol wipe may be used to disinfect the case; however, repeated use of alcohol may damage the case or labels. A diluted solution of bleach in water (<5 % bleach) may be used to disinfect the case exterior by wiping with a dampened cloth. The following items should be periodically checked as part of a yearly preventative inspection program. Check the plastic nuts on the PRESSURE INPUT connectors to ensure that they are secure. Hand-tighten, if needed.
Check all switches to ensure that they are fully seated into the case.
Verify that the plastic feet are securely attached to the bottom of the case. Replace any missing feet.
Check the enclosure to ensure that the cover is securely installed on the base. Inspect the horizontal seam to verify that it does not have a visible clearance that can be pulled apart. To secure the top to the bottom, place the unit on a flat surface and press firmly down on each side to snap the top to the bottom. The PCU-2000 should be tested yearly by the user for electrical safety per the ANSI/AAMI (ES1) standard for Safe Current Limits for Electromedical Apparatus.

Output Connector Wiring

Pressure Output Connection
The customer is to supply a 1/4" phone plug which mates with the model PCU-2000 PRESSURE OUTPUT connector. An example plug is the Switchcraft® #267, which is a 1/4" 3-conductor phone plug or equivalent. The input and output are isolated from ground but they are connected to each other. See accessories section.



DC Amplifier with Differential Input Circuitry

Tip	+ Signal
Ring	- Signal
Sleeve	Cable Shield

DC Amplifier with Single-ended Input Circuitry

Tip	Signal Input Lead
Ring and Sleeve	Cable Shield

Reverse Polarity

Ring	Signal Input Lead
Tip and Sleeve	Cable Shield

CAUTION: Millar Instruments, Inc. cannot assume responsibility for the performance of the PCU-2000 if the plug is incorrectly wired.
Use shielded wire \geq 3 feet in length for the output cable. Using longer cable could result in noise pickup to your monitor.

Troubleshooting

Effect	Cause	Solution
No power light illuminated on power switch	No AC mains power to external power supply	Check to be sure that the AC power cord is securely plugged into power supply
		Ensure that the DC input power cable is securely attached to back of PCU-2000 unit
		Ensure that the circuit breaker supplying AC mains power to the system has not been tripped
No light(s) illuminated on LED bar graph	No AC Mains power to external power supply	Check to be sure that the AC power cord is securely plugged into power supply
	No transducer is plugged into PCU-2000	Plug transducer into PCU-2000
	Faulty Transducer	Replace with known good transducer
	PCU-2000 is defective	Contact Millar Customer Service for RMA to return unit

Vita

Jeffrey C Kahn, Jr. was born in Philadelphia, PA and attended Swarthmore College, graduating in 2010 with a B.A. in English Literature and a B.S. in Engineering. He attended Drexel University from 2010 and graduated in 2016 with a Ph.D. in Mechanical Engineering and Mechanics. He has published and presented work in biologically-inspired robotics, haptics, system identification, and underwater propulsion. He has had a featured article in the *Bioinspiration & Biomimetics* Journal and his work in the *IEEE Transactions on Haptics* Journal was featured in the international *HAPTICS 2016* conference with an invited talk in Philadelphia, PA. He has presented his work and given technical demonstrations in international conferences in Vilamoura, London, Tokyo, and Philadelphia. He has received multiple International Travel Awards and is the recipient of the Koerner Family Fellowship at Drexel University. He is a member of the IEEE Robotics and Automation Society and serves on the Conference Activities Board. He currently lives in Philadelphia with his wife, Lizzie, and his Akita, Oki.

